

NEW APPLICATIONS OF REMOTE SENSING TECHNOLOGY
FOR
OFFSHORE WIND POWER

by

Bruce M. Williams

A thesis submitted to the Faculty of the University of Delaware in partial fulfillment
of the requirements for the degree of Master in Marine Policy

Spring 2013

Copyright 2013 Bruce M. Williams
All Rights Reserved

NEW APPLICATIONS OF REMOTE SENSING TECHNOLOGY
FOR
OFFSHORE WIND POWER

Bruce M. Williams
Spring 2013

Approved: _____
Willett Kempton, Ph.D.
Professor in charge of thesis on behalf of the Advisory Committee

Approved: _____
Mark A. Moline, Ph.D.
Director of the School of Marine Science and Policy

Approved: _____
Nancy M. Targett, Ph.D.
Dean of the College of Earth, Ocean, and Environment

Approved: _____
James G. Richards, Ph.D.
Vice Provost for Graduate and Professional Education

ACKNOWLEDGEMENTS

This effort was enabled, encouraged, and inspired by many people deserving of my gratitude, but I would especially like to thank my official advisor, Dr. Willett Kempton, and my ex officio advisor, Dr. Jeremy Firestone, for the opportunities and guidance they provided, not to mention the excellent academic instruction. I would also like to thank the Okie family for the fellowship assistance provided through the Marian R. Okie memorial endowment.

Thanks to my fellow students, for their camaraderie and feedback, to my family, for understanding and accomodating my long absences and odd hours, to my dog, for his patience, to my old G4 laptop for not breaking down, and to my Dad, for his service as a sounding board and sanity check.

This work is dedicated to my mother, Barbara Roetzel Williams, recently passed, who encouraged and inspired me to persevere in all things of importance.

TABLE OF CONTENTS

LIST OF TABLES.....	ix
LIST OF FIGURES.....	xi
LIST OF ACRONYMS.....	xv
ABSTRACT.....	xx

Chapter

1 BACKGROUND AND METHODOLOGY.....	1
1.1. Introduction.....	1
1.2. Background -Need for Renewables	4
1.2.1. Need to Reduce Cost of Offshore Wind Power	6
1.2.2. Need to Measure Complex Energy Field.....	7
1.2.3. Different Paradigm than Conventional Generation	7
1.3. Methodology.....	8
1.3.1. Study Area	9
1.3.2. Base Case Turbine, Foundations, and Control System.....	10
1.3.3. Base Case Siting, AEP.....	10
1.3.4. Cost Benefit Calculations	11
2 SURFACE SENSOR EVALUATION	13
2.1. Conventional Technology.....	13
2.1.1. Cup and Ultrasonic Anemometers	14
2.1.2. Conventional Meteorological Buoys	15
2.1.3. Meteorological Towers	16
2.1.4. Conventional Nacelle Mounted Anemometers	18
2.2. Light Detection and Ranging (Lidar).....	18

2.2.1. Pulsed Laser (PL) vs. Continuous Wave (CW) Lidar.....	23
2.2.2. Lidar vs. Conventional – Range and Accuracy.....	25
2.2.3. Long Range Lidars.....	32
2.2.4. Other Scanning Lidars	33
2.2.5. Floating Lidar Systems	39
2.2.6. Summary – Floating Platform Lidar	48
3 ORBITING SENSOR EVALUATION	49
3.1. Satellite Microwave Radar/Radiometry (SMRR).....	50
3.1.1. Data Sets and Product Level	51
3.1.2. Geophysical Model Functions and Wind Retrieval Tools	53
3.1.3. Satellites and Instruments	54
3.1.4. Orbits and Coverage, Swaths and Scenes	56
3.1.5. Data Flagging, Masking, and Scrubbing.....	58
3.1.6. Polarization	59
3.1.7. Multi-Modal Operation.....	60
3.1.8. Cross Check Inventory Methodology	60
3.2. Synthetic Aperture Radar.....	62
3.2.1. SAR - ERS-1 and 2	65
3.2.2. ASAR.....	68
3.2.3. ScanSAR/ RadarSAT-1 and 2.....	78
3.2.4. SAR Inventory Summary.....	80
3.2.5. SAR Accuracy Summary	81
3.3. Scatterometers.....	82
3.3.1. QuikSCAT	85
3.3.2. ASCAT -Metop A and B	98
3.3.3. OceanSAT-2	101
3.3.4. Scatterometer Inventory Summary	102
3.3.5. Scatterometer Accuracy Summary.....	103
3.4. Passive Microwave Imaging (Radiometers).....	104
3.4.1. WindSat (Meissner and Wentz 2006).....	105
3.4.2. SSMI (Mears et al 2001).....	106
3.4.3. PMI/SSMI Accuracy, Inventory, Resolution.....	109
3.5. Summary - SMRR Inventory.....	110

3.6. Summary - SMRR Snapshot Accuracy.....	111
3.7. Summary – SMRR for Energy Density, AEP.....	114
3.7.1. Sample Size and Uncertainty	116
3.7.2. Time Series Length and Uncertainty	119
3.7.3. Case Study - Project NorseWind	120
3.7.4. 4C-Offshore	124
3.8. Conclusions - SMRR Wind Mapping and AEP.....	125
4 STRATEGY DEVELOPMENT; COMBINING TECHNOLOGIES	131
4.1. Data Collection Campaign.....	132
4.1.1. Lidar Buoy -Data Collection.....	132
4.1.2. SMRR - Data Collection	134
4.2. Calibration Campaign	135
4.2.1. Sigma-0 Conversion and Vertical Extrapolation Error.....	135
4.2.2. Parametric Uss Correction	136
4.2.1. Parametric Extrapolation Model	137
4.3. Re-processing Archival Datasets With Tuned GMFs.....	138
4.4. Remaining Bias and Mitigating Factors	141
4.5. Conclusions- Accuracy of LCGMF Based AEP Mapping	143
5 SITE SELECTION BENEFITS.....	145
5.1. Resource Assessment – Background and Purpose.....	145
5.2. Site Selection- Current Practices	147
5.2.1. Historic In Situ Datasets	148
5.2.2. Wind Models and Resource Mapping.....	150
5.2.3. Site Selection - Shortcomings.....	160
5.3. Variability of Resource on the MAB OCS	161
5.3.1. Wind Gradients and Variability	163
5.4. Site Selection Benefits– With LCGMF AEP Mapping	164
5.4.1. Cost Reduction vs. Benefit Increase	166
5.4.2. Reference Station Proximity Effect	167

5.4.3. Conclusions – Site Selection/Improved Mapping Benefits	167
5.4.4. Coordinated Vs. Individual RA Efforts	169
6 AEP P90 BENEFITS	170
6.1. Financing and Uncertainty.....	170
6.1.1. Boquet et al 2010	171
6.1.2. DNV Uncertainty Model.....	172
6.1.3. Ecofys 2013	176
6.1.4. Betancur et al 2008	176
6.2. AEP P90 – Benefit Calculations	177
6.2.1. Relating Risk, Finance Cost, and AEP -Levitt et al 2012.....	178
7 ROTOR CONTROL BENEFITS	180
7.1. Background - Rotor Control Systems	180
7.1.1. Fatigue Life and Damage Equivalent Loading	181
7.1.2. Control Strategies and Regions.....	182
7.2. Yaw Control – (Regions 2, 3, and 4) Current Practice	184
7.3. Yaw Control – Lidar Simulation Studies.....	185
7.3.1. Yaw Control Study Y1 –Schlipf 2012	186
7.3.2. Yaw Control Study Y2- Blue Scout (Gaiser et al 2013).....	188
7.3.3. Yaw Control - Fatigue Loading	189
7.3.4. Yaw Control Simulation Studies, Summary.....	190
7.3.5. Lidar Assisted Yaw Control - Future Field Studies.....	190
7.4. Speed Control (Regions 2 and 3) – Current Practice.....	192
7.4.1. Region 2 - Torque Control.....	193
7.4.2. Region 3 - Pitch Control	195
7.5. Speed Control With Lidar	196
7.5.1. Speed Control - Optimal Look Ahead Time and Range.....	197
7.5.2. Speed Control Simulation Studies	199
7.6. Summary - RC Benefits	213

7.6.1. Extreme Operating Gust and Fatigue Loading	214
7.6.2. Increased AEP from Yaw Controls.....	215
7.6.3. Increased AEP from Speed Controls (Pitch)	216
7.6.4. New Blade Designs with Lidar-Assisted Load Reductions	216
7.6.5. Wake Effects	221
7.6.6. Lidar-Assisted Rotor Control – Costs.....	221
7.6.7. Looking Forward-RC Benefits	223
8 SUMMARY DISCUSSION AND CONCLUSIONS.....	225
8.1. Summary Benefits.....	225
8.2. Summary Discussion and Conclusions	226
8.2.1. Conclusions – Rotor Control Benefits	226
8.2.2. Conclusions –Annual Energy Production P90 Benefits	227
8.2.3. Conclusions – Mapping Benefits	228
8.2.4. Areas for Further Research.....	229
REFERENCES.....	231
Appendix	
A MAXIMUM THEORETICAL COVERAGE.....	258
B REPRINT PERMISSIONS.....	262

LIST OF TABLES

Table 1	Basic Performance Specs of Two Wind Lidars	21
Table 2	WindCube Extended Range Performance Specs	33
Table 3	WindSentinel Performance Specifications	41
Table 4	SMRR Satellites Used in This Analysis and Their Service Lives	56
Table 5	Maximum Theoretical Coverage, SMRR	62
Table 6	ASAR coverage per 35 day cycle, by latitude	69
Table 7	Error statistics for three met masts vs. SAR Retrievals	77
Table 8	SAR Coverage and Inventory Summary	81
Table 9	Bias and SD for three resolutions	90
Table 10	Error and Correlation Statistics, QuikSCAT vs. Met Towers	93
Table 11	Scatterometer Inventory.....	103
Table 12	Scatterometer Accuracy Statistics	104
Table 13	Error Characteristics by Satellite Number	108
Table 14	SMRR Inventory Summary	111
Table 15	SMRR Error Statistics Summary.....	112
Table 16	SMRR Energy Density Error Statistics	116
Table 17	Sample Size for Accurate Estimates of Wind Statistics	117
Table 18	The Effects of Time Series Length on Production Estimates	120

Table 19	Properties of Different Wind Sensing Technologies	128
Table 20	SMRR Based AEP Error Sources and Mitigating Factors	142
Table 21	Wind Parameters for AEP and Site Selection.....	146
Table 22	Post-Exclusion Area and Production Capacity by Depth, MAB OCS,	156
Table 23	DNV Model Results – Three Case Studies.....	175
Table 24	Summary of Yaw Control Simulation Studies	190
Table 25	Production and Fatigue Loading for ISC and DSC	201
Table 26	Fatigue Loads, Production, and Deviation, Baseline, NMPC.	202
Table 27	DEL Mitigation by Turbine Class and Rayleigh A	204
Table 28	EOG Loading for Baseline vs. NMPC Control	205
Table 29	Sawtooth Gust Frequency from WindSentinel Data, Lake Michigan	212
Table 30	Rotor Control Benefits Summary Table	215
Table 31	Blade Root Bending DEL Changes with AALC, NMPC.....	220
Table 32	Summary of RC Benefits for Single Turbine, Wind Farm, and Buildout ...	223
Table 33	Summary of Benefits vs. Base Case	226

LIST OF FIGURES

Figure 1	NDBC 44025	17
Figure 2	Cape Wind Met Tower	17
Figure 3	Leosphere WindCube	20
Figure 4	Natural Power ZephIR	20
Figure 5	Doppler Shift Lidar, Beat Detection Schematic	22
Figure 6	Laser vectors and scan configurations of WindCube (L) and ZephIR (R)	22
Figure 7	Error Comparison for CW and Pulsed Lidar by Height	25
Figure 8	Scatter Plot and Correlation Values	28
Figure 9	Deviation and Uncertainty of Cups vs. Lidar	29
Figure 10	Hub Scanning Lidar	35
Figure 11	Radial Plot of U of Incoming Wind Field Profile	36
Figure 12	Wind profile, Spinner Lidar vs. Cup	36
Figure 13	G4000 Image of Turbine Wakes-Alpha Ventus	38
Figure 14	WindSentinel Metocean Buoy System	42
Figure 15	U bias between fixed and moving Lidar	43
Figure 16	Scatter Plot and Correlation Analysis	44
Figure 17	SeaZephIR and LandZephIR wind speed at 90m	45

Figure 18	New Jersey Offshore Research Device (NJORD)	46
Figure 19	Scatter Plot and Correlation Analysis	47
Figure 20	SMRR Systems Included in Analysis.....	55
Figure 21	Polar SunSynchronous Orbits	57
Figure 22	SAR scenes around Denmark	57
Figure 23	RadarSAT-2 SAR Scan Patterns	65
Figure 24	Sample SAR Wind Product around Horns Rev	67
Figure 25	Envisat ASAR image, Horns Rev	72
Figure 26	Backscatter Across Transect, Horns Rev	72
Figure 27	ASAR Product around Denmark	74
Figure 28	NRCS Image from RADARSAT-1	79
Figure 29	ANSWRS retrieval, from Monaldo 2012	79
Figure 30	Scatterometer Scan Pattern Example	84
Figure 31	Scatter Plot, QuikSCAT vs. Horns Rev. f	87
Figure 32	Scatterplot- QuikSCAT vs. 18 Buoys/Stations	89
Figure 33	Ku2011GMF QuikSCAT vs. Buoy Data - Wind Speed PDF	91
Figure 34	Density of Scrubbed QuikSCAT Scans, North and Baltic Seas	94
Figure 35	Wind Index for Various Sources of Wind Data	96
Figure 36	ASCAT Coastal Product, 12.5km resolution	99
Figure 37	Zoom in, ASCAT Coastal Product, 12.5km resolution	99
Figure 38	All Buoys, Mean SSMI Deviation	108
Figure 39	NDBC 44004 vs. SSM/I F11 Deviation	108

Figure 40	No. of samples needed for +/-10% estimate	118
Figure 41	NorseWind Map Product Sample - Hrs. at Full Capacity Vestas V80	122
Figure 42	Mean Wind Speed Around Horns Rev	123
Figure 43	Mean Wind Speed at 100m around Horns Rev	125
Figure 44	Wind Speed Uncertainty at 100m	125
Figure 45	Proposed Lidar Buoy Stations (green stars) and Historic Met Stations	133
Figure 46	Flowchart of Proposed Methodology	140
Figure 47	NDBC Offshore Met Stations in MAB with > 5 yrs. Of Data	149
Figure 48	Meso Map Generation Process Diagram	152
Figure 49	MesoMap Wind Map offshore NJ	153
Figure 50	MAB OCS Depth Zones by Foundation Type	155
Figure 51	Absolute Error, WRF vs. CHLV2, August 2008	157
Figure 52	Mean Wind Speeds @ 90m, MAB OCS	158
Figure 53	Mean Wind Speeds @90m, Wilmington Canyon	159
Figure 54	90m Mean Wind Speeds	164
Figure 55	Effect of Uncertainty on P90 AEP using PDF Curve	172
Figure 56	Sensitivity of BP to Four Cost and Production Factors	179
Figure 57	Lidar Assisted Rotor Control	183
Figure 58	Turbine Operating Regions	183
Figure 59	Feed-Forward Controller Schematic	183
Figure 60	Idealized Torque and Pitch in Regions 2 and 3	193
Figure 61	Tip Speed Ratio versus Power Coefficient	194

Figure 62	Optimal Look-Ahead Times for Pitch Control	198
Figure 63	UPwind Case 4 Simulated Lidar Scan Configuration	204
Figure 64	Wind Speed and Pitch Angle During EOG	209
Figure 65	Power Production and Tower Deflection During EOG	210
Figure 66	Sawtooth Gust Event Frequency	213
Figure 67	AALC Blade Section Schematic, from Berg et al 2009.....	219

LIST OF ACRONYMS

AALC - Active Aerodynamic Load Control

ABS – American Bureau of Shipping

AEP - Annual Energy Production

AMI – Active Microwave Instrument (ERS satellites)

AP – Alternating Polarization

APL – Applied Physics Laboratory

ARW – Advanced Research Weather Forecasting Model

ASAR – Advanced Synthetic Aperture Radar

ASCAT – Advanced Scatterometer

ASL – Above Sea Level

AST – Air Surface Temperature (at sea level)

BOEM – Bureau of Ocean Energy Management

BP - Breakeven Price

BYU – Brigham Young University

CF – Capacity Factor

CMOD – C-Band Modeling

CNR – Carrier to Noise Ratio

CSA – Canadian Space Agency

CW – Continuous Wave

DEL – Damage Equivalent Load

DEWI - German (Deutsche) Wind Energy Institute

DMSP - Defense Meteorological Satellite Program

DNV – Det Norske Veritas

DOD – Department of Defense

DOE – Department of Energy

DOI- Department of Interior

DSC – Direct Speed Control

DTU – Danish Technical University

ECN – Energy Research Center of the Netherlands

ENW –Equivalent Neutral Wind

EOG – Extreme Operating Gust

EOLI – Earth Observation Link

ERS – European Remote Sensing

ESA – European Space Agency

EUMETSAT – European Organisation for the Exploitation of Meteorological Satellites

FAST - Fatigue, Aerodynamics, Structures, and Turbulence modeling software

GIS – Geographic Information System

GMF – Geophysical Model Function

GVSU - Grand Valley State University (Michigan)

HIRLAM – High Resolution Limited Area Model

ISC – Indirect Speed Control

ISRO – Indian Space Research Organisation

LCGMF – Lidar Calibrated Geophysical Model Function

LCOE – Levelized Cost of Energy

Lidar – Light Detection and Ranging

LSS – Low Speed Shaft

MAB - Mid Atlantic Bight

MIMO – Multiple Input Multiple Output

NASA – National Aeronautic and Space Agency

NDBC - National Data Bouy Center

NESDIS - National Environmental Satellite, Data, and Information Service

NJORD - New Jersey Ocean Research Device

NMPC – Non-linear Model Predictive Control

NOAA - National Oceanic and Atmospheric Administration

NPV – Net Present Value

NRCS – Normalized Radar Cross Section

NREL - National Renewable Energy Laboratory

NWP - Numerical Weather Prediction

OCS – Optical Control System

OCS - Outer Continental Shelf

OSI-SAF - Ocean and Sea Ice Satellite Application Facility

P90 – Value with a 90% exceedance probability in any year

PDF – Probability Density Function

PI – Proportional/Integral

PID – Proportional Integral Derivative

PJM-ISO – PJM (Pennsylvania, Jersey, Maryland) - Independent System Operator

PL – Pulsed Laser

PMI- Passive Microwave Imaging

PPA – Power Purchase Agreement

Radar – Radio Detection and Ranging

RA – Resource Assessment

RAVE - Research at Alpha Ventus

RC – Rotor Control

RHC – Receding Horizon Control

RMSE - Root Mean Square Error

RSS – Remote Sensing Systems

SAR – Synthetic Aperture Radar

SD – Standard Deviation

SDIS – Stability Dependent In Situ

SISO- Single Input Single Output

SMRR – Satellite Microwave Radar and Radiometer

Sodar – Sonic Detection and Ranging

SSMI – Special Sensor/Microwave Imager

SST – Sea Surface Temperature

TAO – Tropical Atmosphere Ocean

TSR – Tip Speed Ratio

UHR – Ultra High Resolution

USA – Ultrasonic Anemometer

WASP – Wind Atlas Analysis and Application Program

WEA – Wind Energy Area

WRF – Weather Research and Forecasting

WRF AR – Weather Research and Forecasting–Advanced Research Model

WSM – Wide Swath Mode

ABSTRACT

Efficient development of offshore wind power will require accurate information about the wind field on a wide range of spatial and temporal scales. Lidar and Satellite Microwave Radar/Radiometry have been evaluated and used for wind speed measurement.

Numerous studies have been published that examine the error, bias, and performance characteristics of variants of both technologies under a range of conditions. This paper reviews recent research and technological advances and outlines strategies for applying the technologies to reduce costs, increase energy production and improve energy forecasting through advanced rotor controls and more accurate resource estimation and mapping.

A literature search was conducted to identify the most recent and relevant correlation and validation studies of Lidar, synthetic aperture radar, scatterometers, and radiometers used for estimating wind speed. Database queries were conducted to estimate inventory for satellite wind data. Estimates of the accuracy (bias and uncertainty) and availability (sample density) of these technologies were developed based on the literature search and database queries. Both “snapshot” wind speed and energy density estimates were compared for satellite microwave systems and Lidar technologies. Offshore, where

turbulence is lower, Lidar is found to have very high accuracy and availability, comparable to cup anemometers at a range of up to 200m on fixed platforms. Floating Lidar is rapidly approaching the same level of accuracy and availability, and is easily re-positioned. However, the short time series of Lidar is less useful for long term indexing, and it is limited to a single site per sensor. Satellite microwave wind retrievals are available over a 20 year period and are found to have good time-averaged accuracy at 10 meters above sea level for wind speeds between 3 and 15 m/s, but are subject to minor bias (below +/- 0.2 m/s) from the use of inaccurate shear profiles, from diurnal effects, and from local metocean conditions. Three strategies for use of these technologies are outlined and evaluated.

- Siting and Resource Assessment - By processing all available satellite microwave data sets, calibrated with data from a one year field campaign using floating Lidar systems, cross-correlated through a parametric geophysical model function, bias and error of wind speeds generated from the satellite data can be reduced, and wind mapping can be significantly improved in resolution and accuracy.
- Energy Production Estimates- By using wind profile data from floating Lidars, deployed on site, and indexed to a 20 year time series from calibrated satellite wind data, Annual Energy Production estimates can be greatly improved by reducing uncertainty (and thus, the risk premium on

financing). In the near future, this methodology can obviate the need for a met tower for resource assessment.

- Rotor Control - By using nacelle or hub mounted Lidar to look upstream, new Lidar-assisted control systems can adjust blade pitch and nacelle yaw pro-actively to match rapid changes in wind speed or direction. This can reduce fatigue and extreme gust loading on components, allowing longer blades and greater swept area. It can also improve efficiency by reducing yaw mis-alignment.

In addition to power production benefits, rough, first-order costs were developed to check economic justification, and the expected change in Breakeven Price was calculated for two different build-out scenarios of the study area. The analysis indicates that the recommended strategies for improving Rotor Control and reducing uncertainty of AEP estimates can reduce the Breakeven Price of power for the base case wind farm by at least 4%.

The benefits of improved mapping are more difficult to monetize due to high levels of uncertainty in all the primary factors, so two different scenarios are considered. If the benefits of improved mapping and better siting (2% to 3% lower BP) are available to the first ten or twelve projects, and the mapping effort is federally funded, or the costs are somehow distributed industry-wide over full build-out of the study area, the Breakeven

Price for the first phase of wind farms could be reduced by a total of around 6% to 7%. If mapping benefits are assumed to diminish over time as the study area builds out, the long term, annualized reduction in Breakeven Price over the entire study area will be lower, at around 4% to 5%. In either case the mapping effort is justified, and the cost can be reduced by about \$120 million using Lidar equipped met buoys.

Keywords: offshore wind power, wind resource assessment, satellite radar, Lidar, floating Lidar, AEP estimates, wind turbine pitch control, wind turbine yaw control, wind energy mapping

Chapter 1

BACKGROUND AND METHODOLOGY

1.1. Introduction

This paper investigates three applications of Light Detection and Ranging (Lidar) and Satellite Microwave Radar and Radiometer (hereafter referred to as “SMRR”) remote sensing systems and their potential for improving performance and reducing the cost of energy from offshore wind, which faces challenges unique to the ocean environment. The applications operate on temporal and spatial scales ranging from multi-year, regional wind mapping to single turbine, high frequency upstream sampling, and are described briefly below.

- **Energy Mapping and Site Selection** : By enabling faster, cheaper collection of orders of magnitude more wind data, Lidar and SMRR can allow assessment of offshore wind resources with unprecedented spatial and temporal resolution and accuracy. Orbiting SMRR sensors can provide wide coverage wind speed estimates over multi-year sampling periods, which can be calibrated and corrected using meso-scale modeling and multiple observational data sets from existing met

stations and Lidar buoys. These data can then be spatially resolved and time averaged to produce accurate, detailed wind resource atlases, ensuring selection of the optimal wind farm location.

- **Annual Energy Production (AEP) estimates:** The use of in situ Lidar combined with SMRR data can reduce uncertainty in AEP in two ways. First, by providing a twenty+ year time series, SMRR can help determine where the shorter Lidar time series falls on the wind index¹. Second, by providing accurate, high frequency measurements up to 200m ASL, Lidar can reduce the uncertainty associated with horizontal and vertical extrapolation of the SMRR data. Reducing the uncertainty in wind speed measurements increases the “P90” value (AEP level that has a 90% probability of being met or exceeded in any year), which is a principal measure of the “bankable” value of a wind project.
- **Rotor Control (RC):** Lidar units can be mounted on the nacelle or rotor of a turbine to look upwind to scan the wind field up to 200 m away. The information can be used to direct the rotor control system, providing more accurate information and advance notice of changes in speed or direction of the incoming wind stream. This allows time for pitch and yaw controls to pro-actively

¹ The wind index accounts for the spectrum of both monthly and inter-annual variability. For example if the Lidar time series covered a particularly energetic year, the AEP may overstate the long term average.

optimize the rotor aerodynamics to synchronize more closely with wind speed and direction changes. Lidar assisted pro-active control can increase power output and reduce fatigue loads on turbine components by reducing mis-alignment of the rotor (yaw control) and by feathering the blades to attenuate gust loading during normal operation (pitch control). These load reductions can allow lighter, cheaper components, or conversely, changes to operation that capture more energy (e.g., higher cut-out wind speed or longer blades).

No comprehensive analysis can be found in the published literature that looks at the benefit potential of all three from a power production/cost perspective. Most of the cited studies looked at only one instrument or control system or wind regime, and they do not all share uniform simulation environments or assumptions. Although this makes direct comparison difficult, some valid and valuable conclusions can be synthesized from a careful examination of the overall results.

This paper examines future Lidar and SMRR applications for offshore wind energy and provides a forward looking, first-order estimate of the costs and benefits of implementing the three strategies outlined. The introduction outlines the need for renewable energy in the US and explains why offshore wind power is the only feasible option for meeting that need in the mid-Atlantic region in the foreseeable future. The introduction also discusses the importance of characterizing the wind offshore and the shortcomings of conventional

technology. It then outlines the methodology used, setting up the evaluation of remote sensing technologies and the cost benefit analysis.

1.2. Background -Need for Renewables

Although modern civilization was built on fossil fuels, the vast amounts used to get us here did not come cheaply or cleanly. Coal, oil, and gas extraction, refinement, transport, and combustion release toxins and carcinogens, and are the primary source of atmospheric CO₂ emissions, and thus the primary source of anthropogenic climate change (IPCC 2007, Gale et al 2006) and ocean acidification, (Orr et al 2005) Fossil fuels burned for power generation and transport alone created 63% of global CO₂ emissions in 2010 (IEA 2012, Figure 5). In addition, structural economic dependence on a limited commodity for which global demand will exceed supply by ever increasing margins is a recipe for disaster. There are also huge indirect costs of using fossil fuels. A recent public health study by the Harvard Medical School found that the price of coal energy would nearly double if the public health and environmental costs were included (Epstein et al 2011). Another study from the Brookings Institution estimated it would increase by more than 170% (Greenstone and Looney 2011). The U.S. spends over a quarter trillion dollars a year to buy foreign oil, comprising over half of our trade deficit (US Census, 2009-2011). Dependence on this foreign oil has hobbled our nobler policy objectives in the middle east for decades, arguably costing the U.S. thousands of lives and trillions in defense dollars. Last but certainly not least, the looming threat of a

catastrophic, heat-trapping overdose of atmospheric CO₂ can no longer be ignored by any rational, informed person. The recent shift towards cheaper natural gas may attenuate fuel price escalation for a while, but a recently published, peer-reviewed study found that only by rapidly switching our power generation over to zero emissions sources can we prevent global warming continuing through the second half of this century, potentially reaching 4° C (Mhyrvold and Caldeira 2012).

Renewable energy represents much more than just a safer way of powering the grid or pushing our vehicles; it will transform modern civilization in many ways, powering the transformation from the depletion-combustion-pollution paradigm into the renewable-sustainable-production paradigm. Technology is rapidly advancing to the point where renewable energy can provide much of our electricity and transportation needs without any of the negative impacts of fossil fuels (Kempton et al 2007, Delucchi and Jacobson 2011, Budischak et al 2013). With strategic public investment in research, development, and infrastructure, renewable energy costs will come down steadily. As experience is gained and technology improves, this trend will continue until most renewables can be commercially developed without public support. In contrast, fossil fuel costs will continue to go up, as one would expect with growing demand for a limited resource with rising environmental impacts and production costs.

Unless we discover some long-shot breakthrough such as fusion or safe fission, economics will force a large scale transition to renewable energy over the next few

decades. In this author's opinion, the losers will be those nations that continue to foster their fossil fuel dependency in the face of rapidly mounting costs, looming carbon taxes, and inevitable depletion over the long term. The winners will be those nations with the foresight to invest in new wind, solar, biomass, hydrogen, and geothermal industries now, while developing the technologies and supply chains that will dominate the global energy market for decades to come.

1.2.1. Need to Reduce Cost of Offshore Wind Power

Wind power is by far the fastest growing renewable energy sector, and rivals natural gas for new capacity additions since 2007 (US EIA 2013). It also has the greatest potential for scaling up in the U.S. Many onshore wind farms in the plains states are already operating at grid parity, and a recent study predicts overall grid parity (competitive without subsidies) for the industry average wind farm by 2016 (BNEF 2011). In the northeast US however, there are not a lot of open, windy spaces left for large scale onshore development, but there is great potential offshore. A recent study conducted by the National Renewable Energy Laboratory (NREL) concluded that the available offshore wind power resources of the US exceeds the 2010 US electrical generation capacity by a factor of 4 (Schwartz et al 2010). An even more recent study found that with the exception of summer time peak demand, all East Coast states' electrical demand could be satisfied using east coast offshore wind energy (Dvorak et al. 2012). The study also found that the mid Atlantic Bight of the U.S. outer continental shelf (MAB-OCS)

presents the most favorable area for development, with high winds, shallow water, and low hurricane risk. This revelation has led to a significant interest in offshore wind power to serve the major load centers of the eastern seaboard. At present, finance, construction, and operating costs are much higher offshore (Levitt et al 2012), since the industry is relatively new, the environment is more challenging, and risks are higher.

1.2.2. Need to Measure Complex Energy Field

Many new offshore wind turbine technologies are coming on line that can help achieve the needed cost reductions, including larger rotors, newer generator designs, lower cost foundations, faster installation methods, and advanced monitoring and data acquisition systems. All these technologies are power plant focused, but there is also a great need for information and innovation that is energy supply focused. There is a good reason the wind is used as allegory for something that is unseen, uncontrollable, and unpredictable. Meteorologists can statistically characterize the behavior of weather systems or the wind speed over a given area or a given length of time, but any prediction of the precise wind speed at a single point, more than a few minutes ahead would be highly uncertain.

1.2.3. Different Paradigm than Conventional Generation

A unique feature of wind energy compared to other forms of electrical power generation is that it exists in a space that is effectively bounded on one side only (the earth surface),

is constantly changing at every point, and is beyond human control. Conventional power plants (natural gas, steam, and hydro turbines) also rely on fluid flows to turn a shaft to generate electricity, but they all extract power from a tightly controlled, physically constrained, regulated fluid flow. These older technologies control the flow field inside a machine, while wind turbines control the machine inside the flow field – a fundamental paradigm shift. Since the wind cannot be controlled, it must be closely studied and monitored. For this reason, information about the wind field can help determine the safest and most cost effective siting and operation of the turbines and the wind farm, significantly increasing power output and reducing the cost of energy.

1.3. Methodology

The study methodology is executed in three steps; described below;

- **Literature Search and Synthesis** - Using over 40 recently published case studies on the use of Lidar and SMRR for wind speed and power production estimates, the sensor and database characteristics of Lidar and SMRR are investigated. This is presented in Chapter 2 and Chapter 3 .
- **Strategy Development** - In the second step, strategies are developed to make use of the technologies in an optimized program to increase energy production and/or reduce costs. This is presented in Chapter 4.
- **Net Benefit Calculations and Discussion** - In the third step, the costs and benefits of the strategies are evaluated in terms of their effect on the Breakeven Price (BP) for a base case wind farm in intermediate waters of the mid Atlantic Bight OCS. This is presented in Chapter 5 to 7. Chapter 8 presents a discussion of the costs and benefits, and presents some conclusions.

1.3.1. Study Area

The study area is a roughly rectangular area between the 30m and 60m isobaths in the mid Atlantic Bight Outer Continental Shelf (MAB OCS). Shallower depths in this area, suitable for monopile foundations (up to 30 m) have already been analyzed for developable space, and “Wind Energy Areas” (WEAs) have been identified and are being made available for leasing by the Dept. of Interior (BOEM 2011). The benefits of improved resource assessment will not be as high in the WEAs, since available area is limited due to large exclusion zones. Dvorak et al (2012) estimated that in the MAB region, in depths up to ~30m, where monopile foundations are usually optimal, only about 3–4% of peak mid-Atlantic states (PJM-ISO) grid power demand could be generated, but the fraction goes up to ~ 20% for depths between 30 and 60 m. Beyond about 60m, floating foundation technology will likely be required, which is proving more difficult than anticipated, and is probably at least ten years away from commercial utility scale deployment. Depths from 30m to 60m are generally considered suitable for existing, proven bottom mounted foundations such as tubular strut tripods, quatropods or lattice jackets. The study area for this analysis is therefore this “intermediate” depth zone of the MAB (offshore Virginia to New Jersey, inclusive), which could begin to see development in the next five to ten years, and could benefit from improved resource mapping.

1.3.2. Base Case Turbine, Foundations, and Control System

The costs and benefits are estimated by first defining a base scenario which does not employ any of the technologies evaluated. For the sake of standardization and more direct comparison to other simulation studies, the analysis uses the NREL reference 5MW offshore turbine² on a jacketed quattropod foundation (Jonkman et al 2009). This foundation was selected based on its suitability for the depths considered and its record of service in the North Sea.

1.3.3. Base Case Siting, AEP

To estimate economic benefits of an improved resource assessment strategy, a baseline must be defined. Although there are commonly used standards in the EU for determining AEP, in the U.S no clear strategy for Resource Assessment (RA) is yet emerging, especially for intermediate depths. Changes in energy production can be monetized relative to a base case production fairly easily, but site selection benefits from improved resource mapping are more difficult to quantify. A realistic base case scenario would include a timeline analysis to optimize the siting process, including the selection and deployment of equipment and the sequencing of the RA campaign, because that is

² NREL has developed power curves and other specifications for a standard 5 MW turbine for use as a baseline reference for aero elastic numerical modeling and other systems. See Jonkman et al 2009 for specifications.

what developers do before committing to the cost of a met tower. After that, a statistical analysis of the outcomes of employing this strategy over the entire study area would be required to characterize the expected value of power production over the complete timeline of full build-out. However, that is beyond the scope of this first order analysis, so a different methodology is required to assess the benefits of improved resource mapping. For the purpose of the present study, this methodology consists of estimating the average accuracy of AEP using the new technologies/strategies within the study area, then estimating the cost of obtaining the same level of accuracy using hub height met towers with conventional anemometry. Although hub heights may vary, they are assumed 90m above sea level (ASL) for this analysis unless otherwise noted.

1.3.4. Cost Benefit Calculations

Two of the most useful indicators of the value of a wind project are the Levelized Cost of Energy (LCOE) and the Break Even Price (BP). The LCOE is fundamentally the net present value of financial costs divided by the net present value of energy production. It assumes a standard federally indexed discount rate for return on investment and amortization, but includes no tax or policy inputs, no price change, and no risk premium on finance costs (Levitt et al 2012). It is useful for comparing different technical aspects of wind farm design and operation, but does not capture market conditions like finance costs, price escalation, policy incentives, and tax structures. Breakeven Price (BP), as defined by Levitt et al (2012), includes all these things and more closely reflects the

economic viability of a project from the developers perspective, and thus the value of any change in these parameters, and is therefore the basis of the cost benefit analysis.

There are myriad investment and banking entities and instruments available for financing offshore wind farm projects worldwide, and risk premium can vary significantly from project to project, making accurate projections of finance costs problematic (Levitt et al 2012). The instability of State and Federal wind energy incentive programs adds further uncertainty to any estimate of the cost of capital.

This study therefore makes no attempt to estimate the absolute BP for a wind farm, but only seeks to estimate the change in BP (Δ_{BP}) from implementing new technologies, thus avoiding many of the uncertainties inherent in a fixed estimate. Levitt et al (2012) derived sensitivity curves for BP vs. capital costs, operating costs, and capacity factor, and finance rate, which is a function of risk premium. Thus, the *sensitivity* of BP to changes in input factors, modelled by Levitt et al, is relevant, while the *actual* BP estimated by Levitt et al is not used in this study. This also allows scaling of benefits to larger, or multiple projects, since the value can be expressed as Δ_{BP} times the AEP. This provides a realistic first order estimate of the value of new remote sensing technologies to wind energy development in intermediate waters of the mid Atlantic bight.

Chapter 2

SURFACE SENSOR EVALUATION

2.1. Conventional Technology

Surface based sensors include traditional cup and ultrasonic anemometers, Lidar (light detection and ranging), Radar (radio detection and ranging), and Sodar (sonic detection and ranging). Radar requires large amounts of power, making the technology unsuitable for stand-alone offshore deployment for any extended period, and Sodar is susceptible to noise interference from the environment, including high winds (Brower 2012). Radar is suitable for deployment on satellites, but that is the subject of Section 3.1-“Satellite Microwave Radar/Radiometry (SMRR)”. Of these three remote sensing technologies, only Lidar has the practical capacity to be deployed offshore on a buoy or small platform. The discussion in Section 2 is therefore limited to cups, ultrasonic anemometers, and Lidar. Other types of mechanical anemometers can be as accurate as cups, but cups are

most commonly used in calibration and resource assessment, so other types are not considered further.

2.1.1. Cup and Ultrasonic Anemometers

For about 150 years, the primary sensor used for wind speed measurements has been the vertical axis cup anemometer. The sensor must be positioned in the wind stream and kept free of ice and debris and the internal friction must remain constant. Because a structure is required to hold the sensor in place, a disturbance is introduced into the free-stream wind field and invariably some wind data must be “corrected” or discarded. Cup anemometers are known to be influenced by turbulence, air temperature, air density, and flow inclination (DNV 2011). A significant vertical component to the wind vector can cause overspeeding of cup anemometers. More recently, ultrasonic anemometers (USAs) have been used to more precisely measure wind fields. These sensors detect doppler shifts in an ultrasonic wave transmitted between nearfield (~ 20 cm) transducers.

Ultrasonics also are subject to structure flow disturbance effects, however, as the device must be mounted on a “lightning cage” structure to ground out lightning, and the sensed volume must be bracketed by transducer elements. All anemometers have operational characteristics that are subject to external conditions that may influence the wind speed measurement and introduce error. Despite these shortcomings, the error of class I

anemometers is extremely low – it cannot exceed 0.1 m/s at wind speeds below 16 m/s (IEC61400-12-1, ISO 16622).

2.1.2. Conventional Meteorological Buoys

To collect wind data offshore, the sensor platform can either be bottom-mounted or floating and moored. The most common ocean deployment method is to mount the sensors and power systems on specially designed buoys that are anchored to the seafloor as shown in Figure 1. Typically, the anemometers are installed atop a short mast on the buoy at 3 to 6 m above sea level (ASL)³. These buoys are designed for capsizing resistance and survivability, but can undergo severe motions in all six degrees of freedom during high sea states. Severe motion will corrupt information about turbulence, and bias can be introduced to the time-averaged wind speed or direction if the buoy trim (pitch or roll) is biased, since cup error appears to increase with tilt angle (Bergen 2012). Wind speeds at this height are also subject to sea surface effects depending on sea surface temperature, wave height, and other factors (Karagali 2012).

³ ASL (above sea level) is usually in reference to Mean Sea Level, but is used in this paper to denote height above the sea surface, i.e., tides are neglected unless otherwise indicated.

The National Oceanic and Atmospheric Administration (NOAA) runs the National Data Bouy Center (NDBC) program, which deploys and maintains metocean data buoys around the world, and provides the data to the public (NDBC 2009, 2013). The nominal accuracy of NDBC buoy anemometer time-averaged wind speed data is given as +/- 1m/s or 10%, whichever is greater⁴. This is sufficient for many applications, including short term marine forecasting, numerical weather prediction (NWP) model validation, and storm warning systems, but was never intended nor designed for wind farm siting or wind energy density⁵ estimates. Data from the buoy must be extrapolated at least to hub height to be useful. Without an accurate model of the wind profile, this extrapolation introduces significant uncertainty.

2.1.3. Meteorological Towers

For estimating wind farm power production, the relevant wind field includes the entire rotor disk plane. Since these data are rarely obtainable, the usual alternative is to erect a tall offshore tower to mount sensors and measure the wind speeds up to hub height. The Cape Wind met tower in Nantucket Sound reaches approximately 60m, as shown in Figure 2. Onshore, the cost to erect a tall (90-100m) meteorological mast is on the order of ~\$250,000, but offshore, a tall tower can cost from \$5 million to \$10 million,

⁴ Accessed at (<http://www.ndbc.noaa.gov/rsa.shtml>) 21 Jan 2013.

⁵ Energy density is based on the total kinetic energy in the wind over one year, expressed in Watts per square meter normal to the wind direction. It is dependent on height and location.

depending on water depth, tower facilities, and other factors (Wisseman 2009, Brower 2012). The use of conventional anemometers on a fixed met tower is thus problematic for the following reasons:

- it severely limits the spatial coverage and data that can be collected cost effectively;
- It raises the cost and time required for resource assessment and project development;
- It creates a barrier to competition among developers, limiting the pool to well capitalized firms that can risk the cost of a met tower;
- It creates potential environmental impacts, viewshed impacts, and human use conflicts (e.g., fishing, shipping, aviation).



Figure 1- NDBC 44025, from NOAA/NDBC website

Figure 2- Cape Wind Met Tower, from US Dept of Interior, BOEM website

2.1.4. Conventional Nacelle Mounted Anemometers

After a wind farm is commissioned, the wind speed and direction at each turbine are monitored, primarily for turbine system controls. Conventional anemometers (cups and ultrasonics) are installed on top of each nacelle, but the upwind rotor design (used by all major turbine manufacturers) subjects the nacelle to near-field wake from the rotor. This renders the data nearly useless for accurate measurement of the free-stream wind velocity, but still useful for triggering start-up and shut-down of the turbine and estimating wind direction for turbine yaw control.

2.2. Light Detection and Ranging (Lidar)

A recent adaptation of a common remote sensing technology can help provide the type of wind data required to measure the energy field on the relevant time and spatial scales. Although other remote sensing methods exist for measuring wind speeds (e.g., Sodar, Radar), Light Detection And Ranging (Lidar) using a coherent laser provides the most accurate and versatile way to provide remote measurements. Lidar has been in use for decades to accurately measure distances and generate digital elevation models for topography and mapping. In the last ten years or so it has been adapted to measure wind speed and direction, and in the last few years it has begun to appear in the offshore wind industry. Wind Lidar instruments are capable of providing diverse benefits, including

better resource assessment (ECN 2012) and better turbine control systems (Harris et al 2006).

Lidar measures reflected light just as radar measures reflected radio waves and sonar measures reflected sound underwater. The basic principle underlying Doppler Lidar (the dominant technology for wind speed measurement) is the measurement of the Doppler shift of the reflected radiation from a coherent laser⁶. The laser beam, at frequency ω_0 , hits natural aerosols carried on the wind and is reflected and scattered. Some of the light is reflected back at a frequency altered by the doppler shift (Δf), and the Doppler-shifted frequency of the reflected light is detected by a sensor (see Figure 5). Wave interference between the two signals creates a “beat” frequency that is proportional to the wind speed vector component along the laser. By probing the laser along three or more radial vectors, the wind direction can be resolved⁷, providing an accurate estimate of the average wind speed and direction at the focal distance sampled. Although the detectors may be focused at a set distance, they actually sense the backscatter from a probed volume defined by depth of the focal field. This results in a narrow Gaussian distribution of Doppler shift which must be interpreted with algorithms. A weighting function, ϕ , is used in the algorithm to target the center of the probed volume.

⁶ One new model uses a different strategy – timing the transit of aerosol structures across the sensor cone (SPIDAR 2012)

⁷ Some units provide two dimensional vectors at varying heights, and some can resolve three dimensional vectors.

The Leosphere WindCube™ and the Natural Power ZephIR™ Lidar models are the two most common and most tested models, pictured below. Figure 6 shows the radial vectors and wind vectors for two types of lidar probe patterns, used in The azimuth and zenith angles are labelled θ and ϕ , respectively. The probed volumes may each be 20m to 30m long and be separated by 100m, and the shear and aerosol distribution unknown. First order uncertainties arise from sensing range error and Lidar hardware. Second order uncertainties can arise from necessary assumptions regarding aerosol distribution, horizontal shear, cross-flow and turbulence (Marsden 2009). Though these second order effects may be significant in complex terrain, they are not significant in the offshore environment because aerosol distribution and wind vector fields are generally more homogeneous offshore due to lack of topography and much lower surface roughness.



Figure 3- Leosphere WindCube, reprint courtesy Leosphere

Figure 4- Natural Power ZephIR, reprint courtesy Natural Power

Table 1 - Basic Performance Specs of Two Wind Lidars

	WindCube v2	ZephIR 300
Measurement Height Range:	40m to 200m	10 m to 200 m
Probe Length: measurement height;	20m @ all hts.	0.07 m @ 10 m 7.70 m @ 100 m
Number of Measurement Heights:	12 hgts in 4 sec.	10 hts in 10 sec., user configurable
Sampling Rate*	1 sec	50 Hz
Averaging Period:	4 sec	1 sec. per height level
Wind Speed Accuracy:	<0.1 m/s	< 0.5 %
Wind Speed Range:	0 to 60+ m/s	< 1 m/s to 70 m/s
Wind Direction Accuracy:	2°	< 0.5 %
(*) – WindCube laser pulse rate is 30 kHz.		

The first generation of wind Lidar units came to market in 2005 and for the next seven years, validation testing and calibration was conducted by independent, government funded, university-led research teams in Denmark, Germany, and the UK. In that period, the technology improved significantly in terms of performance and accuracy demonstrated both onshore (Mann et al. 2007; Mann et al. 2009) and offshore (Kindler et al. 2007; Pena et al. 2008, Pena 2010). Offshore testing was conducted for survivability and data availability and to understand the effects of sea surface heat exchange and other factors that can significantly affect the wind profile. This research culminated in 2011/2012 with the introduction of a second generation of commercially available wind Lidar units. These units have upgraded hardware for offshore survivability, improved

laser geometry, and updated calibration of cloud correction and probe volume-averaging algorithms.

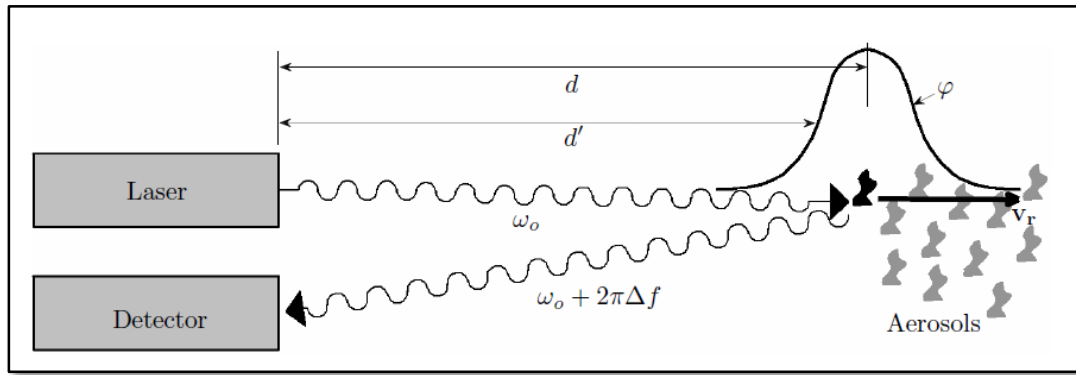


Figure 5--Doppler Shift Lidar, Beat Detection Schematic , from Pena et al 2008

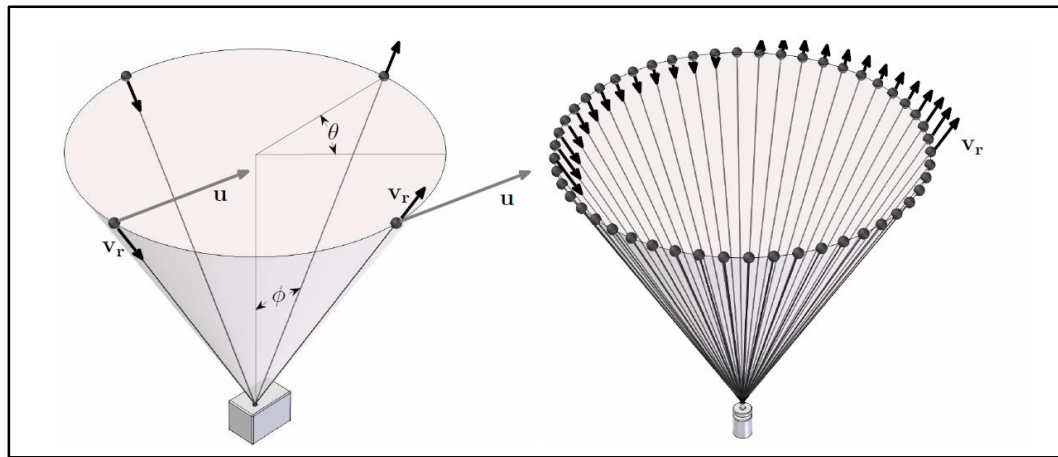


Figure 6- Laser vectors and scan configurations of WindCube (L) and ZephIR (R), from Pena et al 2008.

2.2.1. Pulsed Laser (PL) vs. Continuous Wave (CW) Lidar

Although each Lidar system is slightly different, they are primarily characterized by their laser emission waveform, which is either continuous wave (CW) or pulsed laser (PL). This distinction is the most germane to understanding the subtleties of Lidar wind measurement. A good technical description and comparison of the strengths and weaknesses inherent in PL and CW Lidar can be found in Hill et al (2010), Simley et al (2011), or Courtney et al (2008). The summary below draws information from these three sources.

Continuous Wave -The CW laser emits a continuous (non-pulsed) beam and optically focuses the receiver at the target distance, resulting in a distribution of return signal gain around the focal distance, as shown in Figure 5. Due to its optical focus, the probe length of CW increases with the square of the range (for example, the ZephIR has an effective probe length of $\pm 1\text{m}$, $\pm 6\text{m}$ and $\pm 15\text{m}$ at 40m, 100m and 150m ranges respectively). This larger sample volume boosts the signal while the longer distance attenuates it, resulting in a fairly constant carrier to noise ratio (CNR) over the target range of the unit. Although there is greater potential for range (height) error with the longer probe volume at greater heights, it may not be significant because the wind profile is generally more vertical at greater heights. Beyond several hundred meters, however, the probed volume becomes too large to render a meaningful point estimate, and clouds and other factors come into play (Marsden et al 2009).

Pulsed Laser - The strategy used in PL is to send discrete laser pulses and set timing gates on the receiver to capture the pulse reflection from around the target range. Thus the probe length is proportional to pulse duration (which is fixed) and the reflected signal gain exhibits a Gaussian distribution. PL can probe several different ranges near-simultaneously through the use of multiple range gates, making it valuable for capturing turbulence structures. On the downside, the CNR of PL decreases with distance since the probed volume does not increase to offset the signal fade. This can only be overcome by increasing laser power. Also, PL must use a minimum pulse duration related to the Nyquist frequency⁸, thus a minimum pulse length and a minimum probe length, currently around 30m (distance between targets). PL is therefore ill-suited to ranges below the minimum probe length.

There is no simple, single trade-off between the two technologies, but in general, CW is necessary at short ranges (<30m) and PL is necessary at long ranges (>200m). The transitional region lies between approximately 100 – 150m, (see Figure 7) where various factors could drive selection either way (Simley et al 2011). For example, power draw may be a factor if deployed remotely, and some CW units draw more power than PL.

⁸ Nyquist frequency is one half the highest sampled frequency. Frequencies above the Nyquist frequency cannot be observed in a discretely sampled time series.

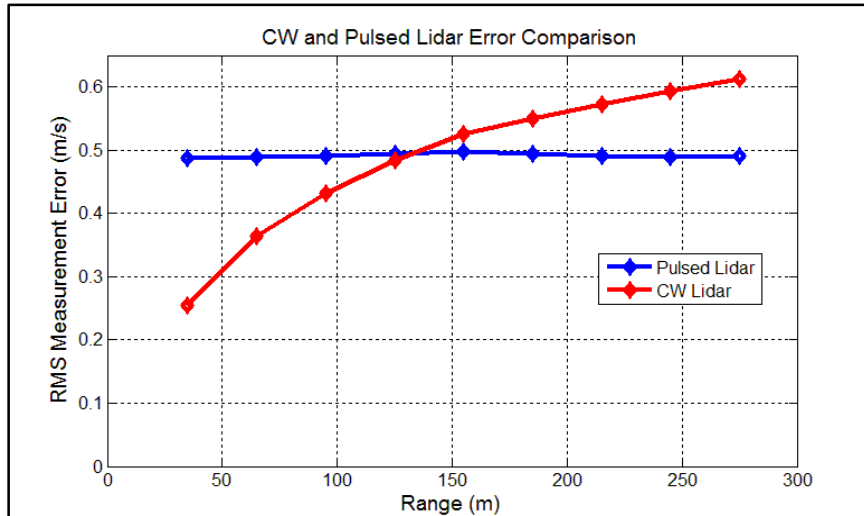


Figure 7- Error Comparison for CW and Pulsed Lidar by Height, from Simley et al 2011, a report prepared by NREL for the U.S. Dept of Energy.

2.2.2. Lidar vs. Conventional – Range and Accuracy

Generally speaking, commercial wind Lidar systems can sense wind speed anywhere from ~20m to several kilometers, with varying performance depending on system power and design, atmospheric conditions, software settings, and hardware configurations. Scanning Lidars may be mounted on nacelles to sense the incoming wind, as discussed in later sections. Long range scanning Lidars with ranges over 5 km are available, but require a larger space on a fixed platform, a cooling system, and a larger power supply.

The fundamental difference between Lidar and conventional sensors is that in the field, Lidar measures a volume, not a point. The sources of uncertainty, and thus the conditions that affect error, are different for Lidar, cups, and ultrasonics. For a point measurement

of scalar velocity along the laser axis, Lidar requires only a simple waveform beat detection⁹, whose accuracy is independent of source voltage. This is considered to be essentially calibration free, with error measured at 0.003 m/s against a calibrated moving belt target (Bergen 2012). Calibrated wind tunnel tests of wind speed measured by an axial, single probe Lidar against a pitot tube show zero bias and a linear regression slope of 1.0042 (Cayla 2010). However, practical application of wind Lidar requires the use of at least three lasers at three different angles to resolve axial components along each laser into a single 2 or 3 dimensional wind vector, which is assumed to represent the wind at the aggregate centroid of the probed volumes. Uncertainty comes from potential error in the technical characteristics of the Lidar (focus, laser angle, range estimate) and from the assumptions required for averaging the wind speeds within the probed volume (aerosol distribution, wind veer, shear). The first source of uncertainty can be mitigated through hardware and calibration improvements, but the second is a function of natural, stochastic processes that are difficult to model.

Three Lidar validation studies are discussed below. Unless otherwise noted, this paper defines bias of a co-incident measurement relative to a reference cup anemometer, and defines accuracy as one standard deviation.

⁹ The beat is generated by the frequency of the source beam combining with the doppler-shifted frequency of the return signal beam. The beat frequency is thus a function of the doppler shift.

2.2.2.1. Westerhellweg et al 2010

In a study conducted by the German Wind Energy Institute (DEWI) as part of Research at Alpha Ventus (RAVE), one year of measurements from a Leosphere WindCube™ Pulsed Lidar were taken on the FINO-1 met tower and compared to the cup anemometer data (Westerhellweg et al 2010). Of all the Lidar validation studies performed, this is one of the most pertinent and useful because it covers the longest time series, involves the shortest distance between the tower and the Lidar, and was conducted 45 km offshore, as opposed to an onshore coastal research station used for many of the other studies. Two figures from the DEWI study are included below. The first, Figure 8, shows the scatter plot for the two data sets at 90m ASL, and indicates extremely high correlation at all speeds above 4 m/s, with R^2 values of 0.998. An analysis of uncertainty was also performed, and used to generate Figure 9, below, comparing data from the cup and the Lidar at 103 m ASL. Availability of Lidar data was 98% at this height. The vertical red bars represent the standard deviation (%) of the Lidar data and the purple line represents the uncertainty (%) of the cup measurements. After binning the ten minute averaged data into 1m/s bins, the range of uncertainty is nearly identical at wind speeds above 4 m/s, with Lidar proving slightly more accurate above approximately 23 m/s. The correlation coefficient (R^2) was higher than 0.99 at all heights. Bias varied from -0.15 m/s to 0.08 m/s and this was attributed to mast and lightning cage effects on airflow. The authors made two important observations regarding accuracy and uncertainty;

- The mean deviation between Lidar and cup measurement is smaller than the uncertainty of the cup measurement.
- The standard deviation of the deviation between Lidar and cup measurement is approximately in the same range as the uncertainty of cup measurement.

The study concluded that any further verification of Lidar accuracy using a met tower is limited by the uncertainties inherent in the cup measurement and the geometrical sensor setup, causing flow disturbance.

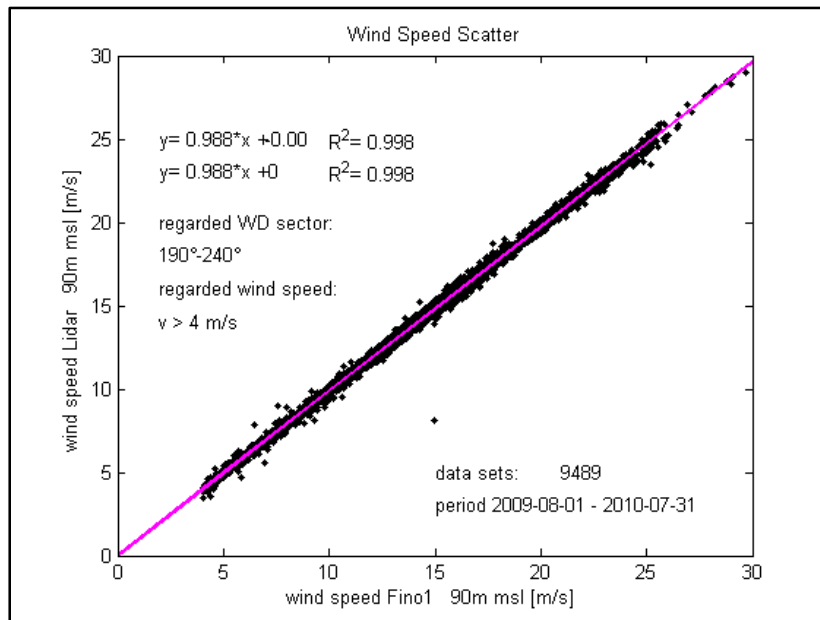


Figure 8-Scatter Plot and Correlation Values (Westerhellweg et al 2010)

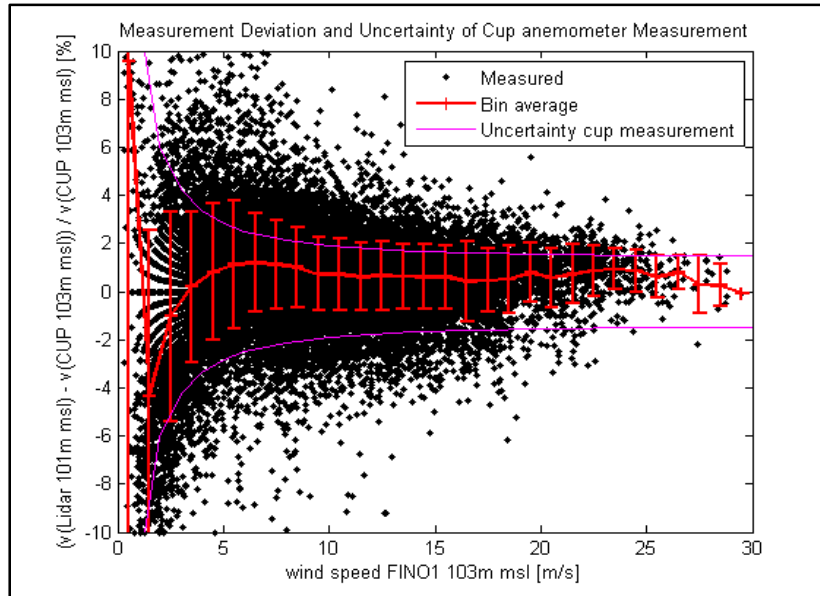


Figure 9- Deviation and Uncertainty of Cups vs. Lidar (Westerhellweg et al 2010)

2.2.2.2. Marsden 2009

In research conducted at the Danish Technical University Wind Energy Dept (DTU), the error and uncertainty of Lidar vs. cup anemometers was examined using three months of data from a Wind Cube and from calibrated cups mounted on a met tower on the coast (Marsden 2009). The met tower data were filtered to remove wake sectors and periods of frozen cups, and the Lidar data were filtered to remove points of low CNR, scrubbing about 6% of the data set. The data were further separated into sectors to represent a coastal climate (wind from offshore) and an inland climate (wind from inland). 941 ten minute average data points were left in the coastal climate set. The data sets were used to

predict AEP for a reference 2 MW turbine with 100m hub height. The study found that AEP predictions using hub-height cup vs. Lidar measurements differed by 1.1 % for the coastal climate. The study concluded that cup-traceable Lidar can likely provide AEP predictions with an accuracy of +/- 2.5%. The study also estimated that a calibrated boom mounted cup has an uncertainty of about 0.2 m/s in the operating range of a typical turbine, which compared to a standard deviation of Lidar error of about 0.21 m/s, and a bias of -0.03 m/s.

2.2.2.3. ECN 2012

In November 2012, the Energy Research Centre for the Netherlands (ECN) completed a 60 week offshore measurement campaign as part of the project “Meteorological Research- Wind at Sea”. Data from the ZephIR 300™ were compared to conventional anemometry data from the 108 m Met Mast Ijmuiden at the ECN Wind Turbine test facility, 75 km offshore in the Dutch sector of the North Sea. Measurements were taken in accordance with IEC 61400-12. Availability of the ZephIR was over 98%, with the only downtime attributed to an external power supply failure. Although the study has not yet been published, the researchers have stated that the ZephIR 300 can be a valid stand-alone system (on a fixed platform) for wind resource assessments, especially given the unit’s ability to reach the top of the rotor disk (ECN 2012).

2.2.2.4. Summary – Fixed Platform Lidar

Five additional Lidar validation studies from DTU and others using coastal and offshore met towers were also reviewed, and showed nearly identical results (Kindler et al. 2007; Pena et al. 2008, Pena 2010, Mann et al 2010), with Pearson correlation (R^2) values of 0.98 - 0.99 for 10-minute average velocities at heights up to 200 m. These studies demonstrate that the accuracy of the newest Lidar technology is comparable to a cup anemometer for estimating power production, primarily because there are no tower wake effects to disturb the wind stream and no vertical extrapolation required to reach blade tip height. Extensive testing of the two models with the longest track records (the Leosphere WindCube™ and the Natural Power ZephIR™), against a met tower on the Danish coast indicates that between 2005 and 2009, improvements in hardware and data processing reduced the mean error in the ten minute average wind speed from 0.1 m/s to 0.05 m/s (Marsden 2009).

Since 2009, every published fixed platform Lidar validation study that includes a regression analysis compared to calibrated cups on an offshore or coastal met tower has found correlation coefficients around 0.99 and biases that rarely exceed 0.1 m/s, which occurs only at wind speeds below ~ 5 m/s. It is becoming clearer with each validation study that Lidar has advanced to the point where it provides accuracy and availability at least comparable to cup anemometry. In a pair of 2013 position papers from Germanischer Lloyd-Garrad Hassan (GL-GH) (Tindal 2012a, Tindal 2012b), a leading

certification and verification agent for the wind industry, states that the use of validated Lidar on fixed platforms is determined to have essentially the same uncertainty as conventional cups on towers, and is deemed to be suitable for offshore Resource Assessment. If cup anemometry data must be extrapolated to height using a wind shear model, the added uncertainty likely exceeds that inherent in Lidar probe volume averaging¹⁰ (see Figure 9).

2.2.3. Long Range Lidars

In addition to the upgraded WindCube V2, Leosphere has also introduced several new models with extended ranges and scanning capabilities. The specifications are given in Table 2. The most recent addition (not listed in the table), model 400S, has a specified scan range of 10km, with a display resolution of 200m and a nominal accuracy of 0.5m/s. The fundamental technology is based on the V2, but the effective range of the newer models is increased by using a more powerful laser coupled with greater accumulation time, larger range gates and less temporal resolution. Bi-axial motorized heads provide motion for the laser and sensors to scan 360 degrees of azimuth and over 190 degrees of elevation (full coverage).

¹⁰ If wind speeds to the blade tip height are desired offshore, Lidar is the only practical solution, because engineering limitations currently make it cost prohibitive to build offshore towers taller than ~110 m in most areas.

Table 2- WindCube Extended Range Performance Specs, reprint courtesy of Leosphere

PERFORMANCES	WINDCUBE _g	WINDCUBE ₇₀	WINDCUBE _{100S}	WINDCUBE ₂₀₀
Range min-max	40 to 500 m	100 to 1500 m	100 to 3000 m	100 to 6000 m
Data output frequency	1 s	10 s	1 s/10 s	10 s
Probed depth	20 m	50 m	50 m	50 m
Number of measurement heights	10	40	100	100
Speed range	0 to 60 m/s	0 to ± 60 m/s	-30m/s to 30m/s	0 to ± 60 m/s
Speed accuracy	0.2 m/s	0.3 m/s	0.3 m/s	0.3 m/s
Direction accuracy	1.5°	1.5°	-	1.5°
Scanning cone angle	0° or 15°	0° or 15°	-	0° or 15°

2.2.4. Other Scanning Lidars

Lidar technology has recently been adapted to rapidly scan large areas or volumes. These units can be either fixed multi-beam type (e.g., conical pattern) or “steerable” designs with programmable scan patterns using servo-motors to control the laser head or the mirror. The systems can sweep selectable probe vector patterns at multiple ranges, providing data for reconstruction of a 3 dimensional wind field (Mikkelsen et al 2010, SGURR 2013).

This scanning technology can be used to improve control of wind turbines in real time operation. Single Lidar units mounted on top of the nacelle can probe the incoming windfield from 30m to 200m away, providing the weighted average velocity and direction within the probed volumes. More accurate upstream windspeed measurements

can also produce more accurate power curves, reducing uncertainty in AEP estimates. However, nacelle mounted Lidar has a significant drawback - the line of sight is blocked whenever a blade passes in front of the unit, about 30% of the time (Schlipf 2012). This restricts the timing of the probes, reduces available data, and increases uncertainty. Lidar mounted in the rotor can avoid this problem, and scanning units mounted on adjacent turbines can also effectively “image” the incoming wind field.

2.2.4.1. ZephIR Spinner Hub- Mikkelsen et al 2010

Hub mounted scanning Lidar systems have been developed to obtain a clear view of the incoming wind field. Field testing has demonstrated the ability to mount a Lidar in the nose of the hub, eliminating rotor and nacelle shadow and allowing detailed scanning of the upwind projection of the rotor disk (Mikkelsen et al 2010). Although these multiple probe scanning units improve spatial resolution, the assumption of linear translation of turbulent structures is still required to account for the scan cycle times (Simley et al 2011). This is known as Taylor’s Frozen Turbulence Hypothesis (Taylor, 1938).

As part of the Wind Scanner project at DTU, The “Tjæreborg Spinner-lidar Experiment” (Mikkelsen et al 2010), mounted a conically scanning CW Lidar (modified ZephIR 175) inside the hub of a large 80 m diameter, 59 m hub height, 2.3 MW Vestas NM80 turbine. Figure 20 shows the dual-conical scan pattern of the Lidar unit mounted in the rotor hub.

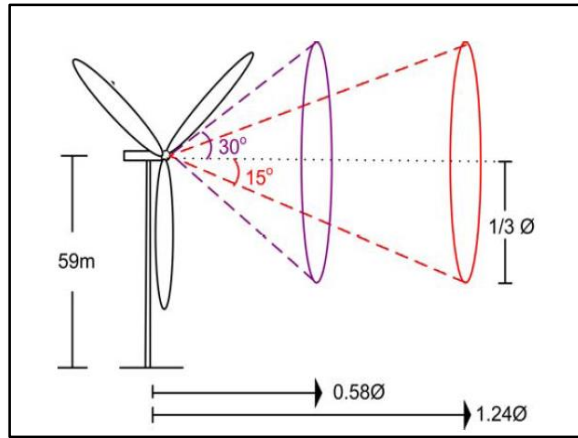


Figure 10- Hub Scanning Lidar, from Mikkelsen et al 2010

The experiment measured the approaching wind and turbulence structures by scanning the wind field about the rotor axis in real time. The approaching wind field was measured at distances of 53m and 160m upwind, using 30 degree and 15 degree optical wedges, respectively. The Lidar radial measurement resolution was estimated to be about 20 m at the 103 meter range and about 5 m at the 53 m range. Data from an adjacent meteorological mast as well as data logged within the wind turbine's control system were used to evaluate the results. The system showed high reliability and data availability throughout the measurement period of April through August 2009. Figure 11 shows a radial plot of the incoming wind speed at the edges of the rotor disk, projected about 53 m upstream, and indicates a relatively coherent windfield, with lower velocities near the ground (180 degrees). Information about the incoming wind profile across the rotor disk can thus be obtained from the plotted data. Figure 12 shows a comparison of the spinner-

lidar measured (10 minute averages) vertical wind profile (blue dots) with data from a co-located adjacent instrumented met mast (red dots).

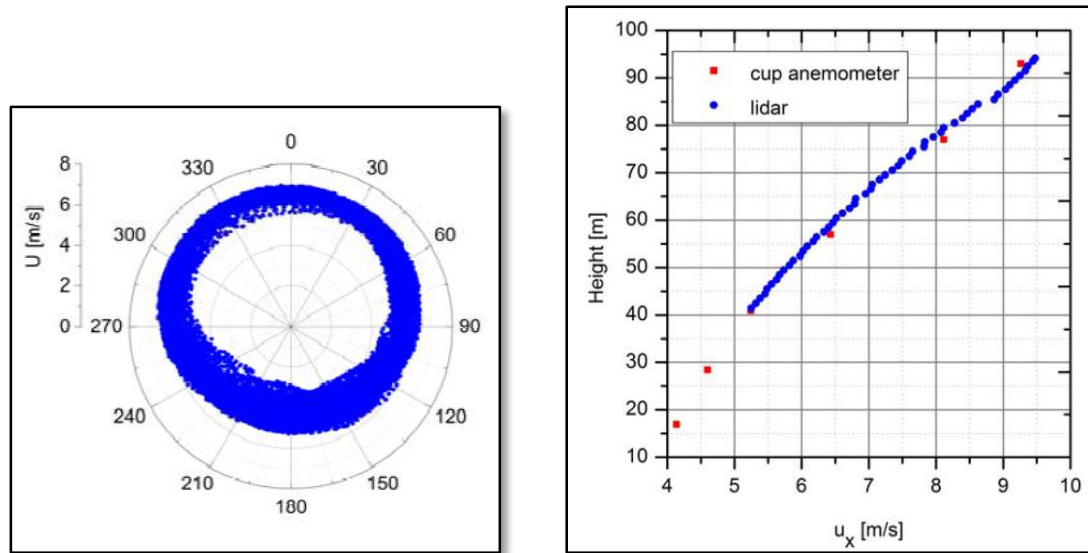


Figure 11- Radial Plot of U of Incoming Wind Field Profile, from Mikkelsen et al 2010

Figure 12- Wind profile, Spinner Lidar vs. Cup, from Mikkelsen et al 2010

The authors concluded;

... the integration of the lidar in the spinner of a wind turbine has proven very useful for the research of the incoming wind towards the rotor plane. Furthermore this innovative measurement concept offers the possibility of active control of a wind turbine through a wind lidar. Incorporation of remote sensing wind data into the turbine control system can lead to improved energy yield and load reduction, through yaw, rpm and pitch control. Implementation of enhanced control algorithms ...is envisioned to contribute to the improvement of active control of wind turbines in the near future.

The research proved that it is possible to accurately measure the incoming wind field 160m upstream of the rotor plane, providing unprecedented ability to define wind

velocity across the rotor disk and provide 2 or 3 dimensional maps of upstream wind fields. With these recent developments, nacelle/rotor mounted Lidar can provide an accurate (± 0.1 m/s) vector image of the incoming wind field across the rotor disk at least 5 seconds in advance.

2.2.4.2. Galion G4000 – SGURR 2013

Figure 13 shows an image of wake fields generated using three identical SGURR Galion G4000™ scanning Lidar units mounted on the nacelle of an Areva M-5000-116 Turbine. This type of deployment (nacelle top) is not a typical placement of the G4000, but demonstrates the potential for mapping winds across multiple turbines in a wind farm. Although no independent validation studies have yet been published for the G4000, the fundamental PL technology employed is the same as that used in the WindCube.

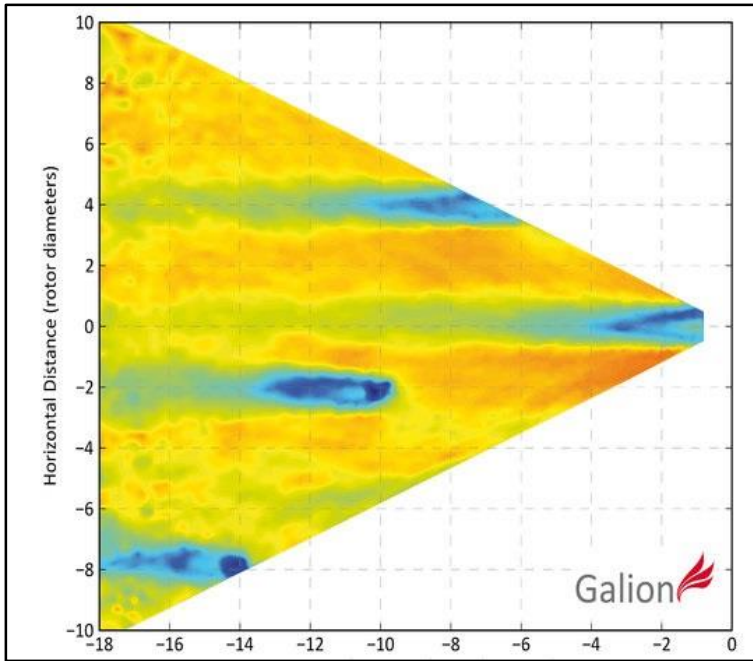


Figure 13- G4000 Image of Turbine Wakes-Alpha Ventus, from Sgurr 2013

2.2.4.3. Latest Entries – Nacelle Mounted

Two recent entries into the market are designed specifically for Rotor Control applications; the Windar Photonics™ system and the Windiris™ from Avent Technologies, a joint venture of NRG and Leosphere. The Windar system is a simplified two beam system based on technology developed by DTU, but designed specifically for mounting on the nacelle to scan incoming wind. With a unit price around \$35,000, the system may be deployed on every turbine, providing accurate wind speeds and directions up to 60 m upstream of the rotor, using only a semiconductor laser and polarization switching to split

the beam. The strategy is to correct yaw error and use proactive pitch to reduce fatigue loading. The manufacturers claim a payback period of 12 to 24 months.

The Windiris is a more powerful PL system with a longer range, and is designed to be deployed on the nacelle for a defined calibration campaign. The strategy is to collect enough data to determine yaw bias from the legacy anemometer, calibrate the control algorithm to take out the bias, then move to the next turbine. In summary, new Lidar technology can be expected to improve control systems, wake modeling, rotor blade design, power curve testing, condition monitoring and wind farm layout.

2.2.5. Floating Lidar Systems

Until very recently, wind Lidar systems required a fixed platform for operation, which made their offshore deployment cost nearly the same as an offshore met tower since most of the cost is for the foundation and platform, not the tower. In the last few years, at least four Lidar systems – the SeaZephIR™, WindSentinel™, WaveScan™, and FLidar™ - have come to market mounted on specially designed floating platforms.

Two basic design philosophies for these platforms are emerging. The SeaZephIR limits the motion of the platform with a vertical spar buoy and a tension leg anchoring system, keeping pitch/roll very close to neutral. This strategy intends to negate the need for a motion compensation algorithm. The other three are based on a barge hull buoy with

catenary anchor lines. The barge buoy data are processed with a digital algorithm to reduce the effects of platform motion. This motion-compensation algorithm subtracts the buoy motion effect from the wind vector data. Processing can occur internally in the unit or in a separate algorithm after data is downloaded. The Wavescan, the WindSentinel and the FLidar systems use some variation of this design. These units include renewable power systems designed for long term (6-12 months) deployments, and they can store the data or transmit via satellite or cel network, in bursts at regular intervals. They can be deployed adjacent to a turbine or far away from the wind farm, depending on the application, and can be easily re-deployed by a buoy tender or similar working vessel, providing the ability to easily and quickly collect data to blade tip height at almost any location. Several recent studies in the US and EU examined the accuracy of these systems, and some validation field tests are currently underway. These are discussed below.

2.2.5.1. GVSU WindSentinel Study

As part of the DOE offshore wind acceleration program, researchers at Grand Valley State University in Michigan are leading a team that is validating a WindSentinel for resource assessment in Lake Michigan. The latest and longest deployment was 36 miles offshore, and lasted from May to December 2012. The system ran continuously, with 100% system availability and no deviation from specified performance, even during the peak winds of Superstorm Sandy, which were measured at hub height at 29.9 m/s, with

wave heights of over 8 m. Issues arose with the satellite uplink and a component of the renewable power supply, but redundant systems performed as designed until repairs could be made, resulting in no loss of data or communications¹¹. Although only limited data are available at this time, the experience to date in Lake Michigan indicates that the system is robust enough for long term (multi-year with 6 month maintenance cycle) offshore deployment.

Table 3-WindSentinel Performance Specifications, from Axys Technologies

Performance Spec	WindSentinel
Measurement Height Range:	30m to 150m
Probe Length	+/- 20m - all hts
Number of Heights:	5 user selectable
Sampling Rate:	1 sec
Data Validity (all hts)	>90%
Wind Speed Accuracy:	0.1 m/s
Wind Speed Range:	0 to 90 m/s
Wind Direction Accuracy:	2°

¹¹ Personal communication with Arn Boezaart, GVSU, 14 Jan 2013.

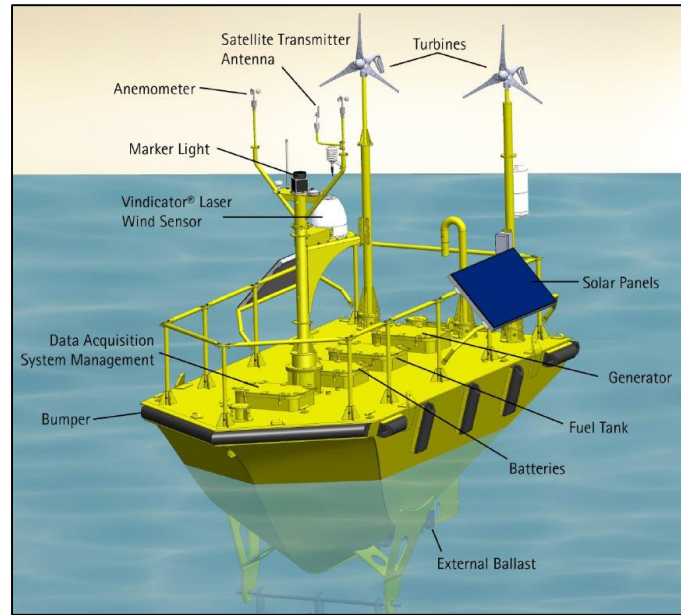


Figure 14 - WindSentinel Metocean Buoy System, reprint courtesy AXYS Systems

2.2.5.2. Fixed Lidar vs. Moving (Floating) Lidar

A Norwegian consortium led by the University of Bergen and Statoil (the Norwegian national energy company) recently assessed the ability of buoy mounted Lidar to accurately measure the wind profile (Bergen 2012). A ZephIR 300 and a WindCube v2 were mounted on a motion simulation platform programmed to simulate 56 different sea conditions, and matching units were placed on the ground beside them. Measurements were taken at 10 levels between 40m and 197m. The test showed little difference between ten minute averages from the fixed units and the moving units, or between the two Lidar models. Most measurements were within the uncertainty criterion of 0.2m/s (or 2%) even without motion compensation. Figure 15, below, shows a typical three minute time series

of the deviation between the ground unit (u-ref) and the “floating” unit (u-obs) WindCubes, at 80m height, before the motion compensation algorithm was applied.

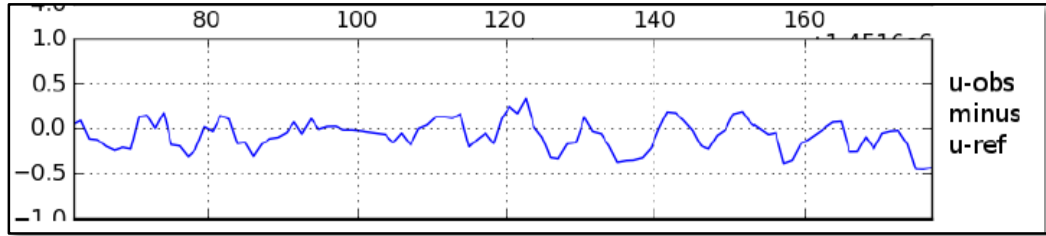


Figure 15-U bias between fixed and moving Lidar, from Bergen 2012

2.2.5.3. Fixed ZephIR vs. Floating Wavescan ZephIR

The second part of the Norwegian study (Bergen 2012) compared a ZephIR on land to a ZephIR mounted on a Fugro Wavescan™ buoy 3 km offshore. The deployment lasted from 24 March 2012 until 19 April 2012. The buoy Lidar recorded 10 minutes average wind profile at 10 heights from 12.5m to 218m every third hour, while the reference Lidar measured the wind at 53 m height continuously. The period included times of significant wave height exceeding 3.5 m. The scatter plot of the data, shown in Figure 16, shows very close correlation and almost no bias. The authors noted that most of the scatter is likely due to the stations being 3 km apart.



Figure 16- Scatter Plot and Correlation Analysis, from Bergen 2012

2.2.5.4. Fixed ZephIR vs. SeaZephIR

In a study conducted by Natural Power in 2009, a SeaZephIR (spar buoy design) was deployed in waters off the coast of Norway about 800m from a land based ZephIR on a small, flat island (Smith 2012). Figure 17, below, shows the two data streams of ten minute average wind speeds at 90m for the period 5-23 November for the SeaZephIR (red), and shore ZephIR (blue). The figure was generated from unfiltered data using an early prototype of the SeaZephIR. The data show high correlation, with low deviation and no significant bias, especially considering they were separated by 800m. This early test proved that the concept was worthy of further development.

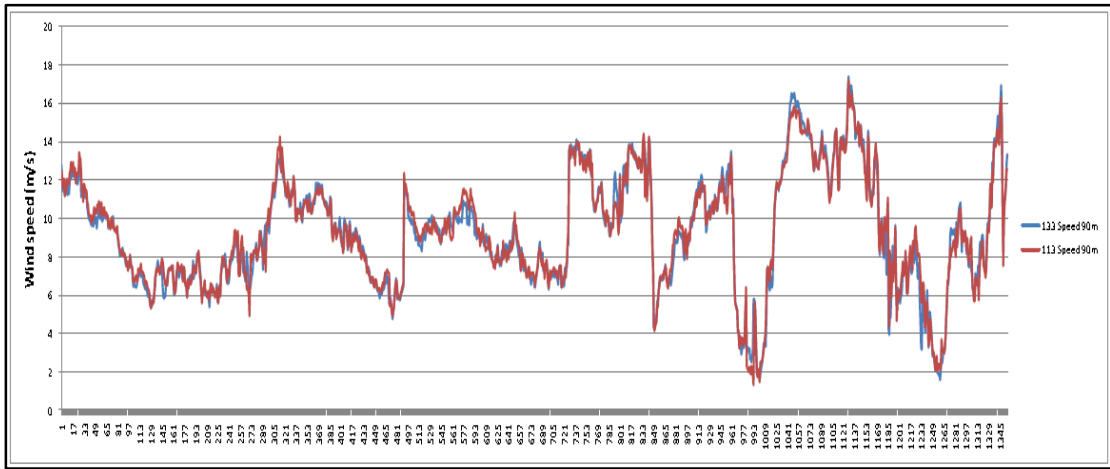


Figure 17- SeaZephIR and LandZephIR wind speed at 90m, from Smith 2012.

2.2.5.5. US Deployments – WindSentinel and NJORD

Floating Lidar systems are gradually gaining acceptance by the wind industry for producing accurate, investment-grade offshore wind data. At their August board meeting in 2010, the New Jersey Board of Public Utilities approved the use of both a SeaZephIR and a WindSentinel for Resource Assessment for two wind projects off the coast of New Jersey. This approval allowed Fishermen’s Energy and Garden State Offshore Energy to tap the state’s Offshore Wind Rebate Program for the cost of their floating Lidars, and prompted them to shelve their plans for offshore meteorological towers. Fishermen’s Energy has since purchased and deployed a WindSentinel, and GSOE has developed and deployed their own floating Lidar/metocean unit. The spar

buoy supports the ZephIR 300 and was re-named the New Jersey Ocean Research Device (NJORD), shown in Figure 19.



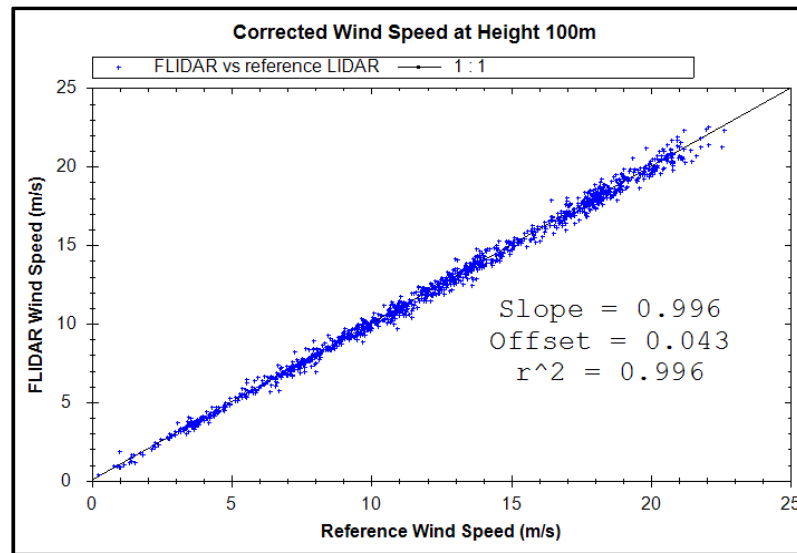
Figure 18-New Jersey Offshore Research Device (NJORD), built by SEAROC, supporting a ZephIR 300. Reprint courtesy of SEAROC

Zephir Ltd., developers of the technology, recently completed (May 2012) field trials of the NJORD, comparing Lidar wind speeds at hub height to an onshore reference met mast with cups, 3.5 km distant, on complex terrain. Despite the distance and significant wave heights up to 3.5 m, the accuracy was found to be reasonable, with the correlation plot showing a linear fit slope of 1.01 and $R = 0.96$. (Rutherford et al 2013)

2.2.5.6. Fixed WindCube vs. Floating FLidar WindCube

A more recent entry into the floating Lidar market is FLidar™, a product of 3E, a Belgian manufacturer. The system uses a WindCube v2 with a novel mechanically stabilized barge hull design. The strategy is to minimize motion before applying a motion compensation algorithm to the data. Data from preliminary sea trials indicate high correlation of wind speeds at 100m compared to a WindCube on shore nearby, as shown in Figure 19.

Figure 19-Scatter Plot and Correlation Analysis, from Thevenoud et al 2012



2.2.6. Summary – Floating Platform Lidar

Although independent validation studies are not yet complete, the simulations, preliminary reports and early data from manufacturers and other investigators, discussed above, indicate that commercially available floating Lidar technology can currently (or will within a few years);

- provide data continuously (with system availability >98%) for at least 6 months;
- provide at least 90% data validity at hub height
- provide 10 min data to 200 m ASL to within +/- 0.1 m/s;
- provide 10 minute average wind speed data that is accurate across the turbine operating range of wind speeds;
- survive extreme conditions

With a market price ~ 10% - 20% of a met tower and much greater range and flexibility, this new technology could greatly improve the way turbines and wind farms are designed, sited, and operated. The buoys can also record a full suite of metocean parameters, which is valuable for calibration of hub height extrapolation and for modeling other geophysical effects, discussed in the following sections.

The analysis in this study therefore assumes that at least one commercially manufactured floating Lidar system is, or will be in a few years, as accurate and reliable as the onshore Lidar units that share their core technology.

Chapter 3

ORBITING SENSOR EVALUATION

Like Lidar, orbiting remote sensing systems detect radiated energy, but at very different scales than surface-based sensors, scanning thousands of square miles in a few seconds. On the downside, they only provide a few data readings per day at any given site. Orbiting instruments are not capable of providing data in real-time for turbine control, so the focus of this analysis is on their use for wind energy mapping and annual power production estimates. Although the technology has some parallels to surface sensors, the applications are somewhat different. Data sets and products from earth-observing satellites are often made available to the public at no cost since the programs are publicly funded. This can enable low-cost, desktop, first-order resource assessment studies that do not require deployment of any instruments. It also provides a long time series (20+ years) for

research and indexing purposes¹². These technologies can improve accuracy, spatial coverage and resolution, yielding more optimal project siting (Christiansen et al 2006; Hasager et al 2008, 2011).

3.1. Satellite Microwave Radar/Radiometry (SMRR)

Satellite Microwave Radar/Radiometry (SMRR) is used to generate (“retrieve”) vector wind estimates (“products”) at 10m ASL¹³. Orbiting radars (active) and radiometers (passive) measure the spectral intensity and polarization of the microwave energy from the sea surface. They can sense millimeter-centimeter waves on the sea surface because the reflected signal spectral power is dominated by Bragg scattering and is critically dependent on the surface roughness at that scale (Naderi et al 1991). Since roughness is a function of capillary waves that are generated by wind in under 1 sec., roughness is closely correlated to the local, instantaneous surface wind speed. The systems collect vast amounts of data, scanning swaths up to 1800 km wide, sweeping the surface at over 6 km per second. Different systems may use different signal frequencies, wave polarizations, antennae configurations, or scan patterns, but most active radar

¹² To ensure accuracy for indexing one or two year data sets, Nielsen et al (2002) indicates a minimum fifteen year length

¹³ The extrapolation of SMRR data from the sea surface to 10m assumes a neutrally stable profile.

instruments operate at either around 5 GHz (C-band), or around 13 GHz (Ku-band), while some can operate on multiple frequencies.

SMRR technology has fulfilled its original purpose by vastly improving operational marine weather warnings, analysis, and forecasting models. The original criteria for SMRR wind products (@ 10m ASL) were: wind speed accuracy better than 2 m/s (or 10%), and wind direction accuracy of ± 20 deg., within the range of ~ 3 to 20 m/s (NASA 2013). However, recent advances in both software and hardware have taken accuracy well beyond these early markers. To characterize the true accuracy and resolution of SMRR wind products, numerous correlation studies have been performed which analyzed Level 1 data and Level 2 wind products and compared them to: each other, to in situ data from met towers and buoys, and to output from calibrated, short term numerical weather prediction (NWP) models. Several of these studies are discussed below, but first, some background information is provided which describes the most salient aspects of SMRR satellites and wind retrievals, common to all three types of SMRR systems.

3.1.1. Data Sets and Product Level

As each antenna sweeps a path along the sea surface, the raw data are stored as pixels of radar signal intensity that are then processed to geo-locate and sequence the data streams to produce images. These images are then normalized to account for the effect of the

beam azimuth, angle of incidence, and satellite motion on the reflected signal strength. Additional processing may be required to synthesize multiple scans from different angles. This produces normalized radar cross section (NRCS) data that describe the measured backscatter coefficient (if active radar) or brightness temperature (if passive radiometer) of the sea surface in the form of a pixelated image. The NRCS image (comprised of “sigma-0” data) is then translated into wind speed at the surface and re-mapped into area-averaged gridded wind speeds at 10m ASL assuming a stable reference wind profile, and these are published as wind map products. SMRR data sets and wind products are roughly classified by the level of data processing as follows¹⁴.

- Level-0 Unprocessed backscatter signal data
- Level-1A Reformatted “scrubbed” signal data plus metadata
- Level-1B NRCS (Sigma-0) data, image corrected, time ordered and geo-located.
- Level-2 Mapped wind vectors at 10m ASL resolved to the scene grid
- Level-3 Mapped wind vectors at 10m ASL, resolved to user preference grid

¹⁴ Definitions derived from http://www.ssmi.com/qscat/qscat_browse.html

3.1.2. Geophysical Model Functions and Wind Retrieval

Tools

The Geophysical Model Function (GMF) is the algorithm used to make these conversions according to physical relationships, calibrated with empirical data. There are two main stages of data processing in a GMF; one to convert return signal data (Level-0 or 1A) into a NRCS image (Level-1B), and one to convert the NRCS image to wind vectors (Level-2). In the first stage, relationships are based primarily on the beam azimuth, angle of incidence, and sometimes polarization, and the GMF may also include an algorithm that can account for changes in orbit or instrument performance over time. In the second stage, the normalized radar image is translated into wind speeds to create Level-2 wind products. This is the translation where most error occurs, and where correct modeling of the effect and calibration of the algorithm is most important. In mathematical terms, the GMF is a transfer function that maps Level 0 or 1A raster data to Level 2 or 3 vector products.

GMFs undergo periodic revisions as they can be empirically tuned, based on correlation studies and input from other satellites, in situ measurements and NWP model simulations. GMFs are combined with graphical user interfaces to create a software package called a wind retrieval tool. Since 1984, when the first GMF was developed for satellite wind retrieval (Wentz et al 1984) several international consortiums of government, industry, and academia have developed new GMFs and wind retrieval tools and made them publicly

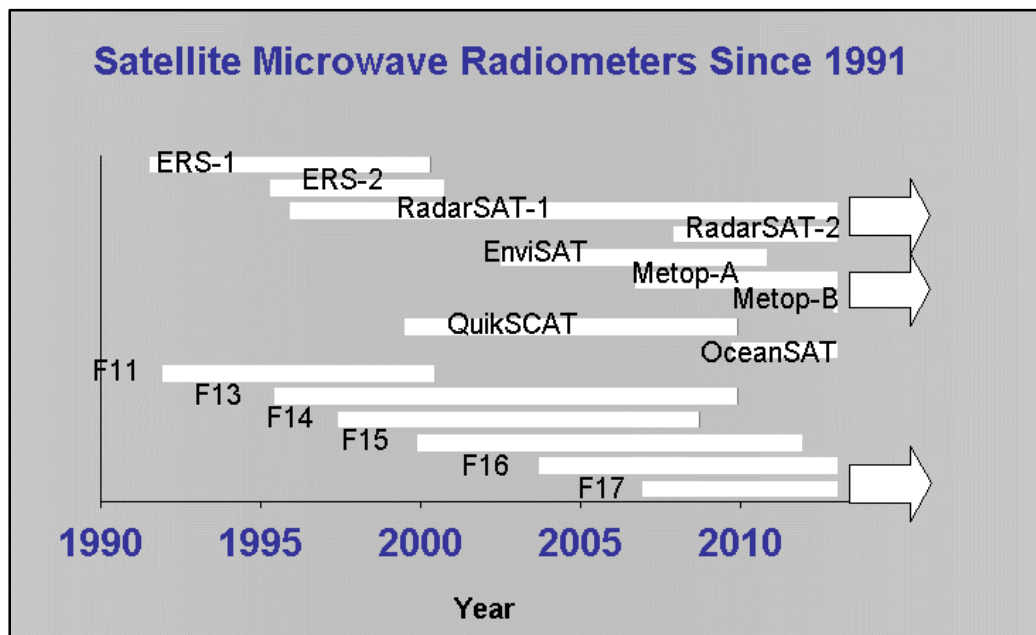
available. A wind retrieval tool may incorporate data sets from more than one instrument to flag corrupted data or improve accuracy. Some incorporate global calibrations, such as a correction for sea surface temperature (Karagali 2012). Others contain modifications to improve accuracy for specific site conditions or wind classes. For example, CMOD-5 (C-band Modeling) is a GMF developed for retrieving C-band radar products. It was empirically calibrated using in situ data to improve high-wind speed estimates (Hersbach 2002). Other GMFs have been developed for Ku-band scatterometers, including NSCAT-2 and Ku2011 (Karagali 2012). ANSWRS 2.0 is a retrieval tool that was recently upgraded to accept data from six different satellites (Monaldo 2012). ANSWRS 2.0 is modular, making it easier to incorporate new GMF's and new data sets as they become available.

3.1.3. Satellites and Instruments

There are three main SMRR sensor types that are used for wind mapping; Synthetic Aperture Radar (SAR), Scatterometry (SCAT), and Passive Microwave Imaging (PMI). The first two are active antennae instruments that emit a signal and measure the backscatter coefficient, and the last, PMI, is a passive system that measures the brightness temperature (ambient microwave radiation) of the sea surface. Figure 20 shows the primary earth observing SMRR instruments and satellites launched by the US, Europe and India in the last 20 years, and the service life of each. The list is not

comprehensive¹⁵, but includes the longest running programs, the largest databases and the most commonly cited sources. The three arrows represent six currently operational (February 2013) satellites, plus OceanSAT makes a total of seven operational. The analysis in this paper is focused primarily on these fifteen satellites. Other systems were not included because they were either short lived, prohibitively costly, or the wind products are still considered experimental.

Figure 20- - SMRR Systems Included in Analysis



¹⁵ e.g., it does not include ALMAZ, JERS-1, PALSAR, TerraSAR-X, WindSAT, Sentinel-1, AMSR-E, Cosmo-SkyMed

Table 4- SMRR Satellites Used in This Analysis and Their Service Lives

Satellite /Instr.	Launch	Life(yrs)
ERS-1/SAR	Jul-91	8.8
ERS-2/SAR	Apr-95	16.4
EnviSAT/ASAR	Jun-02	8.3
RADARSAT-1/SAR-1	Nov-95	17.1(+)
RADARSAT-2/SAR-2	Dec-07	5.1(+)
Metop-A /ASCAT	Oct-06	6.3(+)
Metop-B /ASCAT	Sep-12	0.2(+)
OceanSAT/SCAT	Sep-09	3.3(+)
SeaWinds/QuikSCAT	Jul-99	10.4
F11 SSM/I- Passive	Dec-91	8.5
F13 SSM/I- ""	May-95	14.5
F14 SSM/I-""	May-97	11.3
F15 SSM/I –""	Dec-99	6.7
F16 SSMIS-""	Oct-03	9.3(+)
F17 SSMIS-""	Dec-06	6.1(+)
(+) – still operating as of Feb. 2013		

3.1.4. Orbits and Coverage, Swaths and Scenes

All earth observing SMRR satellites use sun synchronous orbits, which follow a nearly N-S track that crosses the equator twice per orbit at a polar inclination of ~ 8.0 to 8.5 degrees (see Figure 21). These orbits are designed to pass over the equator (or any other parallel) at the same local solar times each day, providing a constant illumination angle for optical sensors. Although SMRR is not an optical sensor, and is impervious to clouds or darkness, this “clockwork” orbit can result in bias due to undetected diurnal effects. Coverage is defined as the average number of scans of a given location, daily, annually or

as a percentage¹⁶. Because tracks converge near the poles, coverage generally increases with latitude. Coverage in non-polar regions varies from ~ twice a day to ~ 2 or 3 times a month, depending primarily on the latitude and the satellite swath width and ground speed. The repeat cycle (time to cover all orbit ground tracks and repeat the pattern) is about 35 days for polar orbiting SMRR satellites.

Data from across the swath are processed and stored in “scenes” the width of the swath, with roughly rectangular dimensions. This is shown in Figure 22, where three scenes intersect in Denmark. These three scenes have been processed through a GMF to represent wind speed by color coding. Each scene takes ~ 1 to 3 minutes to capture. The different arrow directions and scene orientations reflect ascending and descending satellite passes.

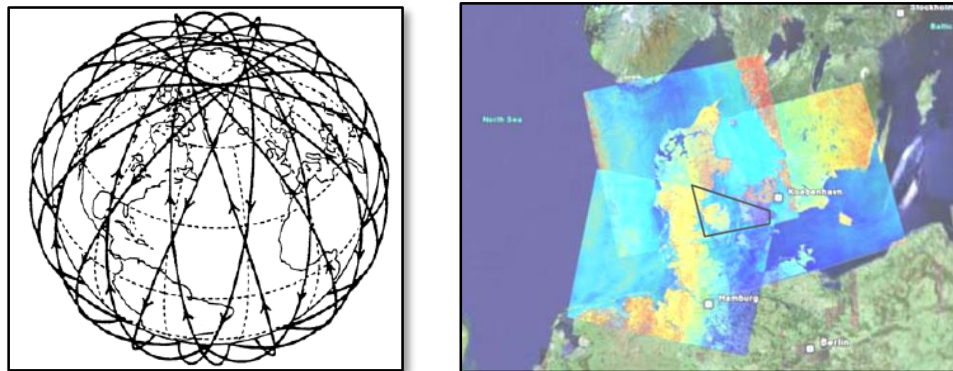


Figure 21- Polar SunSynchronous Orbits, courtesy European Space Agency

Figure 22 – SAR scenes around Denmark, from Hasager et al 2012

¹⁶ Once a day would be 100% coverage

3.1.5. Data Flagging, Masking, and Scrubbing

Before processing data for wind retrievals, it must be “scrubbed” clean of corrupted samples or areas. Four conditions can cause significant data corruption, and these are outlined below;

- **Surface Anomalies** -Land, breaking waves, and sea ice do not support capillary waves, and so will contaminate wind retrievals. They must be flagged and either masked out (removed from the scene or image) or scrubbed (removed from the data set) before wind speeds are estimated (Alsweiss 2007).
- **High or Low Winds** - Error is also higher at very low or high wind speeds (Karagali 2012). To reduce error, corrupted data can either be scrubbed or corrected in the GMF, depending on the SMRR instrument characteristics and the methodology of the wind retrieval.
- **Precipitation** - Rain can cause a positive bias at low wind speeds and a negative bias at high wind speeds, and the effects are non-linear and poorly understood (Ricciarduli et al 2011, Table 1, Alsweiss 2007, Figure 5.11). Rain is therefore almost always scrubbed.
- **Other Capillary Effects** - The signal is also affected to some degree by factors that influence small wave physics including shallow bottom features (Christiansen et al 2004), internal waves, tidal currents, or changed surface tension caused by surfactants like oil spills or algal blooms (Hasager et al, 2005). These effects can be more difficult to discern.

This cleansing of the data set reduces the inventory of valid scans. The percent of the original data set that is removed is called the “scrub rate”. Most of the cited research uses

correlation studies with met towers or buoys to estimate the accuracy of SMRR wind estimates, so the scan inventories in those studies reflect only valid co-located pairs. This means that problems with the reference data stream (in most studies, cup anemometer readings) increase the scrub rate. From published data, it is not always possible to determine how many pairs were scrubbed due to anemometer shortcomings vs. due to bad satellite data. This analysis adopts the conservative assumption that scrub rates derived from cited studies are entirely the fault of bad satellite data. This reduces the risk of underestimating the scrub rate for satellite data.

3.1.6. Polarization

Microwave radiation propagates in waves that can be polarized in two orthogonal directions, designated by convention as horizontal and vertical. Although SMRR polarizations share these designations, they are in reference to the direction of signal propagation, not the earth's surface. Depending on the incident angle of the radar beam with the capillary wave direction, one polarization produces a more robust correlation between backscatter and wind speed¹⁷ (Beal et al 2004, p.5). For older instruments, polarization was either absent, fixed or manually selectable via remote control. For some newer instruments, polarization can be selected independently for the transmitter and receiver, and with at least one instrument (ScanSAR), polarization can be automatically

¹⁷ The same principle is applied when sunglasses are polarized in the horizontal plane to reduce the sun's glare reflecting off the water.

and rapidly switched between vertical and horizontal, creating two interlaced data sets. If the wind direction is known, this information can be used in the GMF to select or favor the dataset with the optimal polarization geometry for each pass according to the wind direction. In general, polarization adds information about the sea surface geometry that can remove wind and wave directional ambiguity (Yueh et al 1994).

3.1.7. Multi-Modal Operation

Some SMRR instruments operated in a number of different modes with different polarizations, scan patterns and swath widths, further complicating estimates of scrub rates and inventory. The instrument settings are (were) routinely changed to accommodate specific user needs. Although a “background mission” is defined which determines the default scan mode, for some instruments, it is difficult to determine average annual coverage accurately without access to complete operational records for the life of each satellite. Unfortunately, these records are not published in any aggregated, geo-referenced format, so a different methodology is adopted which is sufficiently robust for the purpose of this analysis.

3.1.8. Cross Check Inventory Methodology

Coverage and inventory are estimated by two methods and cross-checked. First, in order to establish an upper bound, the maximum theoretical coverage is calculated based on

full-time background mission mode (widest swath) and 100% availability. Second, this upper bound is compared to actual SMRR database queries and retrievals performed in this study and in other studies, and scrub rates and discrepancies are investigated. This is done to determine if the coverage estimates generated in this analysis are supported by both theory and practice. Table 5 summarizes the maximum coverage at the 39th parallel (off Cape May, NJ, near the center of the MAB) and the 56th parallel (North and Baltic Seas – study area for most cited studies). The ratio of theoretical coverage between the two latitudes is 1.4, which is the ratio of the lengths of the two parallels¹⁸. The calculations supporting Table 5 are presented in Appendix A.

Some of the studies reviewed in this report provide information only on accuracy, some evaluated only inventory, and some provided enough data to estimate both. The following sections discuss the coverage, resolution, and accuracy of SMRR instruments based on a survey of published research, databases, and online wind product catalogues.

¹⁸ The orbital inclination of 8 degrees has an insignificant effect on this ratio at the latitudes under investigation.

Table 5- Maximum Theoretical Coverage, SMRR, from Appendix A

Maximum Theoretical Coverage, SMRR			Theoretical Maximum Daily Coverage		Theoretical Maximum Scans/yr	
	Satellite/Instrument	Max Swath Width (km)	39 th paral.	56 th paral.	39 th paral.	56 th paral.
Synthetic Aperture (SAR)	ERS-1,2/SAR	100	9%	13%	34	47
	RADARSAT-1,2	500	46%	64%	169	234
	EnviSAT/ASAR	400	37%	51%	135	187
Scatterometers	ERS-1, 2/ESCAT	400	37%	51%	135	187
	Metop-A, B /ASCAT	1000	92%	128%	337	468
	Sea-Winds/QuikSCAT	1800	166%	231%	607	843
	OceanSAT/SCAT	1400	129%	180%	472	656
PMI (SSM/I)	F11 – F 17 SSM/I	1400	129%	180%	472	656

3.2. Synthetic Aperture Radar

Synthetic Aperture Radar (SAR) uses an active pulsed, phased-array antenna that emulates a much wider antenna by using the satellite motion to collect data along a path spanning the length of an imaginary antenna (synthetic aperture) in an imaginary geosynchronous orbit. The data are processed to reconstruct the synthetic aperture signal, compensating for time delay caused by satellite transit (Beal et al 2004). This simulates a snapshot from an imaginary kilometer scale stationary antenna. The concept is also used in widely spaced, terrestrial dish antenna arrays that simulate one huge antenna for detecting radio waves from deep space. The SAR frequency usually used for ocean wind sensing is C-band, and the signal may be polarized either vertically or horizontally. A

thorough description of the technology can be found in Olmsted (1993). Additional satellite SAR sensors operating at L band (~1.2 GHz) and X band (~10 GHz) have recently come online and new GMFs are being developed and validated for wind retrieval (Thompson et al 2012). These wind products show potential, but the data were not included in the inventory since they are either very sparse or still considered experimental.

SAR has low swath width (~60 to 100 km), but the radar images have very high resolution (~10 m – 100 m) and in most instruments the scan mode is selectable. Figure 23 shows an example for RadarSAT –2 . The image resolution (NRCS pixel size) is on the order of 5 – 50 m, but noise at this level produces “speckle” in the image which must be normalized by area averaging to reduce random noise (Christiansen 2006). The resolution of wind retrievals from SAR is therefore not quite as good, but can be sub-kilometer at any swath width. Some SAR instruments can also operate in wide scan mode with a ~ 500 km swath width

A study conducted by researchers at DTU estimated that SAR images contain sufficient information to produce reliable wind speed estimates on a 500m grid (Christiansen et al 2006). Most SAR wind retrievals in published studies are mapped to a 400 m or 500 m grid. SAR images can be processed closer to the coastline because their higher resolution

allows a “tighter” coastal mask than scatterometers¹⁹. SAR images have also been used successfully to estimate significant wave height and direction (Plant et al 1997), which is useful for calibrating geophysical model functions, as described in Section 4.2.24.3, “Re-processing Archival Datasets With Tuned GMFs”

On the downside, SAR instruments are “single look” sensors that can not reveal wind direction since the backscatter coefficient depends partly on the wind speed relative to the incident angle of the radar beam (Korsbakken et al. 1998). Since the reflected signal strength is partially a function of capillary wave orientation, wind direction must be known to resolve the wind speed. The direction information can come from any source, including in situ sensors, special algorithms built into the GMF (Horstmann et al 2003), NWP models (Monaldo et al 2001), or scatterometer products (Monaldo et al 2004). Error in the input wind direction increases error in the output wind speed. Another disadvantage is that in most cases, SAR data are provided in radar image format only, not wind products. With a few exceptions for government and academia, SAR images must be purchased commercially and wind products must be retrieved by the user with a SAR wind retrieval tool such as ANSWRS (publically available, previously discussed).

¹⁹ Any averaging cells within ~ 3 km of the shoreline are “masked” out of the analysis to avoid any land reflections corrupting the radar data. The larger the averaging cell, the more area removed near the coast.

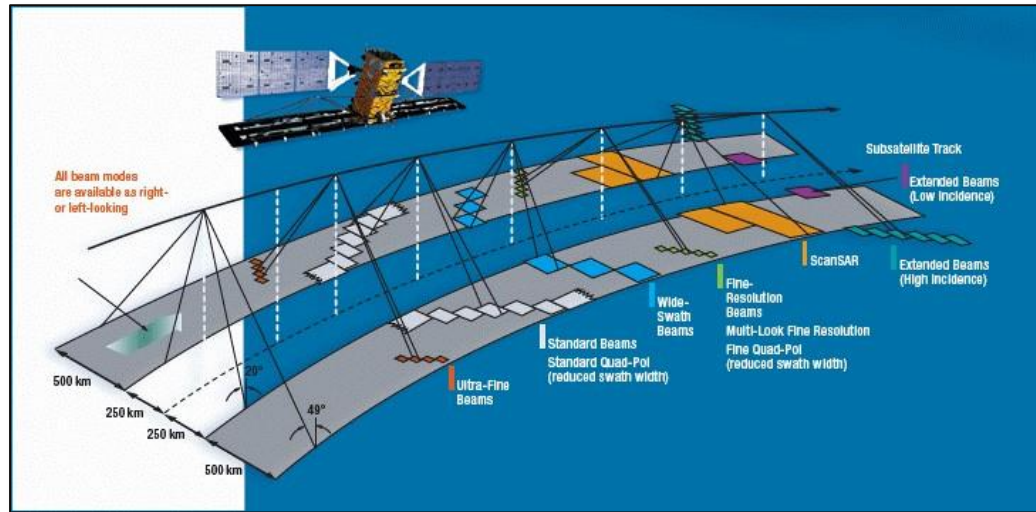


Figure 23 - RadarSAT-2 SAR Scan Patterns, from Canadian Space Agency

3.2.1. SAR - ERS-1 and 2

The first successful multi-year program to collect global satellite wind data began in 1991 with instruments launched by the European Space Agency (ESA) aboard the European Remote Sensing satellites ERS-1 and ERS-2 (ESA 2012). ERS-1 launched on 17 July 1991 and ERS-2 launched on 21 April 1995. These two satellites carried the C-band Active Microwave Instrument (AMI) which offered the unique ability to operate in two modes. In image mode, the SAR swath width for ERS-1 and 2 is 100km, and the NRCS image resolution is ~25 m. Figure 24 shows a sample ERS-2/SAR wind product retrieved from a SAR image from 25 Feb 2003 covering the wind farm at Horns Rev, Denmark (black trapezoid). The velocity deficit downwind of Horns Rev and the land

shadowing effect are clearly visible. For estimating scale, Horns Rev is ~ 6 km wide. The wind speed resolution is ~ 500m.

The AMI instruments aboard ERS-1 and ERS-2 could also operate in scatterometer mode, but only upon user request, so the data are sparse (ESA 2011). Other scatterometers (discussed later) have since compiled far more data and some still collect data full-time, with capabilities beyond those of the ERS scatterometer. ERS wind scatterometer data were therefore not included in this analysis.

The ERS SAR program lasted far longer than expected, and experienced a series of systems failures as time passed, including the loss of on-board gyroscopes, the loss of the on-board data recorder, and the depletion of hydrazine propellant. Despite these setbacks, most failures were managed with technical workarounds. For example, the loss of propellant forced the adoption of a new navigation strategy which allowed orbital inclination to drift, but the drift was known and the data could be calibrated, so it had no significant impact on wind retrieval accuracy or resolution²⁰. The ERS-2 mission ended when contact was lost with the satellite in April 2012.

²⁰ For the 1.5 years of drifting inclination, coverage actually increased by about 15% because the average repeat cycle went from 35 days to 30 days -from <http://earth.esa.int/download/envisat/Impact-of-Envisat-Mission-Ext-SAR-data-aug10.pdf>

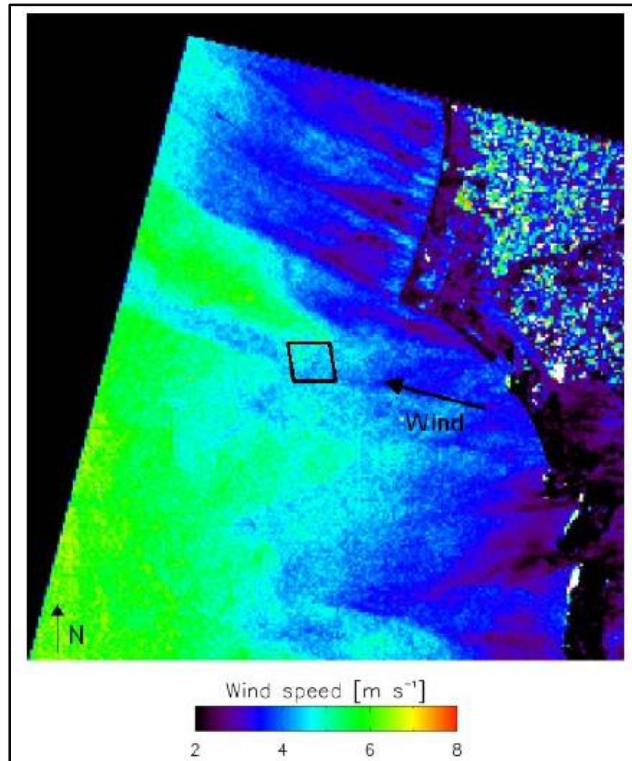


Figure 24 Sample SAR Wind Product around Horns Rev - from Christiansen 2006

3.2.1.1. SAR -ERS- EOLI Inventory

The ESA operates the Earth Observation Link (EOLI) server ²¹, which provides a comprehensive database of available historical Envisat and ERS-1 and 2 scans. A sample 25 km x 25 km block was selected centered on the study area off Cape May, NJ, and the database was geographically queried for SAR products from these two satellites.

²¹ EOLI Server URL - <http://earth.esa.int/EOLi/EOLi.html>

For ERS-1 and ERS-2, 453 SAR wide swath mode and 202 SAR wave mode images were identified beginning Sep 30, 1991, and ending 31 Dec 2008, a period of about 16.2 years. Within that period, the two instruments collected over 24 years of data sets, for a mean sample rate of about 30 ERS -SAR images per satellite year. This compares well to a theoretical maximum of 34 per year from Appendix A, and to two other estimates of about 3 per month in the Baltic Sea, (Hasager et al 2006, Christiansen 2006).

3.2.2. ASAR

EnviSAT was launched in 2002 with advanced synthetic aperture (ASAR) onboard, which allowed sub-kilometer resolution. ASAR could operate in 27 different modes, but only one at a time. Because the background mission²² for ASAR is ScanSAR, most of the scans are in this mode. In ScanSAR mode, the instrument used a checkerboard scanning technique to sample a 400km swath with resolution of about 150 m. Other, user selected modes range from 56 to 100 km swath width, with a resolution of ~ 30 m. ASAR could operate in four polarization modes, independently selectable for transmitter and receiver (designated HH, VV, VH, and HV) and could also operate in alternating polarization (AP) mode, using high frequency switching of polarization to generate two

²² The “background mission” default setting of WSM is designed for widest coverage, at the cost of resolution

interlaced data sets which can be processed independently. The Envisat mission ended on 08 April 2012, following the loss of contact with the satellite²³.

3.2.2.1. ASAR Coverage-Handbook Theoretical Maximum

ASAR wide swath image inventory per 35 day repeat cycle at a given latitude can be estimated by using Table 6, taken from the ASAR Handbook, produced by the European Space Agency (ESA 2007). Based on trigonometric interpolation to 39° latitude (Cape May, NJ), about 6.8 samples should be available per 35 day cycle, counting only descending passes, or 13.6, including ascending passes. There are 10.4 35-day cycles in a year, for a theoretical maximum of ~ 140 ASAR samples per year at 39 latitude. This estimate agrees well with the theoretical maximum of 135 scans/ year calculated in Appendix A.

Table 6- ASAR coverage per 35 day cycle, by latitude. Data from Table 1.2, ASAR handbook (ESA 2007)

ASAR Cyclical Coverage by Latitude					
Latitude (degrees N)	0	39	45	60	70
Scans per 35 day /cycle	5	6.8(*)	7	11	16
(*) – interpolated based on $\cos(\text{latitude})$					

²³ Information from European Space Agency, available at (https://earth.esa.int/web/guest/missions/esa-operational-co-missions/envisat/content?p_r_p_564233524_assetIdentifier=asar-faq-3829)

3.2.2.2. ASAR Coverage- EOLI Query vs DTU Estimate

The ESA operates the Earth Observation Link (EOLI) server²⁴ which provides a fairly comprehensive database of available historical SMRR data including Envisat scans at no charge. A sample 25 km x 25 km block was selected centered on the study area off Cape May, NJ, and the database was geographically queried for ASAR products. 905 Envisat ASAR images were identified over the life of the EnviSAT mission - about 9.8 years. 841 of the images were taken in Wide Swath or Global mode, with a scan width of 400 km, and 64 scans were in Image, Wave, or Polarization modes, with effective scan widths²⁵ at or below 100 km. To ensure a conservative estimate of inventory, these narrow scans (~7% of the total) were discarded. This translates to an average coverage of about 86 scans per year, which is about 64% of the theoretical maximum of 135 scans on the 39th parallel. A DTU study (Hasager et al 2006) estimated the availability of wide swath ASAR images at about 8 per month, or 96 per year, which also agrees reasonably well with the EOLI Cape May query, since the higher estimate in Hasager et al (2006) reflects higher coverage at the 56th parallel.

²⁴ Data available at <http://earth.esa.int/EOLI/EOLI.html>

²⁵ Some scan patterns use alternating or checkerboard patterns, so “effective scan width” reflects the proportional coverage in these cases

3.2.2.3. ASAR Accuracy and Resolution – Horns Rev Wake Study

Wind speed deficits are important in the study of wake effects, where the primary concern is quantifying the velocity differential between free stream and wake, not precisely measuring the absolute wind speed. In a PhD dissertation at DTU (Christiansen et al 2005), the snapshot velocity deficit in the lee of the Horns Rev offshore wind farm was estimated using 5 ERS-2 SAR and 14 ASAR images and compared to the deficit indicated by calibrated wake models. The study concluded that SAR data are useful for measuring wind farm wakes for wind speeds anywhere between 4 and 15 m/sec. At speeds below this range, speckle noise dominated the signal, and at speeds above, the signal began to show signs of saturation.

Figure 25 shows a sample SAR image (Soprano 2013), and Figure 26 shows a plot of return signal strength along a transect within the image. The NRCS image (Level-1 product) was taken on 7 feb 2012, at 21:19 UTC around Horns Rev 1 and 2 using the ASAR instrument. The small white dots are turbines with spacing of ~ 650m. The pixel size is ~30 m. The velocity deficit can clearly be seen as a darker region in the wake of the wind farms. The figure provides a clear illustration of SAR image resolution relative to a wind farm. It also provides a good visual sense of why some area-averaging is required to reduce noise in the signal (“speckle”) before wind products can be retrieved. Figure 26 plots the normalized radar reflectivity across the wake of Horns Rev 2 along the transect indicated in white. The observed maximum signal deficit is about 10%, or

about 1 m/s^{26} . Although the graph in Figure 26 suggests sensitivity on the order of $\sim 1\%$, uncertainty and bias associated with other factors preclude universal claims to this level of accuracy for estimating absolute wind speed. However, within a single scan, the quantification of spatial variation should be possible with great accuracy, since much of the error is scene-dependent and creates nearly uniform bias within a scene (e.g., error in the input wind direction or the NRCS calibration). These types of errors have no significant affect on velocity differentials from spatial vaiation within a scene.

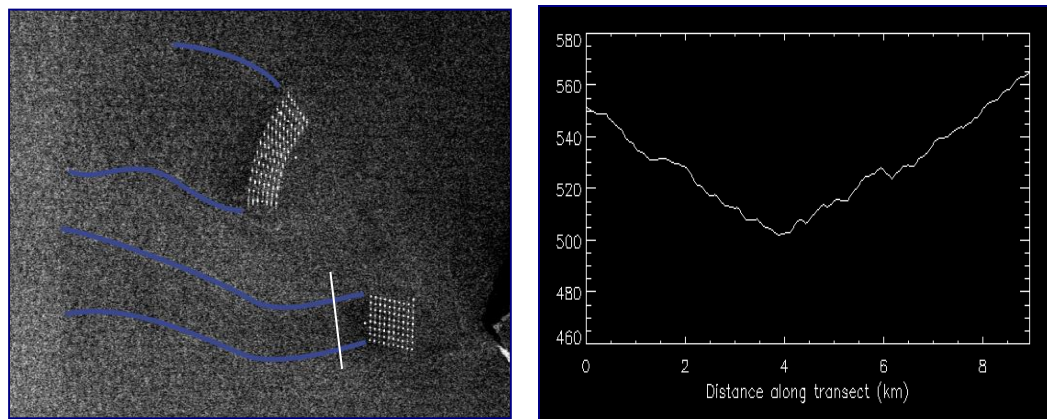


Figure 25- Envisat ASAR image, Horns Rev. downloaded from <http://so-prano.cls.fr/?p=1159>

Figure 26 Backscatter Across Transect, Horns Rev, downloaded from <http://so-prano.cls.fr/?p=1159>

²⁶ A Level 2 wind map product, downloaded²⁶ from the EUMETSAT portal for the same 7 Feb 2012 scan indicates that the wind speed upwind of Horns Rev at the time was approximately 10 m/s, therefore the observed velocity deficit was around 1 m/s, since the relationship between reflectivity and wind speed is roughly linear at this scale (see Christiansen et al 2006, Figure 1).

3.2.2.4. ASAR Coverage and Accuracy– Hasager et al 2011

In a 2011 study published by DTU as part of the NorseWind project (Hasager et al 2011), ASAR scans co-located with ten met towers were correlated with the met tower data. FINO-2 wind readings were collected from 09 Dec 2007 to 21 September 2009, a period of about 1.8 yrs. After scrubbing the data for rain and sea ice and using a ~ 1 km footprint averaging methodology, 180 valid co-located data pairs were identified, for an average rate of about 100 data points per year,. This is about 53% of the theoretical maximum of 187 ASAR wide scans per year along the 56th parallel.

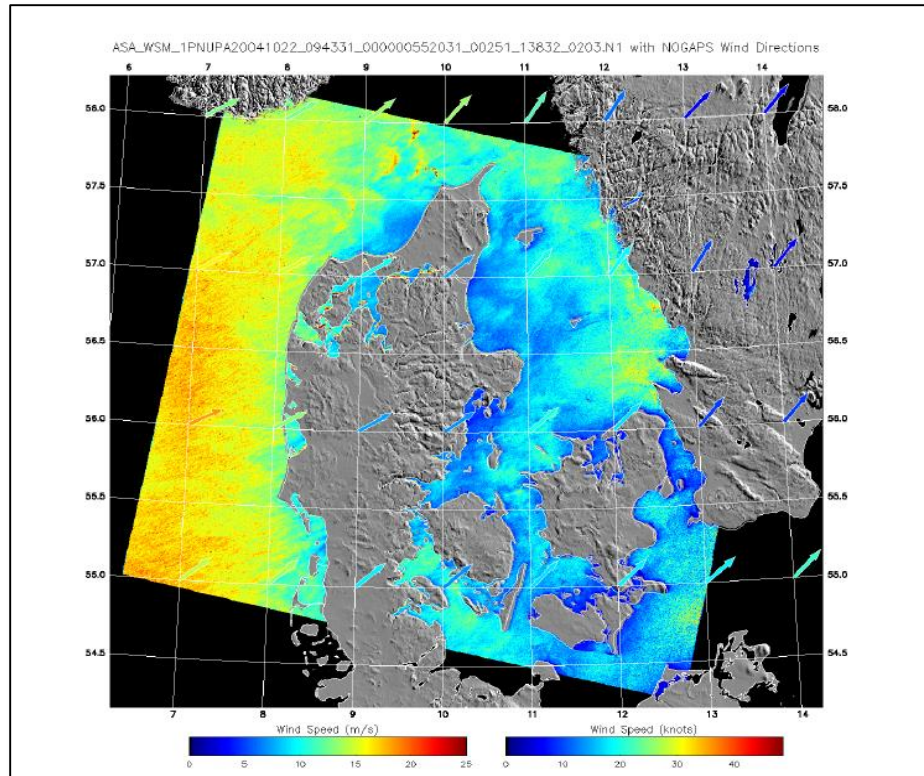


Figure 27-ASAR Product around Denmark, from Hasager et al 2011

The wind products were resolved to 500 m grid cells and then compared to calibrated wind data from 10 meteorological masts in the Baltic Sea and North Sea around Denmark. The Wind Atlas Analysis and Application Program (WasP) developed by DTU²⁷ was used to extrapolate the mast data from the lowest anemometer height down to 10 m ASL to match SAR retrieval height. The study provided a rigorous statistical analysis of SAR wind products, and the results clearly show that accuracy is much better

²⁷ WASP – Software package from Risø DTU for calculating wind distributions/production based on the Wind Atlas Methodology. Includes roughness model, flow model (orography) and obstacle model. Download and info avail. at <http://www.wasp.dk>

than the nominal $\pm 2 \text{ m s}^{-1}$ estimated in Stoffelen, 1997. For the 875 collocated data pairs identified for the ten towers, the correlation study produced the descriptors in Table 7. FINO-2 results are broken out because the sample size was largest of all the meteorological towers. The study scrubbed wake sectors from the tower data, but did not filter out low or high wind speeds, and noted a negative bias above 15 m/s, where the signal shows the first indications of saturation.

In the same DTU study (Hasager et al 2011), images from ENVISAT ASAR were processed with the APL/NOAA SAR Wind Retrieval System (ANSWRS)²⁸. Figure 27, from Hasager et al 2011, shows a sample map of wind speed generated with ANSWRS from an EnviSAT ASAR scene acquired Oct 22 2004 in wide swath mode over Danish waters.

3.2.2.5. ASAR Accuracy – SATWIND (Christiansen et al 2006b)

Project SAT-WIND was a wind mapping research project from 2003 to 2006, funded by the Danish Technical Research Council. The goal of the project was to verify the applicability of satellite wind maps derived from passive microwave, altimeter, scatterometer and imaging SAR technologies for wind energy tools for wind resource

²⁸ ANSWRS was developed jointly by The Johns Hopkins University Applied Physics Laboratory (APL) and NOAA. ANSWRS uses the CMOD-5 GMF (Pichel et al 2000) and was recently upgraded to ANSWRS2.0, which can process most SAR databases.

mapping. The SAT-WIND project examined wind products from EnviSAT/ASAR, retrieved using three different GMFs and a box averaging method, and compared them to hourly average Horns Rev met mast data for wind speeds between 2-15 m/s (Christiansen et al 2006 b). Ninety-one collocated data pairs were identified. Using the CMOD-IFR2 GMF, the standard deviation of error observed was 1.1 m/s and the linear regression showed the slope near 1.0 and a bias of -0.26 m/s. Energy density calculated using a box averaging method was 421 W/m^2 , compared to 422 W/m^2 using in situ data from Horns Rev met mast. The results of the two ASAR correlation studies are statistically summarized in Table 7. The standard deviations observed in Hasager et al 2011 are higher because very low and high wind speeds were not scrubbed from the data in that study.

3.2.2.6. ASAR Coverage, Accuracy for Energy Density, -Badger et al 2010

In this study (Badger et al 2010), researchers investigated the ability of ASAR to generate accurate energy density estimates by comparing them to estimates generated using four years of in situ data from three met masts in the North Sea (Horns Rev, Hovsore²⁹, FINO-1). 627 ASAR images were identified, each including one or more of the met towers. The ASAR scans covered a four year period, so the average scan rate per location is the

²⁹ Hovsore wind data was translated to a site 9 km away, offshore.

average no. of samples divided by 4, which is $(422/4 =)$ 105 per year, which is about 56% of the theoretical maximum of 187 (See Appendix A).

Algorithms were developed for estimating Weibull A and k parameters, which are often used to describe the Probability Density Function (PDF) of wind speed (Weibull 1951). The scale parameter, A, can be considered analagous to the most frequent wind speed, and the shape parameter, k, to the standard deviation. These parameters can be used to estimate energy density (Manwell 2007). Table 7 is extracted from Table 3 of Badger et al 2010, which summarizes the error statistics. The average wind speed bias of the full data set was 0.0 and the error of the energy density estimates varied from ~ 1% to 4%. The authors noted that these deviations (from estimates using calibrated in situ data) are better than most results reported from mesoscale modeling.

Table 7- Error statistics for three met masts vs. SAR Retrievals - adapted from Table 3, Badger et al 2010

	N	U_{SAR} (m/s)	U_{Met} (m/s)	U Bias	E_{SAR} (W/m ²)	E_{Met} (W/m ²)	E_{SAR} σ (%)
Hovsore	444	7.86	7.79	+0.9%	551 +/- 40	532	3.6%
Horns Rev	464	7.72	7.78	-0.8%	504 +/- 33	499	0.9%
FINO-1	359	8.11	8.12	-0.1%	584 +/- 43	561	4.1%

3.2.3. ScanSAR/ RadarSAT-1 and 2

Radarsat- 1 and Radarsat-2 are Canadian Space Agency (CSA) earth observing satellites that both carry SAR sensors operating at a single frequency of 5.3 GHz, in the C band. Radarsat offers 7 different scan modes and could be programmed to look either right or left. They range from fine, with a scan grid of 50 km by 50 km and a resolution of 25 m, to ScanSAR, with a scan width up to 500 km and a resolution of ~100 meters.

Figure 28 shows an NRCS image acquired off Cape May, NJ, by RadarSAT 1 in ScanSAR mode (on the left) . Figure 29 (on the right) shows the image converted to 100 m resolution raster data wind speed using ANSWRS. Topographic images were added to the land mask on the right. The image was acquired May 13 2003 at 22:55:00 UTC. The figures clearly show the streak features on the NRCS image which translate to streaked wind patterns in the ANWRS image. For scale, the Delaware Bay entrance is about 18 km across.

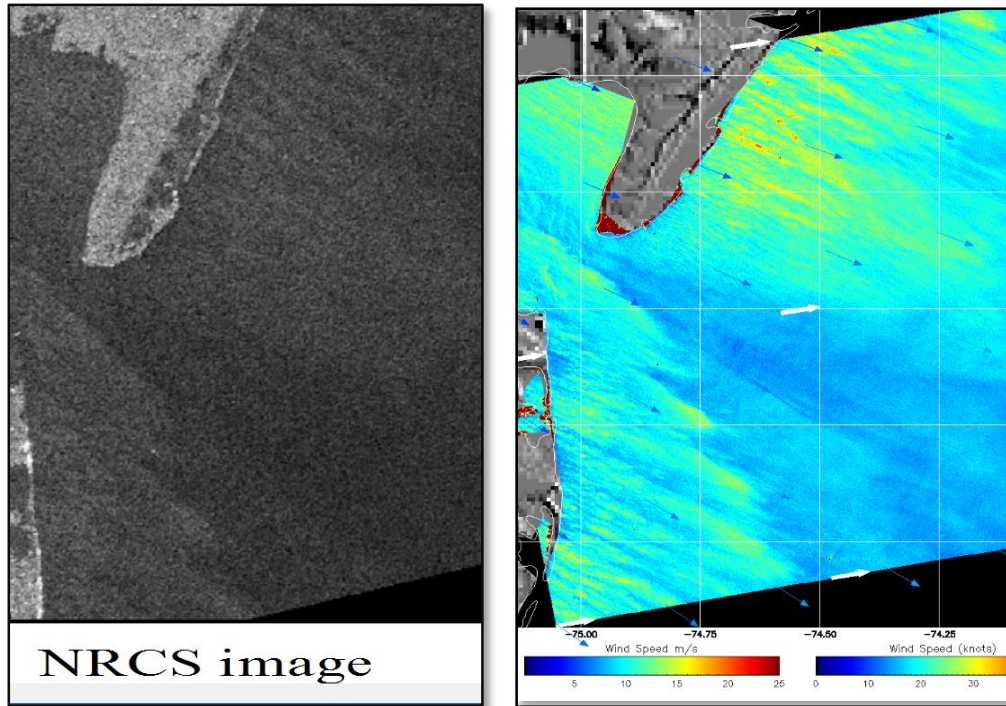


**Figure 28- NRCS Image from RADARSAT-1, from <http://ceocat.ccrs.nrcan.gc.ca>
 Figure 29- ANSWRS retrieval, from Monaldo 2012. Blue is higher wind speeds.**

RadarSAT-1 ScanSAR was somewhat hobbled by a “*non-linear, scene-dependent instrument transfer function*” that made accurate calibration between scenes impossible for high winds (Beal et al 2004). However, it did not affect retrievals below ~ 15 m/s, and because the function was scene dependent, it had no effect on spatial differentials within a single scene. Radarsat-2 was launched on December 14, 2007 with a more advanced C-band SAR system that improves on the NRCS (radar pixel) resolution of RadarSAT-1 (from 10 m to 5 m). The sensor also doubles the options for signal polarity.

3.2.3.1. ScanSAR Inventory

In a study led by Johns Hopkins' Applied Physics Lab (APL-Monaldo 2012), 1495 total RadarSAT-1 scans were identified between 1996-2008 for an area off the coast of MD, very close to Cape May. 44 images were scrubbed due to processing failures and 12 were invalidated for "anomalies", leaving 1439 valid images. The average number of images was around 115 per year. This is about 68% of the theoretical maximum of 169 scans per year given in Appendix A, and reflects the scrubbing of corrupted or invalid scans and those that were not taken in ScanSAR mode.

3.2.4. SAR Inventory Summary

To bracket the range of possibilities, Table 8 shows both the theoretical maximum number of scans and the lowest number of scans retrieved in cited studies and database queries.

- For ERS SAR, the annual rate is assumed to be 30, which agrees well with all sources evaluated.
- For ASAR, queries and estimates ranged from 86 per year to 105 per year, so the lower bound (86) was selected to ensure a conservative estimate, given the uncertainty.
- For ScanSAR, the annual rate is 115 based on Monaldo 2012.

To summarize, there should be well over 4,000 valid, SAR scans available for a typical 39 degree latitude site such as the study area offshore Delaware. The number of valid samples increases at a rate of about 230 per year from the two ScanSAR instruments. The estimates are based on the scrub rates observed in the North Sea, where sea ice sometimes reduces the valid sample size. In the study area, sea ice is extremely rare, so the coverage could be under-estimated.

Table 8-SAR Coverage and Inventory Summary

Satellite/Instrument	Active Life (yrs)	Swath Width (km)	Max. Scans/yr 39 th parallel	Scrubbed Scans/ yr	Total Scans Avail.
ERS-1/SAR/ (1)	8.3	100	34	30	249
ERS-2/SAR	16.4	100	34	30	492
RADARSAT-1/ScanSAR	17.1	500	169	115	1966
RADARSAT-2/ScanSAR-2	5.1	500	169	115	586
EnviSAT/ASAR wide mode	9.8	400	135	86	843
TOTAL SAR scans avail.					4137

3.2.5. SAR Accuracy Summary

Newer GMFs for SAR images are able to generate wind speed products with sub-kilometer resolution and accuracy that far exceeds the original SAR wind product specifications. The five cited studies show that when SAR wind products are compared to time averaged in situ data from met tower anemometers, bias is typically less than

0.25 m/s. Standard deviation of the error varies between ~1 and 2 m/s, depending on the number of data points, the amount of data scrubbing, the distance offshore, the spatial and temporal criteria for “co-located” and other factors. If wind speeds below ~ 2m/s and above ~15 m/s are scrubbed, standard deviation is much closer to 1 m/s. Pearson correlation coefficients of SAR products compared to offshore met towers average around $R= 0.9$. Estimates of energy density using SAR wind speeds deviated between 1% and 4% from estimates using calibrated, scrubbed met tower data. Uncertainty in snapshot SAR wind retrievals is comprised primarily of error in the NRCS image, the input wind direction, and the wind profile model.

3.3. Scatterometers

Scatterometers are active pulsed, real aperture radars that operate at either C-band or Ku-band and can scan a wide swath (~1000 km to 1800 km). Scatterometer data must be area averaged to improve the CNR using geometric sampling strategies, resulting in much larger (~10 km to 20 km) averaging areas. They provide twice daily coverage, but their wind product resolution is limited to 12.5 km³⁰. Most scatterometer products begin at least 12.5 km offshore to avoid “pixels” contaminated by coastal effects and land surfaces. Sea ice and rain are flagged most accurately using data from PMI systems (discussed in the following section), and this can be managed automatically in the GMF

³⁰ One new GMF resolves to 2.5 km, but is still considered experimental

(Ricciarduli 2011). Because PMI systems have a lower resolution (spatial averaging cell size is larger), this flagging is only effective to within 10 to 15 km of the shoreline.

Unlike SAR, the wind direction is derived by scatterometers by using multiple look antennae. The configuration may employ moving beams or three fixed, separate beams, as shown in Figure 30. Three backscatter measurements are taken of the same point from different angles as each beam passes over in rapid succession. Each “triplet” may then be resolved into a wind vector. One other advantage of scatterometers is that the products are numerous and free, providing a large data sample at no cost. On the down side, the signal can’t be resolved beyond a 10 to 15 km grid due to area averaging for boosting the CNR.

Theoretical coverage is simpler to estimate for scatterometers since the swath width is constant. The maximum theoretical coverage, based on the scan width and latitude, is given in Table 5 (see Appendix A for calculations). In practice, coverage is lower since it is affected by the scrubbing of corrupted data. Scatterometers have a nominal wind speed accuracy of ± 2 m/s in the range 3 to 20 m/s (for ASCAT, valid from 2 m/s to 25 m/s) (JPL 2001), however the studies cited below show that accuracy is much higher.

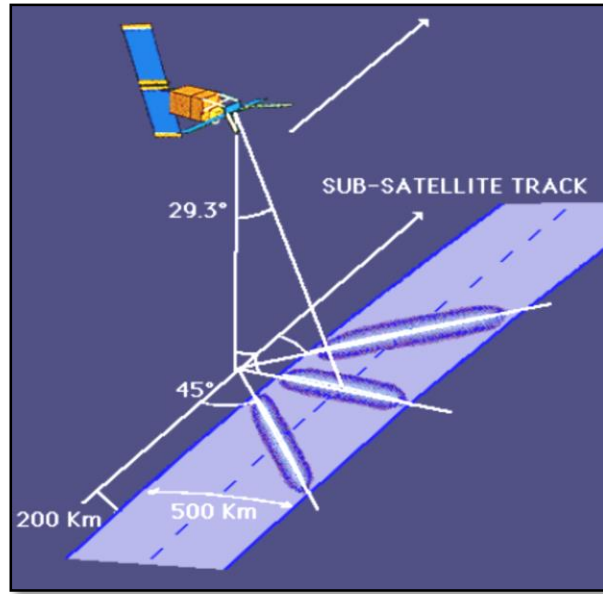


Figure 30- Scatterometer Scan Pattern Example, from
https://earth.esa.int/ers/eo4.10075/scatt_design.html

The analysis in the following sections provides a reasonable, conservative first-order estimate of the coverage, accuracy, and resolution of scatterometers for use in wind products and wind mapping. Three scatterometer instruments and the reasons for their selection are presented below :

- QuikSCAT is considered the workhorse of the wind retrieval world and represents the largest scatterometer database;
- ASCAT (Advanced Scatterometer) is a more advanced system with the fastest growing database, since there are currently two operating instruments; and
- OceanSCAT is another wide scan (~1400 km) workhorse launched by the Indian Space Agency in 2009.

Other instruments were not included due to their short time series, their experimental nature, or both.

3.3.1. QuikSCAT

QuikSCAT (a.k.a. SeaWinds) was a Ku-band scatterometer launched on 19 June 1999. It was designed and launched quickly (thus the name) as an emergency replacement for a failed satellite. It was planned for only a three year mission but finally failed on 23 November 2009. It used two active, conically scanning pencil beam radars directed at incident angles separated by 6° , centered on 50° . The scans covered an 1800 km swath, and provided about ten years of data (NASA 2012a, NASA 2013). Level-2 wind products with 12.5km or 25 km spatial resolution are available from NOAA/NESDIS (NESDIS 2007, NOAA 2012).

3.3.1.1. QuikSCAT JPL study (Pickett et al 2003)

An early but often cited study of QuikSCAT was conducted by a consortium of the Jet Propulsion Laboratory at Cal Tech (JPL), NOAA, and the Naval Postgraduate School. After comparing QuikSCAT wind retrievals to NDBC met buoy data from the U.S.Pacific coastline 5741 co-located samples (defined as wind vector being within 25 km and 30 min of the buoy data) from 12 buoys were identified between Point Conception and the Canadian border. All buoys were less than 27 km offshore. The

correlation coefficient for wind speeds from all the buoys vs. QuikSCAT was 0.9. After removing rain corrupted records and wind speeds below 6 m/s, 3314 data pairs remained, and a bias of 0.2 m/s and an RMS error of 1.3 m/s were observed. The test period was August 1999 to December 2000, about 1.3 years. This implies a sample rate of about $(3314 \text{ samples}/12 \text{ buoys}/1.3 \text{ years} =)$ 212 valid co-locations per year per buoy, averaged over a wide range of latitudes.

3.3.1.2. QuikSCAT SAT-WIND Study (Hasager et al 2006a)

Project SAT-WIND was a research project from 2003 to 2006, funded by the Danish Technical Research Council. The goal of the project was to verify the applicability of satellite wind maps derived from passive microwave, altimeter, scatterometer and imaging SAR technologies for wind energy tools for wind resource mapping. As part of the study, about 300 data points from QuikSCAT wind products were compared to data from the met tower at Horns Rev and the wind speed correlation was analyzed for all wind speeds between 0 and 25 m/s (Hasager et al 2006a). The scatter plot is shown in Figure 31. When hourly averages were used, the standard deviation observed was 1.31 m/s and the bias was -0.3. The regression analysis showed the slope near 0.96, and most of the error and bias occurred at wind speeds below ~ 2 m/s and above ~ 15 m/s.

As part of the SAT-WIND study, QuikSCAT data were also retrieved for the entire southeast Baltic from July 1999 to Feb 2007, a period of about 7.5 years. The number of

scrubbed data points at a given location varied from about 2000 closer to the shoreline (within 25 – 50 km) to over 5000 in open water. This translates to a yearly scan rate of between 267 and 667. This represents between 32% and 80% of the theoretical maximum coverage (843/yr) at that latitude.

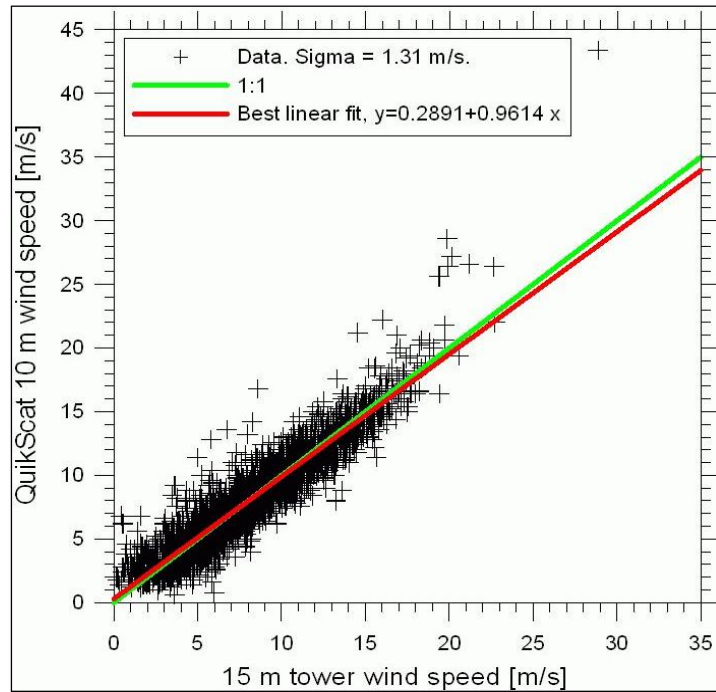


Figure 31 -Scatter Plot, QuikSCAT vs. Horns Rev. from Hasager et al 2006

3.3.1.3. QuikSCAT (Pimenta et al 2008)

As part of a 2008 study of offshore wind resources for Brazil (Pimenta et al 2008), 6 months of QuikSCAT Level 2-B wind products on a 50 km grid were retrieved and compared with wind data from 18 met stations (buoys and platforms) along the coast of

Brazil and the Atlantic and Pacific Coasts of North America. The database covers 7.8 years of records from August 1999 to June 2007, processed to yield daily average wind speed. The hourly wind speed readings of the buoy data were interpolated to match the time of each QuikSCAT scan, producing 32,934 co-located data pairs, which are plotted in Figure 32. The linear regression analysis shows a slope of 0.975 and an offset of -0.146 m/s with a Pearson correlation coefficient of 0.83. This compares to nominal accuracy of ± 1 m/s or 10% for the buoy mounted anemometers. Based on the co-located pairs, the scan rate translates to about 234 per year per met station, or an average coverage of about 64%. It should be noted this low coverage estimate reflects a wide range of latitudes, scrubbing of buoy data, and buoy downtime.

At buoy 44009, near the study area, the bias was 0.2 m/s and the Root Mean Square Error (RMSE) was 2.0 m/s. The study also compared theoretical AEP of a GE 3.6 turbine using the buoy data and compared it to estimates using QuikSCAT data. The QuikSCAT data underestimated output by 4.4%. The authors also noted that much of the scatter is likely due to the buoy data being time averaged over a day, while the QuikSCAT wind is a snapshot, unlikely to match the daily mean.

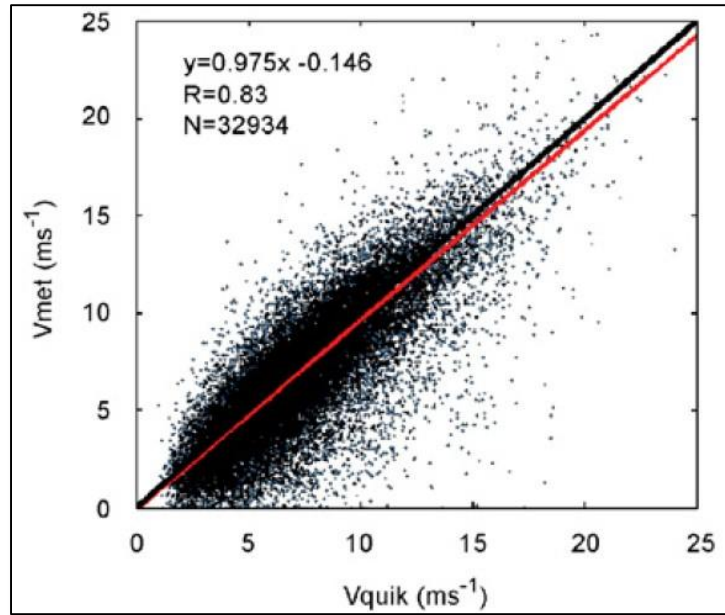


Figure 32-Scatterplot- QuikSCAT vs. 18 Buoy/Station (from Pimenta et al 2008)

3.3.1.4. QuikSCAT BYU Study (Plagge et al 2009)

In a separate study published in 2009 (Plagge et al 2009), researchers at Brigham Young University (BYU) developed an ultra high resolution (UHR) wind retrieval tool that resolves QuikSCAT data to 2.5 km. The accuracies of the UHR product and the 12.5km and 25km QuikSCAT were each estimated by correlation with buoy anemometry data collected in 2006 from 19 metocean buoys anchored throughout the Gulf of Maine. Co-location of QuikSCAT and buoy data pairs is defined by a 10 km radius around each buoy and a +/- 30 minute time window. For the study year, 2006, the average observed bias (wrt buoy data) of the UHR data was -0.29 , which broke down as -0.48m/s nearshore ($< 100\text{ km}$) and -0.09 m/s offshore. The authors noted that all wind speeds

were included, so most of the error likely occurs during very low or very high wind periods. The study found that the UHR bias and standard deviation (SD) were very close to those for the 12.5 km QuikSCAT products, as shown in Table 9. They conclude that the QuikSCAT UHR tool is very useful for improved identification and study of the marine atmospheric boundary layer and other processes that occur at length scales of 5 to 20 km. This research also helped validate the QuikSCAT 12.5 km resolution product.

Wind Speed Bias and Deviation		Nearshore	Offshore	All
Ultra Hi –Res (UHR)	Bias	-0.48	-0.09	-0.29
	Std Deviation	2.65	1.98	2.33
12.5 km product	Bias	-0.62	0.07	-0.29
	Std Deviation	2.29	2.07	2.18
25 km product	Bias	-0.54	0.33	-0.11
	Std Deviation	1.99	2.05	2.02

Table 9- Bias and SD for three resolutions –adapted from Plagge et al 2009

3.3.1.5. QuikSCAT and Ku2011 (Ricciarduli et al 2011)

In a 2011, Remote Sensing Systems™ (RSS) introduced a new QuikSCAT GMF that takes advantage of recent advances in PMI wind products such as SSM/I or WindSat v7. These data sets can help improve accuracy in two ways. PMI radiometers are much better at detecting rain and sea ice, and can be used to flag and scrub QuikSCAT data, which is biased by rain. The GMF also uses PMI data to calibrate QuikSCAT retrievals

at higher wind speeds. A technical report by RSS using this methodology found that after scrubbing for rain, Ku2011 produced mean wind speeds with a bias of 0.01 m/s and a standard deviation of 0.9 m/s when compared to 5 years of wind records from 200 global buoys (Ricciardulli et al 2011). Figure 33 show the normalized PDF for all buoy data compared to Ku2011 wind speeds. The similarity of the curves indicate nearly identical Weibull parameters, which are highly correlated with energy density.

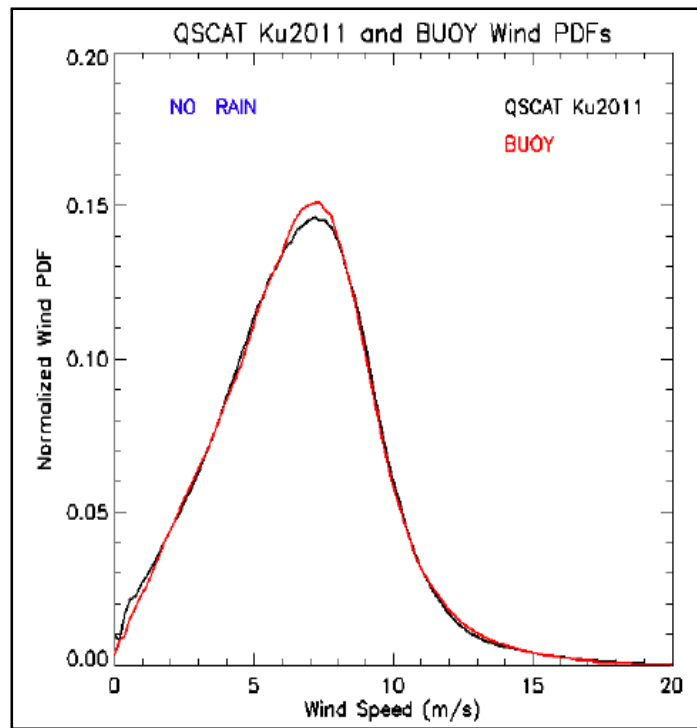


Figure 33- Ku2011GMF QuikSCAT vs. Buoy Data - Wind Speed PDF (from Ricciardulli et al 2011).

3.3.1.6. QuikSCAT DTU study (Karagali 2012)

As part of a DTU PhD dissertation (Karagali 2012), a series of analyses were performed on QuikSCAT data which compared QuikSCAT wind products with three offshore met masts in the North Sea - Greater Gabbard, Horns Rev, and FINO-1. After scrubbing for rain and winds below 3 m/s, 1629 co-located pairs were identified, and bias and standard deviation fell noticeably. Table 10 summarizes the error statistics of the QuikSCAT relative to the tower data, after scrubbing. Bias varied from about -0.1 to -0.2 , R averaged 0.94 and the standard deviation ranged from around 1 to 1.4. The study noted that Greater Gabbard had the fewest samples by roughly an order of magnitude, so the higher standard deviation and bias are to be expected. It also noted that Greater Gabbard estimates were handicapped by inability to estimate the shear profile as accurately as the other towers.

The study also compared energy density³¹ at a single spot, calculated with in situ data from FINO-1 vs. QuikSCAT data. The estimates using FINO-1 data ranged from 564 to 577 W/m^2 , depending on the shear profile selected to extrapolate the FINO-1 data down to 10m ASL, while the QuikSCAT estimate was 592 W/m^2 , a difference of between 2.6% and 5%. The authors also noted that QuikSCAT availability was around 99%

³¹ The energy densities were estimated using a Weibull fit and time series and steady state energy equation

before scrubbing for rain and ice, and a few cells retained over 95% of the scans even after the scrub.

Table 10- Error and Correlation Statistics, QuikSCAT vs. Met Towers, adapted from Karagali 2012, Table II

	Horns Rev	FINO-1	Greater Gabbard	All
Bias(m/s)	-0.09	-0.07	-0.19	-0.09
SD (m/s)	1.32	0.96	1.43	1.21
R	.93	.96	.92	0.94
N	951	594	84	1629

To estimate the frequency of rain contamination and its effect on estimates of power production, the study also looked at all 7417 scans of the North Sea available between August 1999 and October 2009, a period of about 10.2 years. Each scan was broken into ~17 km x 28 km grid cells for flagging rain and mapping wind vectors. The results are shown in the color-coded Figure 34. After scrubbing the data for rain and sea ice, a few cells retained nearly 7000 scans, while most cells retained around 6000 valid scans, but this number decreased close to shore. In the North Sea, within ~25 km of the shoreline the average sample density per cell dips below 3000 in some areas. In the Baltic Sea, the authors found very high scrub rates due to sea ice, so these data are not relevant to the study area (Cape May) inventory estimates. This indicates QuikSCAT yearly coverage (valid products, post scrub) ranging from about 300 nearshore to about 700 offshore, or between 36% and 83% of the theoretical maximum of 843 scans/yr on the 56th parallel, derived in Appendix A.

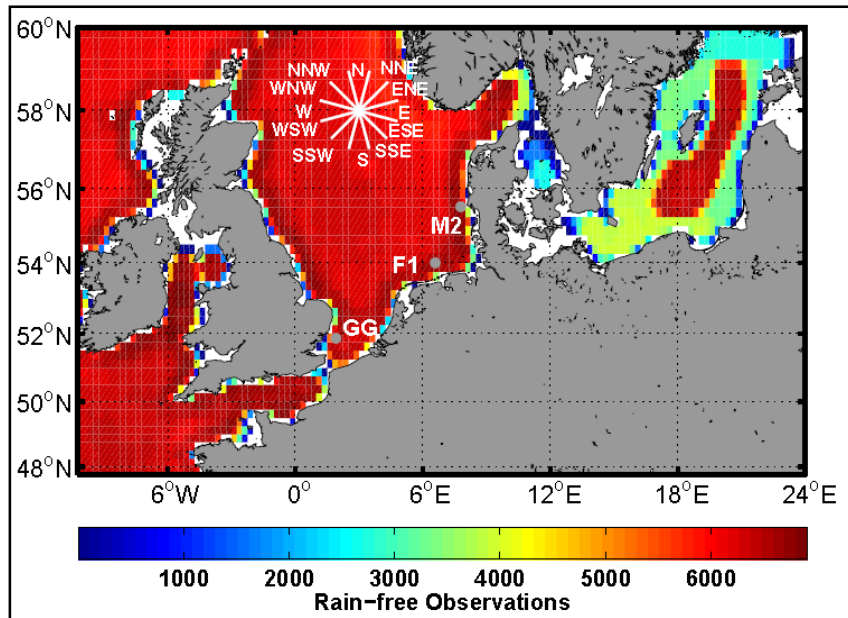


Figure 34- Density of Scrubbed QuikSCAT Scans, North and Baltic Seas, from Karagali 2012 p. 131 Fig 1a

Karagali also assessed the impact of the low sampling frequency and regular timing of scatterometry on the wind index by comparing wind indices generated from different data sets. Over 50,000 ten minute averaged data points from the met tower at FINO-1 were compared to 956 co-located QuikSCAT retrievals and time coincident output from a Weather Research and Forecasting (WRF) model³². Some filtering of the scatterometer data was done to remove rain and ice corrupted samples and winds below 3 m/s. FINO-1

³² WRF is a public domain simulation model

data had to be extrapolated to 10 m ASL, so the equivalent neutral wind (ENW) was calculated at 10 m to match the ENW profile of the QuikSCAT retrieval. FINO1 ENW is the Equivalent Neutral Wind and FINO1 SDIS is the 10 m ASL extrapolated met tower based on Stability Dependent In Situ shear.

A wind index was generated for both shear profiles for FINO-1 and also generated for the 956 co-located QuikSCAT retrievals and two different WRF model runs – one using all the available hourly WRF fields (up to 87,480) and one using only the WRF fields coincident with QuikSCAT scan times (up to 6,913). Figure 35 shows the five different wind indices. Wind speeds are indexed to the average. There does not appear to be a significant difference between the two FINO-1 indices calculated with different profiles (ENW vs. SDIS). There is significant deviations between the WRF and FINO-1 indices, but QuikSCAT matches FINO-1 very closely, with small deviations in Nov, Dec, Jan, and Feb. This error is likely due to contamination or scrubbing of data due to winter ice, both floating on the surface and on met tower anemometers. The study shows the scatterometers ability to index wind more accurately than the WRF models used. The authors also conclude; “*Such results indicate that there is a small impact in the average statistics [wind indices and power density] when 2 daily values are used, instead of 24 hourly values*”. This observation is useful when assessing the impact of low frequency sampling and diurnal bias on energy density estimates.

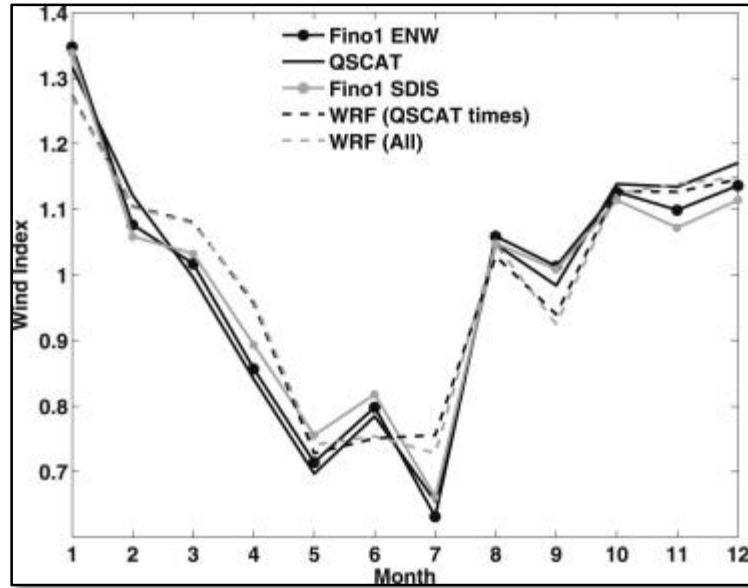


Figure 35- Wind Index for Various Sources of Wind Data, from Karagali et al 2012

3.3.1.7. QuikSCAT Inventory

QuikSCAT coverage estimates from the 7 studies reviewed ranged from 212 scans/yr to 700 scans/yr, reflecting a wide range of latitudes and varying degrees of data scrubbing. However, only two of the QuikSCAT studies (Hasager et al 2006 and Karagali 2012) included “atlas inventories”- estimates of available scan density over a wide, gridded region, unencumbered by co-location criteria or correlation studies. These estimates are more appropriate than correlation studies for assessing coverage for resource assessment. After scrubbing for rain and sea ice, Karagali (2012) found between 500 and 700 scans/yr at almost every cell more than ~ 25 km offshore (beyond the land mask) in the North Sea. This compares reasonably well to a theoretical maximum of 843 in the North Sea region.

To account for the longer parallel at Cape May, this figure should be divided by the ratio of 1.4 (see Appendix A A). An estimate based on the mid-range of the North Sea annual rate (600- from Karagali 2012) translated to Cape May latitude would thus be $(600/1.4 =)$ about 430 scans per year. Sea ice had some impact on the North Sea inventory, but is not an issue in the study area, so this estimate is considered conservative.

The other two QuikSCAT studies cited for coverage estimates (Pickett et al, -234 scans/yr, Pimenta et al - 212 scans/yr) are correlation studies. The correlation study scrub rates are higher than the atlas inventory rates primarily due to scrubbing of the reference in situ data set in the correlation studies. In addition, Pickett et al scrubbed data sets for wind speeds below 6 m/s, a relatively high threshold, and Pimenta et al noted that many of the buoys in the study experienced significant downtime. As expected, those estimates reflect scrub rates significantly higher than what would typically occur without co-location criteria. In order to estimate how much higher, the scrub rates would need to be determined and broken out for each data set and for each criterion (rain, ice, wind speed, technical, etc.) That analysis would require information that is not published, and would be beyond the scope of this paper. Valid QuikSCAT coverage is therefore assumed to be 430 scans/yr for the 39th parallel, which represents a scrub rate of ~30%, and is based on a conservative interpretation of the atlas inventories translated to the 39th parallel. This translates to around 4300 QuikSCAT scans available for the study area.

3.3.2. ASCAT -Metop A and B

The European Space Agency launched the Advanced Scatterometer (ASCAT) in 2006 on their Meteorological Operational (MetOp A) satellite. This program was extended with the launch of MetOp B in 2012 and will continue through 2020 with the launch of Metop C in 2017. ASCAT is a C-band radar that uses vertically polarized antennae. There are now two active ASCAT units on Metop satellites. Each satellite carries the same sensor package including six antennae that scan two parallel tracks 500 km wide on the sea surface (see Figure 30). The data are spectrally analyzed and used to create global ocean wind products that are available from the European Organisation for the Exploitation of Meteorological Satellites, Ocean and Sea Ice Satellite Application Facility (EUMETSAT OSI-SAF). The products are available at a 12.5 km resolution, and begin 20 km off the coastline (EUMETSAT 2011)³³.

Figure 36 and Figure 37, below, show two images of the Mid-Atlantic Bight (MAB) created from ASCAT data and retrieved from the EUMETSAT data portal (OSI-SAF 2012) on 2 Dec 2012. The images are not cartographically projected, so the aspect ratio is slightly distorted. The products were generated using the High

³³ In the US, NOAA and NASA maintain online catalogues of ASCAT products at (<http://manati.star.nesdis.noaa.gov/products/ASCAT.php>) and at (<http://po-daac.jpl.nasa.gov/dataset/ASCAT-L2-12.5km?ids=Measurement&values=Ocean%20Winds>).

Resolution, Limited Area Model (HIRLAM) a GMF algorithm developed by the Applied Physics Laboratory at Johns Hopkins University. The second image shows a portion of the wind product off the Delmarva peninsula. The purple dots represent the center of the wind vector cells for the high resolution coastal product. The 12.5 km spacing of the dots can be seen in the zoomed figure.

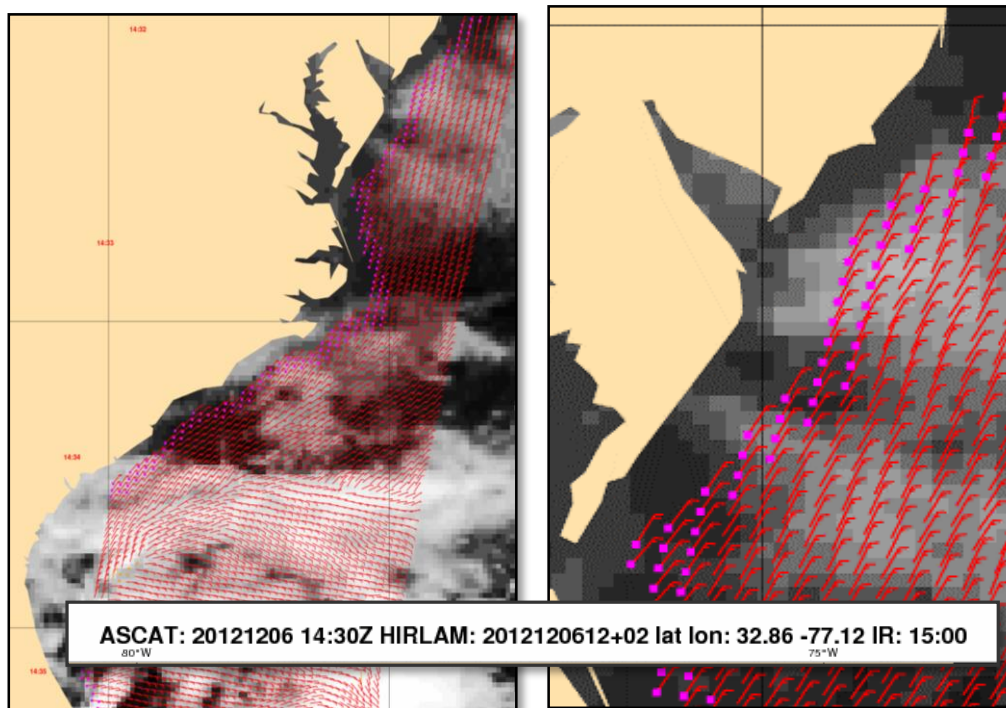


Figure 36- ASCAT Coastal Product, 12.5km resolution, retrieved from NOAA portal at <http://manati.star.nesdis.noaa.gov/products/ASCAT.php>

Figure 37- Zoom in, ASCAT Coastal Product, 12.5km resolution, retrieved from NOAA portal at <http://manati.star.nesdis.noaa.gov/products/ASCAT.php>

3.3.2.1. ASCAT KNMI Hi-Res Product (Verhoefen et al 2011)

A validation study of ASCAT wind mapping, including the 12.5 km coastal product, was conducted by the Royal Netherlands Meteorological Institute using scatterometer data from the Metop-A satellite (Verhoefen et al 2011). Six months of Level 1 ASCAT data were analyzed using different backscatter averaging cut-off radii. Wind products were generated for 20 km, 15 km, and 12.5 km wind vector cells, and mapped to corresponding grid nodes along the coastline of North America. The 12.5 km resolution wind products were then compared to co-located, co-incident (<30 minutes apart) anemometer data from 35 coastal met buoys between 10 and 50 km offshore of the Atlantic and Pacific coastlines of North America. For the 6 month study period a total of 4,596 scrubbed, collocated data sets were identified for these 35 buoys and analyzed. This translates to an average of 263 samples per buoy per year, reflecting a wide range of latitudes. For comparison, this is 78% of the theoretical maximum of 337 at Cape May. The wind speed bias of the 12.5 km ASCAT vectors compared to the met buoy measurements was found to be -0.25 m/s, with vector component standard deviations between 1.45 and 1.57 m/s.

In a triple co-location correlation study, little difference was found in error characteristics between the three grid sizes, with zero bias between them, and standard deviations that differed by less than .05 m/s. The study concluded that all three products

(20 km, 15 km, and 12.5 km) can be considered to have the same error characteristics, and reaffirms the findings of Plagge et al, who used QuikSCAT data.

3.3.2.2. ASCAT Inventory, Accuracy

ASCAT coverage is estimated at 263 samples per year based on the number of valid samples retrieved in (Verhoefen et al 2011). This is ~ 78% of the ASCAT maximum theoretical coverage of 337 samples per year for the study area. No latitude correction is applied because Verhoefen et al (2011) co-locations covered a range of latitudes roughly centered on the study area latitude. For 6.3 years of operation this would produce ~ 1660 ASCAT samples total. The inventory increases at a rate of ~ 525 valid samples per year because there are now two operational ASCAT instruments. ASCAT accuracy is assumed to be at least as accurate as QuikSCAT based on the work of Verhoefen et al and the fact that ASCAT is more advanced than QuikSCAT.

3.3.3. OceanSAT-2

In September, 2009 the Indian Space Research Organisation (ISRO) launched OceanSat-2, which provides scatterometry-based wind speed products at a 25 km resolution (ISRO 2012). It uses an active pencil-beam scanning scatterometer called SCAT , with performance specifications higher than QuikSCAT. Wind retrieval tools developed for ASCAT can be modified and used to improve the resolution down to 12.5 km with no

loss of accuracy from the 25 km product, allowing wind speed estimates in near coastal areas, as demonstrated by Verhoefen et al (2011). The swath width of OceanSCAT is 1400 km, which is 7/9 of the QuickSCAT swath, so OceanSCAT theoretical maximum coverage can be estimated by assuming proportional coverage.

3.3.3.1. OceanSAT-2 Inventor, Accuracy

Because OceanSAT is relatively new, there are few published reports from which to extract the scrub ratio of wind products. The annual coverage is estimated based on the ratio of OceanSCAT to QuikSCAT swath width (1400 km vs. 1800 km). This is a reasonable assumption based on similar scrub rates, since the instruments are otherwise very similar and have the same orbital characteristics. OceanSCAT annual rate is therefore $(430 \times 7/9) = 334$ scans. It has been operating ~3.3 years, for a total of ~1100 valid samples. OceanSCAT accuracy is assumed to at least match that of QuikSCAT based on the fact that OceanSCAT is more advanced and has a narrower swath width.

3.3.4. Scatterometer Inventory Summary

Table 11 summarizes the scatterometer inventory and shows that there are currently over 7,000 valid scatterometer products available for a given location at 39 degrees N latitude. All the scans have been taken since 1991, and the inventory increases by over 700 valid samples per year. These figures do not include scatterometers that were launched before

1991 or that operated for less than two years. Study area inventory can only fall below this estimate if the study area scans must be scrubbed at a rate significantly higher than that observed in the North Sea, and this is extremely unlikely.

Table 11- Scatterometer Inventory

Instrument	Swath Width (km)	N-Estimate	N-Annual Increase
QuikSCAT	1800	4300	0
ASCAT	1000	1660	525
OceanSCAT	1400	1100	200
Total Inventory		7,060	725

3.3.5. Scatterometer Accuracy Summary

Table 12 summarizes the published correlation and error statistics for the seven scatterometer studies reviewed, which used both buoy and met tower data for correlation. Not all statistics were published in all studies. Standard deviation of the error varies between ~ 1 and 2 m/s. Much of the scatter found by Pimenta et al was attributed to the buoy data being time averaged over a day, while the QuikSCAT wind is a snapshot, unlikely to match the daily mean. For those studies that scrubbed lower wind speeds, SD does not exceed 1.3 m/s. The two outlier data points for bias (Hasager et al 2006 and Verhoefen et al 2011) did not scrub for wind speed. In addition, Verhoefen et al used buoy correlation and Hasager et al did not scrub for rain, two more potential sources of

bias. Neglecting these two outliers, bias ranged from -0.15 m/s to $+0.2$ m/s. Energy density estimates generated from QuikSCAT products (Karagali 2012) differed by 1% to 5% from in situ tower estimates, depending primarily on the wind shear profile selected for extrapolation to match the two data sets.

Table 12- Scatterometer Accuracy Statistics

Study	U Range (m/s)	Tower or Buoy	SDE, RMSE	R	Slope	Bias (m/s)
Pickett	6 to 25	B	1.3	0.9		0.2
Pimenta- all buoys	0 to 25	B		0.83	0.98	-0.146
Pimenta -buoy 44009	0 to 25	B	2.0			0.2
Hasager 2006	0 to 25	T	1.3		0.96	-0.3
Hasager nearshore	0 to 25	T	1.3			0.2
Karagali	3 to 25	T	1.2	0.94		-0.09
Ricciarduli Ku2011	0 to 25	B	0.9			0.01
Verhoefen/ASCAT	0 to 25	B	1.5			-0.25
Plagge BYU(*)	0 to 25	B	2.02			-0.1
(*) – The UHR product is considered experimental, thus not included in the summary table						

3.4. Passive Microwave Imaging (Radiometers)

Passive Microwave Instruments measure brightness and temperature of polarized microwave energy from the earth's surface at multiple frequencies. There are several PMI systems and databases including the Advanced Microwave Scanning Radiometer-

Earth (AMSR-E)³⁴, WindSAT³⁵, and the Special Sensor Microwave Imager³⁶ (SSMI). Each has particular strengths and weaknesses as a result of different scan techniques, temperature ranges, and polarization schemes. For example, different frequencies have different sensitivity levels to rain and water vapor, which can be useful for cross-calibrating with other data sets (Atlas et al 2010). PMI (and SAR) can be used to supplement scatterometry by providing better flagging for rain and sea ice (Zhang et al 2006, Bentamy et al 2007, Ricciarduli 2011).

3.4.1. WindSat (Meissner and Wentz 2006)

WindSat is a polarimetric microwave radiometer developed by the Naval Research Laboratory and the Naval Center for Space Technology. It was launched aboard the Coriolis satellite in 2003 and continues to operate despite its 3 year design life. It is the first radiometer to measure wind direction, and is capable of retrieving wind speeds in light rain. It operates in several discrete bands between ~ 6 GHz and 40GHz (WindSAT 2013a, 2013b). Meissner and Wentz (2006) developed a GMF for WindSAT data that uses this multi-spectral data to retrieve wind vectors, sea surface temperature, columnar atmospheric water vapor, columnar liquid cloud water, and rain rate. These parameters can be used by other GMFs to calibrate scatterometer and SAR retrievals. The study

³⁴ Details available at <http://www.ghcc.msfc.nasa.gov/AMSR/>

³⁵ Details available at <http://www.nrl.navy.mil/WindSat/Description.php>

³⁶ Details and downloads available at <http://www.ncdc.noaa.gov/oa/rsad/ssmi/swath/index.html>

tested the GMF using ~ 48,000 co-locations, and average bias compared to buoy data was found to be +0.17 m/s, with a SD = 1.12 (Meissner and Wentz, 2006, Table IV).

WindSAT products are offered by RSS in time-averaged (daily, 3 day, weekly, monthly) 25 km grid form only (WindSAT 2013c).

3.4.2. SSMI (Mears et al 2001)

This analysis focuses primarily on the SSMI database because it is the largest and fastest growing PMI database and has the longest running program of the PMI class of instruments. The program uses overlapping serial missions carrying successively improved versions of the Special Sensor Microwave Imager (SSMI)³⁷. The SSMI was developed as part of the Defense Meteorological Satellite Program (DMSP) (Hollinger et al 1987, Wentz 1997). There have historically been two to four systems orbiting simultaneously for most of the program - a significant advantage compared to other SMRR instruments (Hasager et al 2006, NESDIS 2007). The SSM/I measures at four frequencies from 19.35 GHz to 85.5 GHz, with both vertical and horizontal polarizations. The system sweeps a 1400 km wide swath. 25 km wind vector products are available from RSS (RSS 2013). The nominal performance specification of SSMI systems is accuracy of +/- 2.0 m/s, and a root mean square error of <1.3 m/s for winds between 3 and 25 m/s. There have been six successful SSMI satellites launched since 1991, two of

³⁷ Details available at http://www.ssmi.com/ssmi/ssmi_description.html

which are still operating as of Dec. 2012. The satellites are enumerated F11, F13, F14, F15, F16 and F17 (SSMI 2013).

In a comprehensive 2001 study (Mears et al 2001), wind speed estimates for the period June 1987 through June 1998 were retrieved from SSM/I data from four satellites and compared to data from all operational Tropical Atmosphere Ocean (TAO) and NDBC buoys, for a total of 150 met stations. The TAO array uses Atlas buoys, which measure winds for 6 minutes every hour at a height of 3.8 m with a stated accuracy of 0.3 m/s or 3%, whichever is greater. The nominal accuracy of wind speed from the NDBC buoys is ± 1 m/s. The latitude of the buoys in the study ranged widely. The study analyzed over 88,000 co-located (defined as separated by < 2 hrs and < 25 km) data points and the study noted, *“Typically, a year in which both the buoy and satellite were completely operational resulted in 200-300 collocated observations for the pair.”*

Table 13 shows the error characteristics broken out by satellite. The study concluded that the significant improvement in performance with F11 and F13, reducing bias to ~ 0.1 m/s, was probably due to upgrades and improved system calibration in those instruments.

Table 13- Error Characteristics by Satellite Number, adapted from Mears et al 2001

Satellite No.	Mean ($W_{SSM/I} - W_{Buoy}$)	SD ($W_{SSM/I} - W_{Buoy}$)	No. Observ'ns
F08	-0.20 ± 0.07	1.39	31233
F10	-0.41 ± 0.05	1.25	88857
F11	0.11 ± 0.05	1.26	86780
F13	0.09 ± 0.05	1.25	46959

Figure 38 shows the deviation of the mean wind speed for all buoys compared to the SSMI wind estimates, arranged in order of mean error, negative to positive. The error bars show one standard deviation, and the dashed red lines, added for clarity, show a range of +/- 0.5 m/s. Around 85% of the buoys fall within 0.5 m/s of the SSMI estimates. Figure 39 shows wind speed difference between NDBC 44004 in the Northwest Atlantic and Satellite F11 for wind speeds up to 15 m/s. At NDBC 44004, the F11 error is minimal (< 1 m/s) between around 4 m/s and 13 m/s.

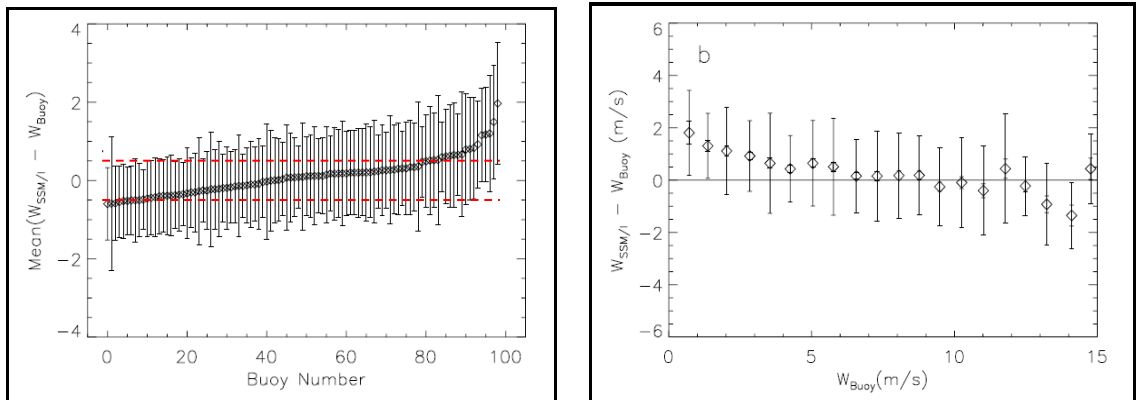


Figure 38- All Buoys, Mean SSMI Deviation, modified from Mears et al 2001

Figure 39- NDBC 44004 vs. SSM/I F11 Deviation, from Mears et al 2001

In October, 2003 and in December 2006, two new satellites (F-16 and F-17) were launched carrying the improved Special Sensor Microwave Imager/Sounder (SSMIS) onboard. SSMIS provides slightly higher resolution and more channels for sea surface temperature and water vapor profile sensing. This additional information can be used to calibrate the GMF to improve retrieval of all wind products, archived and future. SSMI wind products are offered by Remote Sensing Systems, Inc. (RSS 2013).

3.4.3. PMI/SSMI Accuracy, Inventory, Resolution

The inventory and analysis done for this paper begins in 1991 with satellite F11, so previous data sets from the outmoded F8 and F10 are not considered. Based on the work of Mears et al (2001), the bias of F11 and later systems is about half that of the other SMRR types evaluated, with data sets showing a bias around +0.1 m/s and a standard deviation of ~ 1.25 m/s. Meissner and Wentz found a bias of +0.17 m/s and SD of 1.12 for WindSat retrievals, closer to the accuracy of SAR and scatterometer systems.

Based on scan width, the theoretical maximum coverage of SSMI for the study area (from Appendix A A) is 129%, or 472 scenes per satellite year. Mears et al found a typical rate of 200-300 scans per satellite year over a wide range of latitudes, from the tropics to the Bering Sea. Therefore, a conservative assumption for SSMI coverage, based on this and on scrub ratios observed in other data sets (ranging from 11% to 36%),

would be an overall scrub rate of 50%, leaving about $(472/2 =)$ 236 per year. This is adopted as the estimate for SSMI coverage. Since 1991, SSMI satellites have logged a total of ~56.4 years of operating time. The number of valid SSMI samples should therefore be around $(236 \text{ samples/yr} \times 56.4 \text{ years} =)$ ~ 13,300 samples increasing at a rate of ~ 472 annually, since there are currently two satellites orbiting.

SSMI product resolution is currently 25 km gridded vectors, although similar methodologies to those used by Verhoefen et al (2011) could be applied to re-sample the data and resolve the wind vectors to 12.5 km.

3.5. Summary - SMRR Inventory

Table 14 summarizes the SMRR inventory for the study area. The number of valid samples is estimated at over 24,000, comprising over 20,000 gridded vector products from scatterometers and radiometers plus ~ 4,000 SAR images. This number increases annually by about 1200 gridded vector products and 230 SAR images. It bears repeating that this inventory does not include several other satellite data sets used for ocean wind speed estimates, so it represents only a subset of all possible sources.

Table 14 - SMRR Inventory Summary

	Satellite/Instrument	Active Life (yrs)	Theoretical Max. Scans/yr	Valid scans/yr	Scrub rate (pct)	Scans Avail.
<u>SAR</u>	ERS-1/SAR	8.3	34	30	11%	249
	ERS-2/SAR	16.4	34	30	11%	492
	RADARSAT-1/ScanSAR	17.1	168	115	32%	1966
	RADARSAT-2/ScanSAR-2	5.1	168	115	32%	586
	EnviSAT/ASAR	9.8	135	86	36%	843
		SAR subtotal				4137
<u>Scatterometers</u>	Metop-A/ASCAT(7)	6.3	336	250	26%	1575
	Metop-B/ASCAT(7)	0.1	336	250	26%	25
	SeaWinds/QuikSCAT	10.4	605	430	29%	4472
	OceanSAT/SCAT	3.3	471	334	29%	1102
		Scatterometer subtotal				7174
<u>PMI - SSMI</u>	F11 SSM/I	8.5	471	235	50%	2001
	F13 SSM/I	14.5	471	235	50%	3413
	F14 SSM/I	11.3	471	235	50%	2660
	F15 SSM/I	6.7	471	235	50%	1577
	F16 SSMIS	9.3	471	235	50%	2189
	F17 SSMIS	6.1	471	235	50%	1436
		SSMI Subtotal				13277

3.6. Summary - SMRR Snapshot Accuracy

The accuracy of SMRR based resource assessment must be examined at two levels; the snapshot wind retrieval (this section) and the time-averaged energy density estimate (following section). Table 15 summarizes the correlation and error statistics for the 21 separate analyses discussed above. As the spreadsheet shows, some bias (usually

negative vs. in situ) persists in all of the studies. The relatively wide range of SD and bias reflects the wide range of technologies, site conditions, sample sizes, and scrub criteria for the data sets. The independent effects of rain scrubbing on bias and scatter were not clear, due to the non-linear effect of rain on wind retrievals, the dependence on wind speed, and the lack of sufficient data on scrub rates.

Table 15- SMRR Error Statistics Summary

Study	N	U Range (m/s)	Rain scrub	Tower/ Buoy	SDE, RMSE	R	U		Energy Error (%)
							Regr. Slope	Bias (m/s)	
SCATTEROMETERS									
Pickett	3,314	6 to 25	y	B	1.3	0.9		0.2	
Pimenta- all buoys	32,394	0 to 25	n	B		0.83	0.98	-0.146	
Pimenta -buoy 44009	8,292	0 to 25	n	B	2			0.2	4.4%
Hasager - all data	315	0 to 25	?	T	1.3		0.96	-0.3	
Hasager- Horns Rev		0 to 25	?	T	1.3			0.2	
Karagali -Horns Rev	951	3 to 25	y	T	1.3	0.93		-0.09	
Karagali - Fino1	594	3 to 25	y	T	0.96	0.96		-0.07	~2.6% - 5%
Karagali- Greater Gabbard	84	3 to 25	y	T	1.43	0.92		-0.19	
Karagali -all	1,629	3 to 25	y	T	1.21	0.94		-0.09	~1% - 4%
Ricciarduli Ku2011	>10,000	0 to 25	y	B	0.9			0.01	
Verhoefen/ASCAT	4,596	0 to 25	y	B	1.5			-0.25	
Plagge BYU		0 to 25	n	B	2.02			-0.1	
SAR									
Hasager et al 2011 FINO2	180	0 to 25	?	T	2.04	0.87	1.03	-0.21	
Hasager et al 2011 ALL	875	0 to 25	?	T	1.88	0.89	0.96	-0.25	
Christiansen et al 2006	91	2 to 15	?	T	1.1		1.00	-0.26	0.00%
Badger et al - Hovsore	444	0 to 25	?	T				0.07	3.60%
Badger et al - Horns Rev	464	0 to 25	?	T				-0.06	0.90%
Badger et al - FINO-1	359	0 to 25	?	T				-0.01	4.10%
PMI									
Meissner et W. (WindSAT)	48,000	0 to 25	n	B	1.12			0.17	
Mears et al (SSMI - F11)	86,780	0 to 25	n	B	1.26			0.11	
Mears et al (SSMI -F13)	46,959	0 to 25	n	B	1.25			0.09	
(*) – The 2.5 km UHR product in Plagge et al is considered experimental, thus not included									
(**) Pimenta et al estimated AEP change for a GE 3.6 MW turbine									

Although it is difficult to isolate single parameter effects across studies, four important observations can be made;

1. With the exception of one outlier (Christiansen et al 2006) that used an extremely small number of samples (91), every study that restricted wind speed found a bias below ~ 0.2 m/s, with the mean magnitude of bias being 0.13 m/s.
2. Wind speed bias is found to be lowest (< 0.2 m/s, absolute) for wind speeds of ~ 3 to 15 m/s, for all three technologies. This agrees with theory, and reflects the range where capillary waves are most closely correlated with microwave reflectivity/emissivity.
3. Some of the remaining bias can be corrected by improving the GMF, but only if the source of the bias can be accurately modeled. This is not always possible, so data are often rejected as contaminated (e.g., by rain, sea ice, very low, or high winds).
4. The average SD of all studies that restricted wind speeds and scrubbed for rain was around 1.2 m/s, and did not exceed 1.4 m/s. Conversely, every study that found a SD > 1.5 m/s scrubbed neither wind nor rain.

The studies also demonstrate how SMRR wind retrieval accuracy has been improving and should continue to improve due to the following four trends and new techniques;

1. With each new SMRR system launched, instruments upgrade through the use of better system calibration, improved antennae, navigation, and tracking systems, and/or new features such as multi-polarity and multi-frequency functionality.
2. Co-processing data sets from the same systems but with different frequencies and polarizations reduces error by adding information about the atmosphere and sea surface.

3. Co-processing of datasets from different systems can reduce error by providing more accurate wind direction inputs for SAR retrievals, and more accurate and higher resolution flagging and coastal masking. SAR images provide wind speeds within a few km of the coastline, helping to fill information gaps along the shore in scenes from Scatterometers and PMI sensors. It can also help identify diurnal patterns and reduce associated error.
4. New GMFs can flag outliers and mitigate biases in wind retrievals, and these GMFs can be applied to incoming data from operational instruments, or retroactively to archival data sets.

In light of the above, for SMRR snapshot wind retrievals between ~ 3 and 15 m/s, the mean bias can be assumed below 0.2 m/s. Accuracy can be expected to improve as the technology advances and GMFs are upgraded and calibrated. With proper scrubbing and retrieval, some data sets such as SSMI are capable of producing time averaged bias less than 0.1 m/s, however, this is the low end of the range observed, and would not constitute a conservative assumption.

3.7. Summary – SMRR for Energy Density, AEP

Snapshot retrieval products must be collected and translated into histograms, PDFs or time series in order to calculate energy density at any location. A turbine power curve must then be applied to the data to estimate AEP (see Figure 58- Turbine Operating Regions). A turbine produces power only between ~ 3 m/s and ~ 25 m/s. For the lower part of that range (~3-13 m/s) power output is a function of the wind speed and for the upper half (~ 13 m/s to ~25 m/s), power output is at capacity. The lower half is known as Region 2, and is represented by the sloping section of a turbine power curve. Outside

of Region 2, the power is either zero (shut down) or at rated capacity. Therefore, for estimating AEP, wind speed accuracy is only critical in Region 2. This range (~3-15 m/s) matches the range of lowest bias for SMRR retrievals, so the estimate of bias (below 0.2 m/s) for snapshots within this range is justified.

Table 16 summarizes the key findings of those studies that assessed energy correlation. Every study calculated average energy density except Pimenta, which calculated AEP of a GE 3.6 MW turbine. The table shows no clear correlation between the amount of wind speed bias and the error in energy density estimates. This is because the energy density is only loosely correlated to the mean wind speed. Mean wind speed gives no information about the distribution of wind speeds or the Weibull k parameter, which is required for accurate energy density estimates (Pryor et al 2004).

The high (low) end of the error ranges found by Karagali (2012) reflects the least (most) accurate shear profile used. The only outlying data points for wind speed bias are Pimenta and Christiansen et al 2006. The high bias of Pimenta is likely due to use of a buoy for the reference dataset and the inclusion of all wind speeds. The high negative bias found by Christiansen et al does not jibe with the near-zero energy error found, except in light of the fact that the energy density is a function of the entire distribution, not just the mean wind speed, and the sample size of Christiansen et al (2006) was very small, making the distribution and error statistics highly suspect. Excluding Christiansen et al (2006), the wind speed bias ranges from about -0.1 to +0.2 and the energy error

ranges from about 1% to 5%. Choice of the correct shear profile can cut error in half, based on the range of error observed in Karagali (2012) using three different shear assumptions at FINO-1. With the exception of Christiansen et al (2006), Table 16 does not suggest any clear correlation between the number of samples and bias, but that is not surprising given the wide range of study conditions and methodologies. A better method of evaluating correlation between sample size and uncertainty is given in the following section.

Table 16-SMRR Energy Density Error Statistics

Correlation Study	N	U Range (m/s)	Rain-scrub?	Tower/Buoy	U Bias (m/s)	Energy Error (%)
Pimenta -buoy 44009	8,292	0 to 25	n	B	0.2	4.4% (GE3.6)*
Karagali - Fino1	594	3 to 25	y	T	-0.07	~2.6% - 5%
Karagali -all	1,629	3 to 25	y	T	-0.09	~1% - 4%
Christiansen et al 2006	91	2 to 15	y	T	-0.26	0.0%
Badger et al - Hovsore	444	0 to 25	n	T	0.07	3.6%
Badger et al - Horns Rev	464	0 to 25	n	T	-0.06	0.9%
Badger et al - FINO-1	359	0 to 25	n	T	-0.01	4.1%

(*) – Pimenta used GE 3.6 MW turbine to estimate AEP instead of energy density.

3.7.1. Sample Size and Uncertainty

To determine empirically how many samples are required for a robust estimate (+/- 10% with a confidence level of 90%) of the mean wind speed and the Weibull parameters, a

statistical analysis was performed by researchers from Indiana University and Riso National Laboratory in Denmark, using data from four met buoys representing four different wind climates (Pryor et al., 2004).

Table 17- Sample Size for Accurate Estimates of Wind Statistics, from Pryor et al 2004

Descriptor	N required for P90 +/-10%
Mean	91
Std dev	150
Skewness	7599
Kurtosis	>10 000
Weibull k	1744
Weibull A	91
Energy density	1744

The analysis included 24 years of hourly averages from NDBC buoys, including buoy 44004, 370 km east of Cape May, NJ.. This buoy is the closest of the four buoys to the study area, and its long service record provided around 20,000 samples. For the entire dataset analysis, the study estimated that between ~ 70 and 150 randomly selected samples are sufficient for mean wind speed and Weibull A, whereas between ~ 500 and ~ 2000 samples are needed for Weibull k and the mean energy density. Table 17 shows the six descriptors of wind speed distribution analyzed for NDBC 44004 only. The analysis first derived the descriptors for the complete data set, then derived them for a range of sample sizes up to N= 1,000, and plotted the results (solid line). The descriptors

were also generated using a Weibull distribution function fitted to the NDBC data (dashed lines). The plots clearly show the confidence bands narrowing, indicating that accuracy should continue to improve between $N=1,000$ and $N=10,000$.

An imprecise but revealing graphical analysis was conducted by extrapolation. Figure 40 shows the number of samples needed for estimating three key parameters within $\pm 10\%$ with 90% confidence. The solid lines represent data from only buoy 44004, and the dashed lines represent all the buoys in the dataset. For illustration purposes, Figure 40 was adapted from Pryor et al (2004) by adding the red lines, and it indicates that increasing from $N=1,000$ to around $N=7,000$ samples (for example, the number of scatterometer products from the study area inventory) should reduce the P90 band of uncertainty around mean wind speed from about 0.5 m/s to about 0.1 m/s. Other statistical parameters could be expected to show similar improvements depending on the convergence rate of the two curves.

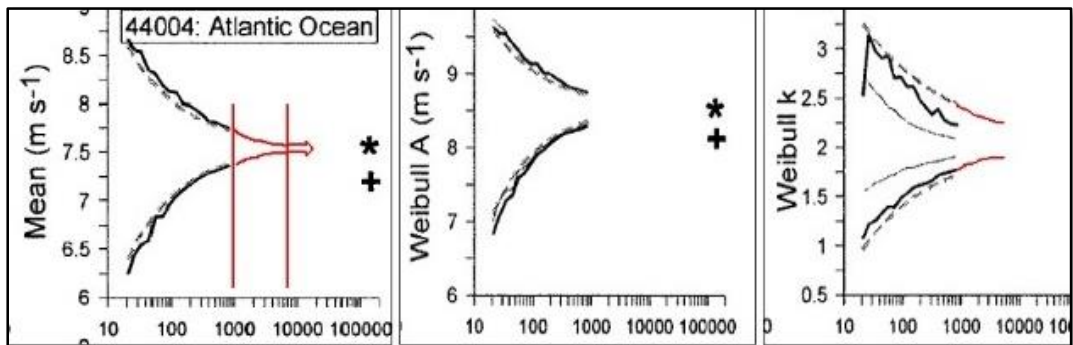


Figure 40-No. of samples needed for $\pm 10\%$ estimate, adapted from Pryor et al 2004.

From the SMRR inventory estimate in Table 14 there are now around 24,000 valid SMRR scans of the study area. This is 14 times more samples than Pryor et al estimated would be needed to achieve the target energy density accuracy of +/- 10% with 90% confidence. It is about 25 times more samples than Karagali (2012) used, and about 48 times more samples than Badger et al used, and those studies found energy density error ranging from ~ 1% to 4%. Based on the cross-check methodology used for the study area inventory, the estimate for N (24,000) could have uncertainty as high as 25%. Even if the true inventory of valid samples were only half of the estimate, N would still be very large statistically and would still represent a time series of over 20 years. In light of this analysis, AEP uncertainty should be closer to the low end of the range found by Karagali (1% to 4%).

3.7.2. Time Series Length and Uncertainty

The Danish Wind Energy Consultant EMD is one of the leading power performance consulting firms in the EU and has been doing wind indexing for hundreds of clients around the world for 15 years. Their expertise lies in estimating power production over the life of a wind farm based on a short time series of wind data. In collaboration with Riso-DTU and several turbine manufacturers, EMD performed detailed case studies for 20 of their projects and estimated the potential error in production estimates from using a short

term data set and a wind-indexed short term data set versus a reference 14 year time series (Nielsen et al 2002).

Table 18 summarizes the overall results. The authors noted that even with nearly four years of data, some production estimates were off by over 10%. This study highlights the value of long time series for wind indexing, and indicates that a time series on the order of 15 years or longer may be required for accurate indexing of short time estimates.

Worst case long-term production estimates	1 year of data	2 years of data	3 years of data
Production error-no indexing	+/- 30 %	+/- 20 %	+/- 10 %
Production error- w/ indexing	+/- 15 %	+/- 10 %	+/- 5 %

Table 18-The Effects of Time Series Length on Production Estimates, adapted from Nielsen et al 2002

3.7.3. Case Study - Project NorseWind

A major effort was recently completed which built on some of the research cited above to generate energy density estimates for the North, Irish, and Baltic Seas. Project NorseWind was a groundbreaking, four year, EU consortium project which culminated in the publication in Sep. 2012 (NorseWind 2012) of a high resolution (2 km x 2 km) wind atlas. This project combined six sources of data;

- SAR data from Envisat, ERS, ALOS, TSX, Radarsat
- SCAT data from QuikSCAT, ASCAT, ERS

- numerical modeling using four complete years of WRF simulation,
- wind (profile) data from 20 Lidar units,
- wind (profile) data from ten met masts
- meteorological data from numerous offshore oil and gas platforms

Researchers demonstrated a method by which SAR and scatterometer data can be combined to produce high spatial resolution and high coverage maps and how sea surface temperature can be sensed and used to calibrate wind profile estimates (Karagali 2012). Other NorseWind papers demonstrate how weighting scans by wind class can improve accuracy (Badger et al 2009), and how the wind profile up to hub height can be modeled using all available data in a multi-variant correlation analysis (Pena et al 2012). These and other papers listed at <http://www.norsewind.eu/norse/index.php/publications> detail the methodologies underlying the production of the NorseWind Atlas.

Figure 41 shows the geographic extent of the project using the “Full Capacity – V80” product layer, which shows the number of annual hours wind speed exceeds its rated value for a Vestas V80. The “full capacity” factor is closely correlated to AEP and is often used as an indicator of production potential.

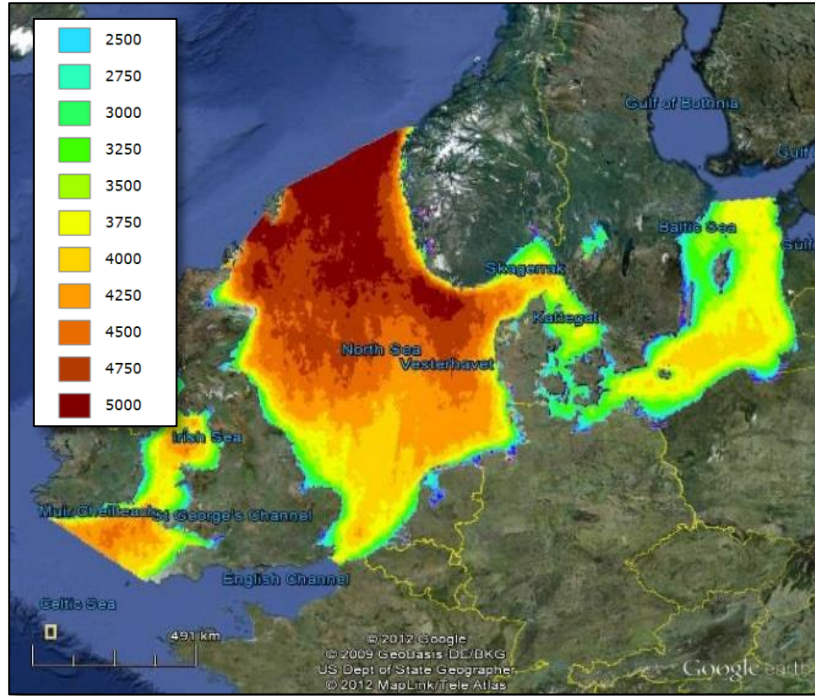


Figure 41- NorseWind Map Product Sample - # Hrs. at Full Capacity for a Vestas V80, retrieved from NorseWind server at <http://geoportal.lneg.pt/ArcGIS/rest/services/Norsewind/MapServer>

The satellite data used by the NorseWind team comprised over 120,000 scenes of the region over a 14 year period. The large inventory is due in part to the size of the study area. First, two maps were produced - one based only on SAR data, and one based only on scatterometer data. These were compared to each other, to the WRF results, and to the in situ measurements. Different shear profiles were developed for different locations, and reproducible methodologies were developed and demonstrated for synthesizing the data into a wind resource atlas with unprecedented resolution and accuracy. The Atlas includes GIS layers for the following parameters;

- Annual long term corrected mean wind speed
- Monthly long term corrected mean wind speed
- Standard deviation of annual values
- Weibull parameters (k & A)
- Wind direction distribution
- Average Wind shear – α exponent
- Temperature
- Static stability
- Uncertainty of all physical parameters

The server can provide all listed parameter layers at 100 m ASL in GIS format. Figure 42 was retrieved from the NorseWind Map Server on 28 Nov. 2012, and show the mean wind speed at 10m. The area around Horns Rev, off the west coast of Denmark, is shown at two scales. The blow-up clearly shows the 2 km. resolution of the averaging cells, and the mean wind speed in increments of 0.2 m/s.

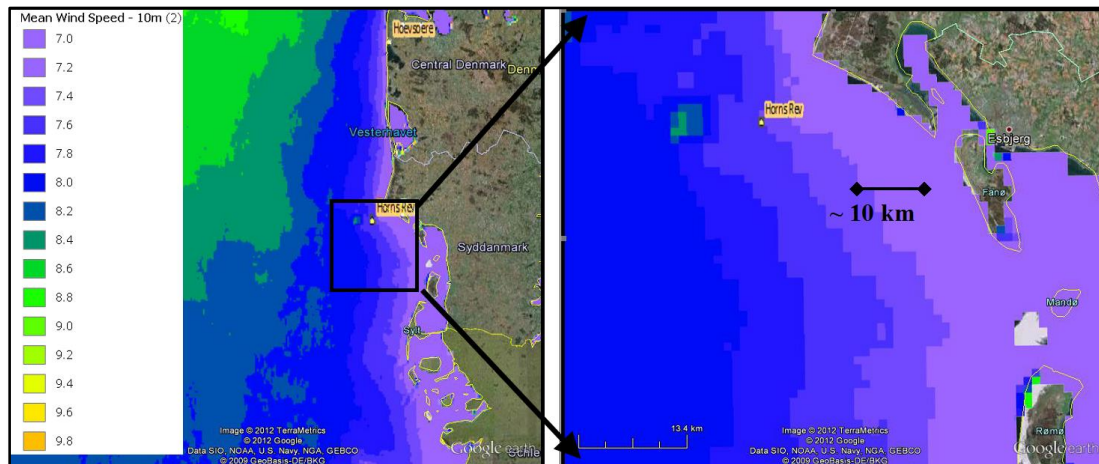


Figure 42- Mean Wind Speed Around Horns Rev- retrieved on 28 Nov. 2012 from <http://geoport.alneg.pt/arcgis/rest/services/Norsewind/MapServer>

Figure 43 and Figure 44 show the NorseWind product around Horns Rev for 100m corrected wind speed and for the uncertainty of the wind speed. Shear profiles were found to be a function of atmospheric stability and boundary layer height, and the study assigned site specific shear exponents for wind shear for certain locations. Uncertainty of the wind speed more than 10km offshore in this region ranges from 0.05 to 0.15 m/s, and is typical of the atlas for the entire NorseWind study area. Each color increment represents 0.05 m/s uncertainty. The highest uncertainty is found around Horns Rev, at the darkest blue dot in Figure 44, with a value of 0.2 m/s. This is because the wake and the radar signature of the wind farm increased the scrub rate in the area, increasing uncertainty in local averaging cells.

3.7.4. 4C-Offshore

At least one commercial firm has also developed a proprietary global offshore 25 km wind atlas product based on satellite data (4Coffshore's "Global Offshore Wind Speed Database"), but there are no published validation studies or methodologies describing the derivation of the wind speeds. The price for access to the monthly averaged wind speed atlas is £ 995 (4Coffshore 2013).

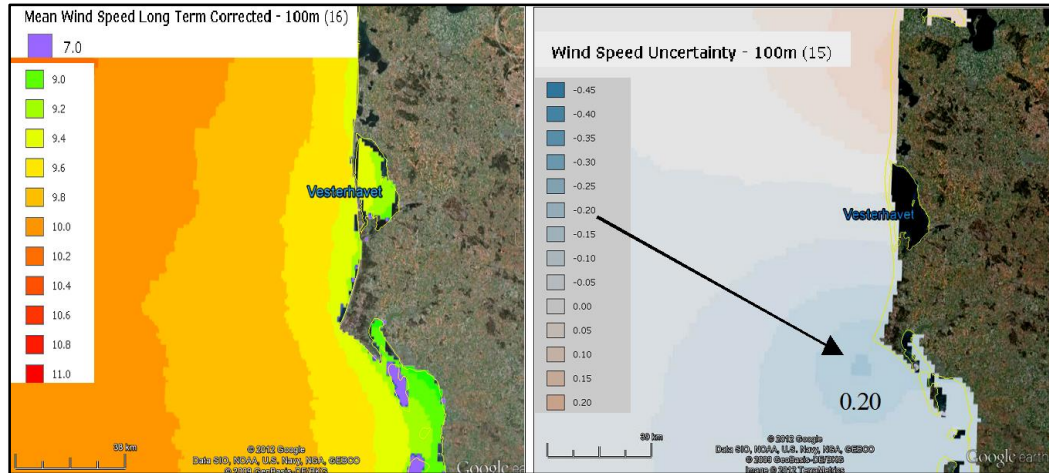


Figure 43- Mean Wind Speed at 100m around Horns Rev, retrieved 28 Nov. 2012, from <http://geoportal.lneg.pt/ArcGIS/rest/services/Norsewind/MapServer/generate-kml>

Figure 44- Wind Speed Uncertainty at 100m, from <http://geoportal.lneg.pt/ArcGIS/rest/services/Norsewind/MapServer/generatekml>

3.8. Conclusions - SMRR Wind Mapping and AEP

Although direct, quantitative comparisons of different studies are not always possible, several conclusions can be drawn regarding SMRR wind energy mapping. These are listed below, with context as needed:

1. **Wind Speed Range** – For estimating AEP, wind speed accuracy is only critical in Region 2, and SMRR wind retrievals show the highest correlation with in situ anemometer data in Region 2 (between about 3 m/s and 15 m/s.), with time-averaged bias typically between 0.1 and 0.2 m/s, and SD typically between 0.8 and 1.3 m/s
2. **Time Series Indexing**– Because AEP is estimated over the life of a project, long time series datasets from SMRR can boost confidence levels compared to short data sets, because year to year variability can be quite large. Although NDBC buoy data sets can also be used for indexing, they provide a single spatial node,

unevenly dispersed, valid only for local indexing. Their accuracy is low (± 1 m/s for snapshot).

3. **Number of Samples** - Processing multiple SMRR data sets from different sensors increases the sampling times per day and the sample population and tends to normalize bias out of AEP estimates. Theoretically, there are enough samples of the study area to provide reasonably accurate ($\pm \sim 3\%$ vs. hub height cups) AEP estimates using existing GMFs.
4. **Cross Correlation** – Different SMRR data sets can be processed in parallel and correlated to improve wind mapping. The, wide coverage, large database, and wind direction input from scatterometers and polarimetric PMI can be leveraged by and supplemented with the high resolution of SAR to reveal differences in energy density at sub-kilometer scales, within a few kilometers of the shore.
5. **Primary Error Sources** -
 - **Wind Shear Error**– Use of inaccurate wind shear profiles is one of the primary sources of error in AEP estimates from SMRR retrievals. Extrapolation to hub height requires either in situ measurement or an accurate vertical profile function.
 - **Other GMF Error** – Fluctuating metocean conditions such as wave height and sea surface temperature can also affect wind shear in the lower boundary layer where turbines operate (Lange et al 2004) and Sigma-0 values (Karagali 2012) and this introduces error into the retrievals. This can be partially mitigated by cross-correlation with PMI data sets where available.
 - **Diurnal Error** – Potential exists for diurnal bias due to the fixed orbital schedules for each satellite. This can be mitigated by using multiple satellite data sets with different orbital schedules.
 - **Rain Error** – SMRR may not be suitable for wind mapping in areas with high precipitation like that found in the tropics, since rain bias is difficult to remove, and scrubbing for rain creates its own bias. In the study area, precipitation is much lower than the tropics, so this will likely be the lowest bias of the three listed.

Table 19, below, summarizes the relevant features and specifications of the baseline methodology and the four technologies evaluated. The table highlights the sensors' complementary characteristics.

Table 19- Properties of Different Wind Sensing Technologies

Data Sources and Properties, Before Co-Processing					
Sensor Data	Cups on Tower	Lidar on Buoy	Scatterometer	Synthetic Aperture	Passive Microwave
Height ASL	30-100 m	20 – 200m	10m	10m	10m
Resolution (m)	0.1	~30	12,500	400	25,000
Coverage (m ² /sec)	1 (static)	400-4000 (static)	>6,000,000	>200,000	>10,000,000
Daily sampling rate	1440	1440	~ 2	~ 0.1 to 0.3	~3-6
Time series (yrs)	1-2	1-2	~20	~20	>20
Wind measurement	speed and direction	speed and direction	speed and direction	speed only	spd + direction if polarimetric
Coastal Mask (km)	0	0	12.5	~2	25
Data cost	~ \$10m cost	~ \$1M - \$2M to	no cost	costs for L 1 data	no cost
Sensor for SST?	Y	Y	N	N	Y
Sensors for other metocean?	all	all	no	wave Hs, direction	rain rate, vapor, currents, Hs
Precip. effects	Not significant	Low availability in heavy rain	Rain corrupts data	Corrupted by <u>heavy</u> rain	Can detect rain and wind speed
Effective speed range	0-25 m/s	0- 50 m/s	4-20 m/s	4-20 m/s	4-20 m/s
Rotor disk coverage	50%	100%	10m surface vector only	10 m surface vector only	10 m surface vector only
Mean accuracy (filtered, t-avg)	+/- 0.1 m/s	+/- 0.1 m/s	+/- 0.2 m/s	+/- 0.2 m/s	+/- 0.2 m/s
AEP error sources	Wake effects, short time, point only	Short time series, low spatial coverage	Shear, diurnal bias, rain scrub, spatial averaging	Shear, diurnal bias, rain scrub, wind direction	Shear spatial averaging

The overall conclusion for SMRR wind energy production mapping is that the wide coverage and long time series are significant advantages, while the potential biases from vertical extrapolation and diurnal effects present the greatest uncertainties and challenges. As hardware (sensors and satellites) and software (onboard and external GMFs) have improved, so has the accuracy and resolution of the wind products, although this trend may be limited by the inherent uncertainty in assuming a static wind shear model and diurnal cycle. Other fluctuating metocean conditions (besides wind speed) can also affect surface roughness and radar reflections/emissions. Accurate calibration for these scene-specific conditions could improve wind retrievals further.

One of the primary impediments to better calibration is the dearth of in situ data, with approximately one offshore met station for every 10,000 sq. km. on the OCS (see Figure 47). If a one or two year time series of continuous in situ data were available, it could be used for calibrating co-incident, co-located SMRR scenes, and developing models of the effects of local conditions on wind retrievals. Theoretically, all three error categories could be reduced to some degree, depending on how accurately the conditions causing the error are modeled in the GMF.

This is the same process that was used in Project NorseWind to successfully improve high speed wind retrievals and calibrate for sea surface temperature (SST) effects, allowing the development of site specific, average wind shear exponents. Project NorseWind was a success due to four years of concentrated effort from a group of

dedicated researchers, but it also reaped the benefits of many years of in situ metocean data from oil and gas facilities in the North Sea. These facilities provided numerous fixed, powered platforms on which to place Lidar and other instruments. Data sets and facilities of that type are not available in the present study area, so another approach is needed.

Chapter 4

STRATEGY DEVELOPMENT

A broad research and data collection program is envisioned whereby US industry, academia, and government combine resources to develop the next generation offshore wind atlas, similar to the NorseWind project, but updated and tailored to the challenges and needs of the US OCS. The NorseWind Project did not include PMI data sets, and the locations of calibration stations were limited to existing fixed offshore platforms. The strategy was to develop a static “shear atlas” for the study area, and apply it to all SMRR retrievals. Though truly groundbreaking, and well suited to the North and Baltic Seas, there is room for improvement in the methodology when transferred to U.S. waters. Four recent developments enable offshore wind energy mapping to be brought to a higher standard in the U.S:

- Critical mass of SMRR databases
- Recent advances in GMFs and satellite SMRR systems, especially PMI
- Development of wind Lidar met buoys

- Cheaper faster data processing

This can be achieved by using strategically placed, moveable, metocean buoys equipped with wind Lidar technology to calibrate SMRR retrievals parametrically. These two remote sensing technologies have complementary qualities that can be combined to improve accuracy, coverage and resolution, yielding more optimal project siting and resource mapping (Hasager et al 2008 and 2011, NorseWind 2012). The following sections lay out a framework proposal for conducting such an effort.

4.1. Data Collection Campaign

4.1.1. Lidar Buoy -Data Collection

The study area (MAB OCS to 60m depth) comprises a long strip of ocean roughly 100 km by 500 km. A fleet of ten moored, floating Lidar units dispersed roughly evenly would provide good coverage of the study area, with about 80% of the area within 30 km of a Lidar station, and no point more than ~50 km distant, as shown in Figure 45. The locations are approximately 50km apart, along the 45 m isobath, and provide only an example, not yet optimized. Some or all of the units could be moved periodically as the campaign adapts to evolving data needs and priorities. Floating Lidar units provide accurate measurements of the wind vector profile at multiple heights up to 200 m, and the buoys

can also record and/or transmit precipitation, humidity, barometric pressure, air temperature, sea surface temperature, current profile, and gravity wave height, period, and direction. A one year campaign should be sufficient to capture a broad range of conditions, suitable for developing site specific parametric models for the lower boundary wind profile (up to ~ 200m) and other metocean conditions that affect SMRR retrievals. After the calibration deployment, the buoys could be serviced and re-deployed to selected development sites to reduce uncertainty further, as described in Chapter 6.

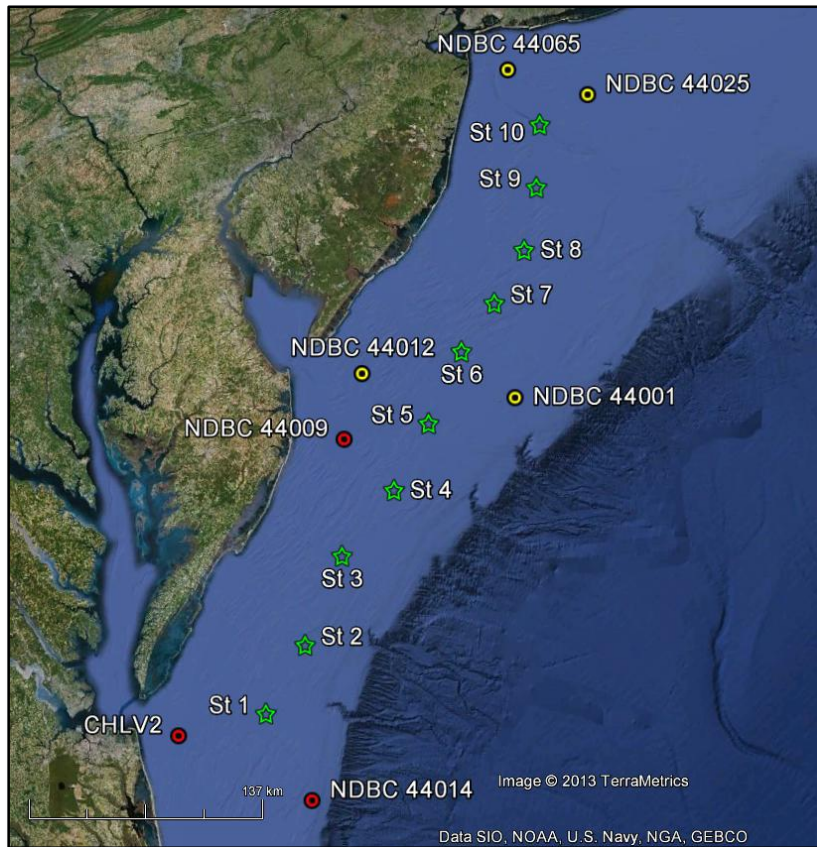


Figure 45- Proposed Lidar Buoy Stations (green stars) and Historic Met Stations w/Over 5 yrs. Data (red and yellow dots).

4.1.2. SMRR - Data Collection

4.1.2.1. Correlation Data

There are at least seven operating SMRR satellites that could be tasked (programmed to acquire desired data stream) or tapped (collect default data stream from public website) to collect scans of the study area co-incident with the Lidar campaign. These seven sensors include all three types; SAR, Scatterometers, and PMI (radiometers), and each can be programmed to use multiple operational modes for optimal detection of the various metocean parameters that can be extracted using GMFs, as described previously. With the Lidar data, this creates multiple paired data sets for correlation analysis. This allows calibration of the SMRR vertical extrapolation based on local conditions. It also allows calibration for wind direction, SST, wave height, wave direction, ocean currents, air temperature, and other parameters that may affect the radar signal/backscatter. For calibration purposes, it may also be advantageous to periodically task some satellites to use alternating polarization or other non “background mission” modes.

Because meteorology and wind mapping falls under the umbrella of the primary public service mission of U.S. Earth observing satellite programs, the costs of collecting such data could be borne by the federal government through the lead agency, whether NASA, NOAA, DOD, DOI or some other branch of government.

4.1.2.1. Archival Data Cost

All available archival SMRR data sets of the study area could be collected at a relatively low cost. Some SAR images may have to be purchased, but govt. and/or academia are often exempt from this cost, and the PMI and scatterometer data are available at no cost. A detailed analysis of the cost of these images was not conducted for this study, but they are not expected to be significant based on the inventory estimate and costs for the NorseWind study.

4.2. Calibration Campaign

4.2.1. Sigma-0 Conversion and Vertical Extrapolation Error

Most SMRR retrieval error is introduced from two conversion processes; first, when the normalized backscatter/brightness temp³⁸ (sigma-0, or σ_0) value is converted into surface roughness, then to shear stress, then to wind speed at the sea surface (U_{ss}); and second, when the wind speed is extrapolated from the sea surface, U_{ss} , to the desired height, $U(z)$. Hagerman (2008) estimated that the uncertainty in power law extrapolation offshore, from 40m to ~90m is in the range of 20% to 25%. Extrapolation from the sea

³⁸ For active instruments (SAR and Scat) this is the backscatter signal strength, and for passive radar it is the brightness temperature/emissivity, but in both cases it may be denoted σ_0 .

surface introduces the potential for even more uncertainty. The greatest improvements to accuracy can therefore be had by examining and correcting retrieval errors in the sigma-0 conversion and the vertical extrapolation.

4.2.2. Parametric U_{ss} Correction

Standard GMFs estimate U_{ss} as a function of σ_0 , wind direction, and a few other geometric parameters, and they assume fixed values for metocean conditions that can affect σ_0 , of which there are several. Backscatter can be affected by the average slope of the water surface, which is a function of gravity waves, since these waves create steeper average slopes, changing the radar incidence angle. Gravity wave information from the Lidar buoy, from NWP models, and from SAR can be fed into the GMF to model this effect and remove error from each scene. Sea surface temperature, surface currents, and atmospheric moisture can also affect σ_0 values, and can also be measured and modelled, as discussed previously in the literature review. In addition to the standard metocean suite, Lidar buoys can also be equipped with capillary wave or surface roughness sensors that can provide direct correlation between wind speed, surface roughness and σ_0 values. A function could be derived through multi-variant regression analysis of paired data sets to estimate the bias introduced to the snapshot sea surface wind speed retrieval by each of these parameters. It would take the form;

$$Bias(U_{ss}) = fn(SST, H_s, H_{cap}, C_{ss}, WV, \dots) \quad (1)$$

where U_{ss} is sea surface vector wind speed, SST is sea surface temp., H_s is significant wave height (gravity waves), H_{cap} is capillary wave height, C_{ss} is sea surface vector current velocity, and WV is atmospheric water vapor. This parametric function could be used to “train” the GMF to reduce error from fluctuating metocean conditions, improving wind retrieval accuracy. With this dynamic GMF, σ_0 conversion uncertainty related to fluctuation of these parameters can be significantly reduced. As long as the model is well calibrated and the input values accurately reflect local, coincident conditions, σ_0 to U_{ss} conversion should be more accurate than standard models, which typically use static parameters for backscatter³⁹.

4.2.1. Parametric Extrapolation Model

Offshore, the wind profile below 200 m height is primarily a function of wind speed, atmospheric stability and surface roughness from gravity waves (Manwell et al 2009). The relevant parameters are therefore those that affect atmospheric stability and sea state, including air temperature at the sea surface (AST), water temperature at the sea surface (SST), barometric pressure (for deriving air density, ρ), and significant wave height (H_s). The wind profile or shear can also change with wind speed. The ability to monitor

³⁹ NorseWind used site specific shear exponents in some areas.

metocean conditions, co-incident and co-located with wind Lidar profiles enables development and calibration of a parametric wind profile function that is tuned to “real-time” local conditions. Using the Lidar profiles and buoy data, a multi-variant regression analysis could be performed to define a parametric wind profile function, $U(z)$ that includes terms to account for local metocean parameters, as given below;

$$U(z) = fn (U_{SS}, AST, SST, H_s, \rho, etc.) \quad (2)$$

The function could be based on any number of wind shear models, depending which one best fits the data. This “trained” parametric profile function would allow automated, customized extrapolation of wind speeds from the sea surface to the top of the rotor disk, for each SMRR scene.

4.3. Re-processing Archival Datasets With Tuned GMFs

The wind profile and sigma-0 conversion models described above can be incorporated into a parametric GMF/Wind Retrieval Tool that processes metocean input from multiple sources and provides accurate hub height wind speed estimates from multiple sets of sigma-0 data. Many of the metocean parameters that affect the wind profile and backscatter (eg. SST, gravity wave height, rain rate, atmospheric vapor, etc.) can also be retrieved from archives of NWP and other metocean models, and from archival data sets from PMI radiometers and X-band and L-band SAR.

This retroactively tuned⁴⁰, Lidar calibrated, cross-correlated, parametric GMF (hereafter referred to as “LCGMF”) would more accurately reflect local metocean and wind shear conditions at the time of each historic scan. The LCGMF can be applied to the archival SMRR scene/data set to retrieve hub height wind speeds and AEP, producing maps with a 5 km resolution⁴¹.

The flowchart in Figure 46 shows how the methodology could be employed to produce more accurate energy production estimates and maps. The first phase includes the field campaign to collect Lidar data and a satellite scanning program to collect co-incident, co-located SMRR data. This phase will develop the parametric algorithms used to determine the wind profile and U_{SS} correction values. The second phase involves retrieving all archival SMRR scenes and re-processing them through the LCGMF that incorporates both models. By filtering for wind speeds between ~ 3 and 15 m/s (Region 2), SMRR bias is kept at its lowest⁴². For AEP estimates, accuracy below 3 m/s is not required since the turbine is shut down, and accuracy above 15 m/s is not critical because the turbine is operating at capacity. For estimating shut down time during extreme winds, NWP model hindcasting and/or archival records would be sufficiently accurate. SMRR wind

⁴⁰ The term “tuning” is used for changing the parametric inputs, to differentiate from “calibration” which applies to changing the underlying GMF algorithm software.

⁴¹ For comparison, NorseWind produced maps on a 2 km grid.

⁴² Energy density or mean wind speed maps would require accurate data from the full range of wind speeds.

retrievals can still be used beyond this range for determining turbine operational status (Region), although with reduced accuracy ($\sim \pm 1$ m/s).

Lidar metocean buoys can also detect recurring or cyclical metocean conditions, and these can be modeled retroactively to improve retrievals. For example, archived sigma-0 from an area with strong tidal or seasonal currents could be re-processed using historic current data or tide tables, which have in turn been validated, calibrated using the Lidar buoy. Knowing the historic time series, the calibrations can be applied in the LCGMF to re-process archival SMRR data sets.

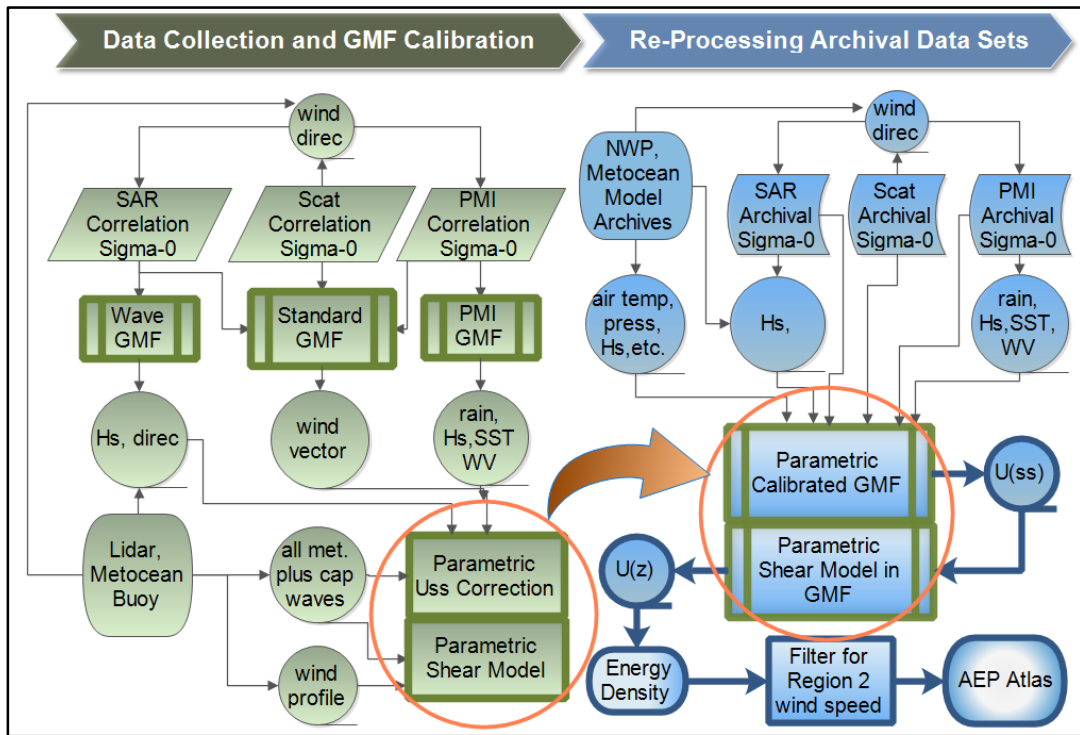


Figure 46- Flowchart of Proposed Methodology

4.4. Remaining Bias and Mitigating Factors

With this strategy, the largest remaining sources of error for AEP estimates are:

- 1) **Weibull Parameter Error** – This arises from a low number of samples, resulting in a fitted Weibull PDF distribution that does not reflect the true distribution of wind speeds, and thus may not reflect the true energy density.
- 2) **Diurnal Coverage Bias**- Time averaging bias can be an issue if there is any statistically significant correlation between time of day and wind speed, since the satellites scan a location at nearly the same local solar time(s) each day. If, for example, there is a persistent low level jet in the late afternoons during hot summer days, the satellite scans may miss it completely, or may capture it almost exclusively.
- 3) **Rain Scrubbing Bias** – Rain bias is difficult to remove because the effects on radar images are highly variable, non-linear, and different for C-band and Ku-band. Rain in the atmosphere reflects but also dissipates microwave energy. Rain on the sea surface can increase roughness but also degrades capillary wave coherence. Hence, rain is almost always scrubbed, but this in itself can create bias if there is a statistically significant correlation between rain and wind speed.
- 4) **Parametric Input Biases** - The LCGMF will require scene-dependent input values for a number of parameters (e.g., wave height, sea surface temperature, atmospheric vapor content). If any of these input values or assumptions are biased, it may bias the output to a lesser degree.

Table 20 is a matrix outlining how each of these SMRR error sources should be mitigated by the proposed methodology.

Table 20- SMRR Based AEP Error Sources and Mitigating Factors

AEP Bias/ Error Source	Mitigating Factor			
	High Number of Samples	High Spatial Resolution	Long Time Series	LCGMF
Weibull fitting (PDF) error	More samples produce better curve fitting, regression	More site spe- cific, hub height Weibull param- eters	Better index- ing for Weibull parameters	More accurate profile, geo- physical models
Diurnal	Multiple observa- tion times/day, Lidar full time for a year (min.)	ID distinct diur- nal features like coastal jets, tides	ID long term changes in di- urnal patterns	Diurnal cycle measured and modelled in GMF
Rain Scrubbing	More samples available for rain scrub/flag calibra- tion	Allows smaller rain mask, less spatial scrub- bing	More data to investigate correlations	Scrub opti- mized and au- tomated using PMI data sets
GMF input, other GMF Error	Helps correlation between metocean param- eters and SMRR retrievals	Allows isolation of local condi- tions for GMF calibration	??	LCGMF tuned to in situ shear and metocean using multiple sources

4.5. Conclusions- Accuracy of LCGMF Based AEP Mapping

The proposed methodology, using optimized, cross-correlated, Lidar-calibrated algorithms, along with more selective data scrubbing and parametric tuning, can significantly reduce error and increase confidence in AEP estimates, with accuracy comparable to hub height met towers. With over 20 years of data, it is likely that AEP error will be at or below the low end of the range found by Karagali (2012); that is, within ~ 2.0% of estimates using cups on a hub height met tower. This is made possible by leveraging four important developments:

- 1) The large and growing databases of SMRR.
- 2) The recent advances in satellite microwave sensors and Geophysical Modeling Functions.
- 3) The ability to process large amounts of data faster and cheaper than before.
- 4) The technical breakthroughs and capabilities of floating Lidar.

This error (2%) is comparable to the uncertainty in the met tower estimates, so it is likely that at some sites, the LCGMF data would be more accurate than the tower estimates. If the met tower does not reach hub height, the proposed methodology is likely more accurate than using data from the tower, under the assumption (discussed in Section 2.2.6-Summary – Floating Platform Lidar) that floating Lidar performance will be equivalent to fixed platform Lidar performance within less than 3 years.

At present, AEP maps based on LCGMF may not inspire sufficient confidence for obtaining project financing in the U.S., but the value for site selection and resource assessment is immediate and significant, and will become greater as development moves into deeper water, where the areas available are much larger, wind data are scarcer, and SMRR retrievals are not subject to land masking or coastal effects like shallow water and tidal currents.

Chapter 5

SITE SELECTION BENEFITS

5.1. Resource Assessment – Background and Purpose

Resource Assessment (RA) is the collection and analysis of in situ wind data and model simulations to characterize the wind resource at a site⁴³. It is analogous in many ways to mapping of mineral resources. It is performed as part of site selection (macro-siting), and to project Annual Energy Production (AEP) of a wind farm. This allows a comparison of available energy between different sites and an estimate of the potential revenue at a given site. It requires a sufficient number of wind speed observations to account for diurnal and seasonal changes in the wind field. Typically, measurements are taken at 10

⁴³ RA can also include other characteristics such as wave climate, annual wind direction distribution (typically represented by a wind rose), turbulence intensity, and extreme wind speeds, and can also be useful in optimizing the layout of the wind farm and selecting the optimal rotor and turbine, but these are secondary considerations outside the scope of this analysis, and are not considered further.

minute or 60 minute intervals over one to two years and observations of wind speed are grouped into intervals (bins) by wind speed or wind direction. A probability density function is then used to describe the wind speed distribution over a year. (Manwell et al 2009, Troen et al 1989, DNV 2011).

The discussion of RA begins with siting and how it can be improved with better resource mapping, then proceeds to AEP, how it is generated and used, and how it affects project finance costs. Table 21 lists three key wind parameters typically generated for RA and briefly describes their use in each application.

Table 21 - Wind Parameters for AEP and Site Selection

Parameter	AEP Estimates	Site Selection
Mean Wind Speed	Indicator of wind class	Identify sites with highest wind class
Wind Speed Energy Spectrum (Weibull Parameters)	PDF or Weibull curve used for AEP estimates	Identify sites with highest energy density
Extreme Wind Speeds	No production for winds above cut-out speed	Avoid/Design for “hot zones” (hurricane prone regions)

5.2. Site Selection- Current Practices

Site selection (a.k.a. macro-siting) is the selection of the optimal wind farm location based primarily on the available energy, seafloor geology, metocean conditions, distance to shore, distance to load center, environmental impacts and human use conflicts. It is analogous to prospecting for mineral resources in many respects. Ideally, a production estimate would be generated with in situ data and used to generate projected revenues for multiple sites within the area of interest. The production estimates would be compared to the costs and impacts of developing and operating in each zone, enabling an informed selection of the optimal site or zone (whether a wind farm or a mine) within the region surveyed. For offshore wind power, this procedure is not practical because of the high cost of obtaining in situ data with met towers. In practice, selection of the site begins with an examination of available lease areas and existing wind maps. In the MAB, in situ data are scarce, and offshore hub-height towers are non-existent⁴⁴, so hub height wind speed maps are usually generated using meso-scale numerical simulation models calibrated with NOAA met station historical data sets⁴⁵. These are discussed below.

⁴⁴ There are a few offshore platforms with sensors up to ~45m, and at least one existing platform, the Chesapeake Light Tower, may be retrofitted with a tall tower in 2013/2014.

⁴⁵ MesoMap was validated using limited SMRR snapshot data

5.2.1. Historic In Situ Datasets

Historical data provide the best starting point for projecting seasonal, stochastic, natural processes like the wind from year to year. Multi- year, offshore, continuous wind observational data sets on the US MAB OCS are available from only one source - NOAA met stations and buoys. At any given time, there are between four and eight offshore NOAA met stations with operational anemometers in the MAB OCS, an area of about 60,000 sq. km., leaving an average coverage per station on the order of 10,000 sq km. In reality, the stations are somewhat clustered. Figure 47 shows the location of all seven buoys that have provided data records exceeding 5 years⁴⁶, including both decommissioned and operational stations. It also shows the service life of each. Only three stations; 44009, 44014, and CHLV2 have data records exceeding ten years, and these are shown in red. The average data record of the red stations is 26 years. The average time series for the remaining stations, shown in yellow, is about 7 years. NDBC 44012 and 44001 are included on the map but they are no longer operational, leaving a 240 km gap between 44009 and 44025. If those two decommissioned buoys are included, the gap is still about 190 km. The gap in the southern half of the MAB is also about 190 km, between NDBC 44009 and CHLV2.

⁴⁶ Data records of less than 5 years have little value for indexing, and high uncertainty for AEP estimation, though they can be used for meso-scale model calibration.

For wind energy mapping, some method of horizontal interpolation is required to fill in the huge spaces. Wind speed data must also be extrapolated vertically, from the buoy sensor height (3 to 5 m) to the turbine hub height (90-110 m) for energy estimates. This is typically done using meso-scale numerical modeling, discussed in the following section.

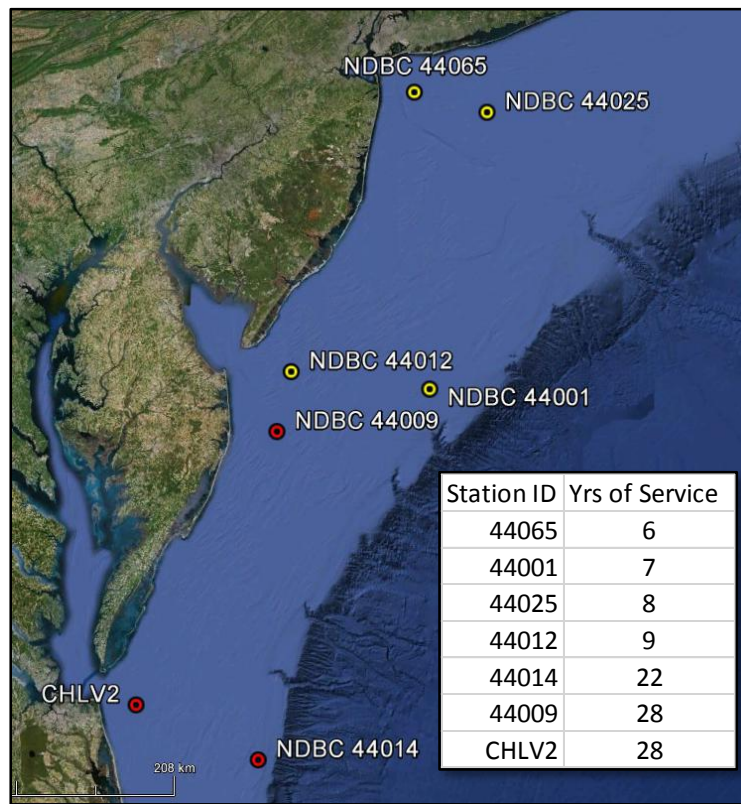


Figure 47 –NDBC Offshore Met Stations in MAB with > 5 yrs. Of Data. Red dots have over 20 years of data, yellow dots have less than ten (locations and service life from NDBC website)

5.2.2. Wind Models and Resource Mapping

Current offshore wind resource maps are based on regional (meso-scale) numerical simulation models. These models are validated and calibrated offshore using coastal met stations, NDBC buoys, and, in some cases a few selected SSMI and QuickScat snapshots for calibration. Although the grid scale of the models can be set as low as one hundred meters, the true accuracy and resolution are limited by the amount of field data available to calibrate the models. These maps are primarily used to obtain gross estimates of available offshore wind energy at various water depth zones, by state or region, and to guide further field investigation.

5.2.2.1. History of Wind Energy Mapping and Exclusion Zone Analysis

Offshore wind energy mapping is a relatively new science, born of the need for resource assessment data for offshore wind energy production. In addition to mapping the energy density at hub height, exclusion zones must also be identified where it is not feasible or advisable to install wind turbines. This exclusion analysis must consider numerous competing human uses and sensitive habitats. A concise but comprehensive history of the development of wind resource mapping in the U.S. can be found in Baker (2011), from which the summary below was extracted.

Baker (2011) on the history of onshore resource assessment and the original WERA-

The national Wind Energy Resource Atlas (WERA) – produced wind power estimates and maps in order to promote further detailed site investigation for wind energy development (Elliott et al., 1987).It was the earliest large-scale wind resource assessment (land-based) that estimated wind speeds and wind power density over a vast area using a combination of quantitative and qualitative methods based on wind power measurements from various meteorological stations around the U.S. and topographic and meteorological indicators that influence the wind resource, The WERA (1986) took wind speed measurements at various heights and extrapolated them to ten meters and fifty meters (10m and 50m) using the log law. The study then converted wind speeds at the reference heights to power densities. Power density was chosen as the preferable metric for the WERA resource assessment, rather than just wind speed, because it combines “the distribution of wind speeds and the dependence of the power density on air density and on wind speed (Elliott et al., 1987; Appendix A A).

Baker (2011) summarizes the status of offshore resource mapping and exclusion zones:

Initial offshore wind resource studies extended models developed for land-based wind analysis to the areas over the ocean via modeling techniques (Musial and Butterfield, 2004; Elliott and Schwartz, 2006; Heimiller et al., 2007). The Musial and Butterfield (2004) and Heimiller et al. (2007) studies (hereafter, NREL studies) both use mesoscale models that estimate wind speeds at 50 meters height. However, those models were only extended a limited distance from shore, employed proprietary algorithms, and did not consider actual exclusion for other ocean uses. studies of the Atlantic region have used offshore wind speed readings from buoy or satellite measurements, converted them to power output at hub height, and made extensive use of actual data on competing uses to develop exclusion areas (Kempton et al., 2007; Pimenta et al., 2008; Garvine and Kempton, 2008; Dhanju et al., 2008).The most recent effort ..., using MesoMap, now calculates wind speeds at 80 and 100 meters. MesoMap was developed with support by the U.S. Department of Energy ...and has been used to update the WERA to provide detailed wind power resource assessments for the U.S. and individual states. (Elliott and Schwartz, 2006). (the maps) also report annual average wind speeds and potential installed capacity in Megawatts as a function of the wind energy capacity factor, (NREL, 2010).

The MesoMap-generated estimates were validated by NREL using data from ocean buoys, marine automated stations, Coast Guard stations and lighthouses, and satellite-derived 10-m wind speeds over the ocean estimated from the “state of the sea” as measured by snapshot SMRR data. Figure 49 shows the NREL/MesoMap 90m wind speeds out to the 60m isobath off NJ.

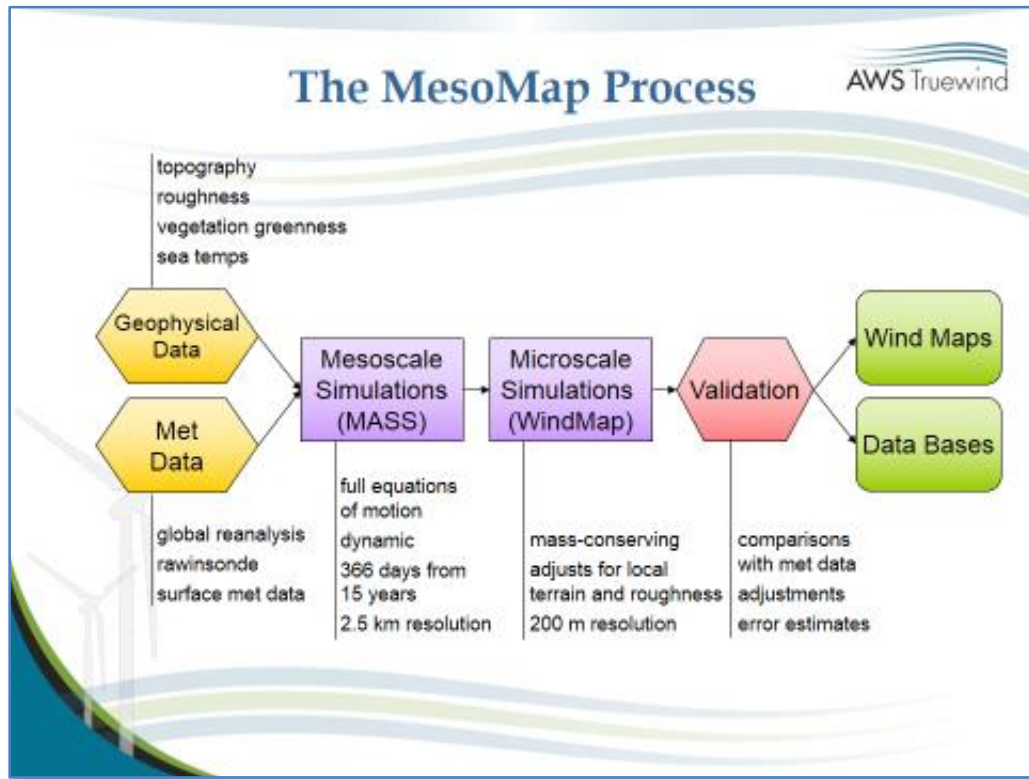


Figure 48- Meso Map Generation Process Diagram, reprint courtesy of B. Bailey, AWS Truewind

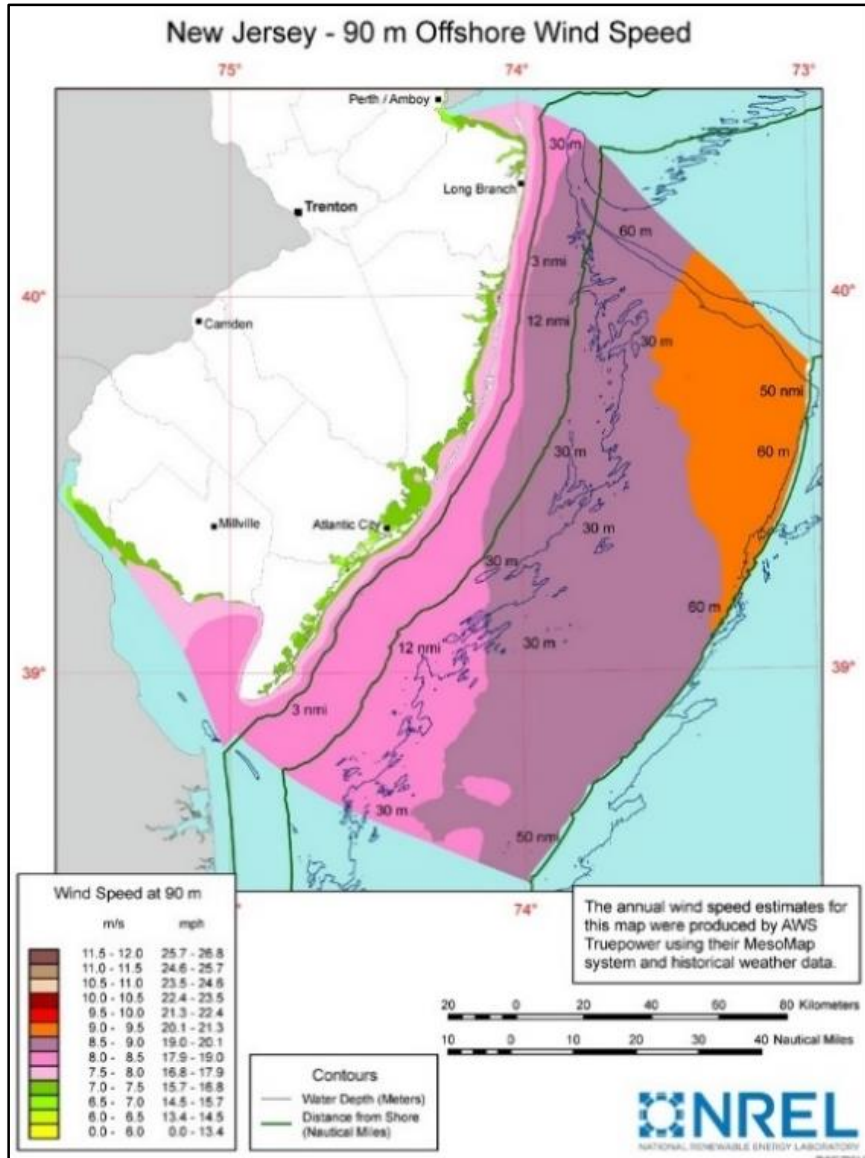


Figure 49- MesoMap Wind Map offshore NJ, from Schwartz et al 2010, original map created by NREL for US Dept of Energy.

5.2.2.2. Exclusion Areas – Baker 2011

Most of the offshore resource studies before 2010 estimated the area of different categories of exclusion zones by using a reducing fraction, not a comprehensive localized analysis. Baker (2011) performed a comprehensive exclusion zone analysis of the MAB OCS to estimate available area for power production. The total area, pre-exclusion, for each bathymetric class (depth zone) is shown in Figure 50. The study estimated that, post-exclusion, the zone between 35 m and 60 m could accommodate enough turbines to generate over 250,000 GW-hr. annually, as shown in Table 22. The analysis assumes a 5 MW turbine and typical offshore spacing and wake losses. The wind speeds were estimated from models developed by AWS Truepower using MesoMap.

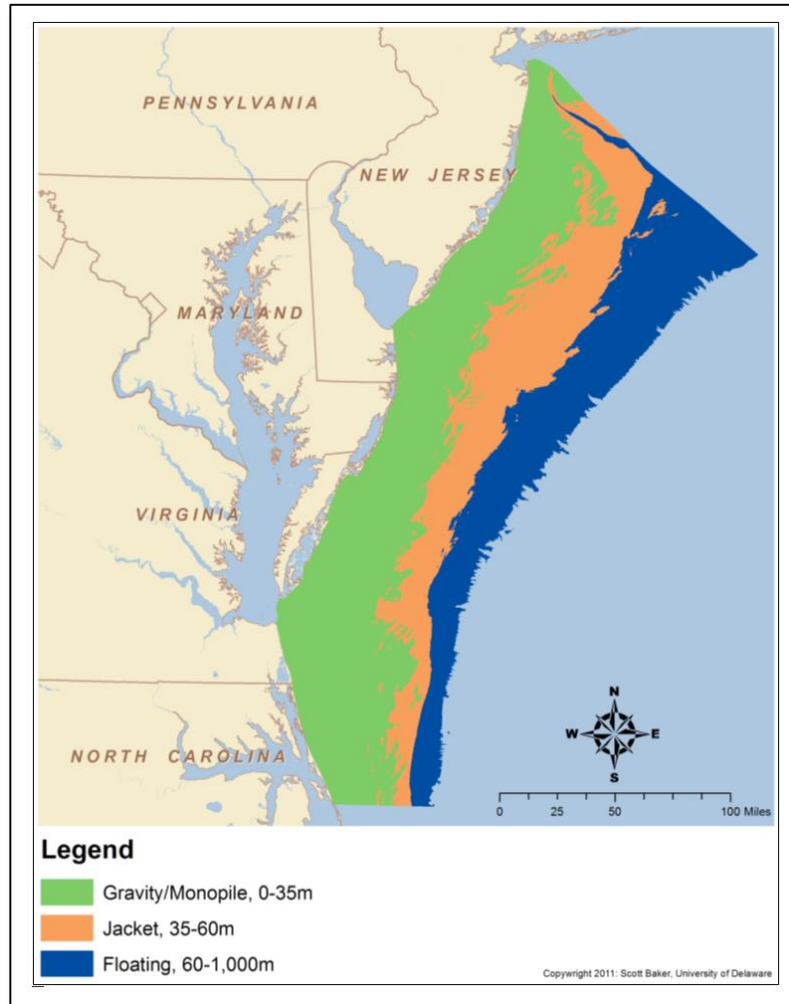


Figure 50-MAB OCS Depth Zones by Foundation Type, from Baker 2011

Table 22- Post-Exclusion Area and Production Capacity by Depth Zone, MAB OCS, from Baker 2011

Bathymetric class	Wind Energy Area (km ²)	Wind Turbines (Count)	Nameplate Capacity (MW)	Average Output (MW _a)	Annual Energy (GWh)
0-35m	12,157	15,314	77,720	28,523	249,862
35-60m	11,468	14,447	73,316	29,335	256,974
60-1,000m	15,656	19,723	100,095	40,049	350,832
Totals	39,280	49,484	251,132	97,907	857,667

5.2.2.3. Advanced WRF-Based Mapping –Dvorak et al 2012

A slightly different approach towards estimating resources was taken by Dvorak et al (2012). This study mapped mean offshore wind energy resource on the basis of 5 years (2006 to 2010) of high-resolution mesoscale model results from ARW (Advanced Research WRF) at 90 m height. The study area included the entire US East Coast OCS out to 60m depth. A 5 km grid spacing was adopted to better resolve localized sea breezes. Model output was evaluated against 23 buoys and nine offshore towers. The north domain of the study included the study area, and found annual mean wind speed bias (ARW vs. in situ) ranging from 0.04 to 0.21 m/s over the five years of analysis. Annual RMSE ranged from 2.06 to 2.6 m/s. Figure 51 shows the vector component absolute error of wind speeds at CHLV2, for August 2008, for ARW output versus a cup anemometer. Although the RMSE was significantly higher than that found for filtered

SMRR retrievals (2.45 m/s versus ~ 1.3 m/s), the bias was roughly the same magnitude for time averaged mean wind speeds.

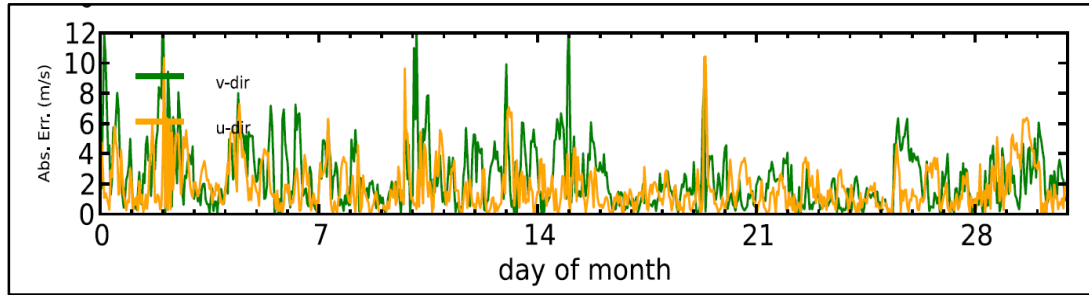


Figure 51-Absolute Error, WRF vs. CHLV2, August 2008, from Dvorak et al 2012

Optimal locations for large-scale development of offshore wind energy from Florida to Maine were identified based on the wind resource, bathymetry, hurricane risk and peak-time generation potential. The offshore region from Virginia to Maine was found to have the greatest potential, with annual turbine capacity factors⁴⁷ (CF) between ~ 45% and 50%, shallow water and low hurricane risk.

A second analysis by Dvorak (2012b) used the same ARW model at a higher resolution to develop maps of mean wind speed, power density, and capacity factor for areas off the coasts of MD, DE and NJ. Figure 52 shows the results mapped as mean wind speed at 90m ASL. An additional analysis was performed for a site within the study area near

⁴⁷ Based on a RePower 5M turbine power curve

Wilmington Canyon. As expected, a slightly higher wind energy resource was found on the E side of the project area, with difference of approximately 0.2 m/s, 46 W/m², and 1%; in mean wind speed, mean power density, and capacity factor, respectively (see Figure 52).

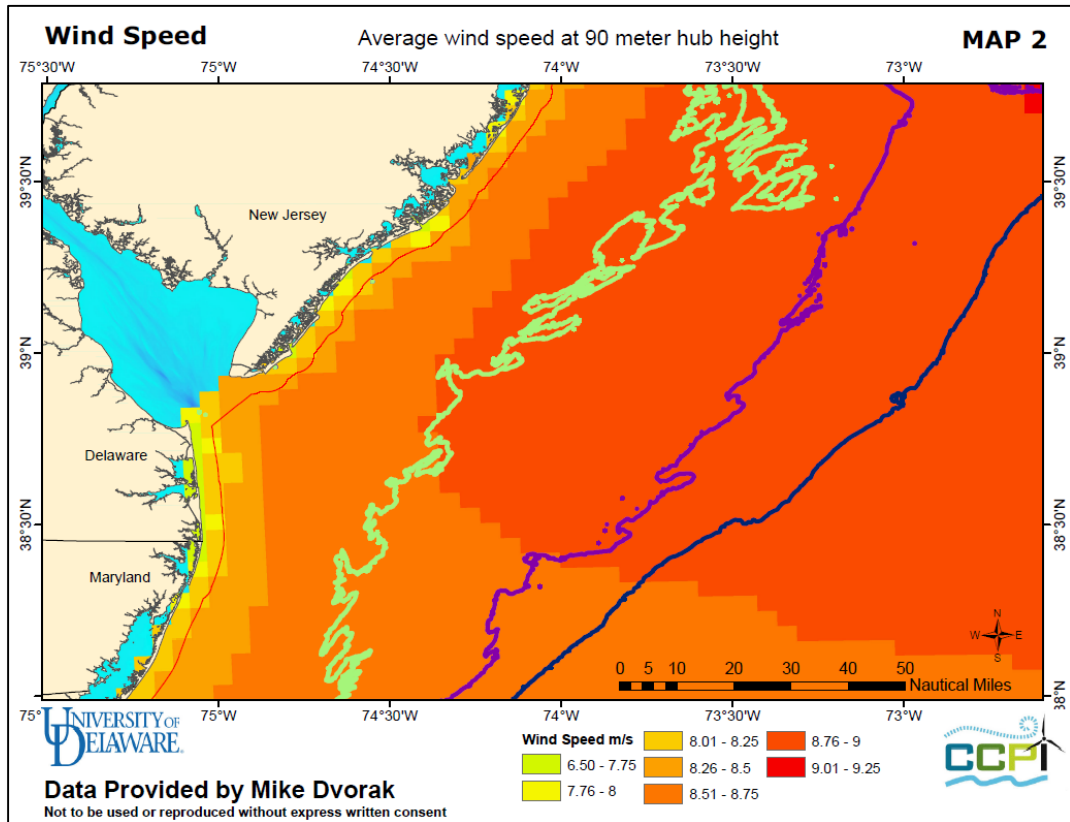


Figure 52-Mean Wind Speeds @ 90m, MAB OCS, reprinted with permission of M. Dvorak and A. Bates (UD, Center for Carbon Free Power Integration)

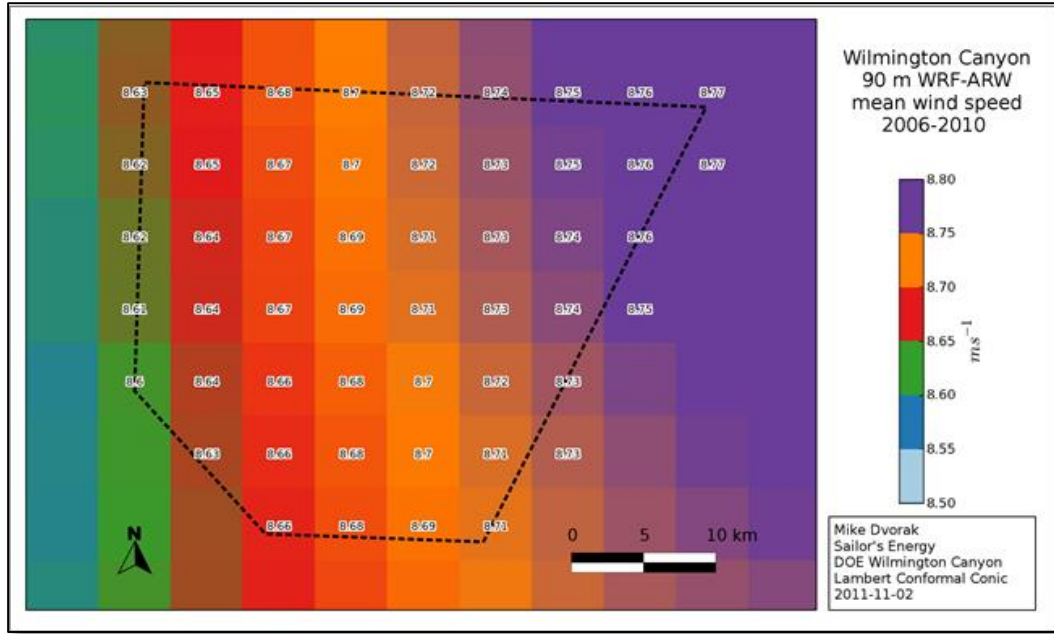


Figure 53- Mean Wind Speeds @90m, Wilmington Canyon, from Dvorak 2011

Although Dvorak et al (2012) found bias of mean wind speed estimates from the model comparable to that from available SMRR products, the large amount of deviation exhibited by the model wind speeds (as evidenced by root-mean-square error values almost twice as high as SMRR products), makes their use for energy density estimates problematic, since there is greater uncertainty in the Weibull k parameter. Further research is needed to reduce model output deviation to more closely match observations.

Commercially available models and maps are not yet considered by financiers in the offshore wind industry to be accurate, reliable, or detailed enough for site selection or

raising capital in the US market⁴⁸. Meso-scale wind maps can provide reasonable interpolation between met stations and help identify large scale features and processes, but are not yet considered “bankable” data for AEP estimates in the industry. However they are extremely useful for estimating historic metocean conditions for derivation and/or calibration of satellite data, as previously described in Section 4.3-“Re-processing Archival Datasets With Tuned GMFs”. A separate program is envisioned whereby the vast SMRR data sets could be used to improve meso-scale modeling, but that is beyond the scope of this study.

5.2.3. Site Selection - Shortcomings

Under the current OCS leasing regime for the US, developers cannot place any met tower or other fixed structure in federal waters without a Department of Interior limited lease or research lease and an approved Site Assessment Plan (BOEM 2011). Before erecting any structure to mount anemometers, they must select lease blocks based on existing wind maps and the limited, flawed data sets that support them. Once the five year lease is granted, the developer may erect a structure and conduct a RA to raise capital. The current recommended practice for RA includes a hub height offshore meteorological mast mounted to the sea floor (DNV 2011). The mast supports both ultrasonic and Class I cup anemometers at a range of different heights. These towers

⁴⁸ Personal communication, Peter Mandelstam, Arcadia Wind Power, 10 October 2012

require substantial permitting effort, an up-front capital outlay on the order of \$2.5 million - \$10 million (Wisseman 2009, Brower 2012), and a minimum of two years for planning and construction. The high cost of these towers limits deployment to one per wind farm, and they are often simply placed at the shallowest spot within or near the site to control costs. A single tower measures the resource at one spot, but does nothing to ensure selection of the optimal site. In effect, developers are compelled to select a site with blinders on. If the site proves commercially viable, the developer can apply for a 20 year production lease, never knowing if the adjacent block has more wind. If the site doesn't prove viable, the tower investment is stranded. This strategy brings to mind the man who was looking only under the streetlight for his lost keys, *because that was where he could see*.

5.3. Variability of Resource on the MAB OCS

In the MAB, beyond a few km offshore, available maps show a general trend of increasing energy offshore and a noticeable increase at higher latitudes, closer to Long Island, NY (see Figure 49, Figure 52, Figure 53, and Figure 54). These maps show some detail and unexpected features, but are still based on numerical models calibrated primarily with buoy data. However, there is a growing body of evidence that low level coastal jets, ocean thermal upwelling, submarine canyons, Gulf Stream gyres, and other oceanographic and meteorological phenomena can cause significant, and likely persistent

spatial variation of average annual wind speed (Pichiguna et al 2011, PERI 2012, Beal et al 2005, Chelton et al 2004, O'Neill et al 2010, Ancona 2012).

In a 2011 study led by NOAA, scanning Lidar was mounted on a ship and survey transects of wind speed were taken off the coast of New England, with most tracklines between 6 and 60 km offshore (Pichiguna et al 2011). The authors investigated this and other scanning Lidar coastal datasets extending over multi-week periods, and concluded that low level jets, in the height range of turbine rotor disks, are a regular occurrence in coastal waters of the area. This research showed that the zone of sea-breeze influence can extend up to 50 km offshore. Sea breeze circulation cells develop in the study area during warm afternoons, which mostly occur during peak power demand in summer months, so the power they generate during these periods is more valuable to grid operators. This specific effect is not analyzed in the present study, but is worth noting.

The study concludes:

...the measurements indicate strong spatial and temporal variability of the wind field in the offshore region, in the atmospheric layer aloft occupied by turbine rotors....Scanning, pulsed Doppler Lidar instruments operated from fixed platforms or ships are well suited for providing much improved characterization of offshore wind fields for use in evaluating potential wind energy sites.

Chelton et al. (2004) used SMRR data to retrieve SST and to examine small scale features in ocean winds. They found persistent small-scale variability in the surface wind field related to SST modification of the low-level winds, through air- sea heat fluxes. More recently, large horizontal variations in surface wind speed near meandering SST

fronts are indicated by O'Neill et al (2010) in the mid-latitudes. Warmer (cooler) sea surface water temperature was found to be correlated with stronger (weaker) mean wind speeds.

5.3.1. Wind Gradients and Variability

For most of the MAB OCS, water depth increases with distance offshore and up the coast, and existing maps generally show mean wind speeds following the same trend, as seen in Figure 54. The isotachs (lines of equal average wind speed) generally run parallel to the shore and are relatively evenly spaced. State by state NREL MesoMaps of the MAB show many areas with a wind speed gradient of about 0.5 m/s per 50 km (NREL 2010, Figures B4, B11, B16, B25). Dvorak found an offshore gradient of about 0.2 m/s per 30 km in the intermediate depth zone (off the coast of northern Delaware). The Dvorak analysis used an upgraded version of WRF and a higher resolutions, so it is likely more accurate. Assuming this gradient (0.1 m/s per 15 km) represents a typical condition in the intermediate depth zone, two locations 100 km apart could easily have mean wind speeds that differ by over 0.7 m/s.

All else being equal, and given a relatively uniform offshore gradient, a logical siting method would use an optimization algorithm to find the distance offshore that maximizes the return on investment. However, the selection of latitude (alongshore) in the MAB south of Long Island is less determinate. Along any isotach indicated on a wind map,

the true mean wind speed will vary to some degree. Persistent, localized sub-regional variability of wind speed (e.g., coastal jets) can create “peaks and troughs” of annual energy density. In fact, the gradient of wind energy density could be steeper alongshore than it is offshore in many areas. At present, no comprehensive, regional analysis of this variability or these features exists for the mid-Atlantic OCS.

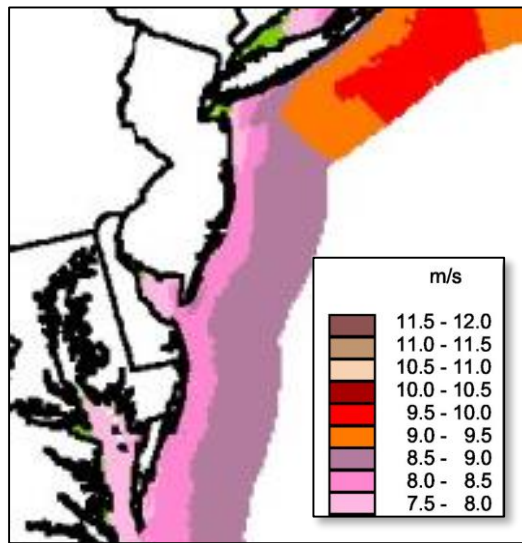


Figure 54- 90m Mean Wind Speeds, adapted from Schwartz et al 2010, figure B1; original map created by NREL for US Dept of Energy.

5.4. Site Selection Benefits– With LCGMF AEP Mapping

The benefits of improved mapping are dependent on many factors and difficult to quantify, but it is likely that such maps will reveal variations of energy density on scales and with accuracy suitable for wind farm siting. Assuming these variations exist, as the

research cited herein strongly suggests they do, this mapping should assure that the first wind farms in the study area are sited in areas with higher energy than if sited using the baseline methodology. In a metaphorical-statistical sense, it moves the archer a few feet closer to the target, increasing the odds of a bulls-eye. Based on the estimated accuracy of 2% for AEP maps, and the high likelihood of sub-regional variability of this magnitude, a reasonable assumption would be that a wind farm sited with such a map could produce between 2% and 3% more energy per year than it would at a site selected with the baseline methodology.

However, these benefits would only apply to the first wave of projects. After that, available area is significantly reduced and site selection is less critical. Under a full build-out scenario, in constant dollar terms, the net benefit would be closer to zero because the last projects would occupy the lowest energy areas. However, if the time value of money is taken into consideration, developing the best sites earlier will increase the Net Present Value (NPV), since the “disbenefits” of developing the low energy sites in the out-years are discounted heavily.

Two other factors that can affect the NPV of the mapping effort are technology development and power pricing structures. At higher energy sites, the turbines are operating at capacity (Region 3) more often, while at lower energy sites, the turbines are operating below capacity (Region 2) more often. Current design efforts intended to increase energy production are therefore primarily focused on Region 2. The benefits of

these improvements will accrue primarily to sites that are developed in the latter stages, where new technologies will squeeze out more power from less wind. This effect partially mitigates the inferior energy density of the sites, and increases the NPV of the mapping effort.

Power pricing structures can also affect the NPV of mapping benefits, since they affect the time stream of revenue. Various arrangements are available; for example, a Power Purchase Agreement (PPA) may be used, which can be any number of fixed or changing pricing structures, or the power may be sold on the PJM market at various clearing cycles (i.e., day ahead, hour ahead), with variable unit prices.

Each of these highly uncertain factors can have a significant effect on the benefits, which are therefore highly uncertain. A thorough NPV analysis would include a range of build-out scenarios, technology development curves, pricing structures, and a financial analysis, but is beyond the scope of this study. A simpler methodology may be employed for this first order analysis, as outlined below.

5.4.1. Cost Reduction vs. Benefit Increase

An alternate method of evaluating the effects of improved mapping is to estimate the accuracy it would provide across the study area, then estimate the cost of achieving the same accuracy with conventional technology. This puts the focus on the cost of

achieving an equivalent output, instead of the benefit of using a different input, and this is the approach taken.

5.4.2. Reference Station Proximity Effect

Due to the nature of calibration, error of the maps will increase with distance from the calibration station. This effect was observed by the NorseWind project when calibrating to existing offshore platform observations. It is assumed that this proximity effect is the same for the baseline methodology (met towers) and for the LCGMF maps (Lidar stations). This is a conservative assumption because the Lidars are assumed to be fixed, when in fact they can be re-deployed periodically to reduce uncertainty from horizontal extrapolation between stations.

5.4.3. Conclusions – Site Selection/Improved Mapping Benefits

The LCGMF regional mapping strategy makes 3 fundamental changes from the baseline regional modeling/mapping strategy;

- It replaces (avoids) met towers using floating Lidars;
- It replaces numerical models, calibrated using hub height anemometer measurements, with satellite data, calibrated using Lidar profiles to 200 m;

- It improves the basis for climatology indexing – replacing unevenly distributed NDBC met stations of the study area (only three of which have records exceeding 10 years), with SMRR datasets, whose record exceeds 20 years for the entire study area.

Taken together with the previous conclusions regarding floating Lidar and met tower accuracy, these findings and assumptions lead to the following conclusion; In order to meet the target average AEP mapping accuracy across the study area (achieved by the LCGMF strategy), the base case must, at a minimum, include a met tower for model calibration at every location where a Lidar is deployed for calibration of SMRR data.

Since it was estimated that ten Lidar buoys could provide the required coverage, the mapping benefits can thus be formulated as the cost savings between ten met towers and ten floating Lidar met buoys. Current market prices of floating Lidar units are in the range of about \$1.5 million, and deployment and O&M for a two year campaign would add about 10 % of the purchase cost per year⁴⁹, for a total of about \$1.8 M per unit. A fully equipped 90 m met tower installed in 45 m of water (roughly the average water depth of the study area) would cost around \$15 million⁵⁰. Since ten met stations would be required to provide the required accuracy in the study area, this first-order analysis indicates a base case cost of at least \$150 million, versus a Lidar buoy cost of \$18 million. Project Norse Wind cost approximately \$6 million, but this included the purchase of several fixed platform Lidars. Even so, this is increased to \$10 million to

⁴⁹ Based on estimated WindSentinel costs

⁵⁰ This is based on the highest cost of existing offshore met towers, in shallower waters

account for the extra size and complexity of the proposed mapping strategy. Thus, the LCGMF Atlas would cost no more than \$28M, for a savings of \$122M versus the base case.

5.4.4. Coordinated Vs. Individual RA Efforts

With the proposed strategy, it is envisioned that after selection of a site using the LCGMF- generated Atlas, developers would deploy floating Lidar units at their site, in order to produce “bankable” AEP estimates with higher P90 values, as described in Chapter 6.

If, on the other hand, the proposed strategy is not adopted and there is no coordinated, regional, strategic planning, developers may opt to construct their own met towers for each project, maintaining separate, proprietary databases. Although the met towers would remain well beyond two years, continuing to collect data for research, their value to the wind farm operator is primarily in pre-finance RA. After that, much of the investment is considered a stranded cost. This scenario would likely result in more met towers being built than necessary, since there would be no strategy for sharing data.

Chapter 6

AEP P90 BENEFITS

6.1. Financing and Uncertainty

Wind farm financing in the U.S. comes primarily from commercial banks and private equity, and the finance cost is largely a risk premium (Levitt et al 2012). Projects that have a low perceived risk can obtain cheaper financing, and can thus borrow a larger portion of the project cost. Projects with high perceived risk, such as offshore wind development, will have higher borrowing costs, but likely lower leverage. In either case, the risk premium is a significant portion of project finance cost. The most commonly used indicator for projecting revenue risk in financial analyses is the P90 AEP - the Annual Energy Production of the project that has a 90% probability of being exceeded in any year. There are no formal standards for the calculation of AEP, but recommended

practices and procedures have been published by several organizations, including Det Norske Veritas⁵¹ (DNV 2010).

The mean expected value, P50, is also useful, but P90 (or in some cases, P99) represents greater certainty to investors, and is normally used as the basis for “bankable” projected revenue. In this context, finance costs can be reduced as much by greater certainty in the AEP as by a higher projected AEP, since they both increase the P90 value. This is simply a generalized statistical model of “*a bird in the hand is worth two in the bush*”. It is illustrated by the PDF function in Figure 55.

6.1.1. Boquet et al 2010

In this study from Leosphere (WindCube manufacturer) and NRG Systems (Resource Assessment and Renewable Energy consultant), uncertainty of AEP estimates were evaluated for a small (50 MW) wind farm using one year of data from a 60 m mast alone versus using one year of the mast plus a moveable Lidar. The study found that by removing uncertainty from hub height extrapolation and from horizontal extrapolation from the met tower to the turbine site, the Lidar data produced a ~3% decrease in uncertainty of the P50 and a 4.5% increase in the P90 AEP value. Figure 55 illustrates this effect. The blue curve represents the stand alone mast estimate, with 15%

⁵¹ DNV, the international standards and certification organization, is one of the top two, with the greatest offshore wind experience worldwide

uncertainty, and the red curve represents the 12% uncertainty with the addition of Lidar data. This case reveals for each percent lower uncertainty, P90 increases by 1.5%.

Although this can be taken as a rule of thumb, the exact ratio is dependent on the shape of the PDF (or Rayleigh parameters), which is site specific.

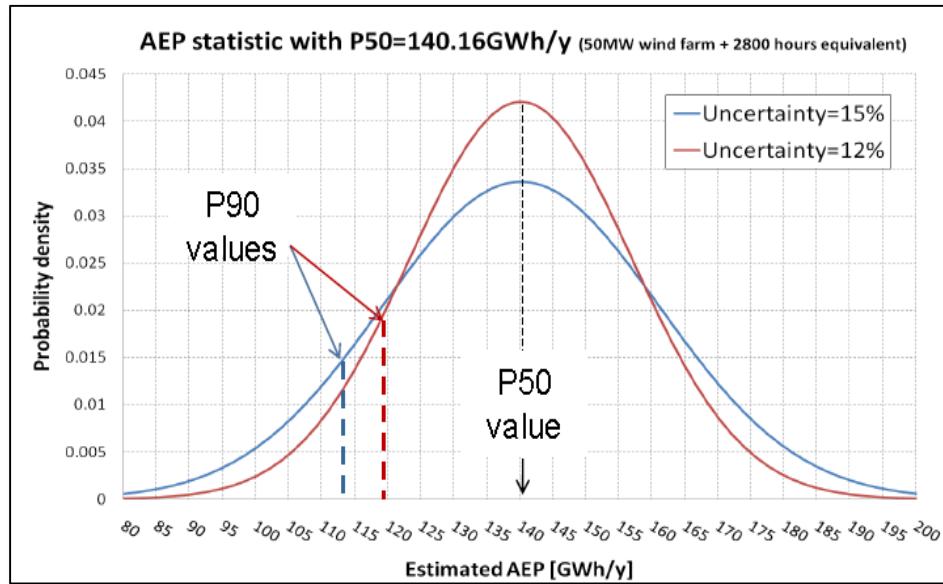


Figure 55- Effect of Uncertainty on P90 AEP using PDF Curve, from Boquet et al 2010

6.1.2. DNV Uncertainty Model

DNVKEMA is a subsidiary of Det Norske Veritas specializing in renewable energy in the US market. They have developed and demonstrated a model for estimating the value of different RA techniques (Rogers 2011, 2012). The model uses a risk premium to put

a cost on the uncertainty inherent in different RA strategies. Three cases were assessed, using different combinations of platform Lidar, floating Lidar, and a met tower. In each case, equipment was deployed on a timeline designed to minimize unnecessary costs as the potential of the project was being evaluated. Equipment costs were levelized over the useful life. Met tower construction was modeled at different points in time and costs were amortized over different periods in the three case studies. The model uses uncertainty estimates to compute both P50 (median estimate) and P99 Net Capacity Factors (NCF).

The first case study looked at a hypothetical build out of the Virginia Wind Energy Area using a high technology resource assessment- with one Lidar on the Chesapeake Light (CHLV2) tower and one floating Lidar. The second and third case studies looked at a hypothetical offshore wind farm in deeper waters with a higher CF. One scenario added a fixed Lidar in Year 2 and a floating Lidar in Year 4. The other added a platform Lidar in Year 2 and a tower in Year 4. The resulting change in P99 NCF of the project are shown in Table 23. The Year 0 case in the DNV model is different than that defined for this paper, so the change between Year 0 and Year 1 is not relevant to the present analysis. However, general trends in uncertainty between Year 2 and Year 5, as Lidar is added, are indicative of a consistent increase in the P99 NCF each year, in all three cases, as more information about the resource is collected. The analysis by DNV reached several conclusions regarding the use of floating Lidar vs. met towers for resource assessment, summarized below (Rogers 2012);

- Each project is unique
- Representative, long term measurements are essential but can be supplemented with short term data
- A combination of technologies/approaches may offer the best results (lowest uncertainty) at lowest costs
- Minimum requirements are clear, but measurement campaigns must be designed for individual projects with full consideration of objectives, risk tolerances, and impacts on uncertainty

Although this results in a wide range of benefits, depending on the project, a general rule-of-thumb observation can be made from the data in Table 23, which allows a first-order estimate of the benefits. Each Lidar-year of deployment adds about a point to the P99 NCF, increasing it by 1% of rated capacity, e.g., from 25% to 26%. These three case studies highlight the ability of Lidar to reduce project finance costs by reducing the risk premium.

Table 23 - DNV Model Results – Three Case Studies

		Uncertainty Source					P99 net CF
		point wind speed	area wind speed	annual wind speed	other	combined	
Case Study No. 1							
YR 1	baseline	8	4	3	2	9.6	27
2	Lidar on platform	4	4	3	2	6.7	32
3	Lidar yr2	3.5	4	2.8	2	6.3	33
4	add Floating	3	3	2.3	2	5.2	35
5	Floating yr2	3	3	2	2	5.1	35
6	add tower	2.5	2	1.8	2	4.2	37
Case Study No. 2							
YR 1	baseline	8	4	3	2	9.6	21
2	Lidar on platform	5	4	3	2	7.3	24
3	Lidar Yr2	4.5	4	3	2	7	25
4	add tower	3.5	3	2.5	2	5.6	27
5	Tower Yr2	3	2.2	2	2	4.7	28
6	Tower Yr3	3	2.5	1.8	2	4.7	28
Case Study No. 3							
YR 1	baseline VA WEA	8	4	3	2	9.6	21
2	Lidar on platform	4	4	3	2	6.7	25
3	Lidar Yr2	3.5	4	2.8	2	6.3	26
4	add 2 floaters	3	2.5	2.3	2	5	28
5	floaters Yr2	2.8	2	2	2	4.5	28
6	add tower	2.5	2	1.8	2	4.2	29

6.1.3. Ecofys 2013

Ecofys is a Dutch renewable energy systems consulting firm that has been advising the wind industry in Europe for over 25 years, and using wind Lidar for the last 5 years or so. This study examined different resource assessment strategies for a flat coastal onshore site and found AEP uncertainty of 17% using climatology models, 14% using a 60m met mast only, versus 12% using a fixed Lidar (WindCube v2) and 10.8% using the WindCube, re-deployed around the site periodically. The P90 value went from 82%, to 85%, to 86%, respectively.

6.1.4. Betancur et al 2008

A paper presented at the WindExpo 2008, organized in Guadalajara by the Latin American Wind Energy Association, looked at AEP estimates using data up to 170m from a WindCube Lidar compared to a 60m anemometer with a WASP model extrapolation to 170m (Betancur et al, 2008). The field trial ran from April 2008 to June 2008. After scrubbing for wake-affected sectors, the two data sets were used to estimate energy production for an onshore 2 MW Enercon turbine in a coastal region (Zeebrugge harbor, NL). The study calculated that uncertainty of the energy production was reduced by 3% by replacing the WASP extrapolation with Lidar data.

6.2. AEP P90 – Benefit Calculations

These four papers provide a total of six different case studies of valuing higher confidence in AEP estimates. Surprisingly, each of them produced roughly similar results, even though the study scenarios, inputs, and outputs varied significantly. Boquet et al compared a 60m mast alone to a 60m tower plus a floating Lidar, and uses P90 as the metric. The DNVKEMA model tracks changes in uncertainty over a five year RA campaign as more wind data is collected with Lidar and met towers. It begins with a baseline of existing information only, and uses P99 for the risk premium metric. Betancur compared a 60m mast, extrapolated using WASP, to data from a WindCube Lidar, and estimated uncertainty of the P50 values for the two methods. The Ecofys study presented the scenario that was closest to the base case and conditions of the present study, and indicates that a solitary Lidar produces 2% greater certainty than a solitary 60m met mast, and if the Lidar is moveable, the first-year advantage goes up to 3%. The base case for the present analysis is a 90m met tower, which is higher than the base case in two of the studies, so the relative benefits may be lower. Higher met towers reduce AEP uncertainty compared to lower met towers, but even if they reach hub height, assumptions about the wind profile above that are still required.

For all the studies reviewed, the range of values found for the increased AEP $P(x)$ probability levels using one year of Lidar varies from 1% to 4.5%, with an increase of about 1% per year after that. The large variance is due to different base cases, PDFs/site

climatologies, deployment strategies, and probability levels $P(x)$, making it difficult to compare directly across studies without a comprehensive uncertainty and correlation analysis, which is beyond the scope of this paper.

In light of this, a conservative value of 2% with one year of data plus 1% in the second year, with no further benefits, is selected as being representative of the decrease in uncertainty from the use of floating Lidar compared to the baseline RA methodology of a hub height met mast. Boquet et al (2010) found that for each 1% lower uncertainty, P90 increases by 1.5%, but because this factor is site-specific, a conservative ratio of 1:1 is assumed for the study area. Thus, the addition of Lidar is estimated to decrease uncertainty by 3% and increase AEP P90 by 3% with two years of data.

6.2.1. Relating Risk, Finance Cost, and AEP

Levitt et al (2012) conducted a literature survey of offshore wind farm construction and financing costs, and also developed a sensitivity model which showed the Breakeven Price (BP) of wholesale electricity as a function of capital expenditures, operating expenditures, the discount rate, and the estimated capacity factor for a reference turbine. The analysis assumed existing policy incentives of the Production Tax Credit and accelerated depreciation but not renewable energy credits, investment tax credits, or any grants or loan guarantees. The study found that the BP was nearly as sensitive to the cost of capital (as defined by discount rate) as it is to the capital costs (CAPEX), as shown in

Figure 56. The graph shows this as the slopes of the solid and dotted lines being very similar. In other words, to reduce the BP, getting a 1% lower finance rate is almost as effective as cutting capital expenditures by 1%, within the likely ranges of each. As would be expected for a flow-rate commodity such as power, the study also found that (ceteris paribus), a 10% increase in the capacity factor (or AEP) would result in a ~10% reduction in the BP of wholesale electricity. Thus a 3% decrease in uncertainty is equivalent to 3% increase in AEP, which is equivalent to a 3% drop in the BP.

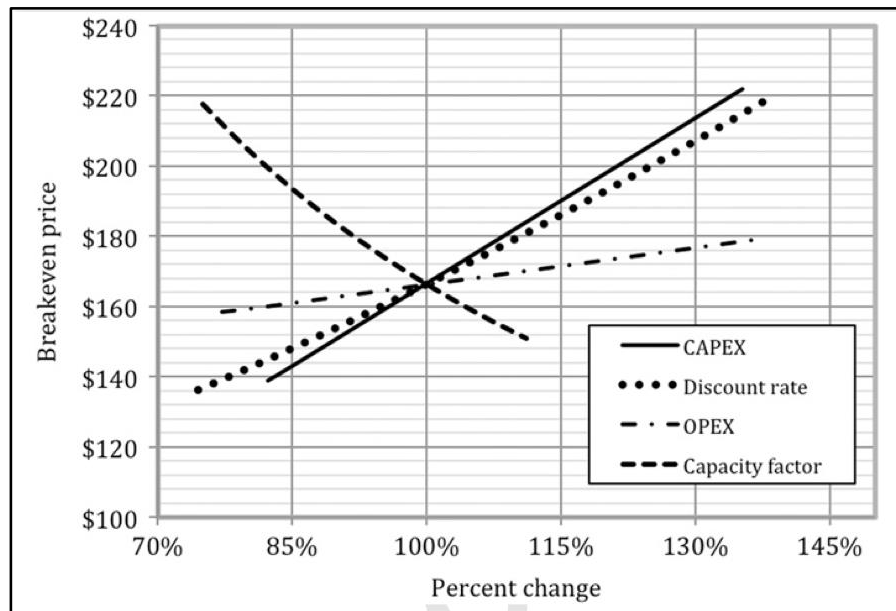


Figure 56- Sensitivity of BP to Four Cost and Production Factors, from Levitt 2012

Chapter 7

ROTOR CONTROL BENEFITS

7.1. Background - Rotor Control Systems

Control systems include three basic elements: sensors used to measure process variables, actuators used to manipulate aerodynamics and loading, and algorithms to coordinate the two. For this analysis, “turbine control systems” are defined as rotor control - active yaw, pitch, and generator torque controls only, and do not include supervisory control (power conditioning, safety systems, fault monitoring, etc.). A turbine control algorithm should have three primary objectives;

1. limiting speed, torque, and power,
2. maximizing power output and
3. minimizing fatigue and stress on components.

Rotor speed, shaft torque, and power output must be kept within design constraints to avoid overloading, while at the same time, the yaw, pitch, and torque must also be optimized for power production. Fatigue damage results from long term cyclical loading of components, and affects component residual strength and life, so should be minimized.

7.1.1. Fatigue Life and Damage Equivalent Loading

Fatigue is the cumulative, localized loading that occurs when a component is subject to repeated cyclical forces that are well below the ultimate strength or yield strength of the material. These loads are caused by yaw errors, turbulence, wind shear, wind upflow, shaft tilt, and the reversing blade root moment from blade weight as the rotor spins (Berg et al 2007, Schubel et al 2012). Turbine components undergo “high cycle” fatigue (defined as between around 10^3 and 10^8 cycles), which can be modeled by stress-based parameters, since it occurs in the elastic deformation region. The relationship between fatigue loading and failure is illustrated by a Wohler curve, which is empirically derived by cyclical, high speed loading of multiple samples to failure. Also called an S-N curve, it is a log-normal graph that describes the number of load cycles that would (on average) produce failure for any given load amplitude. Although wind turbine fatigue loading is a combination of deterministic and stochastic loads, the curve is useful for estimating fatigue life. Another useful quantity for estimating fatigue life is Damage Equivalent Loading (DEL). A threshold value of loading is defined where significant fatigue would occur after a reference number of cycles, N , at this reference load. Any load above this

threshold is considered a DEL. It is a first order indicator of fatigue accumulation estimated by rainflow counting⁵². Since the S-N curve shows that fatigue life is proportional to DEL, any reduction in DEL would produce an increase in fatigue life, or alternately, would allow fatigue resistance (strength) requirements to be relaxed.

7.1.2. Control Strategies and Regions

The control strategy, which is basically the dynamic ranking of the three primary objectives, must change depending on the turbines operational status, or “Region” (see Figure 58- Turbine Operating Regions). In Region 1 (below cut-in wind speed) control is generally inactive, in Region 2 (cut-in speed to rated speed) power output is maximized, while in Region 3 (rated speed to cut-out speed), the primary objective is constant power output. Region 4 is above cut out wind speed, where the blades are feathered, the pitch is locked, and only the yaw is active (survival mode). Transitional control zones are also established at the boundaries between Regions, where linear interpolation of the control signal is implemented to prevent sudden load changes (e.g., when shutting down in high wind). It is also useful to define the *effective rotor wind speed*, U_{eff} , as the uniform wind speed across the rotor disk that would produce the same shaft power output observed for a given turbine. This is the assumption used in power curves. Though it is an

⁵² Rainflow counting is a method of expressing fatigue accumulation through a series of different magnitude cyclic stresses as a single magnitude cyclic stress which would produce the same fatigue accumulation

approximation of the non-uniform wind field, it greatly simplifies control system analysis. For estimating AEP, all Regions must be considered, but only Regions 2 and 3 are relevant to the use of Lidar for controlling component loading during power production, as shown in Figure 57. Figure 59 shows an example schematic of how a Lidar assisted feed forward control system would work, in this case for pitch control.

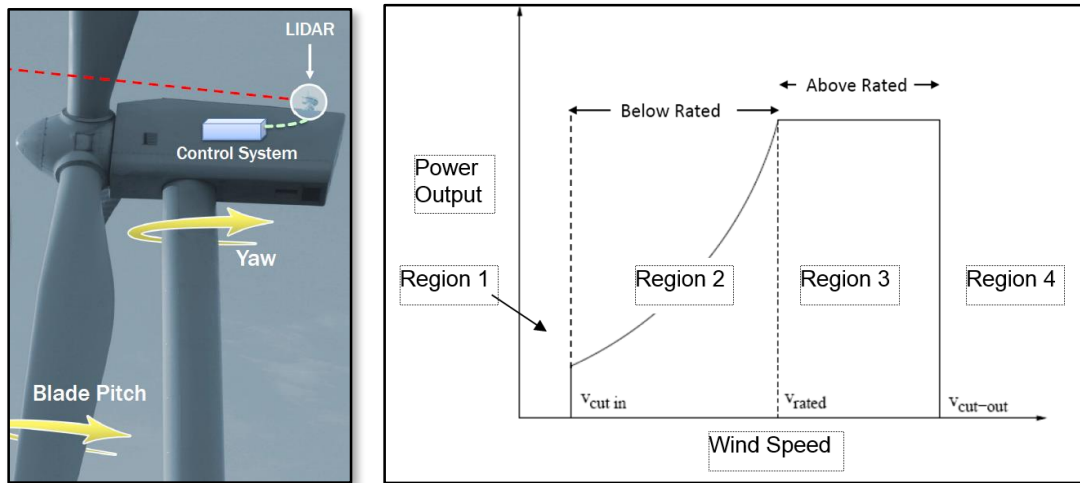


Figure 57-Lidar Assisted Rotor Control, from Dunne et al 2011

Figure 58- Turbine Operating Regions

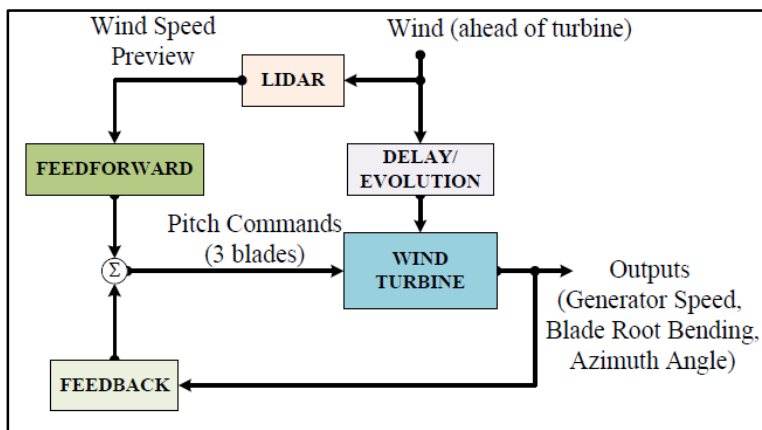


Figure 59- Feed-Forward Controller Schematic, from Dunne et al 2011

7.2. Yaw Control – (Regions 2, 3, and 4) Current Practice

The objective of yaw control is to minimize misalignment with the effective rotor wind direction⁵³, for all wind speeds above cut-in. The turbine should be pointed upwind as nearly as practical to maximize power production and reduce asymmetric fatigue loading of the entire structure. To estimate wind direction, commercial wind turbines currently rely on vanes and ultrasonic anemometers mounted on the nacelle top. These sensors measure wind behind the rotor, and must be time-averaged and calibrated for direction bias caused by the wake of the spinning rotor (Burton et al 2001). Error can exceed 20 degrees, and the calibration is extremely problematic (Gaiser et al 2012, Hopkins 2012). Yaw actuators are almost always electric motors, (though hydraulic systems are available), and they typically operate at speeds around one degree per second. The limiting factor in yaw speed is the stresses produced on gears, bearings, and structural components due to the large moments of inertia of the nacelle and rotor (Hau 2008). Increasing this speed would require larger, more powerful servo motors and major changes to other components, incurring significant extra costs.

⁵³ Effective rotor wind direction is analogous to effective rotor wind speed, defined previously.

Turbine manufacturers have developed yaw control strategies that attempt to balance power optimization and yaw component fatigue by using long averaging times and a high tolerance for yaw error. Commercial turbines initiate yawing when the moving average exceeds a specified threshold. The “stop” signal is sent when the moving average of the direction error is zero degrees. Both the moving average time and the yaw error threshold are parameters that may be adjusted in the algorithm, but typical values are 10 min moving average and 10 degrees error.

7.3. Yaw Control – Lidar Simulation Studies

Lidar mounted on the nacelle or in the rotor can provide “feed-forward” data, so the relatively slow yaw motors are no longer playing catch-up with the moving average, but are more closely synchronized. This is a lower cost strategy than faster mechanical response, since it is focused on reducing latency in the control system with better information, not overcoming inertia in the machine with larger components. Controllers can be adapted to process incoming Lidar data in real time and optimize orientation of the rotor (steer).

The use of Lidar also significantly reduces error in the wind direction measurements, since it is measuring the upstream-free stream wind, not the downstream rotor and nacelle wake. Additional benefit may be gained by optimizing the yaw control algorithms to

make the best use of the Lidar input. Although no validation studies have yet been published using operational turbines with active Lidar yaw controls, several simulation studies have been conducted to estimate the potential benefits, and these are discussed below.

7.3.1. Yaw Control Study Y1 –Schlipf 2012

In a recent study funded by the EU under Project UpWind and led by the University of Stuttgart's Wind Energy Center (SWE), a numerical modeling environment was created to simulate the effects of Lidar assisted turbine controls and new control algorithms (Schlipf 2012). A full turbulent wind field model, an aeroelastic wind turbine model and a wind Lidar model were combined to simulate the use of nacelle mounted Lidar vs. an “undisturbed⁵⁴” idealized nacelle mounted ultrasonic anemometer for turbine control. The simulation environment was created using a full non-linear turbine model provided by the Fatigue, Aerodynamics, Structures, and Turbulence (FAST) software code developed by NREL (Jonkman et al 2005). The NREL TurbSim model (Kelley et al 2007), a stochastic full-field inflow simulator, was used in combination with 5 months of actual nacelle-mounted, forward looking Lidar data, and used to provide realistic wind fields for the turbine simulations. The reference NREL 5MW offshore turbine was used (Jonkman et al 2009) along with GH Bladed⁵⁵ for the blade aeroelastic modeling.

⁵⁴ In reality, the ultrasonic data would be severely corrupted by blade wake

⁵⁵ Information and download available at <http://www.gl-garradhasan.com/en/GHBladed.php>

To generate a realistic wind energy spectrum, the Lidar data were analyzed and filtered for trajectory, turbine status, and Lidar data quality. Only data sets of 4 continuous hours or longer, during normal turbine operation were included in the analysis. After filtering the data, 223 hours of valid data remained. The yaw control strategy was typical of operating turbines, activating when the 10 minute moving average of error exceeds 10 degrees. The study first modeled the effects of simply switching the wind direction input signal from the ultrasonic on the nacelle to the Lidar at a focal distance of 116 m, scanning an 87 x 87 m grid with 49 focal points. Using the reference 5 MW turbine as the baseline, the standard deviation of yaw error was reduced from 6.4 degrees (using ultrasonic) to 4.1 degrees by using input signal from the Lidar, at a range of 116m, versus input from an “assumed perfect” nacelle-mounted wind vane and ultrasonic anemometer. Since the nacelle sensor was assumed perfect, only the benefits that came from the feed-forward aspect of the simulation were able to be evaluated.

The study concluded that this strategy would result in a 1.1% increase in AEP, based on the modeled wind regime and using standard control algorithm parameter settings (ten minute moving averages and a ten degree activation threshold). The author also estimated that the increase would exceed 2% if control algorithms were optimized for Lidar input (Schlipf et al 2011b).

7.3.2. Yaw Control Study Y2- Blue Scout (Gaiser et al 2013)

This study, conducted by BlueScout Technologies (Gaiser et al 2013) took the UPWIND study a step further and estimated the increased power output from optimizing the yaw control algorithm using their Optical Control System (OCS- “look-ahead” Lidar).

Both the OCS Lidar and traditional anemometers were mounted on the nacelle of a GE 1.5 MW turbine, and both sensors recorded wind speed and direction, but the yaw control algorithm only used input from the traditional sensors in a standard configuration (10 minute moving average, 10 degree yaw error threshold). The data were fed into a simulation, where relative power production (pct. of capacity) over the period of analysis was estimated for a range of values for moving average times and yaw error threshold for activation. For a yaw misalignment of α , the relative power production was assumed proportional to $\cos^3 \alpha$, since the wind vector component orthogonal to the rotor disc plane decreases by $\cos \alpha$, and power is proportional to the cube of wind speed. The \cos^3 of the convected wind direction error was therefore the metric for performance in this simulation study. The misalignment was assumed to follow a Gaussian distribution with zero mean (no bias) and a standard deviation $\sigma(\alpha_H)$ per the method of Burton et al (2001).

The static power loss was thus expressed as:

$$P_{el}(\bar{\alpha}_H) = P_{el,max} \cos^3(\bar{\alpha}_H). \quad (3)$$

This study provides a valid and valuable first order estimate of the magnitude of potential benefits from optimizing the yaw control algorithm. The author summarized the study results:

For unlimited yaw activity, a power increase of about 6% is demonstrated. If yaw activity is limited to 8%, it was found that an additional 3% power gain may be achieved with settings for the site/turbine installation evaluated in the study at a moving average time for the wind direction of 60 seconds and a yaw direction threshold of 8 degrees.

7.3.3. Yaw Control - Fatigue Loading

Yaw related fatigue comes from two source; misalignment, and yaw motor activity. Yaw misalignment causes asymmetric loading on the blades and rotor, increasing fatigue in all major structural components. Increased yaw activity reduces misalignment, but wears out yaw motors and bearings faster and thus requires larger, heavier components. An optimum averaging time exists somewhere between 10 minutes and one minute. The UPWIND study (Schlipf et al 2012a) concluded that a moving average of 6 minutes for the wind speed input signal would provide near optimal yaw control for a Lidar based system, with no significant change in overall fatigue loading compared to the baseline. The shorter moving average produced more activation cycles, but also resulted in smaller movements. Yaw control improvements using Lidar is therefore not expected to have a significant net effect on fatigue.

7.3.4. Yaw Control Simulation Studies, Summary

Table 24 summarizes the results of the Lidar- assisted yaw simulation studies examined. Because unlimited yaw activation would require the re-design of major components, Lidar case 4 (BlueScout) can be discarded as a data point. The remaining three Lidar simulation studies showed relative AEP improvements ranging from 1.1% to 3%, with yaw activity ranging from 5% up to 8% for a shorter moving average and lower error threshold.

Table 24- Summary of Yaw Control Simulation Studies

Sensor	Moving Average (min)	Yaw Error Threshold (deg.)	Yaw Activation Time	Relative AEP Gain
Base Case Yaw Control	10	10	5%	0
Lidar (UPWIND) case 1	10	10		1.1%
case 2	6	10		2%
Lidar (BlueScout) case 3	1	8	8%	3%
case 4 (*)	1	0	12%	6%
(*) – assumes no constraints on yaw activity.				

7.3.5. Lidar Assisted Yaw Control - Future Field Studies

Direct comparison of power production using two different yaw control systems is difficult in the field, since controlled experiments are impossible on operating MW scale

turbines. Spatial variability in the wind and power performance variability between turbines complicates the analysis and prevents direct A/B comparison of control systems.

A suitable alternative is to examine the performance of a single turbine with the new system engaged vs. bypassed to a traditional controller that uses nacelle mounted vanes or ultrasonics. The turbine controls could be switched between the two systems (with appropriate transition algorithms) periodically, for a suitable time series, long enough to include a representative sample of wind speeds. The variability between turbines is thus removed from the equation, and the variability of the wind is mostly averaged out by wind classing. The data can be separated into bins by wind speed, sector, veer, or turbulence intensity, and analyzed a number of different ways, allowing a thorough, well calibrated comparison of the two systems and their effect on output. The test can be run on multiple turbines, providing a clearer picture of variability and uncertainty.

As part of their research and development, BlueScout began collecting data to support a similar analysis for Lidar assisted yaw control. In July 2009, the first integrated OCS was installed on a utility scale wind turbine operating onshore, in the U.S. midwest. Other deployments occurred in 2011 and 2012. The experience generated a wealth of operational data and knowledge in controlling the yaw of large wind turbines, but in 2012, legal issues

between the project partners related to bankruptcy and corporate restructuring put further analysis or release of the data on hold until 2014 at the earliest⁵⁶.

7.4. Speed Control (Regions 2 and 3) – Current Practice

Rotor shaft speed must be controlled to optimize power output and to limit loading. Shaft speed is determined by active torque from the blades on one end and reactive torque from the generator on the other end, so it can be controlled by blade pitch or generator load.

Control algorithms also enact strategies that keep rotor speed away from resonant frequencies of the structure, but that is a second order consideration not relevant to this study. Figure 60 illustrates the idealized steady state relationship between torque and blade pitch in Regions 2 and 3.

⁵⁶ Personal communication w/ Brad Gaiser, BlueScout, Feb. 4, 2013

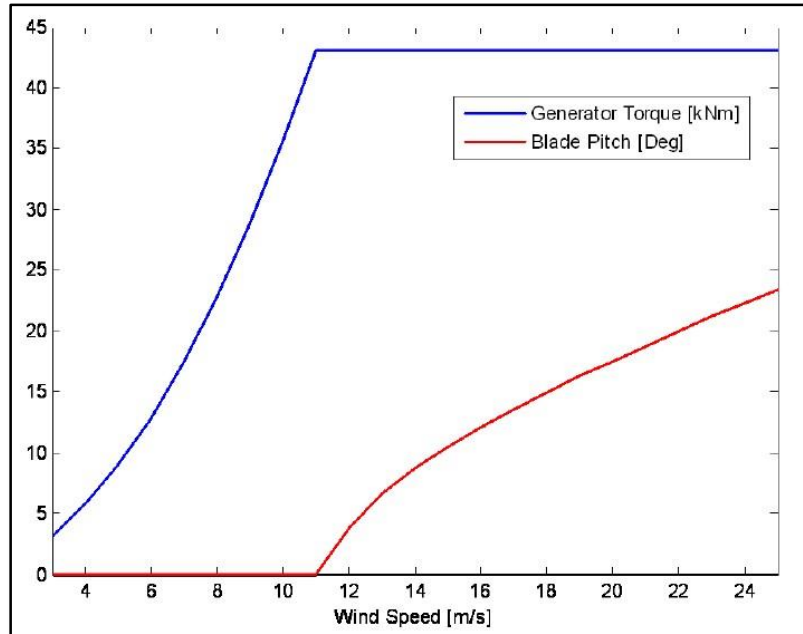


Figure 60- Idealized Torque and Pitch in Regions 2 and 3, from UPWIND 2011a

7.4.1. Region 2 - Torque Control

In Region 2, the objective is to maximize power output, defined by the power coefficient, C_P , which is the ratio between power production and available power, and is a measure of the rotor's aerodynamic efficiency. The laws of fluid mechanics predict, and empirical evidence shows, that for every rotor there is an optimal Tip Speed Ratio (TSR, or λ ; ratio of blade tip speed to wind speed) which maximizes C_P (Manwell et al 2009). In Region 2, standard control systems achieve the optimum TSR by holding the blade pitch constant while the generator torque is set proportional to the square of the filtered generator speed. Double fed induction generators allow the generator torque to be controlled using the induction current, which can be keyed to the rotor speed. This is known as a Single-Input,

Single-Output (SISO) controller. As the wind increases, the speed increases, and the generator torque is increased in response. This ensures the rotor speed stays within a narrow range centered on the optimal TSR. Response time is reasonably short since the control signal is based on instantaneous power output and no servo-motors or time-averaging algorithms are needed. Only the rotor inertia introduces significant lag in the feedback loop. The baseline pitch controller uses this strategy for Region 2 wind speeds. The expressions for C_P and TSR are included in Figure 61 which shows a typical graph of the relationship between the two dimensionless parameters in Region 2 (P = turbine power out, ρ = air density, A = swept rotor area, U =rotor effective wind speed, Ω = angular velocity, λ = Tip Speed Ratio, R =rotor radius).

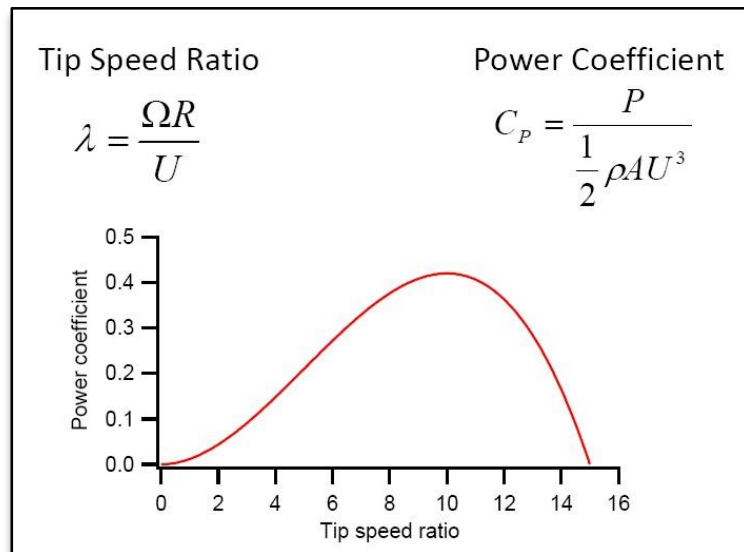


Figure 61- Tip Speed Ratio versus Power Coefficient, from Lackner 2009.

7.4.2. Region 3 - Pitch Control

In Region 3, the objective is to maintain near constant power generation at the turbines rated capacity. This is done by keeping generator torque constant and adjusting blade pitch to control rotor speed. Because there is excess wind in Region 3, this effectively spills wind while maintaining rated output. Pitch control is more difficult to model than yaw control, since its effect on power production is not proportional to some easily modeled or measured parameter such as yaw steering error. Given the complexity of the interacting control feedback loops, including non-linear tower dynamics and stochastic, turbulent wind fields, instability must be actively mitigated in simulations. All pitch control algorithms therefore include filters to damp undesirable resonant frequencies (Soltani et al 2011). The control algorithm is usually based on a conventional SISO gain-scheduled Proportional-Integral (PI) function that takes into account present error (deviation of the signal from optimal) and past accumulated error. Pitch control is updated near continuously, although pitch actuators are limited to eight to ten degrees per second to limit dynamic stress on the blade and servo mechanism.

Because they have a simple structure and can be easily adjusted to improve stability, PI controllers are widely used in industry. However, their performance is sub-optimal during high shear or rapid changes in wind speed (gusts) (Soltani et al 2011). This is because the use of filters and simplified wind fields results in a loss of information and resolution. This control scheme also has delay issues. In standard systems, pitch angle is

based on the rotor speed itself. After the wind changes, the rotor inertia must be overcome, then after the rotor speed changes, the controller reacts by activating pitch servo motors, which then change the pitch. This introduces additional latency in Region 3 since it involves rotor inertia and servo motors in the control loop.

7.5. Speed Control With Lidar

The use of nacelle or rotor mounted Lidar for rotor speed control could improve power output and reduce fatigue loads, since speed is better optimized when controls are proactive instead of reactive. To illustrate, a simple model of a feed forward pitch control system can be constructed by taking traditional nacelle mounted anemometer data and time shifting the windspeed input signal so that the pitch control algorithm is fed data based on conditions just upwind of the rotor, not behind it. The optimum steady state pitch angle (θ_{SS}) is shifted forward in time by some optimum value, τ , as expressed below, where $v_o(t)$ is the rotor effective wind speed at time (t) and (θ_{FF}) is the feed forward pitch angle used in the revised algorithm. This can be represented as:

$$\theta_{FF}(t) = \theta_{SS}(v_o(t - \tau)) \quad (4)$$

The pitch actuator now applies controls to synchronize more closely with fluctuations at the rotor disk. The assumption is made that the 3D wind vector field is translated in space and time from the Lidar probe distance to the rotor disk at the average wind speed, without

change⁵⁷. This simple time-shift modification is simple to model, and has the advantage of not affecting the stability of the control feedback loop.

7.5.1. Speed Control - Optimal Look Ahead Time and Range

The optimal time or distance is greater for pitch control than torque control, since the pitch control feedback loop includes latency from pitch servo motors, and the torque feedback loop does not. The optimal preview time is determined by the lag time in system response, which is determined by three processes – actuator mechanics/dynamics, algorithm delay (primarily low pass filter processing), and turbine response characteristics. However, the available preview time is a function of wind speed and Lidar range - the higher the wind speed, the longer the required sensor range to achieve optimal τ .

A simulation study by NREL and other researchers found that using two Lidar range settings, 70 m for low wind speeds and 120 m for high wind speeds, preview time ranged from 5 to 6 seconds, which was easily greater than the optimal times required, as shown in Figure 62 (Dunne et al 2011). Using the simulated controller, setting τ between ~ 2 and 3 seconds provided near optimal preview time to reduce pitch error. In another NREL sponsored study, the accuracy of CW Lidar at various ranges was examined for

⁵⁷ This is known as Taylor's Frozen Turbulence Hypothesis, from (Taylor 1938)

different cone angles. At a $\frac{3}{4}$ rotor diameter scan radius, typical optimal preview distances for a variety of wind conditions were between 110 and 150 meters (Simley et al 2011). More advanced control systems can use non-linear predictive strategies where τ may vary depending on additional sensor inputs and feedback loops.

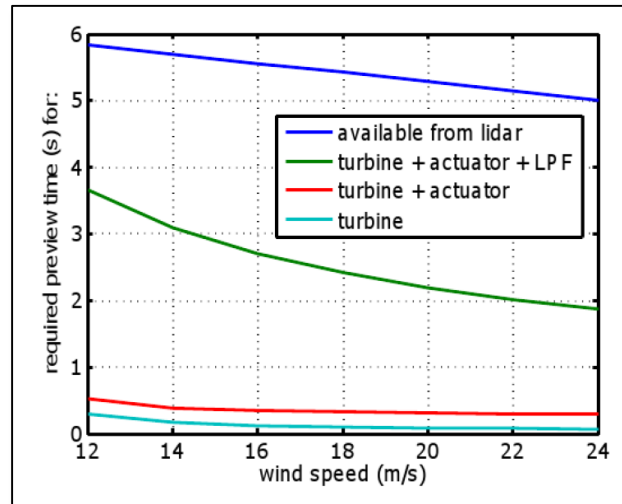


Figure 62-Optimal Look-Ahead Times for Pitch Control, from Dunne et al 2011, an NREL report for the U.S. Dept of Energy.

Dunne et al (2011) examined two different Lidar-assisted individual pitch controllers. Controller A simulated a CW Lidar and Controller B simulated a PL Lidar. The study summarizes the findings;

Feedforward controller A uses a finite-impulse-response design, with 5 seconds of preview, and three rotating LIDAR measurements. Feedforward controller B uses a static-gain design, with the preview time defined by the pitch actuator dynamics, a simulation of a real nacelle-based scanning LIDAR system, and a lowpass filter defined by the LIDAR configuration. These controllers are now directly compared under the

same LIDAR configuration, in terms of fatigue load reduction, rotor speed regulation... ..The LIDAR configuration with more measurement points, covering more of the rotor plane, (B) gives a better estimate of the rotor-effective wind speed.It was also concluded that a greater percent load reduction is possible in more turbulent wind, and that feedback gains should be reduced when feedforward control is used..... Third and finally, the contributing sources of required preview time. The main source is the phase delay of the lowpass filter, which is needed to filter out high-frequency components of the wind measurements, since these higher frequency measurements are usually not accurate enough to be used to mitigate loads. This filter will likely require 2–3 seconds of preview, with both required preview time and available preview time decreasing as wind speed increases.

7.5.2. Speed Control Simulation Studies

The UpWind study on yaw control, cited in the previous section (Schlipf 2012), also included an analysis of Lidar for speed control, simulated using several different control strategies, plus the base case. The base case modeled standard control strategies in all Regions, using wind data from traditional nacelle anemometry, and using the simulation environment described previously in section 7.3.1 (FAST, TurbSim, GL Bladed, etc.) .

The study used the NREL 5 MW offshore reference turbine for the analysis, including the baseline control algorithm, and these are discussed below.

7.5.2.1. Case 1 – UpWind Direct Speed Control (Schlipf 2012)

The first Lidar assisted pitch control case simulated an optimized feed-forward strategy as input to torque-speed control in Region 2 and collective pitch control in Region 3. The control strategy shifts the time series of the wind input signal. The study named this strategy Direct Speed Control (DSC), since the TSR can be directly calculated knowing the wind speed and rotor speed. This is in contrast to the base case, which uses “Indirect Speed Control” (ISC), where the wind speed is derived based on the rotor speed. Table 25 shows the deviation of pitch angle, the energy production and the DEL fatigue on the main shaft.

The study estimated an increase of 0.1% in annual power production, but an 8.9% increase in DEL on the rotor low speed shaft (L_{SS}) using DSC. The power benefits increase linearly with turbine size, but the fatigue damage increases disproportionately due to non-linear inertia effects of a heavier rotor. The study found that the higher fatigue loading of the drive train is not justified by the insignificant gains in power output using this control strategy. In Region 2, the standard deviation of the TSR from its optimum value was reduced by 74%. Even though the TSR tracked much closer to optimum in Region 2, the effect on annual power output was very small. Because the maximum power output gain was trivial and the increased fatigue was not, power output benefits were not considered further in this case.

Table 25 - Production and Fatigue Loading for ISC and DSC, adapted from Schlipf 2012

Control Strategy	Std Dev. of TSR	Energy Prod. (GWh)	DEL M_{LSS} (MNm)
ISC	0.271	458.7	2.65
DSC	0.069	459.1	2.88
DSC/ISC (%)	25.6	100.09	108.9

7.5.2.2. Case 2 – UpWind NMPC (Schlipf 2012)

The second simulation case simulated a novel, nonlinear model predictive control (NMPC) strategy which uses the feed-forward Lidar input to optimize *both* pitch and generator torque throughout Region 3. This is a Multiple Input-Multiple Output (MIMO) controller whose objective is stated very roughly as “*maximizing energy production while minimizing drive train fatigue damage over the life of the turbine*”. Numerical methods were used to solve the optimal control problem in iterative solutions, and the algorithm was tuned to “*have high load reduction on tower and blades together with low pitch activity and slightly improved energy production*”.

Table 26 shows the DEL for the tower overturning moment (M_yT) and out-of-plane blade root bending moment (M_{oopl}) over a 20 year life cycle for both the baseline and NMPC controllers⁵⁸. Expected lifetime energy production and weighted standard deviations of

⁵⁸ M_{oopl} is resolved normal to the rotor plane, and is nearly identical to flapwise bending moment, which reflects a few degrees of blade pre-tensioning away from the tower.

pitch activity, rotor speed, and power output are also shown for both cases, and the change is calculated for all parameters.

Table 26 - Fatigue Loads, Production, and Deviation of Parameters, Baseline and NMPC, adapted from Schlipf 2012

Control Strategy	DEL M_{YT} (MNm)	DEL M_{OOPL} (MNm)	DEL M_{LSS} (MNm)	Energy Prod. (GWh)	$\sigma(d\theta / dt)$ (deg./sec.)	$\sigma(\Omega)$ (rpm)	$\sigma(P_e)$ (MW)
Baseline	87.66	12.87	2.89	548.42	0.46	0.59	0.52
NMPC	62.35	11.37	2.87	550.05	0.32	0.53	0.55
NMPC/Baseline (%)	71.13	88.35	99.01	100.30	70.19	89.72	106.44

Energy production was increased by only 0.3%, while standard deviation of the power output increased by approximately 6.4 %. The simulations also showed a 29% reduction in lifetime DEL on the tower and a 12% reduction in DEL on the blades. The SD of pitch was reduced by 30% and the SD of rotor speed by 10%. Pitch activity decreased at all wind speeds except around 8 m/s, where “the increased activity was justified by the optimization criteria”. The trade-off involved in this control strategy appears to be reduced fatigue loading on the tower and blades in exchange for greater variance in power output, with no significant change in energy production (EP).

7.5.2.3. Case 3 – UpWind Cyclic Pitch Control, Region 3 (Schlipf 2012)

The third Lidar analysis simulated a cyclic pitch feed forward controller using the Lidar measured horizontal and vertical shear. Individual blade pitch control allows further reduction of blade loads. The analysis showed a reduction in blade root bending moment under this strategy, but the authors indicated that further investigation is required to properly quantify any benefits, as it was unclear whether the benefits were any greater than those observed with Lidar assisted collective pitch control.

7.5.2.4. Case 4 – UpWind Controller Tuning and Evaluation (Schlipf et al 2011(a))

A separate but related study (Schlipf et al 2011(a)) included refinements and tuning of the UpWind NMPC (Case 2) controller, based on scanning five upstream ranges (see Figure 63) and optimizing the “look ahead” time. Two different wind turbulence parameters and turbine classes were evaluated. Fatigue loading was considered by simulating A and B-type turbulence intensity using TurbSim with a Rayleigh distribution with $A=10$ and 12 m/s, as per IEC 61400-2. The simulation produced the results in Table 27. Significant reductions in DEL were observed for tower and blades in all simulation runs.

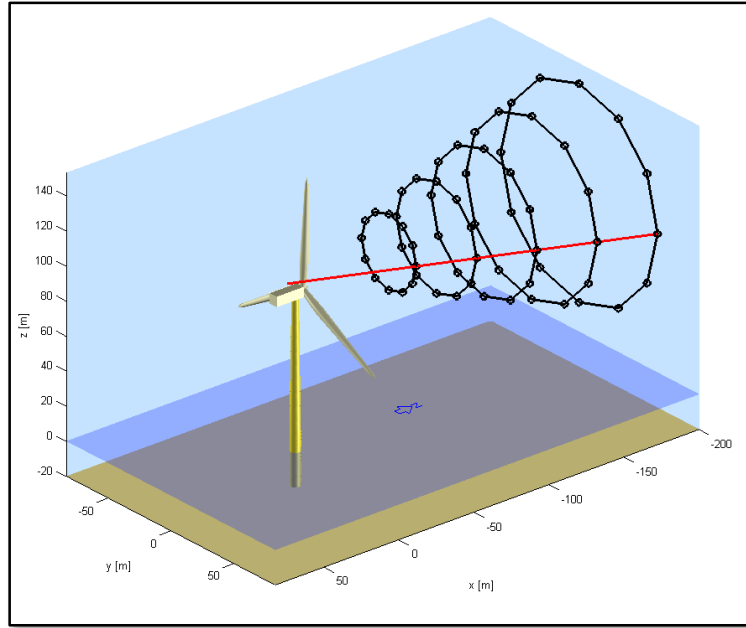


Figure 63- UPwind Case 4 Simulated Lidar Scan Configuration, from Schlipf et al 2011a (EU- funded Project UPWIND Study)

Table 27- DEL Mitigation by Turbine Class and Rayleigh A, adapted from Schlipf et al 2011a

Turbine Class	Rayleigh A (m/s)	Reduction DEL M_{yT} m=4	Reduction DEL M_{yB} m=10
A	12	-20.4%	-11.4%
A	10	-15.8%	-9.2%
B	12	-19.5%	-8.3%
B	10	-15.7%	-6.1%

7.5.2.5. Case 5 – UPWind Extreme Operating Gust Loading

The Extreme Operating Gust (EOG) is characterized by a decrease in speed, followed by a steep rise, a steep drop, and a rise back to the original value. The gust amplitude and duration vary with the return period, turbulence class, and reference wind speed⁵⁹. For this UpWind study (Schlipf et al 2012(a)), the 50 year EOG was used. Table 28 shows that significant benefits were found for the reduction of EOG loads in Region 3. Peak loads were reduced by over 50%, and rotor speed variance during the gust was reduced by over 75%. No analysis of energy capture was included.

Table 28- EOG Loading for Baseline vs. NMPC Control, adapted from Schlipf et al 2012a

Control Strategy	EOG 13.2 m/s		EOG 25 m/s	
	EOG M_{yT} (MNm)	$\Delta \Omega$ (rpm)	EOG M_{yT} (MNm)	$\Delta \Omega$ (rpm)
Baseline	129	2.34	99	3.01
NMPC	63	0.57	36	0.29
NMPC/Baseline (%)	49	24	36	10

⁵⁹ It is important to note that this is different from the Extreme Event Gust (EEG), which is the 3 second sustained gust that has 2% chance of being exceeded in any year (50 year gust). The EEG occurs in Region 4, above cut-out speed, and thus is not an operational event.

7.5.2.6. Case 6 – UpWind Work Package 5, (UpWind 2011)

This analysis (UpWind 2011) was conducted as part of UpWind Work Package 5, and examined the effects of employing a ramping strategy to gradually reduce power output above the cut out speed until shut down occurs at a higher speed. The ability of Lidar assisted individual pitch controls to reduce extreme loading near the cut-out speed allows a more aggressive control strategy, and a resulting increase in AEP. In this scenario, active Lidar controllers act as a limiter on rotor speed and loading during gust events, allowing the turbine to operate at higher avg. wind speeds, with less “overhead” needed for a safety margin. Most turbines have a cut-out speed of ~ 25 m/s. This is based on the 10 minute average wind speed, but can also be triggered by a 5 second gust reaching 35 m/s, or a one minute average pitch value exceeding a threshold. The UPWIND study used a ramp controller that reduced power output from rated capacity at 25 m/s to zero at 35 m/s. The parameters were adjusted to obtain a “crude balance” between fatigue and power production and the study assumed a Class 1 wind regime described by a Rayleigh distribution with a mean wind speed of 10 m/s. For this wind regime, the hourly mean wind speed would be expected to exceed 25 m/s for about 64.7 hours per year, and to exceed 35 m/s for about 0.6 hours per year.

For the ramp to 35 m/s, the study found that AEP was increased by 0.9%, but more significantly, it found that this control strategy actually reduced extreme loading on some components due to the greater operational flexibility of the turbine to handle gusts when

it is active than when it is idled. At some wind speeds above 25 m/s, tower bending moment was greater with a parked rotor than a spinning rotor. No peak loads increased by more than 10%.

7.5.2.7. Stanford Study, Extreme Operating Gust Loading (Soltani et al 2011)

A recent study led by Stanford (Soltani et al 2011) examined the effects Lidar assisted rotor control on extreme loads and power fluctuations in control Region 3. The controller solved two optimization problems: one to predict or estimate mean wind speed, given Lidar data, and the other to carry out receding horizon control (RHC) to choose the optimal control inputs. The feed forward Lidar input was used to determine optimal pitch for a series of discrete time steps. Numerical methods were used to solve the optimal control path at each iteration, then the solution was applied to the next horizon/iteration, ad infinitum. The analysis also used a linear parameter varying model to approximate the non-linear system to account for tower dynamics, defined by fore and aft nacelle displacement. The method was verified against an existing wind turbine control system. Up until recently, the main drawback of this method was the large amount of computation involved and the requisite delay in the control loop. However, faster processors and optimization methods have been developed that solve this problem and do the calculations in a fraction of a second. The optimization model also assigned a negative parametric value to pitch activity, set so that life cycle pitch activity was

effectively the same as the baseline. This was done to ensure that any benefits of RHC were not negated by higher maintenance costs for blades and pitch systems.

The model was used to estimate response to a reference extreme gust as recommended in IEC 61400-3; the so called “mexican hat” gust. Figure 64 shows the gust time series and the blade pitch angle changing in response. The baseline response was first modeled using standard proportional-integral-derivative (PID) torque controls, which modulate generator torque to control rotor speed, then compared to response with Lidar and the RHC algorithm, which uses feed-forward Lidar to modulate pitch to control rotor speed in Region 3. The RHC simulation used a prediction horizon of 4 seconds (based on a typical ten second gust) and a sampling frequency of 0.15 seconds. The analysis indicated an 88% reduction in power output fluctuation, an 80% reduction in tower top fore-aft deflection, and an 82% reduction in the magnitude of fluctuations in main shaft torsion, all with no increase in life-cycle pitch activity. These reductions were a result of effectively eliminating the 3-4 second delay between the gust initiation and the pitch initiation. As the graphs show, this practically eliminates the “mexican canyon” in the PID power production signal. Although the Stanford study did not address power gains, it is apparent from Figure 65 that the use of RHC results in greater energy production in Region 3. The difference in energy produced is the sum of the scalar areas (pos. and neg.) between the two signals over the duration of the gust. While the first part of the gust produces only minor differences that are roughly balanced, the sudden drop in base

case output at 88 seconds produces significant energy loss compared to the RHC controlled power output. Over time, these losses (“Mexican canyons”) accumulate.

This is because the baseline control algorithm activates only after the rotor has accelerated in response to the gust and the generator has exceeded the threshold output. The generator torque can be changed quickly, but even with a time constant an order of magnitude faster than that of the rotor speed., there is still a lag of two to four seconds. The pitch error over the course of the ten second gust varies between five and ten degrees. At $t=88$ sec, the baseline controller produces a pitch angle of about 5 degrees, when the optimum is about -2 deg. This causes baseline power output to drop from 2000kW to about 1300kW momentarily. The lost energy is represented by the area between the two curves from about $t=87.5$ to about $t=90.5$ seconds. If the shape of this area is approximated as triangular, the energy loss per gust is approximately $\frac{1}{2} (3s \times 700 kW) = 1050 \text{ kW-s} = 0.3 \text{ kW-hr}$.

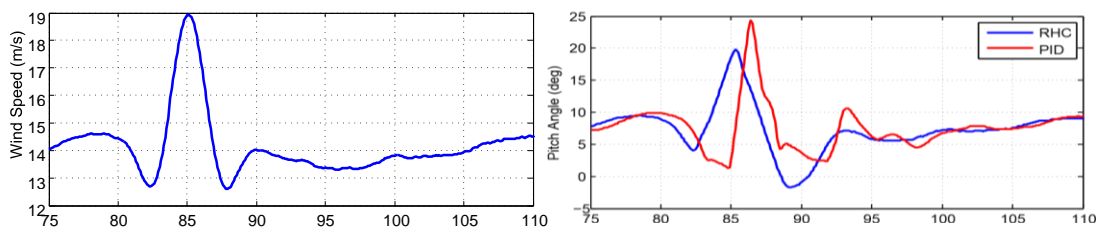


Figure 64- Wind Speed and Pitch Angle During EOG, from Soltani et al 2011

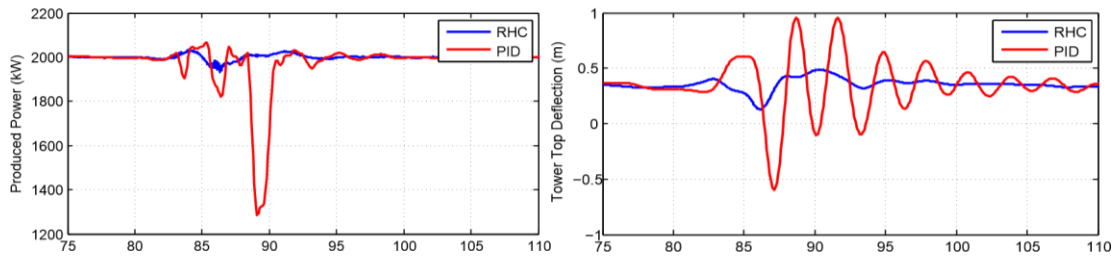


Figure 65-Power Production and Tower Deflection During EOG, from Soltani et al 2011

7.5.2.8. Gust Frequency Analysis

To estimate the frequency of conditions which create these losses, a data set was obtained and analyzed from a WindSentinel deployed in Lake Michigan in 2012 by Grand Valley State University. The data set includes wind speeds and directions sampled at 1 Hz, and ten sequential days in January 2012 were selected as being representative of gusty winter conditions. The data were scrubbed by removing all strings of invalid data exceeding 1 minute and extrapolating to fill in gaps of less than one minute. This left 665,027 records, or the equivalent of about 8 days of measurements. An analysis was performed to identify gust events, defined as “saw tooth” events, where a sudden rise in velocity is followed by a sudden drop. These events are what causes out-of-sync pitch response and power drops. The data stream was scanned multiple times by an algorithm written in the “C” programming language. The algorithm looked for waveforms matching the defining criteria for a “sawtooth gust” event on each pass, and accumulated counts of qualifying events. Those counts were written to a file/table and imported into an excel spreadsheet for presentation. Search

criteria were set for 1, 2, 3, and 4, and 5 second windows, and changes in wind speed were binned according to magnitude, from 0 to 11 m/s, in bins of 1 m/s. For example; 99 events were observed where the wind speed increased by between 3.0 and 4.0 m/s in one second, and then immediately following that ramp up, the wind speed fell by the same amount in one second. A spectral analysis of the data would provide the most accurate estimate of the potential loss of power, but that is beyond the scope of this study. As a first order analysis, to determine if the benefits pass the threshold of significance (greater than 1.0%), the number of events similar to the reference EOG was estimated.

Figure 66 shows the output data plotted as a 3-D surface for all ramp rates and window widths. The reference “mexican hat” EOG has a trough to peak duration of about 3 seconds, and raises the wind speed by about 6 m/s in that period, for a ramp rate of about 2 m/s per second. In Table 29, for the 3 second sliding window, there were 996 events where the wind increased by 6 m/s over a 3 second period, then dropped back to the baseline over the following three seconds. Since this represents about 7.7 days of data, a first order estimate for one year would be $(996 \times 365 / 7.7 =)$ 47,212 similar events. Assuming conservatively that about 25% of the events occur in Region 3 leaves about 11,800 qualifying events per year. If each event can be mitigated with Lidar control, saving 0.3 kWhr per event, this would yield about 3,540 kWhr annually. This translates to only \$531, which is insignificant.

Although this analysis has high levels of uncertainty, and is based on data from Lake Michigan, not the study area, it does not show any evidence of significant gains in AEP from this methodology of pitch control. This agrees with other simulation studies reviewed, which found no direct, significant increase in power production through Lidar assisted pitch control. Further research is warranted to confirm or revise this observation. However, the reduction in fatigue loading is confirmed by several studies, and can be monetized, as discussed below.

Table 29- Sawtooth Gust Frequency from WindSentinel Data, Lake Michigan

Sliding Window Width (seconds, trough to peak)	Frequency Count by Change in Wind Speed, m/s, binned.			
	0 to 1	1 to 2	2 to 3	3 to 4
1	11514	1491	328	99
2	13939	2505	675	215
3	15474	3292	996	376
4	16423	3775	1243	456
5	16692	4141	1348	568
6	17148	4288	1370	555

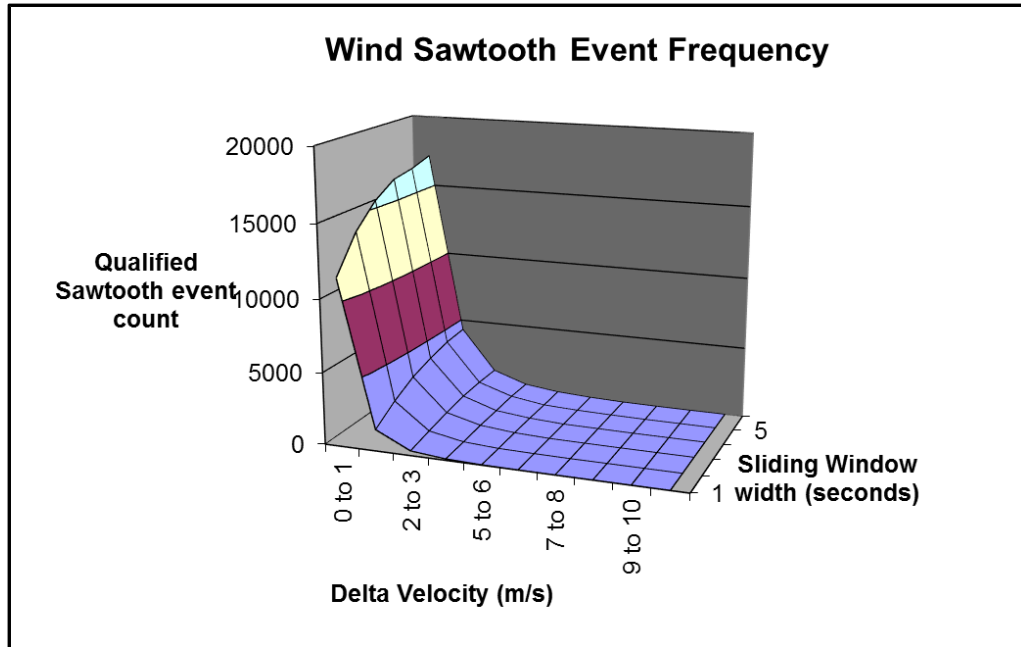


Figure 66- Sawtooth Gust Event Frequency

7.6. Summary - RC Benefits

Each simulation study modeled systems slightly differently, but collectively, they indicate that with optimized range settings and control algorithms, Lidar assisted yaw control can significantly improve power production, and Lidar assisted speed and pitch control can significantly reduce both extreme operating gust loads and fatigue loading. These effects were observed in blade bending moment, tower bending moment, and tower top displacement. For shaft fatigue loading, the effects of Lidar assisted controls were mixed, depending on the algorithm applied. In no case were they observed to be larger than +/-10%, so shaft fatigue was not analyzed further.

7.6.1. Extreme Operating Gust and Fatigue Loading

Blade loading from the EOG produces both a shaft torque and a thrust load. The Stanford study (Case 6- Soltani et al) indicated that the tower top displacement produced by the EOG thrust load can be reduced by 80% with Lidar and improved algorithms. Reductions in shaft speed variance and tower bending moment calculated in the UpWind studies were anywhere from 49% to 90%. Considering the range of thrust load reduction in the simulation studies reviewed (49% to 64%) and the cluster of values near 50%, the value selected for attenuation of EOG loading with Lidar assisted speed control is 50%. These improved control systems were also able to attenuate output drops during the EOG by 75%, resulting in slightly higher net energy capture.

Because the benefits of fatigue reduction involve higher uncertainty, the lower range of the fatigue benefit estimates (tuned DSC) is assumed, yielding a 10% reduction in blade DEL and a 20% reduction in tower DEL. Table 30 summarizes the relevant findings of the simulation studies.

Table 30- Rotor Control Benefits Summary Table

N	Study/Case No.	Notes	AEP(pct gain)	Yaw time (%) ^{-*}	DEL (t)	DEL (b)	DEL (s)	TSR SD Region 2	EOG Thrust , OTM	EOG shaft spd var
Yaw Control	Schlipf -Y1	(10min, 10°)	1.0-2.0%	5.0%	nc	nc				
	Gaiser-Y2a	(unlim. yaw)	6.0%	12.0%						
	Gaiser-Y2b	(1min, 8°)	3.0%	8.0%	nc	nc				
Speed Control	Case 1	DSC	0.1%				8.9%	-74%		
	Case 2	NMPC	0.3%		-29%	-12%	-1%	-76%	-50%	
	Case 3	Cyclic								
	Case 4	Tuned NMPC			-20%	-10%				
EOG Mitigation	Case 5	EOG low U							-51%	-76%
	Case 5b	EOG high U							-64%	-90%
Ext. Range	Case 6	Hi Cut Out	1.0%						10%?	
	Soltani	EOG RHC	??						-50%	
(t)- tower (b) – blade (s) – shaft (nc)- no change										

7.6.2. Increased AEP from Yaw Controls

Based on the evaluation, a small increase of power can result from Lidar assisted yaw control providing more accurate and timely wind direction to they yaw controller. A reasonable estimate would be that using optimized algorithms, annual power output could be raised by ~1% to 2% without significantly increasing yaw activity. This estimate is based on the UPWIND study, which was the most conservative estimate.

7.6.3. Increased AEP from Speed Controls (Pitch)

The only Lidar assisted rotor speed control study that found gains greater than 0.5% in AEP was Case 7- the UpWind study of extending Region 3 to 35 m/s using a power ramp down, which found gains of 0.9%. However, this strategy cannot be implemented with the selected strategy of longer blades (see following section), and so was not considered further

7.6.4. New Blade Designs with Lidar-Assisted Load Reductions

The primary effects of Lidar assisted speed/pitch control were found to be Extreme Operating Gust and DEL (fatigue) loading reduction on the blades and tower. Within the study area, reducing fatigue loading on the tower produces no significant benefits because the tower and foundation strength requirements in intermediate waters are driven primarily by wave and current -driven forces. (ABS 2011, Table 2.45). Therefore, the remainder of this analysis focuses on blades.

In response to reduced fatigue and gust loading with Lidar assisted control, blade design can be changed a few different ways, discussed briefly below.

- **Extending service life?** – Lower fatigue loading translates to longer fatigue life. However, due to the high cost of mobilizing to replace major components offshore, they are all designed for the same service life. It is thus unlikely that blade service life would be increased beyond the service life of other major components.
- **Reducing strength and weight?**- Blade strength is largely defined by the cross sectional modulus of the structure, and thus, the weight per unit length. Reduced loading could allow less structural material in the design, reducing blade weight without sacrificing swept area. Weight reductions can cascade down the tower design if nacelle weight or gyroscopic forces drive tower stiffness requirements. However, for jacket foundations used in the base case, peak loading and jacket stiffness requirements are driven primarily by extreme wave and current forces, not wind or gyroscopic forces (ABS 2011, Table 2.45). Therefore, it is less likely that blade weight would be reduced, since the weight savings would not cascade down the tower structure design⁶⁰.
- **Increasing swept area** - With loading limited by the proactive control system, blade length could be increased without adding weight. Longer blades would increase swept area, which is proportional to power production. The advantages of greater swept area are amplified in summer, when wind speeds are lower and electricity prices are higher. This is the most likely scenario, and is analyzed further below.

In order to determine how much blades could be lengthened in response to reduced fatigue loading, some relationship between increased blade length and DEL fatigue must be defined.

⁶⁰ For a monopile structure, where the foundation and tower stiffness criteria can be defined by resonance and gyroscopic forces, rotor weight is a key factor in tower design. In that case, the greatest benefit may be had by using lighter blades.

7.6.4.1. Berg et al 2009

In a 2009 paper from Sandia National Laboratories (Berg et al 2009), Active Aerodynamic Load Control (AALC) was investigated for reducing fatigue loading on blades by moveable flap control. Two types of AALC devices were investigated, as shown Figure 67. The controller performance was intended to “...*maximize power output while minimizing blade-root bending moment oscillations about a mean value during turbulent conditions.*”

The trailing edge technology was developed by FlexSys of Ann Arbor, MI. The principle of the AALC is similar to Lidar assisted pitch control in the sense that they both seek to attenuate blade-root bending moment fatigue by adjusting aerodynamic geometry. Thus one would expect to see similar effects regarding fatigue loading and blade length. The simulations used Normal Type A Turbulence as defined by IEC, and were run with the NREL FAST, AeroDyn, and TurbSim codes, referenced previously. Fatigue loading was monitored including blade root bending moments on both axes. DEL was estimated using rainflow counting with the NREL CRUNCH code (Buhl 2003) and a Rayleigh wind speed distribution, and results were binned by wind speed range. DEL is a more versatile measure than fatigue life since it assumes nothing about material properties.

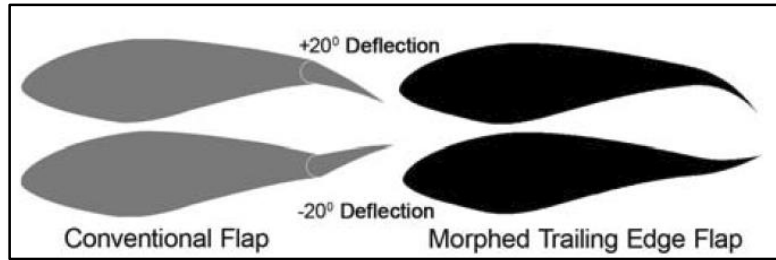


Figure 67- AALC Blade Section Schematic, from Berg et al 2009.

Two separate test cases were run using a standard 1.5 MW WindPACT simulated turbine; one with the flap technology and one with flaps and longer blades. Table 31 shows the results of adding the flap technology to the base case in the simulation, and the results of adding the flaps and increasing blade length 10%. DEL reduction is given as a percent change from base case DEL. Table 31 indicates a reduction of 26.3% in flapwise bending moment DEL with the technology, using a typical Weibull distribution with mean wind speed of 7 m/s. When the modified blades are scaled up 10% a net increase of 4.3% from the baseline was observed. This indicates that in the absence of AALC flaps, the 10% length increase would have increased DEL by ~ 30.6% (26.3% + 4.3%). Assuming a linear relationship within the range considered, this implies an inverse proportion of about 3:1 between the parameters, so that a reduction of 10% in DEL (estimated by Schlipf 2012 for Lidar assisted control) should be balanced by a 3.3% increase in blade length.

Schlipf (2012) used a nearly identical simulation environment, except the simulation used the NREL Reference 5 MW turbine. When Berg et al (2009) simulated the NREL Reference 5 MW turbine with the AALC technology, the reduction in DEL for flapwise moment was just over half that observed in the 1.5 MW turbine simulation (14.3% vs. 26.3%). This implies that AALC is about half as effective for fatigue reduction on larger rotors and turbines. No AALC or any other simulations were performed in either study using longer blades on the 5MW turbine.

Taking the conservative assumption that this 5 MW scale effect would also reduce the effectiveness of Lidar assisted pitch control by the same amount (50%), the following adjustment is made to the blade length /DEL ratio: The allowable increase in blade length is reduced by over half, from 3.3%, to 1.6%. In brief, the 10% reduction in DEL observed by Schlipf (2012) and assumed in the present study would be offset by a ~ 1.6 % increase in blade length. This would increase swept area by 3.23%. Assuming a near constant specific load (output per swept area), this should produce at least 3% more energy per year.

Table 31- Blade Root Bending DEL Changes with AALC, NMPC

Percent Change in DEL from Base Case				
	1.5 MW+Flaps	1.5 MW + Flaps + 110% Blade	NREL 5 MW + Flaps	Schlipf 2012 NMPC Lidar
Flapwise Moment	-26.3	4.3	-14.3	-10

7.6.5. Wake Effects

None of the RC analyses modeled turbine wake effects or estimated AEP for an entire wind farm. Wake effects cause more turbulence within the wind farm, which increases pitch error, yaw error and fatigue loading on components, especially blades. It is unclear how the benefits of Lidar controls would change under wake effects, but it is likely that the benefits are higher since they derive primarily from the use of pro-active controls to manage turbulent conditions (under steady-state winds, they would be inactive). On the other hand, wake effects also reduce the capacity factor of downwind turbines in a wind farm, so any proportional benefits from RC are reduced. Because these two effects are opposite and highly uncertain, wake effects are neglected and benefits for a single turbine (as % gain in AEP) are assumed to be the same for an entire wind farm.

7.6.6. Lidar-Assisted Rotor Control – Costs

The cost of nacelle mounted scanning Lidar units is estimated at \$300,000, and the service life is assumed to be 3 years⁶¹, for an estimated annual cost of \$100,000. Table 32 shows the annualized Benefit Cost breakdown. The base case 5 MW turbine should yield a Net Capacity Factor of about 40% in the study area (Baker 2011, Table 5). Thus,

⁶¹ Typical service life is 3-5 years for electronics in an exposed marine environment

the AEP would be approximately ($2 \text{ MW} \times 8760 \text{ hr/yr} =$) 17,520 MW-hr/yr. Assuming a power price of \$0.15/kw-hr yields a total annual revenue of ~\$2.63 M per turbine. Including the AEP increase from yaw controls (1% to 2%) and pitch control/swept area (3%) yields a total gain of 4% to 5%. A 4.5% gain yields an annual benefit of \$118,260 per turbine. Thus the benefits of Lidar-assisted rotor control appear to be justified, with a Benefit-Cost ratio of between 1.05 and 1.31 (averaging ~1.2). This benefit is included in the present analysis, but further analysis is warranted due to the high level of uncertainty and slim margin of justification. After accounting for the Lidar cost, the change in BP will be approximately 20% of the total AEP gain ($20\% \times 4.5\% =$) 0.9%

To estimate the total cost of this strategy, the cost of a nacelle based Lidar is multiplied by the number of turbines estimated by Baker (2011) in the study area (14,447). With an annualized cost of \$100,00 per turbine/Lidar, the total annual cost for the base case wind farm would be about \$8 million, but the annual benefits would be about \$9.5 million. As mass production drives the cost of Lidar down, this will certainly improve the economics.

Table 32-Summary of RC Benefits for Single Turbine, Wind Farm, and Buildout

Power Price =	0.15	\$/kWhr	
No. of turbines in wind farm=	80		
No. of turbines in build-out=	14,447		
	Single Turbine	Wind Farm	Study Area Build-out
AEP (MW-h/yr)	17520	1401600	253111440
AEP gain	4.5%	4.5%	4.5%
Total Ann. Revenue (*)	\$2,628,000	\$210,240,000	\$37,966,716,000
Ann.Revenue Gain	\$118,260	\$9,460,800	\$1,708,502,220
Annual Cost (**)	\$100,000	\$8,000,000	\$1,444,700,000
Net Benefit	\$18,260	\$1,460,800	\$263,802,220
Benefit Cost Ratio (**)	1.2	1.2	1.2
(*)- @ \$0.15/kWh (**)- Costs should go down with quantities for economies of scale, so BC ratio should actually be higher for wind farm and build-out.			

7.6.7. Looking Forward-RC Benefits

The studies discussed herein show that there are many ways to improve the control system, from the sensors to the algorithms to the servo controllers. Lidar assistance allows the use of more advanced algorithms, which can be dynamically tuned to prioritize and balance multiple competing objectives using multiple input signals. Feed forward Lidar systems can provide pro-active load limiting by feathering the blades when a gust is detected, avoiding sudden overloading and subsequent drops in power output. These systems can increase power output and reduce fatigue on the entire turbine by detecting incoming wind as a 3D vector field. Cyclical pitch controls can take advantage of this information by adjusting pitch according to wind shear and rotational position. Strain

sensors placed in the blade can also be used to limit blade loading and rotor thrust. Recent research in sectional blade technology, shape memory alloys, and torsional clutches will also benefit from Lidar assisted control (UPWind 2011). These and other advances in wind sensors, self calibrating, recursive, non-linear control systems, blade construction, and control surface technology will result in greater and greater efficiency, relentlessly approaching the Betz limit while reducing fatigue loading on blades and other components. How the benefits are captured- whether by relaxing design requirements (e.g. lighter towers and rotors) or increasing performance specifications (e.g. longer blades and more energy) will have to be decided on a case by case basis, but it is clear that Lidar will play a major role enabling this development in the coming years.

Chapter 8

SUMMARY DISCUSSION AND CONCLUSIONS

8.1. Summary Benefits

This analysis shows that there are significant economic benefits to the use of these new technologies. Table 33 summarizes the estimated changes in AEP and BP for the four benefit categories (Mapping, P90, Yaw Control, Pitch/Speed Control). The total boost in Annual Energy Production is estimated between 6% and 8%, while the boost in AEP P90 (from greater certainty) is estimated at 3%. When the costs of strategy implementation are taken into account, the Breakeven Price is reduced by between 5.8% and 7.0%. If the mapping benefits are counted as a cost savings, the BP is reduced by 3.8% to 4.0%, and the cost savings are around \$120 million.

Table 33 - Summary of Benefits vs. Base Case

Percent Change in AEP, Cost from Base Case				
	AEP P50 up	AEP P90 up	BP down	\$\$ down
Mapping – LCGMF Atlas Cost Δ				\$120M
AEP Mapping Boost ⁽¹⁾	2%-3%		2-3%	
AEP P90 Boost ⁽²⁾		3%	3%	
AEP Yaw Control ⁽³⁾	1%-2%		0.2%-0.4%	
AEP Pitch/Speed Control ⁽³⁾	3%		0.6%	
First Phase Buildout ⁽¹⁾	6% - 8%	3%	5.8%-7.0%	
Full Buildout (no AEP-Mapping Boost included)			3.8% - 4.0%	\$120 M
(1)- Benefit only accrues to first wave of wind farms in study area (2) –Pct boost in both P50 and P90 roughly equiv. to pct. cut in BP per Levitt et al, 2011 (3) -BP takes into account the cost of the Lidar on each turbine (4) – Benefits assume cost of LCGMF mapping is spread over industry, over full build out				

8.2. Summary Discussion and Conclusions

While further refinements of the costs and methodologies are needed before implementing the recommended strategies, it appears they are all justified.

8.2.1. Conclusions – Rotor Control Benefits

The addition of Lidar to turbine yaw control systems can increase Annual Energy Production by 1% to 2% by reducing yaw error and optimizing rotor efficiency by sensing the wind direction in the free stream, upstream of the rotor, instead of in its wake, on the

nacelle. The addition of Lidar to rotor speed (pitch and/or generator torque) controls significantly reduces fatigue loading and extreme operating gust loads, but was not found to produce significant benefits in power generation. The benefits of 10% lower fatigue loading can allow blade length to increase by about 1.6%, creating 3.2% more swept area without additional weight. This effect translates into a ~ 3.0% increase in Annual Energy Production. The total energy production gain is therefore estimated at between 4% and 5% for the rotor control strategies. After accounting for Lidar system costs, the Breakeven Price is reduced by between 0.8% and 1.0%.

8.2.2. Conclusions –Annual Energy Production P90 Benefits

The addition of Lidar met buoys at a proposed site can increase projected annual energy production P90 values (value that has a 90% chance of being exceeded in any year) by 3% over a two year campaign. This value comes from reducing uncertainty associated with horizontal and vertical extrapolation from fixed, hub height met towers. This has a nearly proportional effect on the Breakeven Price because of change in the project finance cost, which is driven by the P90 value. Because the cost of the single floating Lidar unit is spread over the entire wind farm, and amortized over multiple resource assessment campaigns, it is considered insignificant, and not counted in this first-order analysis.

8.2.3. Conclusions – Mapping Benefits

The strategy of improved resource mapping using Lidar and satellite microwave data, processed through trained, tuned, Lidar-calibrated Geophysical Model Functions can result in better site selection and boost Annual Energy Production by between 2% and 3% for the first projects. However, this boost is reduced after the first phase of build out. As the study area is developed, these benefits would be lower in constant dollar terms, since later projects would be forced into the lowest energy sites. From the perspective of an early developer, the proposed strategies would reduce the Breakeven Price by 5.8% to 7.0%, assuming the cost of the mapping effort is either publicly funded, or spread out over the entire industry. If the mapping benefits are not included, this leaves a Breakeven Price change of about -3.9%. In this accounting scenario, the cost savings of the proposed atlas vs. the base case atlas add \$120 million to the benefits.

Another way to look at the benefits is to consider only the first group of wind farms in the study area. It is highly uncertain whether all available sites would be developed, as this would be a massive undertaking, requiring the installation of well over 10,000 turbines. Although this may occur in the longer term, a more reasonable mid-term assumption (ten years time frame), based on the number of developers that have expressed interest in the Wind Energy Areas, would be the development of ten large wind farms, of about 100 turbines each. Under this scenario, the \$120 million in savings from using ten floating

Lidar buoys instead of ten met towers would be distributed roughly evenly among the ten developers.

The actual value of improved mapping is difficult to quantify due to high uncertainty about financing, future technology developments, and market conditions, but these values serve as a first order reference from two different perspectives. Roughly stated, the overall conclusion is that implementing the recommended strategies could save \$120 million in resource mapping costs over the long term, and reduce the Breakeven Price by between 4% and 7%, depending on how the mapping benefits are accounted.

8.2.4. Areas for Further Research

Another area recommended for further research is the potential for using the same set of ten (or whatever number is optimal) strategically placed floating Lidar met buoys for calibration of a numerical weather prediction model such as the Weather Research and Forecasting model from NOAA. This approach has the advantage of high temporal resolution, which effectively eliminates the problem of diurnal bias found in satellite retrievals. It also eliminates the problem of data scrubbing and coastal masking. The model can also be set up to assimilate snapshot wind speed retrievals from SSMI and QuikScat data bases. Due to advances in computing power and technology, it is now practical to use WRF to generate multi-year databases due to the processing time required (Dvorak et al

2012) Although not investigated in this paper, there appears to be great potential for leveraging the positive attributes of Numerical Weather Prediction models with the proposed mapping strategy, reducing error and bias even more. Further research is recommended.

Although recent advances indicate great potential, substantial research is still needed to develop the detailed methodologies for building the Lidar Calibrated Geophysical Model Function. Extremely large data bases will need to be managed and processed. Parallels may be drawn to the early days of sub-surface geophysical acoustic imaging and modeling. Refinements in both sensing and image interpretation will lead to greater levels of precision, resolution, and confidence as the technology matures.

As blades and rotors become more actively adaptable, the benefits of Lidar control will increase by allowing control systems to keep parameters in their optimal ranges. As the price of Lidar technology drops, the justification becomes more robust, and as the science of satellite wind retrievals advances, and the database grows, mapping accuracy will increase, driving benefits up. It is clear that remote sensing technologies have much to offer in the development of offshore wind power in the U.S.

REFERENCES

- 4C Offshore (2012). Global Offshore Wind Speed Database - 23 Years of Wind Speed Observations. European Wind Energy Association. Retrieved March 23, 2013 from <http://www.4coffshore.com/windfarms/request.aspx?id=owsdb&version=1>
- Alsweiss, S. O. (2007). An improved ocean vector winds retrieval approach using c and ku-band scatterometer and multi-frequency microwave radiometere measurements (Doctoral dissertation, University of Central Florida, 2007). Available at http://www2.cecs.ucf.edu/centers/cfrsl/team/suleiman_alsweiss/Dissertation.pdf
- American Bureau of Shipping (2011). Contract M10PC00105: Design Standards for Offshore Wind Farms, Final Report. Retrieved Nov. 12, 2012 from <http://bsee.gov/Research-and-Training/Technology-Assessment-and-Research/Project-670.aspx>
- Ancona, D. (2012). Mid-Atlantic Wind Resource: How Well Do We Know It? Poster presented at American Wind Energy Association, Offshore Expo 2012, October 10 – 12, 2012, Virginia Beach, VA.

- Atlas, R., Hoffman, R. N., Ardizzone, J., Leidner, S.M., Jusem, J.C., Smith, D.K., & Gombos, D. (2010). A cross-calibrated, multiplatform ocean surface wind velocity product for meteorological and oceanographic applications [Electronic version]. *Bulletin of American Meteorological Society*, 92, 157-174.
- Badger, M., Badger, J., Hasager, C. B., Nielson, M., & Peña, A. (2010). Wind class sampling of satellite SAR imagery for offshore wind resource mapping. *Journal of Applied Meteorology and Climatology*, 49, 2474-2491. Available at <http://dx.doi.org/10.1175/2010JAMC2523.1>
- Badger, M., Badger, J., Hasager, C., & Nielson, M. (2009, September 14-16). A novel sampling method for satellite-based offshore wind resource estimation offshore wind resource estimation. Paper presented at the American Wind Energy Association 2009 Conference & Exhibition, Stockholm, Sweden.
- Beal, B., Young, G., Monaldo, F., Thompson, D., Winstead, N., & Scott, C. (2004) - High resolution wind monitoring with wide swath SAR: A user's guide. Retrieved Nov. 12 2012 from http://fermi.jhuapl.edu/sar/storm-watch/user_guide/bealguide_072_V3.pdf
- Beal, R.C.; Young, G.S.; Monaldo, F.; Thompson, D.R.; Winstead, N.S.; Schott, C.A. (2005). High resolution wind monitoring with wide swath SAR: A user's guide (pp. 1-155). Washington, D.C, U.S.A.: U.S. Department of Commerce.

- Bentamy, A., Ayina, H. L., Queffeulou, P., & CroizeFillon, D. (2007). Improved near real time surface wind resolution over the Mediterranean Sea. *Ocean Science*, 3, 259-271.
- Berg, D.E., Zayas, J.R., Lobitz, D.W., van Dam, C.P., Chow, R., and Baker, J.P. (2007). Active aerodynamic load control of wind turbine blades. Proceedings of the 5th Joint American Society of Mechanical Engineers Journal of Advanced Mechanical Design, Systems, and Manufacturing Fluids Engineering Conference, San Diego, CA.
- Berge, E., Bredesen, R.E., Byrkjedal, Ø., Harstveit, K., & Kravik, R. (2012). The NORSEWIND wind atlas. Description of input data, methodologies and documentation of the wind atlas data [Report KVT/RK/2012/R012]. Kjeller, Norway: European Wind Energy Association.
- Bergen (2012) -University of Bergen, Statoil, Norwegian Marine Technology Research Institute, & Fugro Oceanor (2012). Measurements of wind profile from a buoy using Lidar: Final Report. Reference No: 9631 5 June 2012
- Betancur, S., Lemoine, R., Boinne, R., Mali, P., & Dewilde, L. (2008, November 5-7). Reducing risks in resource assessment using Lidar. Paper presented at the American Wind Energy Association 2008 Conference and Exposition, Guadalajara, Mexico.

Bloomberg New Energy Finance (2011). Onshore wind energy to reach parity with fossil-fuel electricity by 2016 [Press release]. Retrieved November 10, 2011, from <http://bnef.com/PressReleases/view/172>

BOEMRE (2011). - Department Of The Interior Bureau Of Ocean Energy Management, Regulation, And Enforcement Renewable Energy Alternate Uses Of Existing Facilities On The Outer Continental Shelf 2011 CFR 285.600 and 285.601 Title 30 - Mineral Resources. Chapter II -, Subchapter B - Offshore. Part 285 -. Subpart F - Plans and Information Requirements. Washington, D.C.: BOEMRE.

Boquet, M., Callard, P., Deve, N., & Sauvage, E.G (2010, April 20-23). Return on investment of a Lidar system for wind resource assessment. Paper presented at the European Wind Energy Conference and Exhibition 2010, Warsaw, Poland.

Brower, M. (2012). Wind resource assessment: a practical guide to developing a wind project. Sussex, UK: John Wiley and Sons.

Budischak, C., Sewell, D., Thomson, H., Mach, L., Veron, D.E., & Kempton, W. (2013). Cost-minimized combinations of wind power, solar power and electrochemical storage, powering the grid up to 99.9% of the time. *Journal of Power Sources*, 225, 60-74.

Buhl, Jr., M.L. (2003). Crunch user's guide. Retrieved from <http://wind.nrel.gov/design-codes/postprocessors/crunch/Crunch.pdf>

- Burton, T., Sharpe, D., Jenkins, N., & Bossanyi, E. (2001). Wind energy handbook. West Sussex, UK: John Wiley and Sons.
- Cayla, M. (2010). Production Zephir testing - comparison of Zephir measurements against cup anemometry and power curve assessment. Retrieved March 8, 2012, from http://s.campbellsci.com/documents/us/miscellaneous/zephir_validation.pdf
- Chelton D, Schlax, M.G., Freilich, M.H., & Milli, R.F., (2004). Satellite measurements reveal persistent small-scale features in ocean winds. *Science*, 303, 978-983.
- Christiansen, M.B. (2006). Wind Energy Applications of Synthetic Aperture Radar (Doctoral dissertation, Danish Technical University, 2006). Available at [http://orbit.dtu.dk/en/publications/wind-energy-applications-of-synthetic-aperture-radar\(e4fd69dc-afe1-42df-a869-7843c66a2f80\).html](http://orbit.dtu.dk/en/publications/wind-energy-applications-of-synthetic-aperture-radar(e4fd69dc-afe1-42df-a869-7843c66a2f80).html)
- Christiansen, M.B., & Hasager, C.B. (2005). Wake effects of large offshore wind farms identified from satellite SAR. [White paper]. Retrieved from <http://dx.doi.org/10.1016/j.rse.2005.07.009>,
- Christiansen, M.B., Koch, W., Horstmann, J., Hasager, C.B., & Nielsen, M. (2006). Wind resource assessment from C-band SAR. [White paper]. Retrieved from www.risoe.dk/rispubl/art/2006_96.pdf
- Courtney, M., Wagner, R., & Lindelöw, P. (2008). Commercial Lidar profilers for wind energy: A comparative guide. Roskilde, Denmark: European Union Project UP-

Wind. Available at <http://proceedings.ewea.org/ewec2008/index2.php?page=info2&id=105&id2=359&ordre=12&tr=&searchin=&what=&search-text=&day=&top=23&fil1=&fil2=&fil2&ord1=&sess=103>

Det Norske Veritas (2011, April). Recommended practice: use of remote sensing for wind energy assessments [Report DNV-Rp-J101]. Available from <http://www.dnvkema.com/services/ces/wind-energy/standards-guidelines.aspx>

Dhanju A, Whitaker P, Kempton W.(2008). Assessing offshore wind resources: An accessible methodology [Electronic version]. *Renewable Energy*, 33(1), 55–64.

Dunne, F., Schlipf, D., & Pao, L.Y. (2011, August). Comparison of two independent Lidar-based pitch control designs [Subcontract Report NREL/SR-5000-55544]. Golden, CO: National Renewable Energy Lab.

Dvorak, M. Corcoran, B., Ten Hoeve, J, McIntyre, N. Jacobson, M. (2012). US East Coast offshore wind energy resources and their relationship to peak time electricity. *Earth and Environmental Science*, 1. 1.

ECN 2012 - Netherlands Renewable Energy Centre (ECN), (2012, November 20). The Netherlands: ECN approves ZephIR 300 as valid stand-alone system for wind resource assessments [Press Release]. Retrieved December 30, 2012, from <http://www.offshorewind.biz/2012/11/20/the-netherlands-ecn-approves-zephir-300-as-valid-stand-alone-system-for-wind-resource-assessments/>

- Ecofys (2013). Improved Bankability-The Ecofys position on LiDAR use. [White paper]. Retrieved on January 22, 2013, from <http://www.ecofys.com/files/files/ecofys-2013-position-paper-on-lidar-use.pdf>
- Edson, J. B., Hinton, A. A., Prada, K. E., Hare, J. E. , & Fairall, C. W. (1998). Direct covariance flux estimates from mobile platforms at sea. *Journal of Atmospheric and Oceanic Technology* (15)547-562.
- Elliott, D., and Schwartz, M. (2006). Wind resource mapping for United States offshore areas [Report no. CP-500-40045a]. Golden, CO: National Renewable Energy Laboratory.
- Elliott, D., Holliday, C., Barchet, W., Foote, H., & Sandusky, W. (1987). Wind energy resource atlas of the United States. [Report No. DOE/CH 10093-4]. Golden, CO: National Renewable Energy Laboratory.
- Epstein, P.R., Buonocore, J.J., Eckerle, K., Hendryx, M., Stout III, B.M., Heinberg, R., Clapp, R.W., May, B., Reinhart, N.L., Ahern, M.M., Doshi, S.K., & Glustrom, L. (2011). Full cost accounting for the life cycle of Coal [Electronic version]. *Annals Of The New York Academy Of Sciences*; Issue: Ecological Economics Reviews, 1219, 73-98.
- European Meteorological Satellite Program (2011). ASCAT product guide, technical document EUM/OPS-EPS/MAN/04/0028, issue v4C. Retrieved November 18,

2012, from <http://oiswww.eumetsat.org/WEBOPS/eps-pg/ASCAT/ASCAT-PG-4ProdOverview.htm#TOC421>

European Space Agency (2007, February 27). ASAR products handbook (Issue 2.2, 27).

Available at

https://earth.esa.int/pub/ESA_DOC/ENVISAT/ASAR/asar.ProductHandbook.2_2.pdf

European Space Agency (2011, March). Envisat and ERS missions: Data access guide

(version 1.0). Available from https://earth.esa.int/c/document_library/get_file?folderId=13019&name=DLFE-570.pdf

European Space Agency (2012). Envisat mission overview page. Retrieved November

20, 2012 from European Space Agency Web site:

http://www.esa.int/SPECIALS/Envisat/SEMHV05Y1ZG_0.html

Gaiser, B.D., Hopkins, A., Belen, F, & Major, Jr., (2013, January). Yaw control optimi-

zation - Precise optical yaw control can yield noticeable power gains. Wind Sys-

tems Magazine Jan. 2013. Available at [http://windsystemsmag.com/me-](http://windsystemsmag.com/media/pdfs/Articles/2013_Jan/0113_BlueScout.pdf)

[dia/pdfs/Articles/2013_Jan/0113_BlueScout.pdf](http://windsystemsmag.com/media/pdfs/Articles/2013_Jan/0113_BlueScout.pdf)

Gaiser, B. , Major, J., 2012 - Analysis of traditional yaw measurements, Blue Scout

Technologies White Paper, downloaded 20 Jan 2013 from

http://www.bluescout.com/files/Analysis_of_Traditional_Yaw_Measurement.pdf

Gale, J., Bradshaw, J., Chen, Z., Gomez., D., Roger, H., Simbeck, D., & Williams, R.

(2006). "Sources of CO₂, an IPCC Special Report on carbon dioxide capture and storage" available at http://www.ipcc.ch/pdf/special-reports/srccs/srccs_chapter2.pdf

Garvine, R., and Kempton, W. (2008). Assessing the wind field over the Continental

Shelf as a resource for electric power. *Journal of Marine Research* 66, 751-773.

Greenstone, M., & Looney, A. (2011). A strategy for America's energy future: Illuminat-

ing energy's full costs. Retrieved from http://www.brookings.edu/~media/research/files/papers/2011/5/energy%20greenstone%20looney/05_energy_greenstone_looney

Hagerman, G. (2008). Design environment for offshore wind: examples from the Mid-

Atlantic [PowerPoint slides]. Retrieved from www.ebcne.org/fileadmin/misc/Hagerman.pdf

Harris, M., Hand, M. & Wright, A. (2006). Lidar for turbine control. Golden, CO: National Renewable Energy Laboratory.

Hasager, C., Alexis, M., Badger, M., Nielsen, M, Astrup, P., & Husson, R. (2009). Satel-

lite winds in EU. Paper presented at the European Wind Energy Conference 2009, Marseilles, France.

Hasager, C.B., Badger, M., Badger, J., Bingaol, F.C., Niels, E., Hahmann, A. N., Kara-

gali, I., & Pena Diaz, A. (2011, March 14-17). Combining satellite wind maps and

mesoscale modeling for a wind atlas of the South Baltic Sea. Paper presented at EWEA Annual Event 2011, Brussels, Belgium.

- Hasager, C.B., Astrup, P., Nielsen, M., Christiansen, M.B., Badger, J., Neilsen, P., Sorenson, P.B. Barthelmie, R.J., Pryor, S.C., & Bergstrom, H. (2007, April). SAT-WIND Project Final Report, from Riso DTU (Danish Tech Univ). Available at http://orbit.dtu.dk/fedora/objects/orbit:79895/datastreams/file_7703216/content
- Hau, E. (2008). Windkraftanlagen, 4th ed. Springer Science+Business Media, Berlin | Germany
- Heimiller, D., Haymes, S., Schwartz, M., Musial, W. (2007). Offshore wind resource potential of the United States. National Renewable Energy Laboratory (Report No. CP-581-43404). Presented at Oceans 2007, Vancouver, BC, Canada.
- Hersbach, H. (2002, September). CMOD5: An improved geophysical model function for ERS C-band scatterometry [Technical Memorandum 000]. Research Department European Center for Medium Range Forecasts.
- Hill, C., & Harris, M. (2010, September). Remote Sensing [Project UpWind WP6 Report on Contract No.:019945 (SES6)Deliverable 6.1.1]. QinetiQ Lidar Measurement Report 15. Available at <http://www.upwind.eu/media/591/D6.1.1-b.pdf>
- Hollinger, J., Lo, R., Poe, G., Savage, R., & Pierce, J. (1987). The special sensor microwave/imager user's guide [Technical Report, pp. 1-120]. Washington, D.C: Naval Research Laboratory.

Hopkins, A. - Yaw control optimization [White paper]. from BlueScout Technologies, downloaded Dec. 20, 2012 from http://www.bluescout.com/files/Yaw_Control_Optimization.pdf

Horstmann, J., Schiller, H., Schulz-Stellenfleth, J, & Lehner, S. (2003 October,). Global wind speed retrieval from SAR. IEEE Transactions On Geoscience And Remote Sensing (41)10, 2277.

Indian Space Research Organisation (2012). Oceansat – 2 [Brochure]. Retrieved November 20, 2012 from <http://www.isro.org/pslv-c14/pdf/Oceansat-2-Brochure-1.pdf#OCEANSAT2>

Intergovernmental Panel on Climate Change (2007). Contribution of Working Group I to the Fourth Assessment Report of the Intergovernmental Panel on Climate Change. Geneva: IPCC. Solomon, S., D. Qin, M. Manning, Z. Chen, M. Marquis, K.B. Averyt, M. Tignor and H.L. Miller (eds.) Cambridge University Press, Cambridge, United Kingdom and New York, NY, USA. (IPCC2007 authors)

International Electrotechnical Commission (2005). Wind turbines – Part 12-1: Power performance measurements of electricity producing wind turbines: Edition 1.0 2005-12. Available at http://webstore.iec.ch/preview/info_iec61400-12-1%7Bed1.0%7Den.pdf

- International Energy Agency (2012). CO2 emissions from fuel combustion highlights: 2012 Edition. Retrieved March 4, 2013 from <http://www.iea.org/co2highlights/co2highlights.pdf>
- Jacobson, M.Z., & Delucchi, M.A. (2011, March). Providing all global energy with wind, water, and solar power, Part I: Technologies, energy resources, quantities and areas of infrastructure, and materials [Electronic version]. *Energy Policy* (39)3, 1154–1169.
- Jet Propulsion Laboratory (2001). Seawinds on QuikSCAT Level 3. Daily, gridded ocean wind vectors [Report]. Pasadena, CA: Physical Oceanography Division, California Institute of Technology .
- Jonkman, J., & Buhl, M. L. (2005, August). FAST user's guide, NREL/EL-500-38230, NREL Report. Golden, CO: National Renewable Energy Laboratory.
- Jonkman, J., & TurbSim, B.J. (2009, September). User's Guide, NREL/TP-500-46198, NREL Report. Golden, CO: National Renewable Energy Laboratory.
- Jonkman, J., Butterfield, S., Musial, W., & Scott, G. (2009, February). Definition of a 5-mw reference wind turbine for offshore system development: technical report NREL/TP-500-38060. Golden, CO: National Renewable Energy Laboratory.

- Karagali et al (2012). -Ioanna Karagali, Merete Badger, Andrea N. Hahmann, Alfredo Peña, Charlotte B. Hasager, Anna Maria Sempreviva. Spatial and temporal variability of winds in the Northern European Seas. *Renewable Energy*, Volume 57, September 2013, Pages 200–210. <http://dx.doi.org/10.1016/j.renene.2013.01.017>
- Karagali, I. (2012). Offshore wind energy: Wind and sea surface temperature from satellite observations (Doctoral dissertation, Danish Technical University, 2012).
- Kelley, N.D., & Jonkman, B.J. (2007, April). Overview of the TurbSim Stochastic Inflow Turbulence Simulator: Version 1.21 (Revised Feb. 1, 2007), NREL/TP-500-41137, NREL Report. Golden, CO: National Renewable Energy Laboratory.
- Kempton, W., Archer, C., Dhanju, A., Garvine, R., & Jacobson, M. (2007). Large CO₂ reductions via offshore wind power matched to inherent storage in energy end uses. *Geophysical Research Letters*, (32). doi:10.1029/2006GL028016
- Korsbakken, E., J. A. Johannessen, & O. M. Johannessen, (1998). Coastal wind field retrievals from ERS synthetic aperture radar images. *Journal of Geophysical Research*, 103, 7857-7874.
- Lackner M.A., van Kuik G.A.M., (2009). Comparison of smart rotor control approaches using trailing edge flaps and individual pitch control. *Wind Energy*, (13), 2-3: 117-134.

- Lange, B., Larsen, S., Hojstrup, J., & Barthelmie, R. (2004). Importance of thermal effects and sea surface roughness for offshore wind resource assessment. *Journal of Wind Engineering and Industrial Aerodynamics*, (92), 11, 959-988.
- Levitt, A.C., Kempton, W., Smith, A.P., Musial, W., & Firestone, J. (2011). Pricing offshore wind power. *Energy Policy* (2011), doi:10.1016/j.enpol.2011.07.044
- Manwell, J.F., Mcgowan, J.G., & Rogers A.L. (2009). *Wind energy explained*, 2nd ed. Sussex, UK: John Wiley & Sons
- Marsden, P.L. *Uncertainties in remote wind sensing with lidars*, Risø R 1681(EN) ISBN 978-87-550-3735-9, Risø DTU National Laboratory for Sustainable Energy, (2009)
- Marsden, P.L., Mortensen, G., & Courtney, M.S. (2009). Are Lidars good enough for resource assessments? Accuracy of AEP predictions in flat terrain generated from measurements by conically scanning Lidars. Paper presented at the 2009 European Wind Energy Conference and Exhibition, Marseilles, France.
- Mears, C. A., D. K. Smith, and F. J. Wentz (2001), Comparison of Special Sensor Microwave Imager and buoy-measured wind speeds from 1987 to 1997, *J. Geophys. Res.*, 106(C6), 11719–11729, doi:10.1029/1999JC000097.
- Meissner, T., & Wentz, F. (2006). *Ocean retrievals for WindSat Radiative Transfer Model, Algorithm*. Retrieved December 12, 2012 from

http://www.remss.com/papers/wind/meissner_wentz_wind_vector_retrieval_rain_IEEE.pdf

Mhyrvold, N. P. & Caldeira, K. (2012). Greenhouse gases, climate change and the transition from coal to low-carbon electricity. *Environmental Research Letters* 7, 14019 (8) doi:10.1088/1748-9326/7/1/014019

Mikkelsen, T., Angelou, N., Hansen, K., Sjöholm, M., Harris, M., Slinger, C., Hadley, P., Scullion, R., Ellis, G. and Vives, G. (2012), A spinner-integrated wind lidar for enhanced wind turbine control. *Wind Energ.* doi: 10.1002/we.1564

Mikkelsen, T., Hansen, K.H., Angelou, N., Sjöholm, M., Harris, M., Hadley, P., Scullion, R., Ellis, G. & Vives, G. (2010, April 20-23). Lidar wind speed measurements from a rotating spinner. Paper presented at the 2010 European Wind Energy Conference and Exhibition, Warsaw, Poland.

Monaldo, F. (2012, June 11-15). [Lecture given at Boulder, CO] SAR wind measurements for wind climatology: Application to wind power. *Remote Sensing for Wind Energy*. Johns Hopkins University Applied Physics Laboratory,

Monaldo, F. M ., Thompson, D. R ., Pichel, G ., & Clemente-Colón,P. (2004). A systematic comparison of QuikSCAT and SAR ocean surface wind speeds. *Geoscience and Remote Sensing*. 42(2), 283-291.

- Monaldo, F. M ., Thompson, D. R., Beal, R. C., Pichel, W. G ., & Clemente-Colón, P .
(2001). Comparison of SAR-derived wind speed with model predictions and buoy comparisons. *Geoscience and Remote Sensing*, 39(12), 2587–2600.
- Monaldo, F., Sherwell, J., & Sparling, L. "Climatology evaluation of offshore Maryland wind resources". American Wind Energy Association Offshore WINDPOWER 2012, Virginia Beach, Virginia, October, 2012.
- Monaldo, F.M., Thompson, D.R., Winstead, N.S., Pichle, W.G.,Clemente-Colon, P., & Christiansen, M.B. (2005). Ocean wind field mapping from synthetic aperture radar and its application to research and applied problems. *Johns Hopkins Applied Technical Digest*, 26(2), 102-113.
- Musial et al 2010 W. Musial, R. Thresher, B. Ram (2010). Large-scale offshore wind energy for the United States: Assessment of opportunities and barriers. Golden, CO: National Renewable Energy Laboratory.
- Musial, W., Butterfield, S. (2004, June 28-29). Future for offshore wind energy in the United States. NREL/CP-500-36313. Proceedings of Energy, Ocean. Palm Beach, Florida.
- Naderi, F., Freilich, M.H., & Long., D.G. (1991, June). Spaceborne radar measurement of wind velocity over the ocean--An overview of the NSCAT Scatterometer System. *Proceedings of the 1991 IEEE* 79 (6): 850-866.

NASA (2012a). QuikSCAT mission and instrument specification sheets. Retrieved November 22, 2012, from <http://podaac.jpl.nasa.gov/OceanWind/QuikSCAT>
<http://podaac.jpl.nasa.gov/datasetlist?ids=Measurement&values=Ocean+Winds&search=>

NASA (2012b). NSCAT mission and instrument specification sheets. Retrieved November 22, 2012 from <http://podaac.jpl.nasa.gov/OceanWind/NSCAT>

NASA 2013 - QuikSCAT specifications from NASA website downloaded 12 Jan 2013 from <http://winds.jpl.nasa.gov/missions/quikscat/index.cfm>

National Data Buoy Center (2013). Information on NDBC data and program accessed on 2/12/13 at <http://www.ndbc.noaa.gov/>

National Oceanic and Atmospheric Administration (2012). QuikSCAT coastal and 25 km products. Available from <http://manati.star.nesdis.noaa.gov/datasets/QuikSCAT-Data.php?parname=ww2/>

National Oceanic and Atmospheric Administration National Data Buoy Center (2009). NDBC Technical Document 09-02: Handbook of automated data quality control checks and procedures. National Data Buoy Center Stennis Space Center, Mississippi: U.S. Department of Commerce.

Naval Facilities Engineering Services Center (NFESC) (2012). Request for Task Order Proposal No. N62583-09-RFTOP: Validation of floating offshore wind measurement systems. RFP issued May, 2012.

- NESDIS 2007- National Environmental Satellite, Data, and Information Service (2007, March). Special Sensor Microwave Imager and Sounder (SSMIS) Antenna Brightness Temperature Data Record (TDR) Calibration and Validation User Manual. Washington, D.C.: Center for Satellite Applications and Research, National Oceanic and Atmospheric Administration.
- Nielsen, P., EMD, (2002). Case studies calculating wind farm production. Retrieved January 12, 2013 from <http://www.emd.dk/projects/Projekter/20%20Detailed%20Case%20Studies/Document%20Information.pdf>
- Olmsted, C. (1993). Alaska SAR facility scientific SAR user's guide. Retrieved from <http://www.asf.alaska.edu/sites/all/files/documents/sci-sar-userguide.pdf>
- O'Neill, L.W., Chelton, D.B., & Esbensen, S.K. (2010). The effects of SST-induced surface wind speed and direction gradients on midlatitude surface vorticity and divergence. *Journal of Climatology*, 255-281. 23 (2), 255-28. Available at <http://hdl.handle.net/1957/27725>
- Orr, J.C., Fabry, V.J., Aumont, O., Bopp, L., Doney, S.C. (2005). Anthropogenic ocean acidification over the twenty-first century and its impact on calcifying organisms. *Science* 437, 681-686
- OSI-SAF (2012) Online Ocean and Sea Ice Satellite Application Facility wind map product accessed through http://www.knmi.nl/scatterometer/ascat_osi_co_prod/ascat_app.cgi on Nov. 10 2012

- Peña A. Sensing the wind profile. Risø-PhD-45(EN) ISBN 978-87-550-3709-0, Risø DTU, 80 pp. (2009)
- Pena, A. and S.-E. Gryning, (2008). Charnock's roughness length model and non-dimensional wind profiles over the sea. *Boundary Layer Meteorology.*, 128, 191-203.
- Pena, A., C. B. Hasager, S.-E. Gryning, M. Courtney, I. Antoniou, and T. Mikkelsen, (2008). Offshore wind profiling using light detection and ranging measurements. *Wind Energy*, 12, 105-124. <http://130.226.56.153/rispubl/reports/ris-phd-45.pdf>
- Pena, A., Mikkelsen, T., Gryning, S.-E., Hasager, C.B., Hahmann, A.N., Badger, M., Kargali, I., & Courtney, M., (2012, August). Offshore vertical wind shear: Final report on NORSEWIND's work task 3.1. [DTU Wind Energy-E-Report-0005(EN)]. Retrieved from http://orbit.dtu.dk/fedora/objects/orbit:114358/datastreams/file_10591005/content
- Pena, A., S.-E. Gryning, and C. B. Hasager, (2008): Measurements and modelling of the wind speed profile in the marine atmospheric boundary layer. *Boundary Layer Meteorology*, 129, 479-495.
- Pichel, W. G., & Clemente-Colón, P. (2000, January). NOAA coast watch SAR applications and demonstration. Johns Hopkins Applied Physics Laboratory Technical Digest 21(1), 49-57.
- Pielke, Roger A., Sr. (2002). *Mesoscale Meteorological Modeling*. San Diego, C: Academic Press.

- Plagge, A.M., & Long, D.G. (2009, July). Coastal validation of ultra-high resolution wind vector retrieval from QuikSCAT in the Gulf of Maine. *IEEE Geoscience And Remote Sensing Letters* (6)3, (413-417).
- Plant, W.J., & Zurk, L.M. (1997). Dominant wave directions and significant wave heights from synthetic aperture radar imagery of the ocean. *Journal of Geophysical Research*, 102(C2), 3473–3482. doi:10.1029/96JC03674
- Pryor, S.C. (2004). Satellite information for wind energy applications. [Report No. Risø-R-1479(EN)]. Roskilde, Denmark: Risø National Laboratory.
- Pryor, S.C., Nielsen, M., Barthelmie, R.J., Mann, J. (2004), Can satellite sampling of offshore wind speeds realistically represent wind speed distributions? Part II: Quantifying Uncertainties Associated with Distribution Fitting Methods, *Journal of Applied Meteorology*, (43) 739-750.
- Ricciardulli, R., & Wentz, F. (2011). Reprocessed QuikSCAT (V04) wind vectors with Ku-2011 geophysical model function [Remote Sensing Systems Technical Report 0430111]. Retrieved from http://www.remss.com/qscat/qscat_Ku2011_tech_report.pdf
- Rogers, A. L., et al (2011). Innovative Methods for Offshore Wind Resource Assessment. Presentation poster at European Wind Energy Association Conference, Brussels, Belgium.

Rogers, A.L., (2011b). Innovative Methods for Offshore Wind Resource Assessment.
Presentation of 12 Oct. 2011.

Rogers, A.L., Hagerman, G., Howe, G., (2012). Lowering offshore wind energy costs through effective metocean measurement and modeling. Poster presentation at American Wind Energy Association Offshore Wind Power 2012 Conference & Exhibition, Virginia Beach, VA.

RSS 2013 –Information retrieved from Remote Sensing Systems website at
(http://www.remss.com/ssmi/ssmi_browse.html)

Rutherford A., Pitter, M., Slinger, C. des Roziers E., , Barker, W. , Harris, M. The effect of motion on continuous wave lidar wind measurements. Poster presented at WINDPOWER 2013, Chicago, May 5-8, 2013.

Schlipf et al 2009- D. Schlipf, J. J. Trujillo, V. Basterra, and M. Kuhn (2009). Development of a wind turbine LIDAR simulator, presentation at European Wind Energy Conference, 2009.

Schlipf et al 2012 (a) - David Schlipf, D., Do Schlipf, D.J., & Kühn, M., (2012). Nonlinear model predictive control of wind turbines using LIDAR Wind Energy. Sussex, UK: John Wiley and Sons, Ltd. doi:10.1002/we.1533.

Schlipf et al 2012 (b) - Schlipf, D., Anger, J., Bischoff, O., , M. Hofsaß, M., Rettenmeier, A., Würth, I., Siegmeier, B., & Cheng, P.W. (2012b). Lidar Assisted Wind

Turbine Control. Poster presented at RAVE 2012 Bremerhaven, Germany, May 8-9, 2012.

Schlipf, D. (2012). Lidar assisted control of wind turbines [White paper]. Retrieved from http://rasei.colorado.edu/wind-research-internal1/David_Schlipf.pdf

Schlipf, D., Bossanyi, E., Carcangui, C.E., Fischer, T., Maul, T., & Rossetti, M.(2011, February 11). "LIDAR assisted collective pitch control" Project UpWind]. Stuttgart, Germany: University of Stuttgart.

Schlipf, D., Kapp, S., Anger, J., Bischoff, O., Hofsäß, M., Rettenmeier, A., Smolka, U., & Kühn, M. (2011b). Prospects of Optimization of Energy Production by LiDAR Assisted Control of Wind Turbines, Wind Energy. Poster presented at EWEA Annual Event 2011, Brussels, Belgium.

Schubel, P.J., & Crossley, R.J., (2012) Wind turbine blade design. *Energies* 2012(5) 3425-3449. doi:10.3390/en5093425. available at <http://www.mdpi.com/1996-1073/5/9/3425>

Schwartz, M., Elliot, D., Haymes, S., Heimiller, D. Scott, G., Flowers L. Brower, M., Hale, E., Phelps, B. (2010). 80 and 100 Meter Wind Energy Resource Potential for the United States 2010. Available online at www.windpoweringamerica.gov/pdfs/wind_maps/poster_2010.pdf.

- Schwartz, M., Heimiller, D., Haymes, S., Musial, H.W. (2010). Assessment of offshore wind energy resources for the United States. Golden, CO: National Renewable Energy Laboratory.
- SGURR (2013). Galion produces 1st image of offshore wakes ever captured by a nacelle-mounted lidar [Press release]. Retrieved March 2, 2013, from <http://www.sgurrenergy.com/first-results-from-sgurrenergy-areva-wind-measurement-campaign/>
- Simley, E., Pao, L.Y., Frehlich, R., Jonkman, B., & Kelley, N., (2011). Analysis of wind speed measurements using continuous wave LIDAR for wind turbine control. Paper presented at the 49th AIAA Aerospace Sciences Meeting/New Horizons Forum and Aerospace Exposition 4 - 7 January 4-7, 2011, Orlando, Florida.
- Skou, N. and Le Vine, David (1989). Microwave radiometer systems: design and analysis. Norwood, MA: Artech House.
- Smith, M., (2012, January 26). An insight into Lidars for offshore wind measurements [PowerPoint presentation]. Retrieved from http://www.sintef.no/project/Deepwind%202012/Deepwind%20presentations%202012/C2/Smith_M.pdf
- Soltani, M., Wisniewski, R., Brath, P., & Boyd, S. (2011). - Load reduction of wind turbines using receding horizon control. Proceedings of the 2011 IEEE International Conference on Control Applications, pp. 852-857.

Soprano (2013). Wakes behind Horn Rev 1 & 2 wind farms [SAR figure]. Retrieved from <http://soprano.cls.fr/?p=1159>

SSMI 2013 –Information about SSMI Systems retrieved from http://www.ssmi.com/ssmi/ssmi_description.html

Stoffelen, A., Anderson, D.L. (1997). Scatterometer data interpretation: Estimation and validation of the transfer function CMOD4. *Journal of Geophysical Resources*, (102), 5767-5780.

Taylor, G.I., (1938). The spectrum of turbulence. *Proceedings of the Royal Society of London*, London, UK, 164, 476–490.

Thevenoud, J.M., Boquet, M., Thobois, L. Davoust, S., (2012). Lidar for offshore applications. PO. ID 287, poster presented at 2012 European Wind Energy Association Exposition, Copenhagen, Denmark.

Thompson, D. R., J. Horstmann, J., Mouche, A., Winstead, N.S., Sterner, R., & Monaldo, F.M. (2012). Comparison of high-resolution wind fields extracted from TerraSAR-X SAR imagery with predictions from the WRF mesoscale model. *Journal of Geophysical Research*, 117. doi:10.1029/2011JC007526.

Thompson, D.R., Moaldo, F.M., Horstmann, J., & Christiansen, M.B. (2008). Geophysical model functions for the retrieval of ocean surface winds. *Proceedings of SEASAR 2008-Advances in SAR Oceanography from ENVISAT and ERS missions*, Frascati, Italy, European Space Agency, Special Publication SP-656

Tindal 2012a.- Tindal, A. 2012. GL GH position statement on the WINDCUBE Remote Sensing Device. GL Technical Note 111593-UKBR-T-02. Issued Nov. 2, 2012

Tindal 2012b. -Tindal, A. 2012. GL GH position statement on the ZephIR Remote Sensing Device. GL Technical Note 111593-UKBR-T-01. Issued Nov. 2, 2012

Troen, I., & Petersen, E. L., (1989). European wind atlas, Roskilde, Denmark: Risø National Laboratory.

U.S. Energy Information Administration (2013). Annual Electric Generator Report (Form EIA-860) and U.S. Energy Information Administration, Monthly Update to the Annual Electric Generator Report (Form EIA-860M).

UD 2011 - Wilmington Canyon Study -UD/DOE GrantDOE Research Project Titled "System Design Optimized for a LargeTurbine Wind Farm near Wilmington Canyon", FY 11 Offshore Wind:Technology Development Funding No. 0000415. Information available at (http://www1.eere.energy.gov/wind/pdfs/offshore_energy_projects.pdf)

UPWIND (2011a). UpWind Work Package 5, Design limits and solutions for very large wind turbines [Report 21895]. Roskilde, Denmark: Riso National Laboratory. Available at http://www.ewea.org/fileadmin/ewea_documents/documents/upwind/21895_UpWind_Report_low_web.pdf

UPWIND (2011b). UpWind Work Package 6, Remote Sensing. Final Report, Deliverable D6.17, M. Courtney, Risoe, Danish Technical University, 10 Feb 2011.

Available at http://www.upwind.eu/media/645/D6.17.1_Final_Report.pdf

Verhoefen, A., & Stoffelen, A., (2011, July). ASCAT coastal winds validation report.

[Technical Note SAF/OSI/CDOP/KNMI/TEC/RP/176, Product OSI-104, July 2011]. Available from http://www.knmi.nl/scatterometer/publications/pdf/ASCAT_validation_coa.pdf

Weibull, W. (1951). A statistical distribution function of wide applicability. Transactions Of The American Society Of Mechanical Engineers, Journal Of Applied Mechanics 18(3): 293-297.

Westerhellweg, A., Canadillas, B., Beeken, A., & Neumann, T. (2010). One year Of Lidar measurements at Fino1-Platform: Comparison and verification to Met-Mast data. Paper presented at the 10th German Wind Energy Conference 2010, Wilhelmshaven, Germany. Available at http://www.leosphere.com/file/1829186232010_11_17_dewek_lidar_final.pdf

WindSat 2013a.- Information retrieved on Nov. 12 2012 from <http://po-daac.jpl.nasa.gov/windsat>

WindSat 2013b.- Specifications retrieved Nov. 12 2012 from <http://www.nrl.navy.mil/WindSat/Description.php>

WindSat 2013c.- Data retrieved Nov. 12 2012 from http://www.ssmi.com/windsat/windsat_data_description.html

Wisseman, C. (2009). IOOS offshore wind energy meeting [PowerPoint slides]. Available at http://marine.rutgers.edu/cool/coolresults/2009/ioos_020209/GSOE%20-%20IOOS%20Rutgers%20-%20020209.ppt!!

Yueh, S.H., Kwok, R., & Nghiem,, S.V. (1994). Polarimetric scattering and emission properties of targets with reflection symmetry," *Radio Science* (29)6, 1409-1420.

Zhang, H.-M., Bates, J.J., & Reynolds, R.W. (2006). Assessment of composite global sampling: Sea surface wind speed. *Geophysical Research Letters*, (33).
doi:10.1029/2006GL027086.

Appendix A – MAXIMUM THEORETICAL COVERAGE

Theoretical daily coverage at each latitude or parallel can be estimated based on the instrument's scan width (SW) and the circumference of the earth along that parallel as follows:

Taking the latitude of Cape May as representative of the MAB, the circumference of the globe at 39 degrees N is 31,186 km. Neglecting 8 degrees of orbital inclination⁶², this circumference divided by the scan width yields the number of scans that would provide full coverage at the 39th parallel if spaced evenly and contiguously. Sun synchronous orbits circle the earth about every 100 minutes, in which time the earth rotates ~ 25 degrees, so the ground track is shifted west by about 25 degrees on each orbit; this is the precession rate⁶³.

Although in reality there are gaps and overlap, the precession of the orbit means the gaps shift position with each orbit, so the coverage averages out very quickly. This provides

⁶² Sun synchronous orbital inclination is ~ 8 degrees, so the “effective” scan width (SW_E) is actually: $(\cos 8^\circ \times SW) \Rightarrow 0.99 \times SW$

⁶³ The “precession rate” is the rotation of the earth during one full satellite orbit.

roughly the same number of scans per year for all points along the same parallel. There are some differences due to the orbital inclination, but these are not significant at the latitudes investigated. At a latitude of 39 degrees, each degree of longitude covers about 86.6 km, so 25 degrees covers about 2166 km. Each satellite completes approximately 14.4 orbits per 24 hrs, and each orbit crosses the parallel twice, so, neglecting orbital inclination and downtime, the expression for maximum theoretical percent daily coverage as a function of effective scan width is:

$$\begin{aligned} \% \text{ Coverage} &= (\text{Swath Width}) \times (\text{orbits per day}) \times (\text{equatorial crossings per orbit}) / \\ &(\text{Length of the parallel}) \\ &= (\text{SW}) \times (14.4) \times (2) / (L) \end{aligned}$$

Where the length, L, of any parallel can be found by

$$\begin{aligned} L &= \text{circumference of equator} \times \cos(\text{latitude}) \\ &= 6378 \text{ km} \times \cos(\text{latitude}) \end{aligned}$$

The study area is at a latitude of 39N and many of the reviewed studies cover the North Sea, at a latitude around 56N. The ratio of the lengths of the two parallels (39th to 56th) is the ratio of the cosines of the two latitudes.

cos 39 =	0.78
cos 56 =	0.56
ratio C39/C56	1.393

This ratio is useful for translating scan density between the two latitudes.

Using this basic formula, the maximum theoretical coverages for each instrument are given below.

	Satellite/Instrument	Max Swath Width (km)	Daily Coverage		Scans/yr	
			39 th paral.	56 th paral.	39 th paral.	56 th paral.
Synthetic Aperture (SAR)	ERS-1/SAR/ (1)	100	9%	13%	34	47
	ERS-2/SAR	100	9%	13%	34	47
	RADARSAT-1	500	46%	64%	169	234
	RADARSAT-2	500	46%	64%	169	234
	EnviSAT/ASAR	400	37%	51%	135	187
Scatterometers	ERS-1/ESCAT(8)	400	37%	51%	135	187
	ERS-2/ESCAT(8)	400	37%	51%	135	187
	Metop-A/ASCAT(7)	1000	92%	128%	337	468
	Metop-B/ASCAT(7)	1000	92%	128%	337	468
	SeaWinds/QuikSCAT	1800	166%	231%	607	843
	OceanSAT/SCAT	1400	129%	180%	472	656
PMI	F11 – F 17 SSM/I	1400	129%	180%	472	656

Scatterometry and PMI coverage is relatively simple to estimate, since scan width is fixed. In principle, two satellite passes per day should produce two wind products per day for a given node or location. In practice, the number of scans is reduced by scrubbing to remove corrupted data and by systems downtime for (remote) maintenance, testing, etc. There is also downtime for re-setting the instrument between scans.

SAR coverage is complicated in practice by numerous different swath patterns causing uncertainty about the average effective scan width. For this reason, the estimates rely more on actual database queries.

Appendix B – REPRINT PERMISSIONS

Note – Many of the figures used come from publicly funded, open access U.S. , U.K., and E.U. government-published studies where reprint permission is implicitly granted.

The permissions and authorizations below are for the remainder of the figures, where reprint permission was sought and obtained.

Figure 3, Figure 55

----- Forwarded message -----
From: **Bruce Williams** <brucew@udel.edu>
Date: Thu, May 2, 2013 at 1:16 PM
Subject: reprint permissions
To: mboquet@leosphere.fr

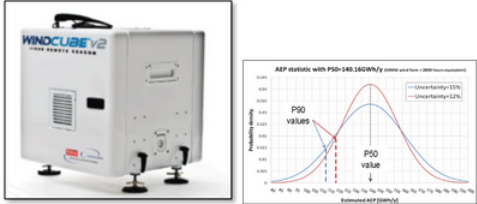
Hello Matthieu - I'm a graduate student at Univ of Delaware, and I would like to use the following two figures in my masters thesis, which will be published in electronic format on the University server only. The first is from the Leosphere web site and the second is from your paper presented at EWEC 2010 Warsaw. The source will be properly cited in my thesis. Evan Osler has provided me with the latest product info and specifications. I have also provided a link to the draft in case you are interested. It is a literature survey of Lidar technology and satellite radar/radiometry systems, entitled "New Remote Sensing Technologies for Offshore Wind Power".

<https://www.dropbox.com/s/t7ef0hxq3humemg/Williams%20thesis%2029%20Apr.docx>

If you or Leosphere are the copyright holders and there is no problem with my intended use, a simple affirmative response to this email is sufficient.

Thanks, and Regards,
Bruce

Bruce M. Williams
Fellow, Marine Science and Policy
University of Delaware
cel [410 330 4479](tel:410-330-4479)
brucew@udel.edu
Skype ID [brucemorganwilliams](#)



Jean-Marc THEVENOUD <jmthevenoud@leosphere.com> 3:01 AM (5 hours ago) ☆

to Matthieu, me ▾

Hi Bruce,

You can use the 2 pictures.

Regards,

Jean-Marc

De : Bruce Williams [brucew@udel.edu]
Envoyé : jeudi 2 mai 2013 19:22
À : jmthevenoud@leosphere.fr
Objet : Fwd: reprint permissions

Figure 4 , Figure 17

FW: reprint permission CRM:0007757 Inbox x

Matt Smith <matt@zephirlidar.com> 7:23 AM (2 hours ago) ☆

to me

Images are not displayed.
Display images below - Always display images from matt@zephirlidar.com

Bruce

I am happy for you to use this as long as it is described as early prototype work and that it's unfiltered.

Context – the ZephIRs were 800m apart and although the islands were low they will have had some minimal effect. This early test was to prove that the broad concept was worthy of further development.

Without creating too much work for myself I want to ask what more you could do with. I've attached a poster that is going to AWEA this year that offers some current information. Ecofys – whom you mention issued the attached positioning statement for WC and ZephIR. I'd also suggest looking around our recently updated publications section on www.windlidar.com

Please consider this email as permission to use the image of the ZephIR lidar that you identified.

I'm going to pass your draft to our scientists to see whether they can add anything; although time may prevent a thorough review.... I will explain it's a draft

I look forward to seeing the final version

Good Luck

Matt

Matt Smith
ZephIR Sales

ZephIR Lidar
wind speed at light speed

tel: [+44 1531 651 004](tel:+441531651004)
mobile: [+44 7787 158 197](tel:+447787158197)
email: matt@zephirlidar.com

ZephIR is a registered trademark of ZephIR Ltd., a registered company (SC177881) in Scotland. Our Registered Office is The Greenhouse, Dalry, Castle Douglas, DG7 3XS, UK.
[Disclaimer](#)

Please note our email addresses have now changed – update your contact details for me as soon as you can!

From: Jim Adams
Sent: 24 April 2013 8:36 PM
To: Matt Smith
Subject: Fwd: reprint permission

Howdy sir,

Please see the note below. Can you get back to him?

Thanks and hope you're well!

Jim Adams
[518.867.6090](tel:5188676090)

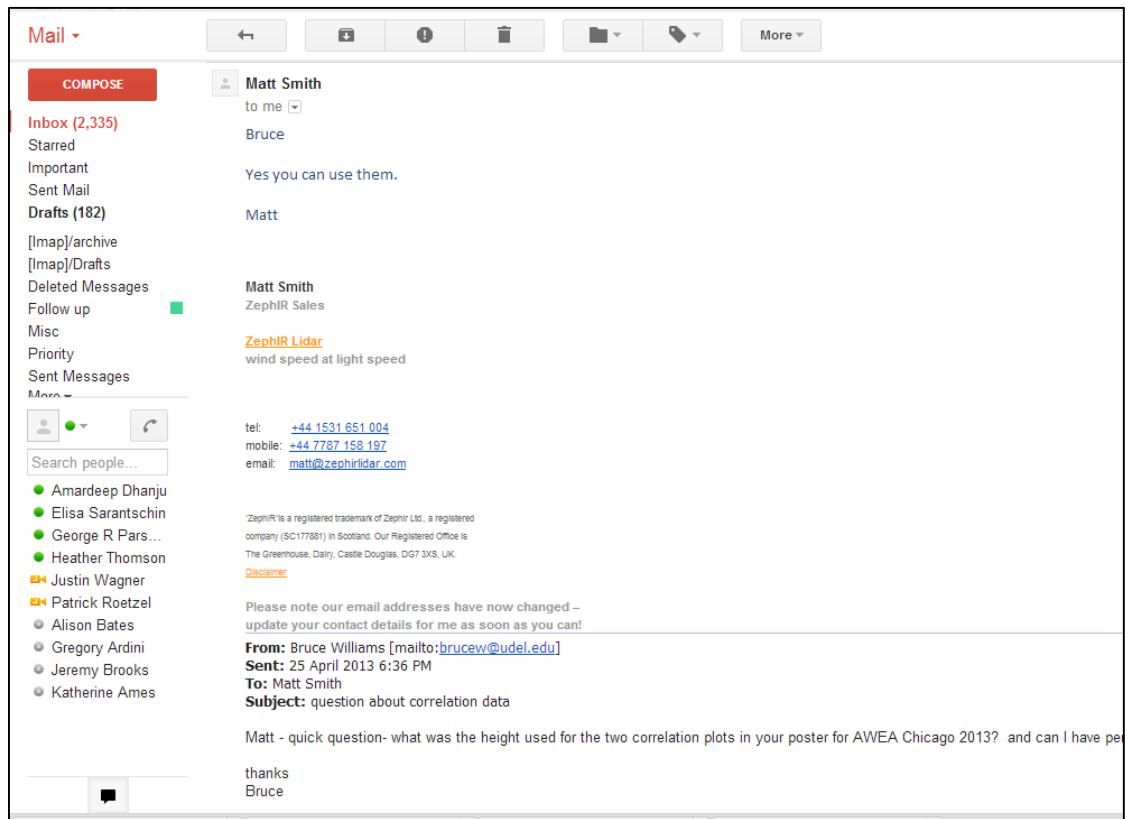
Begin forwarded message:

From: Bruce Williams <brucew@udel.edu>
Date: April 24, 2013, 15:22:21 EDT
To: Jim Adams <jima@naturalpower.com>
Subject: reprint permission

Hi Jim - can you put me in touch with Matt Smith in your UK office? I'm seeking reprint permission to use a figure in one of his presentations (see below). Or -do you know who manages the copyright for the figure? It's from a SeazephIR validation trial in 2009.

Wind speed time series data from height 90m above sea level:
SeaZephIR data in red
LandZephIR data in blue
Data plotted here from 5-23 November 2009
inline image 1

Figure 4



Figures 5 and 6


Rightslink Printable L

https://s100.copyright.com/AppDispatchServlet

**JOHN WILEY AND SONS LICENSE
TERMS AND CONDITIONS**

Apr 23, 2013

This is a License Agreement between Bruce M Williams ("You") and John Wiley and Sons ("John Wiley and Sons") provided by Copyright Clearance Center ("CCC"). The license consists of your order details, the terms and conditions provided by John Wiley and Sons, and the payment terms and conditions.

All payments must be made in full to CCC. For payment instructions, please see information listed at the bottom of this form.

License Number	3135000165609
License date	Apr 23, 2013
Licensed content publisher	John Wiley and Sons
Licensed content publication	Wind Energy
Licensed content title	Offshore wind profiling using light detection and ranging measurements
Licensed copyright line	Copyright © 2008 John Wiley & Sons, Ltd.
Licensed content author	Alfredo Peña,Charlotte Bay Hasager,Sven-Erik Gryning,Michael Courtney,Ioannis Antoniou,Torben Mikkelsen
Licensed content date	Sep 24, 2008
Start page	105
End page	124
Type of use	Dissertation/Thesis
Requestor type	University/Academic
Format	Electronic
Portion	Figure/table
Number of figures/tables	3
Original Wiley figure/table number(s)	Figures 5, 6, 8
Will you be translating?	No
Total	0.00 USD
Terms and Conditions	

TERMS AND CONDITIONS

Confirmation Number: 11088870
Order Date: 04/29/2013

If you pay by credit card, your order will be finalized and your card will be charged within 24 hours. If you pay by invoice, you can change or cancel your order until the invoice is generated.

Payment Information

Bruce Williams
brucew@udel.edu
+1 (410)3304479
Payment Method: n/a

Order Details

Boundary-layer meteorology

Order detail ID: 63627023
Order License Id: 3138280907041

Permission Status:  **Granted**

Permission type: Republish or display content use in a thesis/dissertation

Article Title: Charnock's Roughness Length Model and Non-dimensional Wind Profiles Over the Sea

Type of use: [View details](#)

Author(s): Peña, Alfredo ; Gryning, Sven-Erik
DOI: 10.1007/S10546-008-9285-Y
Date: Jan 01, 2008
ISSN: 0006-8314
Publication Type: Journal
Volume: 128
Issue: 2
Start page: 191
Publisher: SPRINGER-VERLAG DORDRECHT

Note: This item will be invoiced or charged separately through CCC's **RightsLink** service. More info **\$ 0.00**

Total order items: 1 **Order Total: 0.00 USD**

Confirmation Number: 11088872
Order Date: 04/29/2013

If you pay by credit card, your order will be finalized and your card will be charged within 24 hours. If you pay by invoice, you can change or cancel your order until the invoice is generated.

Payment Information

Bruce Williams
brucew@udel.edu
+1 (410)3304479
Payment Method: n/a

Order Details

Boundary-layer meteorology

Order detail ID: 63627041
Order License Id: 3138281247989

Permission Status:  **Granted**

Permission type: Republish or display content
Type of use: use in a thesis/dissertation

Article Title: Measurements and Modelling of the Wind Speed Profile in the Marine Atmospheric Boundary Layer

[View details](#)

Author(s): Peña, Alfredo ; Gryning, Sven-Erik ; Hasager, Charlotte B.

DOI: 10.1007/S10546-008-9323-9

Date: Dec 01, 2008

ISSN: 0006-8314

Publication Type: Journal

Volume: 129

Issue: 3

Start page: 479

Publisher: SPRINGER-VERLAG DORDRECHT

Note: This item will be invoiced or charged separately through CCC's **RightsLink** service. [More info](#)

\$ 0.00

Total order items: 1

Order Total: 0.00 USD

Figure 7

Drive Calendar Sites Groups Contacts Mobile More »

Search

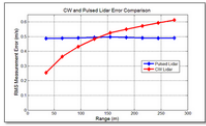
← [Icons] More ▾

Bruce Williams <brucew@udel.edu> Apr 24 (8 days ago) ☆ ↶ ▾
to eric.simley ▾

Hi Eric - I'm a grad student at Univ. of Delaware, and I have a quick question - Where would I obtain reprint permission for Figure 13, below, from the AIAA white paper titled "Analysis of Wind Speed Measurements using Continuous Wave LIDAR for Wind Turbine Control y Simley et al" 49th AIAA Aerospace Sciences Meeting including the New Horizons Forum and Aerospace Exposition 4 - 7 January 2011, Orlando, Florida

I tried to find the paper at Wiley and Elsevier, and a few others, but no luck. I would like to use it in my master's thesis which will be published in electronic form only on the University of Delaware web site, open access, no paywall. It is an overview of remote sensing technologies for offshore wind applications. I also attached a link to my draft thesis if you're interested, although it is NOT for release. All comments appreciated.

<https://www.dropbox.com/s/t7ef0hxq3humemg/Williams%20thesis%2029%20Apr.docx>



Range (m)	CW Error (m/s)	Pulsed Error (m/s)
0	0.2	0.2
100	0.25	0.2
200	0.3	0.2
300	0.35	0.2
400	0.38	0.2
500	0.4	0.2

...

Eric Simley 2:45 AM (6 hours ago) ☆ ↶ ▾
to me ▾

Bruce,

Sorry for the late reply. If you just reference the 2011 AIAA paper in the figure caption that should be fine. I look forward to checking out your thesis soon.

...

Figures 8 and 9

← + ! 🗑️ 📁 📧 More ▾

 **Bruce Williams** <brucew@udel.edu> 2:11 PM (22 hours ago) ☆ ↩️ ▾

to a.westerhellweg ▾

Hi Annette - - I am a grad. student at the University of Delaware. How do I request permission to reprint two figures (Figures 5 and 6) from the paper you presented at DEWEK 2010 on the Lidar verification campaign? They will be used, with proper citation, if allowed, in my master's thesis which will be published in electronic form only on the University of Delaware web site, open access, no paywall. It is a broad summary of remote sensing technologies for offshore wind power. It is still a draft, not for release, but I have included a link if you would like to preview it.

<https://www.dropbox.com/s/p98nxcif15s96z3u/Williams%20thesis%2010%20Apr.docx>

thank you,
Bruce

...

 **DEWI - A. Westerhellweg** 5:40 AM (6 hours ago) ☆ ↩️ ▾

to me ▾

Dear Bruce,

of course you can print the two figures.

Thank you for sending the link to your work. It is very interesting. When it is finished I would be pleased if you could you send me the link to the master work?

I wish you good luck and success in you work!
If you have any questions please do not hesitate to contact me.

Best regards,

Annette

Figures 10-12

JOHN WILEY AND SONS LICENSE TERMS AND CONDITIONS	
	Apr 23, 2013
<p>This is a License Agreement between Bruce M Williams ("You") and John Wiley and Sons ("John Wiley and Sons") provided by Copyright Clearance Center ("CCC"). The license consists of your order details, the terms and conditions provided by John Wiley and Sons, and the payment terms and conditions.</p>	
<p>All payments must be made in full to CCC. For payment instructions, please see information listed at the bottom of this form.</p>	
License Number	3134971424014
License date	Apr 23, 2013
Licensed content publisher	John Wiley and Sons
Licensed content publication	Wind Energy
Licensed content title	A spinner-integrated wind lidar for enhanced wind turbine control
Licensed copyright line	Copyright © 2012 John Wiley & Sons, Ltd.
Licensed content author	T. Mikkelsen, N. Angelou, K. Hansen, M. Sjöholm, M. Harris, C. Slinger, P. Hadley, R. Scullion, G. Ellis, G. Vives
Licensed content date	Oct 16, 2012
Start page	n/a
End page	n/a
Type of use	Dissertation/Thesis
Requestor type	University/Academic
Format	Electronic
Portion	Figure/table
Number of figures/tables	3
Original Wiley figure/table number(s)	Figures 4, 6, 7
Will you be translating?	No
Total	0.00 USD
Terms and Conditions	TERMS AND CONDITIONS
<p><small>This copyrighted material is owned by or exclusively licensed to John Wiley & Sons, Inc. or one of</small></p>	

Figure 13

LinkedIn

Peter Clive has sent you a message.

Date: 4/30/2013

Subject: RE: reprint permission for Gallion image

Hi Bruce

We are delighted for you to use material that we have already placed in the public domain, such as this image, as long as you attribute it appropriately.

On another note, I felt the pioneering role played by the Gallion Lidar since 2008 in the wind industry was not as well represented as it might be - almost everything you allude to can be illustrated with a Gallion example, it isn't just a device for measuring wakes.

I would like to send you through some more papers and presentations if you like?

Warm regards

Peter

On 04/24/13 11:26 AM, Bruce Williams wrote:

Hello Dr. Clive- I'm a grad student at Univ. of Delaware, and I have a quick question - can you grant copyright permission for me to reprint the Gallion image from the press release linked below? I would like to use it in my master's thesis which will be published in electronic form only on the University of Delaware web site, open access, no paywall. It is an overview of remote sensing technologies for offshore wind applications. I also attached a link to my draft thesis if you're interested, although it is NOT for release. All comments appreciated.

<https://www.dropbox.com/s/t7ef0hxq3humemq/Williams%20thesis%2029%20Apr.docx>

<http://www.squrenergy.com/first-results-from-squrenergy-areva-wind-measurement-campaign/>

Thanks and Regards,
Bruce Williams
Fellow, Graduate Researcher, Offshore Wind Power
Univ. of Delaware

Figure 15, 16

mail.google.com/mail/u/0/?shva=1#inbox/13e41e9ee991d0bd?compose=13e52c57df086876

Drive Calendar Sites Groups Contacts Mobile More »

to j.mathisen

Hi Jan Petter - I'm a grad student at Univ. of Delaware, and I'm collecting reprint permissions for a few graphics I would like to use in my May 2013 masters thesis. Are you the copyright holder, and can you grant permission to use Figure 2.6, and Figure 4.8 from "Measurements of Wind Profile from a Buoy using Lidar" Report Reference No: 9631 of 5 June 2012 (figures included below)?

My masters thesis will be published in electronic form only, on the University servers, open access. It is an overview of remote sensing technologies for offshore wind. I included a link, below if you are interested in reading the draft, although it is not finished, and not for public release. All comments are appreciated.

<https://www.dropbox.com/s/t7ef0hxq3humemg/Williams%20thesis%2029%20Apr.docx>

Thanks and Regards,
Bruce

Mathisen, Jan Petter [FOAS] 1:26 PM (27 minutes ago)

to me

Bruce

You can use the figures in your master thesis

Good luck with your thesis!

Best regards
Jan-Petter Mathisen
Kolstadunet 7A
7098 Saupstad
email: j.mathisen@online.no
Tel: [+47 91566279](tel:+4791566279)

Fra: Bruce Williams [brucew@udel.edu]
Sendt: 25. april 2013 18:50
Til: Mathisen, Jan Petter [FOAS]
Emne: Fwd: Bruk av artikkel

Figure 19

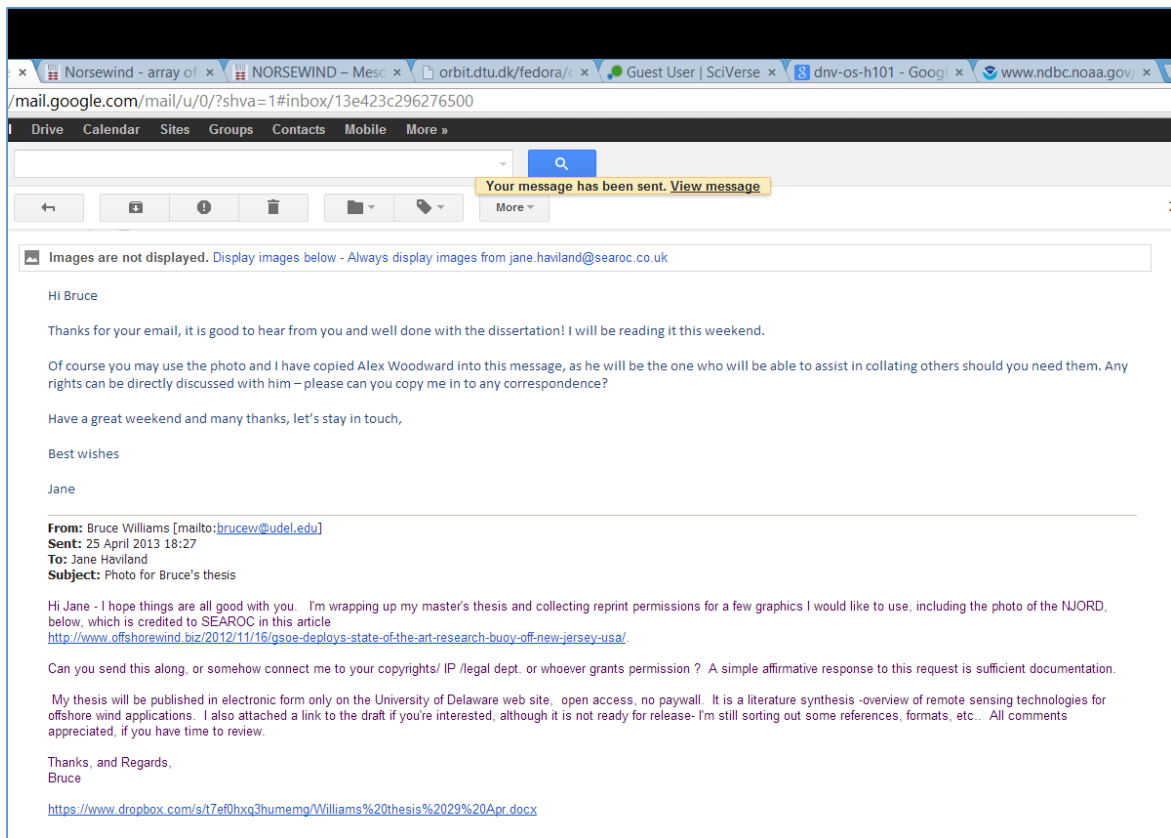


Figure 24, 27.

://mail.google.com/mail/u/0/?shva=1#inbox/13e3dd7556438d03?compose=13e52c57df086876

mail Drive Calendar Sites Groups Contacts Mobile More »

Search

← [Attachments] [Attachments] [Attachments] [Attachments] [Attachments] More ▾

Bruce Williams <brucew@udel.edu> Apr 24 (5 days ago) ☆ ↶ ▾
to Merete ▾

Hi Merete - I'm trying to obtain reprint permission for Figure 6- 1 and Figure 9-3 from your PhD Dissertation - Rise-PhD-27(EN) Wind Energy Applications of Synthetic Aperture Radar.

but I can't find it on Orbit and I don't know who manages the copyrights. Can you help?

These are the color SAR images of Denmark and surrounding seas, and a closer color SAR image of Horns Rev.

My thesis will be published in electronic form only on the University of Delaware web site, open access, no paywall. It is a literature synthesis -overview of remote sensing technologies for offshore wind applications. I also attached a link to the draft if you're interested, although it is not ready for release- I'm still sorting out some references, formats, etc... All comments appreciated, if you have time to review.

Thanks, and Regards,
Bruce

<https://www.dropbox.com/s/t7ef0hxq3humemg/Williams%20thesis%2029%20Apr.docx>

Bruce M. Williams
Fellow, Marine Science and Policy
University of Delaware
cel 410 330 4479
brucew@udel.edu
Skype ID brucemorganwilliams

...

Merete Badger 7:30 AM (3 hours ago) ☆ ↶ ▾
to me ▾

Hi Bruce,

Thanks for your interest. My PhD thesis can be found here: <http://www.risoe.dtu.dk/rispubl/VEA/veapdf/ris-phd-27.pdf>

You are welcome to use the two figures you mention for your own thesis – please make sure the source is stated for both. As far as I understand, the author has the copyright of any publication, unless a copyright transfer has taken place. I have not transferred the copyright for this work.

I wish you all the best for your dissertation process. I have just returned from two weeks of vacation so I am a bit too busy to read your manuscript at this point. But please keep me informed when the final version is out.

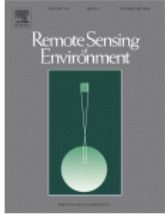
New!

Figure 24



RightsLink[®]

Home
Account Info
Help



Title: Wake effects of large offshore wind farms identified from satellite SAR

Author: Merete Bruun Christiansen, Charlotte B. Hasager

Publication: Remote Sensing of Environment

Publisher: Elsevier

Date: 15 October 2005

Copyright © 2005, Elsevier

Logged in as:
Bruce Williams

Account #:
3000645309

LOGOUT

Order Completed

Thank you very much for your order.

This is a License Agreement between Bruce M Williams ("You") and Elsevier ("Elsevier"). The license consists of your order details, the terms and conditions provided by Elsevier, and the [payment terms and conditions](#).

[Get the printable license.](#)

License Number	3135551043296
License date	Apr 24, 2013
Licensed content publisher	Elsevier
Licensed content publication	Remote Sensing of Environment
Licensed content title	Wake effects of large offshore wind farms identified from satellite SAR
Licensed content author	Merete Bruun Christiansen, Charlotte B. Hasager
Licensed content date	15 October 2005
Licensed content volume number	98
Licensed content issue number	2-3
Number of pages	18
Type of Use	reuse in a thesis/dissertation
Portion	figures/tables/illustrations
Number of figures/tables/illustrations	3
Format	electronic
Are you the author of this Elsevier article?	No
Will you be translating?	No
Order reference number	
Title of your thesis/dissertation	New Remote Sensing Technologies for Offshore Wind Power
Expected completion date	May 2013
Estimated size (number of pages)	240
Elsevier VAT number	GB 494 6272 12
Permissions price	0.00 USD
VAT/Local Sales Tax	0.00 USD

Figure 29

JOHNS HOPKINS
UNIVERSITY

Applied Physics Laboratory
11100 Johns Hopkins Road
Laurel MD 20722-6099
240-228-5000 / Washington
443-778-5000 / Baltimore

April 29, 2013

Bruce M. Williams
110 Regulator Dr.
Cambridge, MD 21613

Dear Mr. Williams:

You have requested from the Johns Hopkins University/Applied Physics Laboratory LLC (JHU/APL) copyrights in the figure, shown in Appendix A attached hereto, taken from Francis M. Monaldo's presentation entitled "SAR Wind Measurements for Wind Climatology: Application to Wind Power," given at Summer School in Remote Sensing for Wind Energy, Boulder, Colorado, June 11-15, 2012 ("Material") for publication in your Master's Thesis entitled "New Remote Sensing Technologies for Offshore Wind Power," Marine Policy, College of Earth, Ocean and Environment, University of Delaware, Newark Delaware, in or about May 2013 ("Requested Use").

JHU/APL hereby grants to you a non-exclusive, royalty-free, non-transferable, worldwide right and license to copy, distribute, and publicly display the Material for the Requested Use. Any further use above and beyond the Requested Use must be authorized by advance, written permission of JHU/APL.

In return, you agree to defend, indemnify and hold harmless JHU/APL, The Johns Hopkins University, their present and former regents, trustees, officers, inventors/creators/developers of the Material, agents, faculty, employees, and students as against any and all judgments, fees, expenses, losses or other costs arising from or incidental to any lawsuit, claim, demand or other action brought as a consequence of the practice of the Material, or derivative works thereof, by any of the foregoing entities, whether or not JHU/APL, The Johns Hopkins University, or said inventors/creators/developers, either jointly or severally, is named as a party defendant in any such lawsuit.

FURTHER, YOU AGREE THAT THE MATERIAL IS PROVIDED "AS IS", AND THAT JHU/APL MAKES NO REPRESENTATION OR WARRANTY WITH RESPECT TO THE PERFORMANCE OF THE MATERIAL INCLUDING ITS SAFETY, EFFECTIVENESS, OR COMMERCIAL VIABILITY. JHU/APL DISCLAIMS ALL WARRANTIES WITH REGARD TO THE MATERIAL, INCLUDING, BUT NOT LIMITED TO, ALL WARRANTIES, EXPRESS OR IMPLIED, OF MERCHANTABILITY AND FITNESS FOR ANY PARTICULAR PURPOSE, AND NON-INFRINGEMENT OF THIRD PARTY PROPRIETARY RIGHTS. JHU/APL ADDITIONALLY DISCLAIMS ALL OBLIGATIONS AND LIABILITIES ON THE PART OF JHU/APL AND

Mr. Williams
Page 2

INVENTORS/CREATORS/DEVELOPERS, FOR DAMAGES, INCLUDING, BUT NOT LIMITED TO, DIRECT, INDIRECT, SPECIAL, AND CONSEQUENTIAL DAMAGES, ATTORNEYS' AND EXPERTS' FEES, AND COURT COSTS (EVEN IF JHU/APL HAS BEEN ADVISED OF THE POSSIBILITY OF SUCH DAMAGES, FEES OR COSTS), ARISING OUT OF OR IN CONNECTION WITH THE-MANUFACTURE, USE, SALE, OR PRACTICE OF THE MATERIAL OR DERIVATIVE WORKS THEREOF. YOU ASSUME ALL RESPONSIBILITY AND LIABILITY FOR LOSS OR DAMAGE CAUSED BY A PRODUCT MANUFACTURED, USED, OR SOLD, OR A SERVICE PRACTICED, BY LICENSEE AND ITS AFFILIATED COMPANIES WHICH USES THE MATERIAL OR DERIVATIVE WORKS THEREOF.

Except to cite JHU/APL as the source of the Material, you may not use or make reference to JHU/APL's name (or that of any affiliate or constituent parts, including, but not limited to, The Johns Hopkins University), logo or marks in any manner whatsoever.

You may not assign or sublicense your rights hereunder.

If the foregoing statements accurately reflect our agreement relative to this matter, please execute the statement of agreement appearing below on the enclosed copy of this letter and return the executed copy to me.

If you have any questions, please contact me at phone: (443) 778-4386; facsimile: (443) 778-5254; or e-mail: noah.hayward@jhuapl.edu.

Yours truly,



Noah J. Hayward, Esq.
Assistant General Counsel (IP)

Figure 32

Thank you for your... x Rightslink Printabl... x NASA - Quiet Sun

← → ↻ <https://s100.copyright.com/CustomerAdmin/PLF.jsp?>

**ELSEVIER LICENSE
TERMS AND CONDITIONS**

Apr 24, 2013

This is a License Agreement between Bruce M Williams ("You") and Elsevier ("Elsevier") provided by Copyright Clearance Center ("CCC"). The license consists of your order details, the terms and conditions provided by Elsevier, and the payment terms and conditions.

All payments must be made in full to CCC. For payment instructions, please see information listed at the bottom of this form.

Supplier	Elsevier Limited The Boulevard, Langford Lane Kidlington, Oxford, OX5 1GB, UK
Registered Company Number	1982084
Customer name	Bruce M Williams
Customer address	110 regulator dr cambridge, MD 21613
License number	3135450179032
License date	Apr 24, 2013
Licensed content publisher	Elsevier
Licensed content publication	Renewable Energy
Licensed content title	Combining meteorological stations and satellite data to evaluate the offshore wind power resource of Southeastern Brazil
Licensed content author	Felipe Pimenta, Willett Kempton, Richard Garvine
Licensed content date	November 2008
Licensed content volume number	33
Licensed content issue number	11
Number of pages	13
Start Page	2375
End Page	2387
Type of Use	reuse in a thesis/dissertation
Intended publisher of new work	other
Portion	figures/tables/illustrations
Number of figures/tables/illustrations	2
Format	electronic
Are you the author of this Elsevier article?	No
Will you be translating?	No
Order reference number	
Title of your thesis/dissertation	New Remote Sensing Technologies for Offshore Wind Power
Expected completion date	May 2013
Estimated size (number of pages)	240
Elsevier VAT number	GB 494 6272 12
Permissions price	0.00 USD
VAT/Local Sales Tax	0.0 USD / 0.0 GBP
Total	0.00 USD
Terms and Conditions	

INTRODUCTION

1. The publisher for this copyrighted material is Elsevier. By clicking "accept" in

Figure 33

Drive Calendar Sites Groups Contacts Mobile More »

10 of

Bruce Williams <brucew@udel.edu> 1:39 PM (20 hours ago)

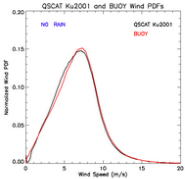
to support ▾

Hello - I'm a grad student at Univ. of Delaware, and I have a quick question - can you grant copyright permission for me to reprint Figure 1 from the TR cited (link below) ?

I would like to use it in my master's thesis which will be published in electronic form only on the University of Delaware web site, open access, no paywall. It is an overview of remote sensing technologies for offshore wind applications. I also attached a link to my draft thesis if you're interested, although it is NOT for release. All comments appreciated.

<https://www.dropbox.com/s/t7ef0hxq3humemg/Williams%20thesis%2029%20Apr.docx>

Remote Sensing Systems Technical Report 0430111
Reprocessed QuikSCAT (V04) Wind Vectors with Ku-2011
Geophysical Model Function
Lucrezia Ricciardulli and Frank Wentz



If approved, you can simply respond in the affirmative to this email, confirming you are the copyright holder.

Thanks, and Regards,
Bruce

RSS Support 7:48 PM (14 hours ago)

to support_box, me ▾

Hi Bruce,
You may use the figure with the authors permission.
Sincerely,
Deborah

Deborah K. Smith
DISCOVER Project Scientist
Support Services
Remote Sensing Systems
support@remss.com
www.discover-march.org

Figure 35

mCoiCartPurchase.do?operation=confirmPurchase

Get Permission / Find Title

[Advanced Search Options](#) **Go**

1 PAYMENT 2 REVIEW 3 **CONFIRMATION**

Step 3: Order Confirmation

[Start new search >](#) [View your Order History >](#)

Print order information: includes order confirmation, terms and conditions, and citation information [\(What's this?\)](#)

Thank you for your order! A confirmation for your order will be sent to your account email address. If you have questions about your order, you can call us at 978-646-2600, M-F between 8:00 AM and 6:00 PM (Eastern), or write to us at info@copyright.com.

Confirmation Number: 11088877
Order Date: 04/29/2013

If you pay by credit card, your order will be finalized and your card will be charged within 24 hours. If you pay by invoice, you can change or cancel your order until the invoice is generated.

Payment Information

Bruce Williams
 brucew@udel.edu
 +1 (410)3304479
 Payment Method: n/a

Order Details

Renewable energy

<p>Order detail ID: 63627130 Order License Id: 3138290747894 Article Title: Spatial and temporal variability of winds in the Northern European Seas Author(s): Karagali, Ioanna ; et al DOI: 10.1016/J.RENENE.2013.01.017 Date: Jan 01, 2013 ISSN: 0960-1481 Publication Type: Journal Volume: 57 Issue: Start page: 200 Publisher: PERGAMON Author/Editor: SAYIGH, A A M. ; et al</p>	<p>Permission Status: ✔ Granted Permission type: Republish or display content Type of use: reuse in a thesis/dissertation View details</p>
---	--

Note: This item will be invoiced or charged separately through CCC's **RightsLink** service. [More info](#) **\$ 0.00**

Figure 38, 39, Table 13


https://s100.copyright.com/AppDispatchServlet
Rightslink Printab

**JOHN WILEY AND SONS LICENSE
TERMS AND CONDITIONS**

Apr 23, 2013

This is a License Agreement between Bruce M Williams ("You") and John Wiley and Sons ("John Wiley and Sons") provided by Copyright Clearance Center ("CCC"). The license consists of your order details, the terms and conditions provided by John Wiley and Sons, and the payment terms and conditions.

All payments must be made in full to CCC. For payment instructions, please see information listed at the bottom of this form.

License Number	3134970018824
License date	Apr 23, 2013
Licensed content publisher	John Wiley and Sons
Licensed content publication	Journal of Geophysical Research: Oceans
Licensed content title	Comparison of Special Sensor Microwave Imager and buoy-measured wind speeds from 1987 to 1997
Licensed copyright line	Copyright 2001 by the American Geophysical Union.
Licensed content author	C. A. Mears, Deborah K. Smith, Frank J. Wentz
Licensed content date	Sep 20, 2012
Start page	11719
End page	11729
Type of use	Dissertation/Thesis
Requestor type	University/Academic
Format	Electronic
Portion	Figure/table
Number of figures/tables	2
Original Wiley figure/table number(s)	Figure 6, Table 3
Will you be translating?	No
Total	0.00 USD

Terms and Conditions

TERMS AND CONDITIONS

This copyrighted material is owned by or exclusively licensed to John Wiley & Sons, Inc. or one of

Figure 40

 **Bruce Williams** <brucew@udel.edu> Apr 18 (5 days ago) ☆ ↶ ▾
to kheideman ▾

Hi Ken - I'm trying to obtain permission to use a portion of a figure published in 2004 (citation below) in my master's thesis which will be electronically published in May 2013 on the University of Delaware internal servers only, which are open access, with no pay-wall. The portion of the figure is used to support a broader analysis of wind statistics, which supports my analysis of remote sensing technologies. It is my understanding that this falls under fair use, but I'd rather be safe than sorry. I sent an email to "permissions@ametsoc.org" but it bounced back.

Figure 3, specifically the upper right quadrant which gives data for buoy No. 44004.
Journal of Applied Meteorology
MAY 2004 P R Y O R E T A L . pp- 739-750
American Meteorological Society
"Can Satellite Sampling of Offshore Wind Speeds Realistically Represent Wind Speed Distributions? Part II: Quantifying Uncertainties Associated with Distribution Fitting Methods"
S. C. PRYOR, M. NIELSEN, R. J. BARTHELMIE, J. MANN

Please let me know asap if you need any more info, or there is a problem, or if I'm going about this the wrong way.....

Thank you,
Bruce M. Williams

 **Ken Heideman** Apr 18 (5 days ago) ☆ ↶ ▾
to me ▾

Hi Bruce. Permission is granted provided standard attribution (citation) is given.

Best,
Ken

Kenneth F. Heideman
Director of Publications
American Meteorological Society
President, Council of Science Editors
45 Beacon St.
Boston, Ma. 02108

Figure 48 permission

...

 **Bruce Bailey** Apr 18 (5 days ago) ☆ ↶ ▼

to me ▾

Hi Bruce:

AWS Truepower is the copyright holder to Figure 48 of your document. We grant consent to the use of that figure in your thesis.

Best regards,

Bruce

Bruce H. Bailey
President/CEO
AWS Truepower, LLC
463 New Karner Road
Albany, NY 12205
phone: [518-213-0044](tel:518-213-0044) (ext 1003)
fax: [518-213-0045](tel:518-213-0045)
bbailey@awstruepower.com
www.awstruepower.com

 **AWS Truepower™**

CONFIDENTIALITY NOTICE: This electronic mail transmission is intended for the use of the individual or entity to which it is addressed and may contain confidential information which is privileged by law. If you are not the intended recipient, you are hereby notified that any disclosure, copying, distribution, or the taking of any action in reliance on the contents of this information is strictly prohibited. If you have received this transmission in error, please notify the sender immediately by e-mail and delete the original message.

From: Bruce Williams [<mailto:brucew@udel.edu>]
Sent: Thursday, April 18, 2013 1:07 PM
To: Bruce Bailey

Figure 50, Table 22, excerpts

The screenshot shows a Gmail interface with a browser window at the top. The address bar shows a Gmail URL. The navigation bar includes links for Drive, Calendar, Sites, Groups, Contacts, Mobile, and More. The main content area displays an email titled "reprint permission" in the "Inbox".

The first email is from Bruce Williams <brucew@udel.edu> to bakers1, sent at 2:10 PM (54 minutes ago). The body text reads: "Hey Scott - I hope things are good with you. I'm rounding up reprint permissions for my thesis, and I'd like to use your Fig. 12 and Table 6 - the depth zone map and the energy production summary table, and also quote a few paragraphs from your thesis. In my draft thesis (link below), they are all in section 5.2.2 <https://www.dropbox.com/s/t7ef0hxq3humemg/Williams%20thesis%2029%20Apr.docx> As far as I know, you are still the copyright holder, and a simple affirmative response to this email is sufficient. Thanks, and Best Regards, Bruce".

The second email is from bakers1@pjm.com to me, sent at 3:02 PM (2 minutes ago). The body text reads: "Bruce, You have my approval. Thanks for the email and good luck on the defense! Best, Scott".

At the bottom of the email thread, there is a text box with a link that says "Click here to Reply or Forward".

The footer of the Gmail interface includes: "9% full Using 2.3 GB of your 25 GB", "©2013 Google - Terms of Service - Privacy Policy - Program Policies", "Powered by Google", and "Last account activity: 1 hour ago Details".

Figure 51-53

Rightslink Printable License

<https://s100.copyright.com/AppDispatchServlet>

**JOHN WILEY AND SONS LICENSE
TERMS AND CONDITIONS**

Apr 23, 2013

This is a License Agreement between Bruce M Williams ("You") and John Wiley and Sons ("John Wiley and Sons") provided by Copyright Clearance Center ("CCC"). The license consists of your order details, the terms and conditions provided by John Wiley and Sons, and the payment terms and conditions.

All payments must be made in full to CCC. For payment instructions, please see information listed at the bottom of this form.

License Number	3134970563171
License date	Apr 23, 2013
Licensed content publisher	John Wiley and Sons
Licensed content publication	Wind Energy
Licensed content title	US East Coast offshore wind energy resources and their relationship to peak-time electricity demand
Licensed copyright line	Copyright © 2012 John Wiley & Sons, Ltd.
Licensed content author	Michael J. Dvorak, Bethany A. Corcoran, John E. Ten Hoeve, Nicolas G. McIntyre, Mark Z. Jacobson
Licensed content date	Jul 25, 2012
Start page	n/a
End page	n/a
Type of use	Dissertation/Thesis
Requestor type	University/Academic
Format	Electronic
Portion	Figure/table
Number of figures/tables	2
Original Wiley figure/table number(s)	Figure 2, 3, 4
Will you be translating?	No
Total	0.00 USD
Terms and Conditions	

TERMS AND CONDITIONS

Figure 52

Drive Calendar Sites Groups Contacts Mobile More »

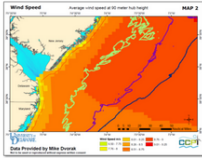
reprints Inbox x

Bruce Williams <brucew@udel.edu> 6:09 PM (15 hours ago) ☆

to Alison ▾

Hi Alison - Can you grant permission for a reprint of the figure below, for use in my May 2013 master's thesis (in which it is Figure 52)? Mike Dvorak already approved his data use, and JF indicated you are the primary author of the figure.

thanks,
Bruce



Alison Bates 7:23 PM (14 hours ago) ☆

to me ▾

I approve.

Congrats on finishing!

Do you want me to send you the original? Can send it to you in pdf or jpg.

On Apr 24, 2013, at 6:09 PM, Bruce Williams <brucew@UDeI Edu> wrote:

Figure 56

Copyright Clearance Center

Welcome, Bruce
Not you?

Log out | Cart (0) | Manage Account | Feedback | Help | Live Help

GET PERMISSION | LICENSE YOUR CONTENT | PRODUCTS AND SOLUTIONS | PARTNERS | EDUCATION | ABOUT US

Get Permission / Find Title
energy policy
Advanced Search Options

1 PAYMENT | 2 REVIEW | 3 CONFIRMATION

Step 3: Order Confirmation

[Start new search >](#) [View your Order History >](#)

Print order information: includes order confirmation, terms and conditions, and citation information [\(What's this?\)](#)

Thank you for your order! A confirmation for your order will be sent to your account email address. If you have questions about your order, you can call us at 978-646-2600, M-F between 8:00 AM and 6:00 PM (Eastern), or write to us at info@copyright.com.

Confirmation Number: 11087764
Order Date: 04/23/2013

If you pay by credit card, your order will be finalized and your card will be charged within 24 hours. If you pay by invoice, you can change or cancel your order until the invoice is generated.

Payment Information

Bruce Williams
brucew@udel.edu
+1 (410)3304479
Payment Method: n/a

Order Details

Energy policy

Order detail ID:	63620568	Permission Status:	Granted
Order License Id:	3134910666067	Permission type:	Republish or display content
Article Title:	Pricing offshore wind power	Type of use:	reuse in a thesis/dissertation
Author(s):	Levitt, Andrew C. ; et al	<input type="checkbox"/> View details	
DOI:	10.1016/J.ENPOL.2011.07.044		
Date:	Oct 01, 2011		
ISSN:	1873-6777		
Publication Type:	e-Journal		
Volume:	39		
Issue:	10		
Start page:	6408		
Publisher:	Elsevier Science		

Figure 61

reprint permission. Inbox x 🗑️ 🖨️ 📎

 **Bruce Williams** <brucew@udel.edu> 4:24 PM (59 minutes ago) ☆ ↩️ ▼
to lackner ▼

Hi Dr. Lackner - - I'm a grad student at Univ. of Delaware, and I have a quick question - can you grant copyright permission to reprint slides 7, 9, and 13 from your presentation of 4/3/09 (link below) ?
If allowed, they will be used in my master's thesis which will be published in electronic form only on the University of Delaware web site, open access, no paywall. It is an overview of remote sensing technologies for offshore wind applications. I also attached a link to my draft thesis if you're interested, although it is not ready for release.

Regards, and thanks,
Bruce

<https://www.dropbox.com/s/rqzdkxtv2ypbl71/Pitch%20Control%20Lackner.pdf>
<https://www.dropbox.com/s/t7ef0hq3humemg/Williams%20thesis%202029%20Apr.docx>

 **Matthew Lackner** 4:49 PM (34 minutes ago) ☆ ↩️ ▼
to me ▼

Hi Bruce,

Sure, no problem. Wow, that was awhile ago!

Good luck finishing up.

 Click here to [Reply](#) or [Forward](#)

9% full ©2013 Google - Terms of Service - Privacy Policy - Program

Figure 63

<https://store.copyright.com/AppDispatchServlet>

**JOHN WILEY AND SONS LICENSE
TERMS AND CONDITIONS**

Apr 23, 2013

This is a License Agreement between Bruce M Williams ("You") and John Wiley and Sons ("John Wiley and Sons") provided by Copyright Clearance Center ("CCC"). The license consists of your order details, the terms and conditions provided by John Wiley and Sons, and the payment terms and conditions.

All payments must be made in full to CCC. For payment instructions, please see information listed at the bottom of this form.

License Number	3135001262532
License date	Apr 23, 2013
Licensed content publisher	John Wiley and Sons
Licensed content publication	Wind Energy
Licensed content title	Nonlinear model predictive control of wind turbines using LIDAR
Licensed copyright line	Copyright © 2012 John Wiley & Sons, Ltd.
Licensed content author	David Schlipf, Dominik Johannes Schlipf, Martin Kühn
Licensed content date	Aug 17, 2012
Start page	n/a
End page	n/a
Type of use	Dissertation/Thesis
Requestor type	University/Academic
Format	Electronic
Portion	Figure/table
Number of figures/tables	3
Original Wiley figure/table number(s)	Figure 9.10, Table VIII
Will you be translating?	No
Total	0.00 USD

Terms and Conditions

TERMS AND CONDITIONS

This copyrighted material is owned by or exclusively licensed to John Wiley & Sons, Inc. or one of

Figure 64, 65



[Home](#)
[Account Info](#)
[Help](#)



Requesting permission to reuse content from an IEEE publication

Title: Load reduction of wind turbines using receding horizon control

Conference Proceedings: Control Applications (CCA), 2011 IEEE International Conference on

Author: Soltani, M.; Wisniewski, R.; Brath, P.; Boyd, S.

Publisher: IEEE

Date: 28-30 Sept. 2011

Copyright © 2011. IEEE

Logged in as:
Bruce Williams
Account #: 3000645309

LOGOUT

Thesis / Dissertation Reuse

The IEEE does not require individuals working on a thesis to obtain a formal reuse license, however, you may print out this statement to be used as a permission grant:

Requirements to be followed when using any portion (e.g., figure, graph, table, or textual material) of an IEEE copyrighted paper in a thesis:

- 1) In the case of textual material (e.g., using short quotes or referring to the work within these papers) users must give full credit to the original source (author, paper, publication) followed by the IEEE copyright line © 2011 IEEE.
- 2) In the case of illustrations or tabular material, we require that the copyright line © [Year of original publication] IEEE appear prominently with each reprinted figure and/or table.
- 3) If a substantial portion of the original paper is to be used, and if you are not the senior author, also obtain the senior author's approval.

Requirements to be followed when using an entire IEEE copyrighted paper in a thesis:

- 1) The following IEEE copyright/ credit notice should be placed prominently in the references: © [year of original publication] IEEE. Reprinted, with permission, from [author names, paper title, IEEE publication title, and month/year of publication]
- 2) Only the accepted version of an IEEE copyrighted paper can be used when posting the paper or your thesis on-line.
- 3) In placing the thesis on the author's university website, please display the following message in a prominent place on the website: In reference to IEEE copyrighted material which is used with permission in this thesis, the IEEE does not endorse any of [university/educational entity's name goes here]'s products or services. Internal or personal use of this material is permitted. If interested in reprinting/republishing IEEE copyrighted material for advertising or promotional purposes or for creating new collective works for resale or redistribution, please go to http://www.ieee.org/publications_standards/publications/rights/rights_link.html to learn how to obtain a License from RightsLink.

If applicable, University Microfilms and/or ProQuest Library, or the Archives of Canada may supply single copies of the dissertation.

BACK
CLOSE WINDOW

Copyright © 2013 Copyright Clearance Center, Inc. All Rights Reserved. [Privacy statement](#).
 Comments? We would like to hear from you. E-mail us at customercare@copyright.com

Creative Commons License (Figures xxxxx)

Copyright Clearance x Republication x Creative Commons - x

0/



Attribution 3.0 Unported (CC BY 3.0)

This is a human-readable summary of the [Legal Code \(the full license\)](#).

[Disclaimer](#)

You are free:

- to **Share** — to copy, distribute and transmit the work
- to **Remix** — to adapt the work
- to make commercial use of the work



Under the following conditions:

-  **Attribution** — You must attribute the work in the manner specified by the author or licensor (but not in any way that suggests that they endorse you or your use of the work).

With the understanding that:

- Waiver** — Any of the above conditions can be **waived** if you get permission from the copyright holder.
- Public Domain** — Where the work or any of its elements is in the **public domain** under applicable law, that status is in no way affected by the license.
- Other Rights** — In no way are any of the following rights affected by the license:
 - Your fair dealing or **fair use** rights, or other applicable copyright exceptions and limitations;
 - The author's **moral** rights;
 - Rights other persons may have either in the work itself or in how the work is used, such as **publicity** or privacy rights.

Blanket permission for DTU-Orbit Studies (in addition to/redundant with explicit permissions above)

reprint permissions Inbox x

Bruce Williams <brucew@udel.edu> Apr 29 (1 day ago) ☆

to orbit ▾

Hello - what is the best way to obtain reprint permissions for publication of DTU Orbit? I would like to use several figures from several DTU reports and dissertations in my own masters thesis, which will be published in electronic format only on the university server. Is there a centralized process or do I need to contact each author individually?

thank you

...

Melissa Kia Gleie Just <melju@dtic.dtu.dk> 6:58 AM (8 hours ago) ☆

to me ▾

Hi Bruce

We do not have a specific procedure for this, and as long as you cite properly, there should be no problems. If you are unsure in some cases, you have to contact the authors.

Kind regards

Melissa Just

Melissa Kia Gleie Just
Information consultant
DTU Library

Technical University of Denmark **DTU**
Technical Information Center of Denmark
Anker Engelunds Vej 1 P.O. Box 777
Building 101D
DK - 2800 Kgs. Lyngby
Denmark

Blanket Permission for UpWind Figs (Schlipf-in addition to/redundant w/ explicit permissions above)

UPwind reports and copyright Inbox x

Bruce Williams <brucew@udel.edu> 5:18 PM (16 ho)
to Hans.e.joergen. ▾
Hello Hans - I'm a graduate student at Univ of Delaware, and was wondering:
Are the Work Packages from Project UpWIND copyrighted, or are they OK for public re-use?

I would like to use several figures from Upwind WP6 reports in my masters thesis, which will be published in electronic format on the University server only.

Can you tell me how to proceed if reprint permission is required? Or is proper citation within my thesis sufficient?

thanks
...

Hans Ejsing Jørgensen <haej@dtu.dk> 4:25 AM (4 ho)
to me ▾
Please go ahead , and remember to use the righth citations. Then everything should be fine

/hans

Sendt fra min iPad

Den 30/04/2013 kl. 23.26 skrev "Bruce Williams" <brucew@udel.edu>:
...

Click here to [Reply](#) or [Forward](#)

9% full
Using 2.3 GB of your 25 GB

©2013 Google - [Terms of Service](#) - [Privacy Policy](#) - [Program Policies](#)
Powered by Last ad